INTERFACING COMPREHENSIVE ROTORCRAFT ANALYSIS WITH ADVANCED AEROMECHANICS AND VORTEX WAKE MODELS

A Thesis
Presented to
The Academic Faculty

by

Haiying Liu

In Partial Fulfillment
of the Requirements for the Degree
Doctor of Philosophy in the
School of Aerospace Engineering

Georgia Institute of Technology
April 2008

INTERFACING COMPREHENSIVE ROTORCRAFT ANALYSIS WITH ADVANCED AEROMECHANICS AND VORTEX WAKE MODELS

Approved by:

Professor Olivier A. Bauchau,
Committee Chair
School of Aerospace Engineering
Georgia Institute of Technology

Professor Olivier A. Bauchau, Advisor
School of Aerospace Engineering
Georgia Institute of Technology

Professor Dewey H. Hodges
School of Aerospace Engineering
Georgia Institute of Technology

Professor Massimo Ruzzene
School of Aerospace Engineering
Georgia Institute of Technology

Professor Erian A. Armanios
School of Aerospace Engineering
Georgia Institute of Technology

Professor Michael P. Stallybrass
School of Mathematics
Georgia Institute of Technology

Date Approved: December 10 2007

To

my dear parents and siblings

ACKNOWLEDGEMENTS

I would like to express my wholehearted gratitude and appreciation to Prof. Olivier A. Bauchau, who has been my thesis advisor, for his wisdom, patience, generosity, and guidance, which have been uniquely instrumental in the successful completion of this thesis.

I would also like to express my sincere gratitude to my thesis committee members: Profs. Dewey H. Hodges, Massimo Ruzzene, Erian A. Armanios, and Michael P. Stallybrass for taking the time to read and evaluate my thesis and giving valuable comments to improve it.

I would like to give my special thanks to Prof. Hodges who initially recruited me, so that I could come to the Georgia Institute of Technology to pursue my Ph.D. degree and get a chance to study and work with Prof. Bauchau.

Also, special thanks to Prof. Zvi Rusak at Rensselaer Polytechnic Institute who has provided me with insightful suggestions and generous help. In addition, I would like to extend my appreciation to Prof. Lakshmi Sankar for his kindness, patience, and warm-hearted help. As well, I would also like to thank Dr. Beatrice Roget at the National Institute of Aerospace for her unselfish help.

I would like to thank the students in our group at the Georgia Institute of Technology for their encouragement and help, in particular, Changkuan Ju, Alexander Epple, Afifa Adel Zaki, Shang Zhou, Jielong Wang, Huimin Song, Chang-Yong Lee, Jimmy Ho, Eric Lynch, Roxana Vasilescu. I feel fortunate to get to know and work with you all.

I am also grateful to my friends for their caring about me all the time, particularly, Ling Zhang, Zhaohui Tong, Bo Gong, Huafen Hu, Haiyan Deng, Wei He, Jin Tang,

Dongning Zhao, Jingshu Wu, and Fei Qian, who have accompanied me and helped me overcome the difficulties encountered during my Ph.D. study here at Georgia Tech.

In the meantime, I want to thank my high-school classmate and life-long friend Dr. Hui Wang, who is always standing beside me to share my unhappiness and happiness at any time and keep encouraging me to get through toughness in my life.

Finally, but most importantly, I would like to thank my parents, my sister and brother for their love, support and encouragement. Without them I could not have succeeded in completing this thesis.

This work was sponsored by the National Rotorcraft Technology Center and the Rotorcraft Industry Technology Association under contract WBS No. 2003-B-01-01.1-A1; Dr. Yung Yu is the contract monitor.

TABLE OF CONTENTS

LIST OF TABLES

LIST OF FIGURES

SUMMARY

This dissertation describes three aspects of the comprehensive rotorcraft analysis. First, a physics-based methodology for the modeling of hydraulic devices within multibody-based comprehensive models of rotorcraft systems is developed. This newly proposed approach can predict the fully nonlinear behavior of hydraulic devices, and pressure levels in the hydraulic chambers are coupled with the dynamic response of the system. The proposed hydraulic device models are implemented in a multibody code and calibrated by comparing their predictions with test bench measurements for the UH-60 helicopter lead-lag damper. Predicted peak damping forces were found to be in good agreement with measurements, while the model did not predict the entire time history of damper force to the same level of accuracy. The proposed model evaluates relevant hydraulic quantities such as chamber pressures, orifice flow rates, and pressure relief valve displacements. This model could be used to design lead-lag dampers with desirable force and damping characteristics.

The second part of this research is in the area of computational aeroelasticity, in which an interface between computational fluid dynamics (CFD) and computational structural dynamics (CSD) is established. This interface enables data exchange between CFD and CSD with the goal of achieving accurate airloads predictions. In this work, a loose coupling approach based on the delta-airloads method is developed in a finite-element method based multibody dynamics formulation, DYMORE. To validate this aerodynamic interface, a CFD code, OVERFLOW-2, is loosely coupled with a CSD program, DYMORE, to compute the airloads of different flight conditions for Sikorsky UH-60 aircraft. This loose coupling approach has good convergence

characteristics. The predicted airloads are found to be in good agreement with the experimental data, although not for all flight conditions. In addition, the tight coupling interface between the CFD program, OVERFLOW-2, and the CSD program, DYMORE, is also established.

The ability to accurately capture the wake structure around a helicopter rotor is crucial for rotorcraft performance analysis. In the third part of this thesis, a new representation of the wake vortex structure based on Non-Uniform Rational B-Spline (NURBS) curves and surfaces is proposed to develop an efficient model for prescribed and free wakes. NURBS curves and surfaces are able to represent complex shapes with remarkably little data. The proposed formulation has the potential to reduce the computational cost associated with the use of Helmholtz's law and the Biot-Savart law when calculating the induced flow field around the rotor. An efficient free-wake analysis will considerably decrease the computational cost of comprehensive rotorcraft analysis, making the approach more attractive to routine use in industrial settings.

CHAPTER I

INTRODUCTION

1.1 Lead-lag Dampers

Helicopters are versatile machines with rotors or rotating wings. The clear advantage of helicopters is their capability to take off or land vertically and hover in the air. For conventional helicopters, both the lift and propulsive force are provided by a main rotor. In reaction to the torque generated due to the high-speed rotation of main rotor, a tail rotor is designed as an anti-torque device to balance the helicopter. Meanwhile, tail rotors provide yaw control.

Typically, rotor blades or rotating wings are relatively long, soft beam structures compared to fixed-wing aircrafts and strengthened by large centrifugal forces due to their high-speed rotation. Accordingly, out-of-plane motions, such as flapping, torsion and pitching of rotor blades or rotating wings, are typically restricted to small values. Furthermore, flap response is typically well damped by aerodynamic forces, less so for pitching and torsional motions. On the other hand, in-plane or lag motions are not as well damped as out-of-plane motions. The lead-lag degree of freedom, with its low aerodynamic and structural damping, is a critical mode in most rotary-wing aeroelastic problems.

In addition, modern helicopters are required to be as light as possible. Therefore, advanced rotors are designed to be soft in-plane: first in-plane frequency is often about 0.7/rev, or 70% of the rotor speed [105]. It follows that helicopter rotors are vulnerable to aeromechanical instabilities, namely, air and ground resonances, associated with in-plane motion of rotor blade. These belong to another important class of rotary-wing aeroelastic problems. Air resonance occurs when rotor lag mode

coalesces with a fuselage mode during forward flight or hover, while ground resonance occurs when rotor lag mode coalesces with landing gear mode of helicopters on the ground. More often than not, lead-lag dampers are used to prevent the appearance of aeromechanical instabilities.

Because the control of the lag motions of rotor blades plays an important role in aeromechanical stability prediction, lead-lag damper modeling has attracted a great deal of attention. For hingeless and bearingless rotors, elastomeric lead-lag dampers are often used to control aeromechanical instabilities. The nonlinear behavior of these dampers is heavily dependent on frequency, temperature and loading conditions such as pre-loads and amplitude of motion. In conventional articulated rotors, hydraulic dampers are often used because they can provide a higher level of damping that their elastomeric counterparts.

Hydraulic devices have been widely used in rotorcraft systems and are often purposely designed to behave in a nonlinear manner. On the other hand, hydraulic actuators can be used in the control system of main rotor. In addition to these applications, landing gear often involves hydraulic or pneumatic elements as well. In the first part of the thesis work, a physics-based, fully nonlinear representation of hydraulic devices is developed to model basic hydraulic elements, namely, the hydraulic chamber, the hydraulic orifice, and the pressure relief valve. Models for entire hydraulic devices are then constructed by assembling the models of a number of these hydraulic elements. This approach enables the determination of the complex interaction phenomena between the structural and actuator dynamics: pressure levels in the hydraulic chambers are now coupled with the dynamic response of the system. Such an approach is described in Chapter 2 and its predictions are validated against bench test measurements and flight test data for Sikorsky's UH-60 aircraft.

1.2 Fluid-Structure Coupling

Modern helicopter designs focus more on the rotorcraft performance, loads and vibration, aeroelastic stability and handling qualities. In the development of helicopter design, aeroelasticity continues to play a critical role and there are still many poorly understood problems [48]. Ref. [50] provides a historical perspective of the rotary-wing aeroelasticity, presenting the evolution of the aeroelastic problem and its formulation and solution procedures with primary emphasis on aeroelastic stability issues. Prediction of aerodynamic response remains an important aspect in the design process of helicopters. To achieve better designs with improved aerodynamic performance, lower vibrations, and maneuver capabilities, it is imperative to accurately predict the aerodynamic environment around helicopter rotors, resulting in accurate rotor airloads prediction. Two approaches have been followed for aerodynamic modeling.

The simplest method of aerodynamic modeling for airloads prediction is based on lifting-line theory commonly used in comprehensive rotorcraft analysis codes. In this method, sectional lift, drag and pitch moment predictions are based on two-dimensional experimental airfoil data. Approximations are used to account for unsteady and three-dimensional effects near the blade tip. Rotor wake is modeled with discrete vortex segments that are tracked in a Lagrangian manner and wake induced inflow on the rotor disc is evaluated by the use of the Biot-Savart law. The averaged inflow can also be computed using dynamic inflow model developed by Peters *et al.* [81]. The rotor wake, aerodynamics and dynamics computations are coupled together in an iterative manner with trim analysis to balance the forces on the entire helicopter. This simple method is easy to apply and computational efficient, but rely heavily on experiments and testing.

An alternative to the simple lifting-line theory for blade aerodynamic models are computational fluid dynamics (CFD) schemes that compute the full three-dimensional

flow around rotor blades. These methods typically solve Navier-Stokes, Euler or potential flow equations. The advantage of these methods is their capability to capture nonlinear, three-dimensional and transonic flows associated with high-speed advancing blades. Commonly used grid systems to model the flow field are $C-$, $O-$, and $H-$type. Overset grid systems, also known as structured grid systems, allow local grid refinement to improve the computational efficiency. It should be noted that the accuracy of the procedure transferring information between various overset grids should be carefully studied to avoid degrading the overall accuracy of the numerical solution. Unstructured grid systems are composed of irregularly distributed elements and can be generated using semi-automatic mesh generation software to accommodate complex surface geometries. However, the accuracy of aerodynamic load predictions depends on the number of grid cells and their sizes. Typically, a large amount of cells is used to ensure accuracy, resulting in high computational costs limiting their routine use in industry.

Given the characteristics of these two approaches, flow solvers have been coupled with computational structural dynamics (CSD) codes, typically, comprehensive rotorcraft analysis codes, by means of interfaces transferring data between the two codes. The coupling between CFD with CSD is likely to becomes a major tool in computational aeroelasticity for both fixed and rotary-wing aircraft designs [75, 49]. Loads and vibrations continue to confront dynamists in the rotorcraft industry and the reduction of vibration has been the major problem of rotary-wing design. Bousman [34] pointed out that two problems, negative lift in high-speed flight and under prediction of aerodynamic pitching moments, still remain unsolved in the airloads prediction for articulated rotors. These issues must be resolved before substantial progress is made in the accuracy of predicted loads and vibrations.

In this dissertation, the coupling between the comprehensive rotorcraft analysis code, DYMORE, and the computational fluid dynamics code, OVERFLOW-2, is

implemented. In this coupling procedure, DYMORE predicts the configuration of the rotor and passes it to OVERFLOW-2. This new configuration is computed with the help of lifting-line theory combined with dynamic inflow model and trim procedure, as well as the delta airloads, which are the differences between the airloads predicted by DYMORE and OVERFLOW-2. OVERFLOW-2 then computes the new airloads on the rotor based on the present rotor configuration. The interface used for transferring data comprises a kinematic and a load interfaces. Both are defined according to the standard proposed by Nygaard and Saberi [78]. The validation of this interface is performed on Sikorsky's UH-60 aircraft. The airloads for different flight conditions, such as high speed case (flight counter 8534) and high thrust case (flight counter 9017), for UH-60 aircraft are predicted using the loose coupling approach. In loose coupling, a delta-airloads method [84] is used to improve convergence. The hydraulic damper formulation described above is included to model the lead-lag damper of the UH-60 helicopter.

1.3 Rotor Wake Modeling

As mentioned in ref. [34], the key factors contribution to accurate predictions of rotor airloads are still unknown. Therefore, rotor wake modeling is worthy of continued studies. An appropriate modeling of the flow field around a rotor implies the accurate capturing of its wake structure, and plays an important role in the accurate prediction of airloads. For fixed-wing aircraft, the wake structure behind a wing is composed of a strong tip vortex and a vortex sheet with smaller strength along the inner board of the blade. In flight, the tip vortex and trailed vortex sheet are quickly convected away from the wing and their influence on the flow field in the vicinity of the wing is relatively small.

In contrast, the flow field around the rotor is very difficult to model because of the strong vorticity in the vicinity of rotor, whether in hover or forward flight. In

hover, the trailed and shed vortices linger in the vicinity of the rotor and the strong tip vortex coils beneath the rotor, which leads to significant changes in the effective angle of attack seen by the rotor blades [51]. In forward flight, the entire vortex system is swept back, resulting in an intense interaction between the blade tip vortices with successive blades, known as blade vortex interaction (BVI), which is a major source of aerodynamic noise and structural vibration. Particularly, in high-speed forward flight, the advancing blade experiences transonic flow conditions leading to shocks and shock-boundary layer interactions. Meanwhile, the retreating blade experiences a three-dimensional dynamic stall due to the separation of the flow from the blade surface.

In addition, modern helicopter designs prefer to place the rotor close to the fuselage for compact configurations, and to reduce the drag associated with the mast. Consequently, the vortex system produced by the rotor blades will interact with the airframe in an even more complex unsteady manner. Therefore, it follows that the wake modeling around a rotor is more difficult than that of the fixed-wing aircraft.

To accurately capture the unsteady effects and nonlinearity in the flow field around a rotor, first-principle based flow solvers, *i.e.* CFD schemes, are satisfactory choices because of their capabilities to capture the flow environment near the blade tip, where three-dimensional flow and compressibility effects dominate. The first implementation of a CFD scheme was attempted by Caradonna and Isom [38], who developed transonic flow theory from the extension of the transonic small-disturbance theory. In this analysis, the effect of the vortex wake was considered by including changes in the angle of attack that were obtained from an external comprehensive analysis. More recently, CFD flow solvers have been used to model the flow field around a rotor; in particular, full potential [94, 95], Euler [86], and Navier-Stokes [101] equations have been used. The effect of the vortex wake was considered by including a separate comprehensive analysis, such as CAMRAD.

It was not until the early 1990's that the CFD method could model the vortex wake effect itself, because of the vast improvement in the computer speed and storage. A problem associated with the CFD method is the numerical dissipation, also called as "artificial dissipation." Steinhoff [92] *et al.* and Wang [102] *et al.* added artificial convective velocities to reduce numerical dissipation. Higher-order CFD schemes with overset grid structures were developed to capture the entire wake of a rotor without resorting to the external wake models [52]. However, high computational expense and numerical dissipations hamper the popularity of CFD methods in the rotorcraft industry, especially in the preliminary design phases.

To overcome the shortcomings of CFD approaches, rotor blades are modeled based on lifting-line theory, combined with wake models to account for the effect of the vortex wake behind the blade. The vortex method is an efficient and easy-to-use approach because once the positions and strengths of the wake vorticity are determined, the induced velocity field can be calculated by the use of the Biot-Savart law [9]. The vortex wake structure is typically represented by vortex filaments and vortex sheets. The motion of vortex filaments will be governed by Helmholtz's law [97], also known as the "transport theorem."

Vortex filaments are modeled as curves along which vortices of known strength travel. The vortex distribution is represented by Lagrangian markers, which are linked together by straight line segments. Typically, vortex filaments may be discretized by several hundred individual segments. The numerical evaluation of the Biot-Savart integral is straightforward for a single vortex segment. However, it is the very large number of segments required to model the entire wake that determines the computational expense because the vortex wake is usually composed of many such vortex filaments. The computational expense will dramatically increase when a free-wake analysis is performed, because the new position of each Lagrangian marker must be solved for with the help of the vorticity transportation theorem. To find the new

position of each Lagrangian marker, it requires the knowledge of the induced velocity at each Lagrangian marker due to the vortex wake, which is very computational expensive. Although the vortex method is many orders of magnitude less expensive than first-principle based CFD methods, it is still computational demanding if fine-grid discretizations are used. It is the relatively high cost of the vortex method that limits their routine use for practical applications in rotor wake analysis.

In light of these considerations, a NURBS-based [47, 83] representation of vortex filaments and sheets is proposed in this work. NURBS curves and surfaces can represent very complex shapes with remarkable little data and have great control over the shape and smoothness of curves and surfaces. Consequently, the computation associated with the evaluation of the Biot-Savart integral and solving the vorticity transportation theorem will be dramatically reduced, and enhance the efficiency of preliminary rotor design process. This new wake model will be a good addition to existing rotorcraft comprehensive codes, providing a consistent and balanced approach to the various disciplines [62].

1.4 Organization of Dissertation

This dissertation deals with three aspects of comprehensive rotorcraft analysis. The background and the motivation of this dissertation are introduced in chapter 1. The main objectives of the present work are proposed after the brief introduction. Following chapter 1 three main chapters separately present the methodologies, results, and discussions of each aspect.

Chapter 2 reviews the present approaches to model the hydraulic devices, such as hydraulic actuators and hydraulic dampers. A physics-based, fully nonlinear representation of hydraulic components is presented and the implementation of this approach in a comprehensive rotorcraft analysis formulation is described. The validation of this approach and its applications are discussed. The lead-lag damper modeling for

the UH60A Black Hawk aircraft is emphasized. Finally, the conclusions drawn from this analysis are summarized.

Chapter 3 first introduces the background of the computational aeroelastic analysis and previous work in this area. The fluid-structure interface between the CFD program, OVERFLOW-2, and the CSD program, DYMORE, is specifically discussed. Details involved in the coupling analysis between DYMORE and OVERFLOW are described, including aerodynamic models and aerodynamic interfaces available in DYMORE, components required in the interaction between CFD and CSD programs, and coupling strategies. The delta-airloads method used in the loose coupling analysis is introduced and examples of the loose coupling between DYMORE and OVERFLOW-2 are presented to validate the interface that enable the computational aeroelastic analysis.

Chapter 4 describes the NURBS-based representation of the vortex wake modeling. A review of vortex wake modeling is given, including the background of the vortex wake modeling and the fundamental concepts used in the vortex method. The NURBS representation of the vortex wake structure is described, including NURBS curves for the modeling of vortex filaments, and NURBS surfaces for that of vortex sheets. Two time integration schemes for solving the vorticity transportation theorem are introduced. The two and three-dimensional aerodynamic problems with the wake modeling using the newly proposed approach are described, with focus on the establishment of the system to solve for the vorticity in the wake. The computation of the inflow due to the vortex wake is detailed separately for two and three-dimensional problems. Numerical examples for the validation of the present wake model are presented. Based on these analysis, the conclusions of this part of work are drawn.

Finally, Chapter 5 summarizes the main work of this dissertation and provides some recommendation for the future research.

CHAPTER II

LEAD-LAG DAMPER MODELING

2.1 Introduction

The behavior of hydraulic actuators and dampers can be modeled in several manners. In the first approach, very simple idealizations of hydraulic components are used. For instance, a hydraulic damper would be idealized as a dashpot: the force in the damper in proportional to the relative velocity of the piston. More often than not, actual damper will exhibit a nonlinear force-velocity relationship and a linear approximation is clearly too crude. The accuracy of the predictions might be improved if the damper is modeled as a nonlinear dashpot; this approach is widely used in industry. In that case, the nonlinear characteristics of the device are identified by a number of bench experiments, typically involving harmonic excitations of the device at various frequencies and amplitudes. The main drawback of this approach is that physical characteristics identified under harmonic excitation might not yield good results when the device is subjected to arbitrary excitation in time.

In the second approach, the hydrodynamic behavior of the device is linearized to obtain one or more ordinary differential equations relating control inputs to the forces generated by the device; typical equations are given in textbooks such as those of Viersma [100] or Canon [37]. While this approach is physics-based and captures some basic aspects of hydraulic devices, the linearization process is clearly too restrictive. In fact, rotorcraft lead-lag dampers are often purposely designed to behave in a nonlinear manner. Indeed, a linear device would generate high damping forces under high stroking rates; these high forces must be reacted at the hub and at the root of the blade, creating high stresses and decreasing fatigue life. A possible remedy

to this situation is to use pressure relief valves that act as force limiters, implying a nonlinearity essential to the design and behavior of the device.

In the last approach[15], a physics based, fully nonlinear representation of hydraulic devices is implemented. This enables the determination of the complex interaction phenomena between the structural and actuator dynamics: pressure levels in the hydraulic chambers are now coupled with the dynamic response of the system. This paper describes such an approach in detail, and its predictions are validated against bench test measurements and flight test data for Sikorsky's UH-60 aircraft.

The modeling of the hydraulic devices has been the subject of detailed studies of the first part of this dissertation. In ref. [103], Welsh proposed a detailed model for predicting the dynamic response of helicopter air-oil landing gear that included several degrees of freedom representing the tire, floating piston, orifice piston, and simple fluid and adiabatic gas models. In a later effort, ref. [104], the same author addressed the problem of modeling the lubrication system of a helicopter using a similar approach. In both cases, detailed models of hydraulic systems were developed, but not coupled with the dynamic response of the vehicle.

A variety of hydraulic devices are used in the rotorcraft industry: hydraulic actuators are crucial components of many main rotor control systems, hydraulic lead-lag dampers are used in many rotor designs, and landing gear often involve hydraulic or pneumatic elements. In the case of lead-lag dampers, the hydraulic device tightly interacts with rotor response; in fact, blade root edgewise moments depend to a large extent on damper response characteristics. To deal with this variety of devices, a modular approach is taken. At first, models are developed for three basic hydraulic elements: the hydraulic chamber, the hydraulic orifice, and the pressure relief valve. Models for entire hydraulic devices are then constructed by assembling the models of a number these hydraulic elements. In this work, models for simple hydraulic dampers, and hydraulic dampers with pressure relief valves are discussed.

Once a model of the hydraulic device is in hand, it is to be coupled with a comprehensive rotorcraft simulation code. In this effort, hydraulic device models is coupled to a finite element based multibody formulation of a helicopter rotor system within a comprehensive analysis, see ref. [13]. Within the framework of flexible mechanism analysis programs, the modeling of hydraulic devices has attracted limited attention; in ref. [39], models were proposed for a hydraulic jack and for the actuator of an aircraft retractable landing gear.

Conceptually, the coupling of a hydraulic device model with a comprehensive rotorcraft modeling code is straightforward. First, the hydraulic device model predicts the instantaneous force the device applies on the supporting structure. In turn, this force is applied to the dynamic model of the vehicle to predict displacements and velocities. Finally, these kinematic quantities change the stroke of the hydraulic device, and hence, its force output. In a finite element formulation, this is readily achieved by connecting the end points of the hydraulic device to two nodes of the finite element discretization.

This part of the thesis work has two main goals. First, a comprehensive modeling approach will be presented for hydraulic devices, such as hydraulic actuators and dampers. Second, these models will be coupled to a comprehensive rotorcraft model using a finite element based multibody formulation. This chapter is organized in the following manner. The first section presents models for the basic hydraulic elements, and the second section shows how these basic models can be combined to deal with various hydraulic devices. Next, issues associated with the coupling of hydraulic devices models with finite element based multibody formulations of rotorcraft dynamic simulation are discussed, with special focus on the integration of the hydraulic equations. The modeling approach is then validated using a number of numerical examples. Finally, conclusions of this work are offered.

2.2 Basic Hydraulic Elements

Hydraulic devices can be seen as an assembly of simple hydraulic elements; in this dissertation, three basic hydraulic elements will be presented: hydraulic chambers, orifices, and pressure relief valves. These basic elements are described in the following sections. Of course, a variety of other elements could be developed such as hydraulic accumulators or check valves.

2.2.1 Hydraulic chamber

The hydraulic chamber, shown in fig. 1, is probably the most common hydraulic component. The chamber, of volume V and cross-sectional area A, is filled with a hydraulic fluid of bulk modulus B under pressure p. Often, due to the presence of a piston, the length of the chamber can vary. The change in length of the chamber, due to piston motion, is denoted d. Finally, hydraulic fluid can flow into the chamber; Q denotes the net volumetric flow rate into the chamber.

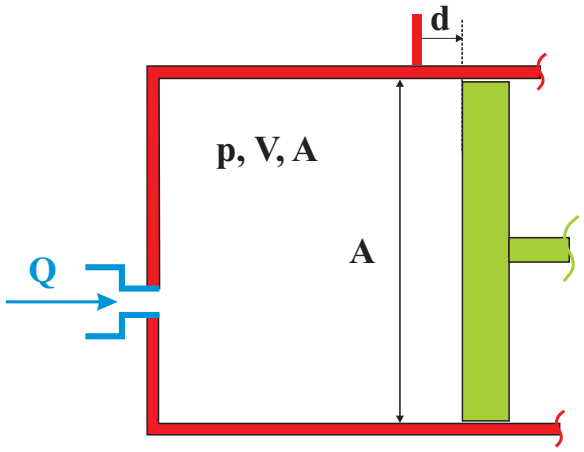

Figure 1: Configuration of a hydraulic chamber.

The evolution of the pressure in the chamber is governed by the following first order differential equation

$$\dot{p} = \frac{B}{V}\,(Q - A\,\lambda\dot{d}). \tag{1}$$

The factor λ is a configuration dependent parameter: if a positive value of d increases the volume of the chamber, $\lambda = +1$; $\lambda = -1$ in the opposite case. The instantaneous volume of the chamber is

$$V = V_0 + A\lambda d, \tag{2}$$

The bulk modulus of the hydraulic fluid is a function of the fluid pressure; an accurate approximation of this dependency is written as

$$B = \frac{1 + \alpha p + \beta p^2}{\alpha + 2\beta p}, \tag{3}$$

where α and β are physical constants for the hydraulic fluid, see ref. [100].

2.2.2 Hydraulic orifice

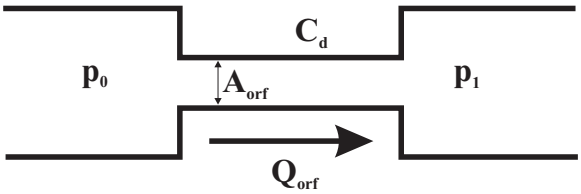

Figure 2: Configuration of a hydraulic orifice.

The hydraulic orifice, shown in fig. 2, allows the flow of hydraulic fluid through an orifice of sectional area A_{orf}. The orifice is connected to two hydraulic chambers with pressures p_0 and p_1, respectively. A pressure differential, $\Delta p = p_0 - p_1$, will drive a flow rate Q_{orf} across the orifice; the positive direction of this flow rate is indicated on the figure.

The magnitude of this volumetric flow rate is related to the pressure differential by the following equation

$$Q_{\text{orf}} = A_{\text{orf}} C_d \sqrt{\frac{2|\Delta p|}{\rho}} \, \frac{\Delta p}{|\Delta p|}, \tag{4}$$

For turbulent flow conditions, the theoretical value of the discharge coefficient is $C_d = 0.611$, see ref. [100].

2.2.3 Pressure relief valve

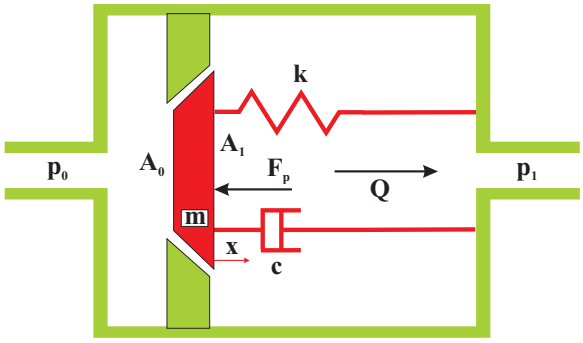

Figure 3: Configuration of a pressure relief valve.

The pressure relief valve, shown in fig. 3, is connected to two hydraulic chambers with pressures p_0 and p_1, respectively. It features a poppet connected to a spring and dashpot; the spring is preloaded with a pre-load force. The equation of motion of the pressure relief valve is:

$$m\,\ddot{x} + c\dot{x} + kx = (p_0 A_0 - p_1 A_1) - F_p. \tag{5}$$

When the net force acting on the poppet is smaller than the pre-load force, *i.e.* when $p_0 A_0 - p_1 A_1 < F_p$, the valve remains closed, $x = \dot{x} = 0$. On the other hand, when the net force is large enough to overcome the pre-load force, the poppet opens and its motion is governed by eq. (5). Once the valve is open, fluid will flow through the valve at the following volumetric rate

$$Q_{\text{prvl}} = A_{\text{prvl}} C_d \sqrt{\frac{2|\Delta p|}{\rho}}\,\frac{\Delta p}{|\Delta p|}, \tag{6}$$

where $\Delta p = p_0 - p_1$ is the pressure differential across the valve. The area A_{prvl} through which the fluid flows is a function of the valve opening

$$A_{\text{prvl}} = \begin{cases} ax + bx^2 & x > 0 \\ 0 & x \leq 0 \end{cases}. \tag{7}$$

The pressure relief valve acts as a pressure regulator: when the pressure differential across the valve becomes high enough, $p_0 A_0 > p_1 A_1 + F_p$, the valve open and the ensuing flow tends to equilibrate the pressures, at which point, the valve closes.

2.3 Hydraulic devices

The hydraulic elements described in the previous section can be combined to form practical hydraulic devices such as linear hydraulic actuators, simple dampers, or dampers with pressure relief valves. In the following sections, examples of simple hydraulic damper and hydraulic damper with pressure relief valves will be described. More complex devices could be modeled using the same technique.

2.3.1 Hydraulic linear actuator

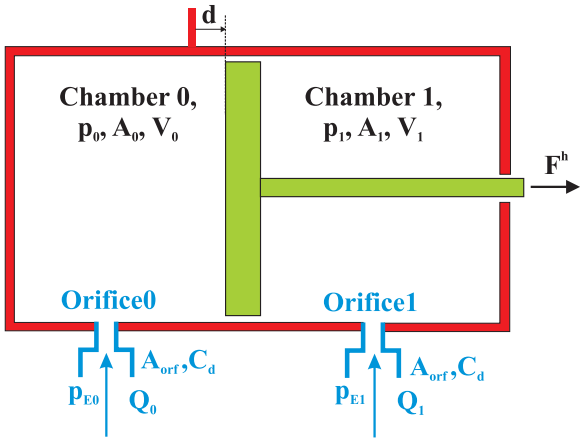

Figure 4: Configuration of the hydraulic actuator.

The linear hydraulic actuator combines two hydraulic chambers, chamber 0 and chamber 1, and two orifices, orifice 0 and orifice 1, to form the configuration depicted in fig. 4. The hydraulic chamber 0 and chamber 1 are under pressures p_0 and p_1, respectively; note that the λ factors are $+1$ and -1 for the two chambers, respectively. The hydraulic orifice 0 and orifice 1 generate flow rates Q_0 and Q_1 into chambers 0 and 1, respectively. The two orifices have entrance pressures p_{E0} and p_{E1}, respectively.

To increase the length of the actuator, control valves (not part of the present model) will set the entrance pressure of orifice 0 to a high value, p_h, such that $p_{E0} = p_h$, while the entrance pressure of orifice 1 remains at a low value, p_s, such that $p_{E1} = p_s$. To decrease the length of the actuator, the control valves reverse the pressure level at the entrance to the two orifices.

The force generated by the actuator is

$$F^h = p_0 A_0 - p_1 A_1. \tag{8}$$

The governing equations for the linear hydraulic actuator include equations for the pressures p_0 and p_1 in the two chambers, eq. (1), and equations for the flow rates Q_0 and Q_1 through the orifices, eq. (4).

Most hydraulic actuators are also equipped with check valves that connect the hydraulic chambers to the circuit background pressure when the chamber pressure falls below the background pressure, in an effort to avoid cavitation in the chamber.

2.3.2 Simple hydraulic damper

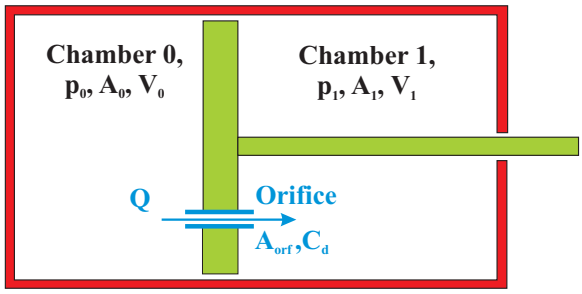

Figure 5: Configuration of the simple hydraulic damper.

The simple hydraulic damper combines two hydraulic chambers, chamber 0 and chamber 1, and one orifice connecting the two chambers to form the configuration depicted in fig. 5. The hydraulic chamber 0 and chamber 1 are under pressures p_0 and p_1, respectively; note that the λ factors are $+1$ and -1 for the two chambers,

respectively. The hydraulic orifice generates a flow rate Q from chamber 0 into chamber 1. If the length of the damper increases (*i.e.* piston and rod move to the right in fig. 5), pressure p_1 increases whereas pressure p_0 decreases. This generates a pressure differential across the orifice and hence, a flow rate Q into chamber 0 that tends to equilibrate the pressures in the chambers. The force generated by the damper always opposes the motion and is therefore a damping force.

The force generated by the damper is again given by eq. (8). The governing equations for the simple hydraulic damper include equations for the pressure p_0 and p_1 in the two chambers, eq. (1), and one equation for the flow rate Q through the orifice, eq. (4).

2.3.3 Hydraulic damper with pressure relief valves

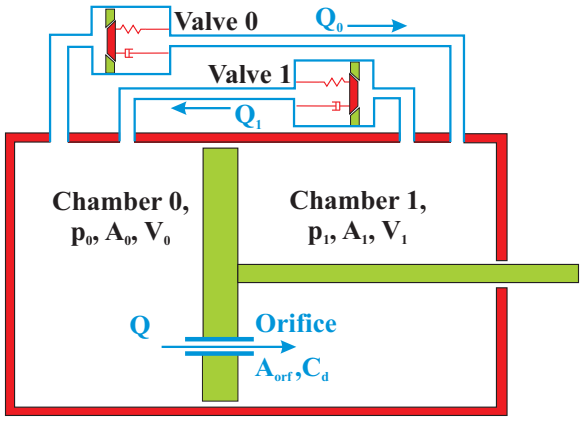

Figure 6: Configuration of the hydraulic damper with pressure relief valves.

Rotorcraft hydraulic lead-lag dampers present a configuration similar to simple damper described in previous section. However, this simple design suffers an important drawback: under a high stroking rate, the pressure differential in the chambers can be rather high, and hence, high damping forces are generated. These high forces must be reacted at the hub and at the root of the blade, creating high stresses and decreasing fatigue life. To limit the forces in the hydraulic damper, two pressure relief valves are added to the configuration, as shown in fig. 6. The new design combines

two hydraulic chambers, chamber 0 and chamber 1, one orifice connecting the two chambers and two pressure relief valves, valve 0 and valve 1. The hydraulic chamber 0 and chamber 1 are under pressures p_0 and p_1, respectively; note that the λ factors are $+1$ and -1 for the two chambers, respectively. The hydraulic orifice generates a flow rate Q from chamber 0 into chamber 1. Finally, when open, the pressure relief valves regulate the pressures in chambers 0 and 1.

If the length of the damper increases, pressure p_1 increases whereas pressure p_0 decreases. This generates a pressure differential across the orifice and hence, a flow rate Q into chamber 0 that tends to equilibrate the pressures in the chambers. If the stroking rate is high, the pressure differential in the chambers will become high enough to open pressure relief valve 1, resulting in an additional flow rate Q_1 from chamber 1 into chamber 0. Given the sign of the pressure differential, valve 0 will remain closed. The opening of the valve and the ensuing flow controls the magnitude of the pressure differential, and hence of the damper force that is still given by eq. (8). The force generated by the damper always opposes the motion and is therefore a damping force. In practical designs, hydraulic dampers are also equipped with check valves, as discussed for actuators.

The governing equations for the hydraulic damper with pressure relief valves include equations for the pressures p_0 and p_1 in the two chambers, eq. (1), one equation for the flow rate Q through the orifice, eq. (4), two equations of motion for the valve poppets, eq. (5), and two equations for the flow rates trough the valves, eq. (6). The flow area of the valves is computed with the help of eq. (7).

2.4 Finite Element Implementation

The various hydraulic devices described in the previous section interact with the dynamics of the mechanical system they are connected to. For instance, a helicopter

lead-lag damper interacts with rotor blade dynamics; this effect is particularly pronounced on the fundamental blade lead-lag mode. This section describes the coupling of the hydraulic device model with a structural dynamics model, within the framework of multibody system dynamics, see ref. [13]. The following sections describe the coupling procedure in terms of the applied structural forces, their time discretization, and the time integration scheme for the equations governing the behavior of hydraulic devices.

2.4.1 Applied structural forces

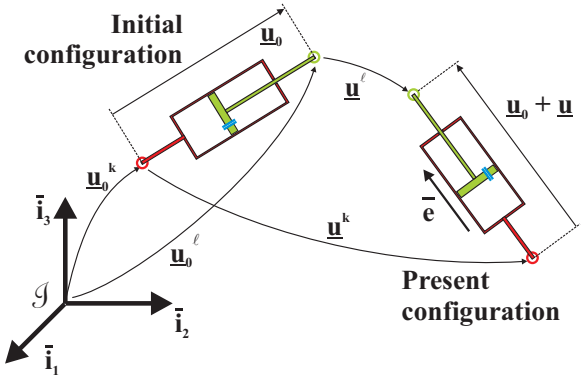

Figure 7: Configuration of the hydraulic device.

In general, hydraulic devices generate hydraulic forces given by eq. (8) that are functions of the stroke d (through eq. (2)) and stoke rate $\dot{d}$ (through eq. (1)). This stroking can be evaluated from the configuration of the device depicted in fig. 7. In the initial configuration, the end points of the device are at location $\underline{u}_0^k$ and $\underline{u}_0^\ell$, respectively, with respect to an inertial frame $\mathcal{I} = (\bar{\imath}_1, \bar{\imath}_2, \bar{\imath}_3)$. At those points, the device is connected to a dynamical system of arbitrary topology. In the deformed configuration, the displacements of the end points of the device are $\underline{u}^k$ and $\underline{u}^\ell$, respectively. The relative position of the end points will be denoted $\underline{u}_0 = \underline{u}_0^\ell - \underline{u}_0^k$ and $\underline{u} = \underline{u}^\ell - \underline{u}^k$, in the initial and present configurations, respectively.

The virtual work done by the hydraulic force, F^h, is $\delta W = F^h \delta d$, where $\delta d =$

$\delta(\|\underline{u}\| - \|\underline{u}_0\|)$ is a virtual change in device length. This expression then becomes

$$\delta W = F^h \ \frac{\underline{u}^T \delta \underline{u}}{\|\underline{u}\|} = F^h \ \bar{e}^T (\delta \underline{u}^\ell - \delta \underline{u}^k), \tag{9}$$

where $\bar{e} = \underline{u}/\|\underline{u}\|$. The forces applied to the external dynamic system are

$$\underline{F} = F^h \ \begin{bmatrix} -\bar{e} \\ \bar{e} \end{bmatrix}, \tag{10}$$

two forces of equal magnitude and opposite sign applied at the connection points.

2.4.2 Time discretization of the structural forces

In a typical finite element implementation, the simulation of the system dynamics is discretized in time. The force generated by the hydraulic device will be assumed to remain a constant, F_m^h, over the time step and the work done by this force over the time step now becomes $\Delta W = F_m^h (d_f - d_i)$. This expression is manipulated to become

$$\Delta W = \frac{F_m^h}{2 d_m} (d_f^2 - d_i^2) = \frac{F_m^h}{2 d_m} (\underline{u}_f^T \underline{u}_f - \underline{u}_i^T \underline{u}_i), \tag{11}$$

where $d_m = (d_f + d_i)/2$ is the average stroke of the device over the time step. The mid-point relative position vector is defined as $\underline{u}_m = (\underline{u}_f + \underline{u}_i)/2$, and the work expression now becomes

$$\Delta W = F_m^h \ \frac{\underline{u}_m^T}{d_m} \ (\underline{u}_f - \underline{u}_i) = F_m^h \ \underline{e}_m^T \ (\underline{u}_f - \underline{u}_i), \tag{12}$$

where $\underline{e}_m = \underline{u}_m / d_m$. The discretized hydraulic forces will be selected as

$$\underline{F}_m = F_m^h \ \begin{bmatrix} -\underline{e}_m \\ \underline{e}_m \end{bmatrix}. \tag{13}$$

By construction, this discretization guarantees that the work done by the hydraulic force over one time step, eq. (11), is evaluated exactly.

Since the expression for the hydraulic forces and the governing equation of dynamical systems are non-linear, the solution process involves iteration and linearization.

Linearization of the discretized forces, eq. (13), leads to

$$\Delta \underline{F}_m = K_m \begin{bmatrix} \Delta \underline{u}^k \\ \Delta \underline{u}^\ell \end{bmatrix}, \tag{14}$$

where

$$K_m = \frac{1}{2} \left\{ \frac{F_m^h}{d_m} \begin{bmatrix} (U - \underline{e}_m \bar{e}_f^T) & -(U - \underline{e}_m \bar{e}_f^T) \\ -(U - \underline{e}_m \bar{e}_f^T) & (U - \underline{e}_m \bar{e}_f^T) \end{bmatrix} + \frac{\mathrm{d}F_m^h}{\mathrm{d}d_m} \begin{bmatrix} \underline{e}_m \bar{e}_f^T & -\underline{e}_m \bar{e}_f^T \\ -\underline{e}_m \bar{e}_f^T & \underline{e}_m \bar{e}_f^T \end{bmatrix} \right\}, \tag{15}$$

and U is the 3 by 3 identity matrix. This expression requires the evaluation of the derivative of the hydraulic force with respect to the stroke, $\mathrm{d}F_m^h/\mathrm{d}d_m$, that could be computed from the governing equations for the hydraulic device. However, this process is, in general, quite involved. The following approximation was found to be suitable

$$\frac{\mathrm{d}F_m^h}{\mathrm{d}d_m} = \frac{BA_0^2}{V_0} + \frac{BA_1^2}{V_1}; \tag{16}$$

it corresponds to an approximation to the static stiffness of the device.

2.4.3 Time integration of hydraulic equations

The model described in the previous section requires the knowledge of the hydraulic force acting in the device, given by eq. (8). In turn, this requires the solution of the equations governing the behavior of the hydraulic device, as discussed in earlier sections. Although the model of the hydraulic device is rather simple, a few first order, nonlinear differential equations, it is a numerically stiff set of equations because of the very high "stiffness" of the hydraulic fluid (for typical systems, the bulk modulus of the fluid is about 1.5 GPa). Typically, this problem is overcome by using a very small time step for the integration of the hydraulic equations; for instance, Welsh, ref. [103], used a time step of $\Delta t = 10^{-6}$ sec to integrate the equations of a helicopter air-oil strut. While this approach is acceptable when dealing with the sole hydraulic equations, it is not practical to integrate both hydraulic and structural dynamics

equations with such a small time step because the computational effort would become overwhelming. Consequently, it is imperative to decouple the integration of the two systems: the structural dynamics equations are integrated with a time step dictated by the frequency content of the structural response, whereas the hydraulic equations are integrated with a much smaller time step.

In this work, the following strategy was used: the structural dynamics equations are integrated with a time step $\Delta t = t_f - t_i$; energy decaying schemes that guarantee nonlinear unconditional stability of the time integration process are used for this purpose, see Refs. [16, 17, 11, 12, 14]. This produces a prediction of the stroking of the hydraulic device, $d_i = \|\underline{u}_i\| - d_0$ and $d_f = \|\underline{u}_f\| - d_0$, the stroking rate has a constant value $\dot{d}_m = (d_f - d_i)/\Delta t$. This information was used to integrate the governing equations of the hydraulic device using a fourth order Runge-Kutta integrator, see ref. [85]. The time step used in this integrator was $h = \Delta t/N$, *i.e.* N Runge-Kutta steps are performed for each structural time step. Once the hydraulic equations are solved, the pressures in the chambers are predicted and hence the hydraulic device force. The nonlinear solution of the problem is then obtained by iterating between the structural dynamics equations and the hydraulic equations.

2.5 Numerical Examples

2.5.1 Hydraulic linear actuator

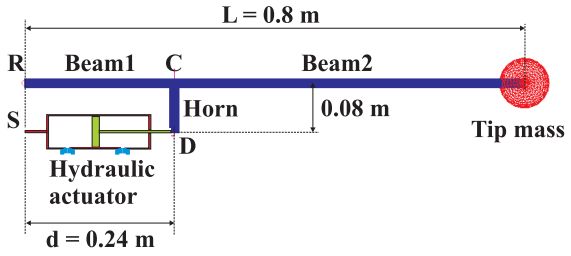

Figure 8: Configuration of the hydraulic linear actuator pitching a beam.

The first example deals with a hydraulic linear actuator that is used to pitch a

Table 1: Physical properties of the hydraulic actuator.

Quantity	Value
$A_0 = A_1$	7.85 10^{-5} m^2
$V_0 = V_1$	9.42 10^{-6} m^3
$p_{E0} = p_{E1}$	1.25 MPa
$A_{\text{orf0}} = A_{\text{orf1}}$	6.0 10^{-6} m^2
$C_{d0} = C_{d1}$	0.611
p_s	1.0 MPa
B	1.53 MPa

beam, as depicted in fig. 8. The system consists of a flexible beam of length $L = 0.8$ m with a 10 kg tip mass connected to a revolute joint at point **R**. At point **C**, located at a distance $d = 0.24$ m from the root of the beam, a flexible horn connects to the beam. Finally, a hydraulic linear actuator is connected between the ground and the tip of the horn at points **S** and **D**, respectively.

The physical properties of the beam and horn are as follows: axial stiffness, 5.7 10^7 N, bending stiffness, 4.275 10^3 N.m^2, shearing stiffness, 1.80 10^7 N, mass per unit span, 2.4 kg/m. The configuration of the hydraulic linear actuator is that depicted in fig. 4. The physical properties of the actuator are listed in Table 1.

The system was initially at rest. To simulate the actuator's control valves, the throttling areas of both orifices were linearly ramped up from zero to their nominal value in 0.5 s. In the next 0.5 s, the throttling areas were linearly ramped back down to zero. The time step for the structural analysis was set to $\Delta t = 1.0\ 10^{-4}$ s; for each structural step, 48 sub steps were used for the integration of the hydraulic equations. These time step sizes were selected by a convergence study; it is interesting to note that a large number of sub steps, 48, was required to achieve the convergence of the integration of the hydraulic equations. The system was simulated for a total period of 1.5 s.

Figure 9 shows the time history of the force generated by the hydraulic actuator.

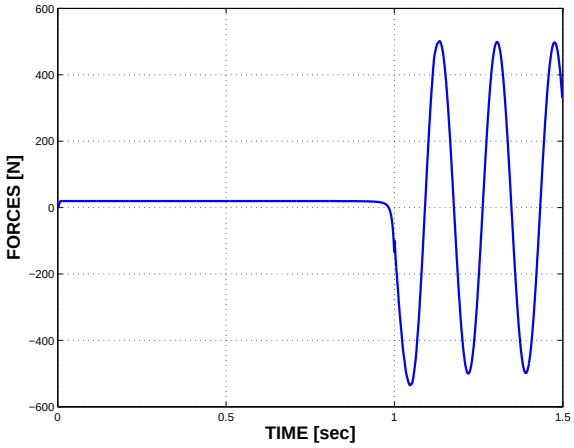

Figure 9: Time history of the force generated by the hydraulic actuator.

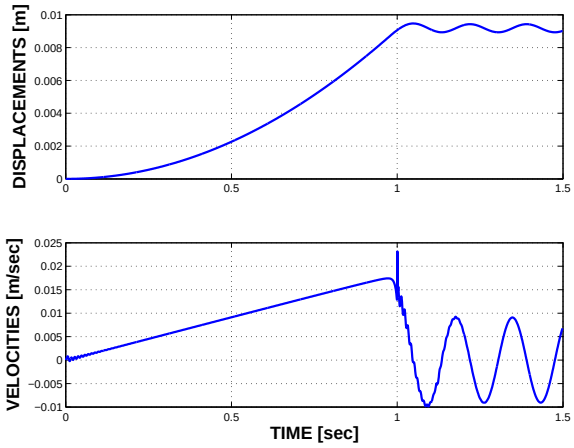

Figure 10: Time histories of the displacement (top figure) and velocity (bottom figure) of the piston of the hydraulic actuator.

Note the nearly constant force generated by the actuator while the throttling areas non zero. Once the throttling areas vanish, the actuator becomes much stiffer. Indeed, the apparent stiffness of the devices is now dictated by the bulk modulus of the oil and it applies much higher forces to the supporting structure. The time histories of the displacement and velocity of the piston of the hydraulic actuator are shown in fig. 10. Once the throttling areas vanish, the length of the actuator remains nearly constant; the observed oscillations are due to vibrations of the beam-tip mass system following actuation. The interaction between the hydraulic device and the structure

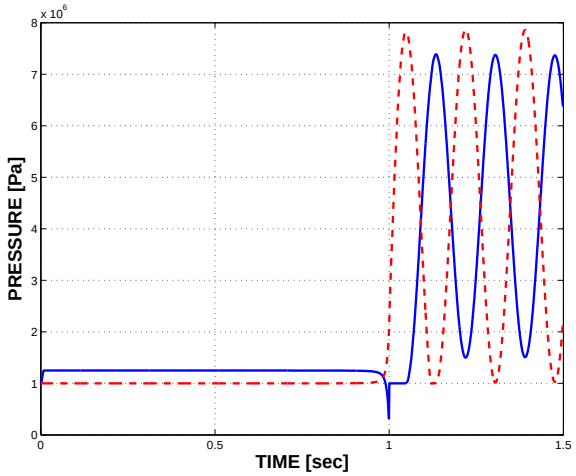

Figure 11: Time histories of the pressures in the two chambers; chamber 0: solid line, chamber 1: dashed line.

is further demonstrated in fig. 11 that shows the time histories of the pressures in the two chambers. Note the sudden drop in chamber 0 pressure at time $t = 1$ s due to the opening of the check valve; the effects of this pressure spike are noticeable on the device velocity and output force, see Figs. 10 and 9, respectively. After the closing of the throttling areas, large variations in chamber pressures are observed resulting from structural vibrations. Finally, fig. 12 depicts the time histories of the volumetric flow rates into chamber 0 and chamber 1. The flow rates that are observed after the closing of the throttling areas are flow rates through the actuator check valves. The very rapid variations in chamber pressure and orifice flow rates are further evidence of the very high stiffness of the system and help explain the need for the numerous sub time steps required to integrate the hydraulic equations.

2.5.2 Validation of the model of the UH-60 lead-lag damper

In the next example, a model of the lead-lag damper used in Sikorsky's UH-60 helicopter will be validated by comparing the predictions of the proposed model with measurements taken on a test bench experiment. The physical properties of the hydraulic device are described in ref. [103]. The damper was tested under harmonic

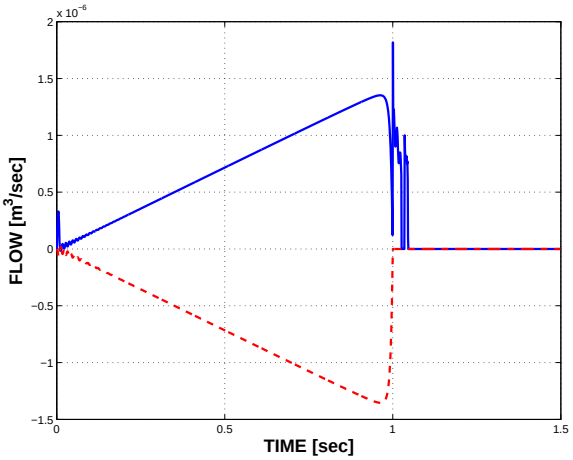

Figure 12: Time histories of the volumetric flow rates into chamber 0 (solid line) and chamber 1 (dashed line).

stroking conditions at a constant circular frequency $\omega = 27.02$ rad/s. Tests were run at various amplitudes of the harmonic motion; fig. 13 shows the experimentally measured peak force in the damper as a function of peak velocity. This figure also shows the predictions of the present model; good agreement is found between measurements and predictions. The time history of the damper force at a peak velocity of 2 in/s is shown in fig. 14 for both model and experiment. While peak loads are in good agreement, force time histories exhibit qualitative differences. First, the experimentally measured force dwells for a short period when it reaches a value near zero; this phenomenon is not predicted by the model and its physical origin is not known; possible explanations are discussed in the next paragraph. Second, the experimental measurements exhibit a different behavior at peak positive and negative forces. This dissymmetry is not present in the model and its physical origin is also unclear.

The following conclusions can be drawn from this calibration effort. The proposed model seems to predict damper peak loads with reasonable accuracy, while the details of the force time history are not predicted to the same level of accuracy. The probable cause of these discrepancies is the highly idealized nature of the present model. Several components of the device, such as the hydraulic accumulators and check valves, have

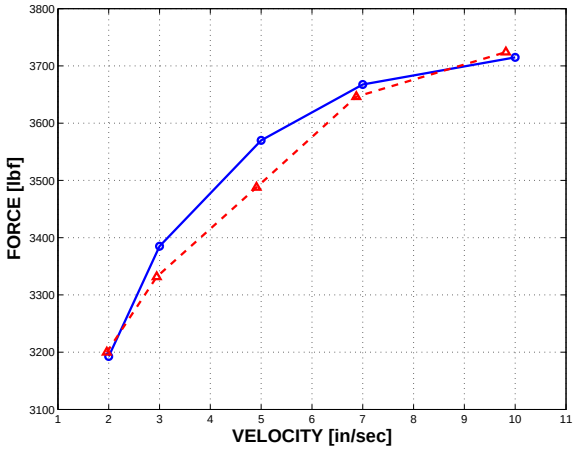

Figure 13: Peak force versus peak velocity; experimental measurements (solid line) and present model predictions (dashed line).

intrinsic characteristics that have not been modeled in the present effort. Several coefficients of the model, such as the orifice discharge coefficient, have been set to their theoretical values. Other coefficients, such as those appearing in eq. (7), were selected based on indirect, uncertain measurements. Parametric studies performed with the present model have demonstrated the great sensitivity of the predictions to the choice of these coefficients.

2.5.3 Modeling the UH-60 blade and lead-lag damper

In the final example, the dynamic response of Sikorsky's UH-60 rotor system will be evaluated using a finite element based multibody formulation and a detailed model of the blade hydraulic lead-lag damper. The UH-60 is a four-bladed helicopter whose physical properties are described in ref. [35] and references therein. In this work, a single blade model will be used. Figure 15 shows the configuration of the rotor system featuring the blade root retention structure, pitch link, pitch horn, swash plate, and lead-lag damper.

The blade was modeled using thirteen cubic beam elements. The root retention structure, from hub to blade, was separated into three segment, having three, two, and

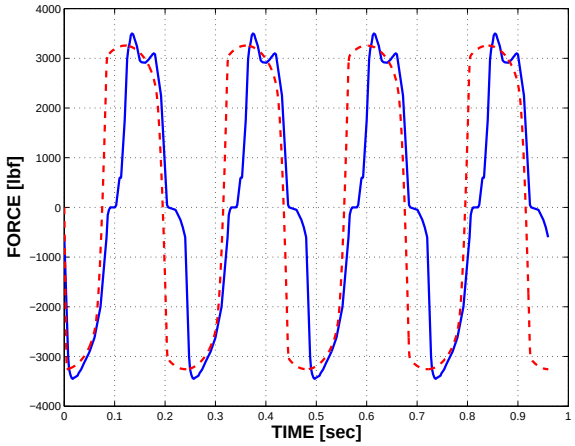

Figure 14: Time history of the lead-lag damper force at a peak velocity of 2 in/s. Experimental measurements: solid line, present predictions: dashed line.

two cubic beam elements, respectively, and labeled segment 1, 2 and 3 in fig. 15. The first segment was attached to the rigid hub. The first two segments were connected to each other by an elastomeric bearing modeled by three co-located revolute joints with the following sequence: lag, flap, then pitch rotations. The physical characteristics of the bearing were simulated by springs and dampers in the joints. The next two segments were rigidly connected to each other and to the pitch horn. Finally, the last segment rigidly connected to the blade and damper horn.

The pitch angle of the blade was set by the following control linkages: the swash plate, pitch link, and pitch horn. The pitch link, modeled by three cubic beam elements, was attached to the rigid swash plate by means of a universal joint and to the rigid pitch horn by a spherical joint. The damper arm and damper horn were modeled with rigid bodies. The lead-lag damper was modeled as a hydraulic damper with pressure relief valves, as described in earlier sections; its end points were connected to the damper arm and horn; the physical properties of the device can be found in ref. [54].

The loads applied to the rotor consisted of the measured aerodynamic loads obtained from in flight test measurements, see ref. [61]. The results presented below

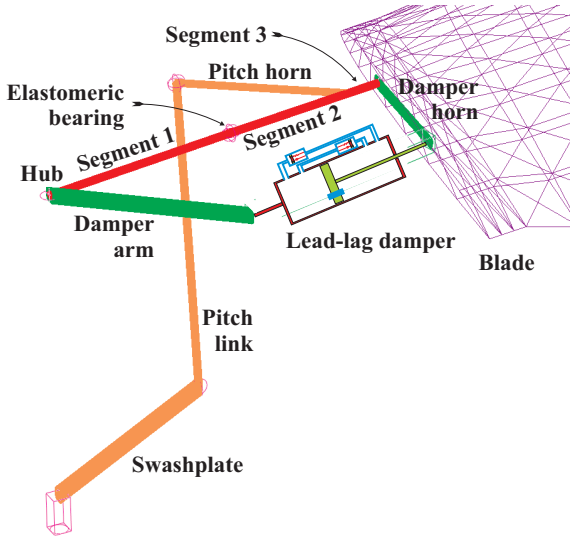

Figure 15: Configuration of Sikorsky's UH-60 rotor system: close-up view of the blade root retention structure, pitch link and pith horn, swashplate, and hydraulic damper.

correspond to flight counter 8534, a forward flight case with a forward speed of 158 knots. A total of 75 rotor revolutions were simulated to allow all transients to die out and obtain a periodic solution. The results presented in the figures below depict the last revolution of the simulation, as a function of the azimuthal angle Ψ. A constant time step size of 256 steps per revolution was used for the structural equations and 25 sub steps were used for the integration of the hydraulic equations.

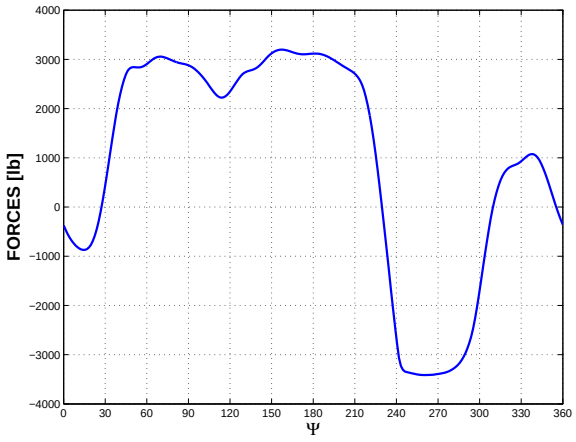

Figure 16: Time history of the lead-lag damper force.

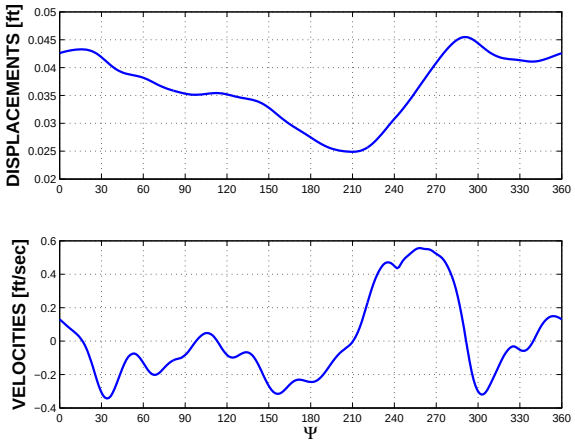

Figure 17: Time history of the lead-lag damper stroking (top figure) and stroking velocity (bottom figure).

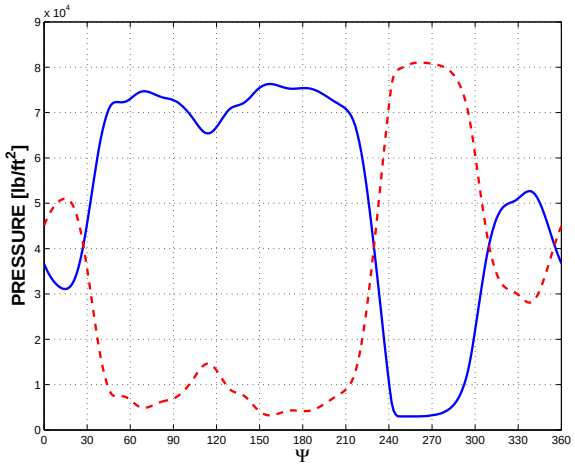

Figure 18: Time history of the predicted pressures in chamber 0 (solid line) and chamber 1 (dashed line).

Figure 16 displays the time history of the predicted damper force. Note the effectiveness of the pressure relief valves that limit the maximum damping force to about $\pm$ 3200 lbs. The stroke and stroke velocity of the damper are presented in fig. 17. These quantities are the variables forming the basis for empirical models of dampers: the output force is assumed to be a nonlinear function of the instantaneous velocity. In the present model, additional information is available that describes the

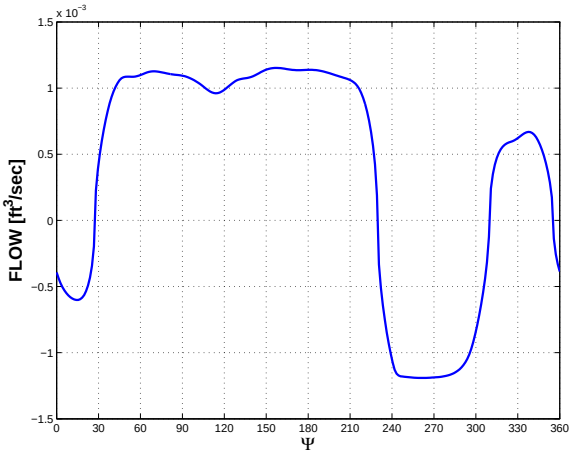

Figure 19: Time history of the predicted volumetric flow rate through the orifice.

internal behavior of the device. The pressures in the two chambers of the dampers are shown in fig. 18. Next, the volumetric flow rate through the orifice is shown in fig. 19, this flow rate tends to equilibrate the pressures in the two hydraulic chambers. As expected, the shape of this time history closely follows that of the damper force.

The role of the pressure relief valves is illustrated in Figs. 20 and 21 that depict the displacement and velocities of the valves, and the flow rate through these valves, respectively. Valve 0 opens over the azimuthal range $\Psi \in [45, 100]$ then $[125, 215]$ deg, whereas valve 1 opens for $\Psi \in [240, 290]$ deg. These ranges are clearly correlated with the high damper force ranges: positive forces for valve 0, negative forces for valve 1 (see fig. 16). This correlation is also reflected in the hydraulic chamber pressure histories, see fig. 18. When a pressure relief valve opens, the volumetric flow rate through the orifice remains nearly constant, see fig. 19, consistent with the nearly constant pressures in the chambers, see fig. 18. Note that the maximum magnitude of the flow rate through the orifice is of the order of 1.2 10^{-3} ft^3/s, whereas the flow rate through the pressure relief valves, see fig. 21, is nearly an order of magnitude larger, due to larger sectional areas. When open, the pressure relief valve nearly short circuits the two hydraulic chambers, effectively limiting the maximum force output

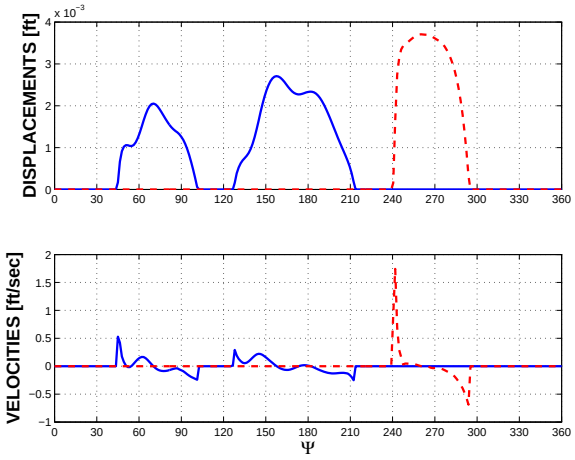

Figure 20: Time history of the predicted displacement (top figure) and velocity (bottom figure) of pressure relief valves, valve 0 (solid line) and valve 1 (dashed line).

of the device.

Finally, fig. 22 shows a comparison between the flight test measurement of damper force and various numerical predictions. In the first simulation, the damper was modeled as a linear dashpot with constant $c = 4659.6$ lb/(ft/s). In the second simulation, a nonlinear dashpot model was used to represent the damper. The nonlinear dashpot characteristics were obtained from a curve fit of the experimentally measured peak force versus peak velocity relationship given in ref. [54]. The last simulation uses the proposed model of the hydraulic device. This figure shows that the peak damper force of the present model agrees well with the flight test data, as well as the time history of the damper force in the azimuthal range $[270, 360]$. Therefore, the present model gives a better correlation with the experimental measurements when compared to the simpler models, although discrepancies still exist. Of course, the observed discrepancies are not necessarily a consequence of a lack of accuracy of the damper model. Indeed, the predicted dynamic response of the rotor system involves a complex model with many interacting components; the damper model is but one of these many components.

The probable cause of the observed discrepancy is the cursory nature of the present

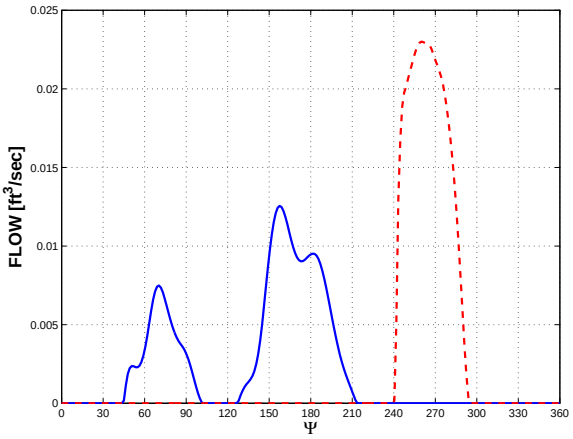

Figure 21: Time history of the predicted volumetric flow rates through the pressure relief valves, valve 0 (solid line) and valve 1 (dashed line).

formulation that models the various components of hydraulic devices with simple equations involving empirical parameters. Some model parameters were set to their theoretical values; others were not known with sufficient accuracy in the experimental set-up, in particular, the hydraulic circuit pressure or the relief valve sectional area. The physical behavior of several components of the device, such as the hydraulic accumulators and check valves, were highly idealized. Other physical phenomena, such as friction in the damper, are not presently modeled and are difficult to quantify with the available experimental data.

This discussion clearly points to the need for more detailed experimental studies of hydraulic devices. Systematic bench test experiments with detailed measurements of chamber pressures, relief valve positions, check valves positions and their associated flow rates or velocities would provide the needed experimental basis for the validation of advanced models.

2.6 Conclusions

The following conclusions listed below can be drawn from this work:

1. A methodology allowing physics based modeling of hydraulic devices within

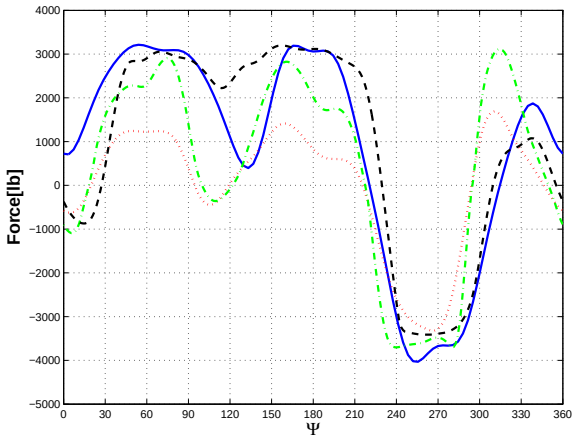

Figure 22: Comparison of the time histories of the lead-lag damper force. Experimental measurements (flight test data): solid lines; linearized model of the damper: dotted line; nonlinear model of the damper: dashed-dotted line; present model: dashed line.

multibody-based comprehensive models of rotorcraft systems was developed.

2. The new mathematical models of hydraulic devices were implemented in a multibody code and calibrated by comparing their predictions with bench test measurements. While predicted peak damping forces were found to be in good agreement with measurements, the model did not predict the entire time history of damper force to the same level of accuracy.

3. The validated model of the UH-60 lead-lag damper model was coupled with a comprehensive model of the rotor system. Measured aerodynamic loads were applied to the blade and predicted damper forces were compared with experimental measurements. A qualitative improvement in the prediction was observed when using the proposed model rather than a linear approximation of the damper behavior.

4. The proposed model also evaluates relevant hydraulic quantities such as chamber pressures, orifice flow rates, and pressure relief valve displacements. Hence, the present model could be used to design lead-lag dampers presenting desirable

force and damping characteristics.

5. To further calibrate the proposed model, additional experimental results would be required. For instance, experimental results including measured hydraulic chamber pressures and orifice flows would allow verification of the internal states of the device and the determination of some of the model parameters, such as the discharge coefficient, which was taken as a given constant in the present simulation.

CHAPTER III

FLUID-STRUCTURE COUPLING

3.1 Introduction

A new area involving the coupling between computational fluid programs and finite element method based structural dynamics programs to solve aeroelastic problems, known as computational aeroelasticity, has been attracting considerable attention in the rotorcraft community and continues to be one of the trends of aeroelastic analysis. The main idea of this approach is to replace the aerodynamic loading, which is computed based on simple lifting-line theory, inflow models, and necessary approximation of unsteady effects as well in the comprehensive analysis, with those computed by CFD program based on the configuration of the model attained from CSD program. Therefore, the coupling process requires the data communication including aerodynamic loads and structural deformations or displacements and velocities, between CFD and CSD programs. To achieve such a coupling analysis, two strategies are available, namely, loose coupling and tight coupling strategies. The first one, also referred to as weak coupling approach, is such an approach where boundary conditions, aerodynamic loads and structural deformations, are exchanged after a periodic solution has been obtained in both codes' simulations. In effect, the solutions of the two disciplines are lagged by one entire period of the rotor. An iterative procedure, often involving a trimming analysis, is required to achieve converged solutions. Therefore, the loose coupling analysis is suitable for periodic problems. In another approach, called tight coupling, the CFD and CSD codes are exchanging these boundary conditions at each time step; in such case, the solutions of the two disciplines are lagged by a time step only. Finally, it is also possible to simultaneously

solve the CFD and CSD equations, although this approach will prevent the use of legacy codes. With the latter strategies, trimming analysis may become difficult to implement and computational efficiency may be decreased.

A comparison study between these two strategies has first been demonstrated by Altmikus *et al.* [2] who coupled CFD code, WAVES [32], with structural code, HOST (Helicopter Overall Simulation Tool) [23]. This study showed that these two methods with specific advantages can yield similar results in terms of control angles, sectional lift coefficients and tip torsion response, although tight coupling required more computational cost. The loose coupling analysis is computational efficient. However, it is not suitable for dealing with flow conditions with strong nonlinearities. On the contrary, tight coupling is a more rigorous approach with a wider range of applications. Recently, Bhagwat *et al.* [30] and Nygaard *et al.* [78] both conducted tight coupling analysis of CFD code, OVERFLOW-2 and the comprehensive rotorcraft code, RCAS (Rotorcraft Comprehensive Analysis System), which gave good correlations with test data. A comparison between loose coupling and tight coupling with fixed control angles was performed in these two studies and they demonstrated that identical results can be obtained within engineering accuracy and no significant improvements were achieved. However, these comparison studies provided practical significance in saving the computational time because only a loose coupling analysis is sufficient to achieve the comparable results, which can compromise the complexity and computationally less efficiency of tight coupling.

The idea of coupling CFD with comprehensive rotorcraft analysis has been first demonstrated by Tung, Caradonna, and Johnson [98] through a transonic small-disturbance code loosely coupled with the CAMRAD comprehensive analysis [55, 56]. Since then, this coupling approach has been implemented to full potential flow solvers and different comprehensive rotorcraft codes with different focuses [96, 93, 19], in which inflow angles were computed by comprehensive analysis. Strawn *et al.* [96, 93]

coupled full-potential rotor codes with CAMRAD/JA [57],which demonstrated the importance of accurately transferring unsteady information to the CFD code and convergence problems encountered in the case of addition of pitching moments to the coupling procedure.

With the development of computational fluid dynamics, comprehensive codes have been coupled with Euler solvers [88, 2]. However, these studies have shown that Euler solvers only show minor improvements in airloads predictions as compared to comprehensive codes. Taking advantages of super computers, Reynolds Averaged Navier-Stokes (RANS) based solvers become possible intriguing the coupling between such kind of CFD solvers with other comprehensive analysis codes. Considering viscous effect, a loose coupling between Navier-Stokes aerodynamic code FLOWer and DLR rotor simulation code S4 performed by Pahlke *et al.* [79] showed that computations with viscosity were in better agreement with experimental data for the rotors in high-speed forward flight. Stable and convergent coupling analysis between RANS-based CFD codes and comprehensive rotorcraft codes have been conducted successfully in recent development in the area of computational aeroelasticity. Refs. [90, 91, 45, 43, 46, 42, 44] focused on the coupling of CFD code TURNS (Transonic Unsteady Rotor Navier-Stokes) and CSD code UMARC (University of Maryland Advanced Rotorcraft Code), both developed by the University of Maryland, to perform the structural and aerodynamic load predictions in steady and transient flight conditions. Aiming to investigate two unresolved key problems in the airloads prediction, as mentioned in ref. [34], the under prediction of pitching moments and the advancing blade negative lift phase lag, Potsdam *et al.* [84] coupled CFD program OVERFLOW-D [40] loosely with a comprehensive code, CAMRAD II [58] to predict the aerodynamic loading for UH-60A Black Hawk helicopter. Noteworthily, the CFD/CSD coupling algorithm has been widely applied in many aspects of the rotorcraft analysis, including the aerodynamic loading [84], rotor vibratory loading [91, 45],

stall [43, 46] and blade vortex interaction [53] phenomena occurring in steady level flight and transient flight conditions.

The difference of the CFD codes OVERFLOW and TURNS is the way they capture the effect of the far wake. OVERFLOW includes all four blades in the analysis and directly computes the far-field inflow using an overset mesh approach, and is, therefore a wholly first principles-based wake capturing CFD code. On the other hand TURNS includes only a single blade and obtains the far wake inflow from a separate free-wake model. The methodology that models rotor systems and entire wake structures, as used in OVERFLOW, is referred to as wake capturing methodology. On the contrary, capturing the effect of the far wake by imposing an external model to CFD analysis, as used in TURNS, is referred to as wake coupling methodology. An assessment of these two methodologies used in aerodynamic airloads prediction for critical steady flight conditions using CFD/CSD coupling approach, has been evaluated by Sitaraman and Baeder [90] showing that wake capturing methodology is of higher accuracy, but a high resolution of grids may be required for those wake dominated problems, thus leading to less computational efficiency. Wake coupling is favorable in terms of the computational efficiency, but more accurate wake model is required so as to achieve more accurate prediction of airloads.

Even earlier in the mid of 1990's, Bauchau and Ahmad [18] have attempted to couple the CFD code OVERFLOW with the finite element method based multibody dynamic analysis formulation, DYMORE[13, 10]. The tight coupling strategy was validated by the airloads prediction for the UH60A black hawk helicopter. Unfortunately, large differences were observed between the result obtained from the coupling analysis and experimental measurements. In this effort, the emphasis was placed on the establishment of an I/O files interface, between DYMORE and OVERFLOW-2 based on the standard provided in ref.[78]. The goal of this work is to enable the coupling between DYMORE and OVERFLOW-2 in both loose and tight manners.

The main function of the interface files is to transform the data information including rotor configurations and aerodynamic loadings. This interface is validated through a loose coupling procedure applied on these two codes with the delta airloads method to improve the convergence. The components involved in the aerodynamic interface are introduced, including aerodynamic models, aerodynamic dynamic computation options available in DYMORE, coupling components and strategies, as well as a concise introduction of coupled programs, followed by coupling examples. The conclusions drawn through this work are offered at the end of this chapter.

3.2 Aerodynamic Model

In aeroelastic problems, aerodynamic forces are applied to a flexible structural system. The aerodynamic forces deform the elastic system, modifying its positions and velocities. In turn, this new configuration of the system changes the aerodynamic problem, and hence, the aerodynamic loads. Clearly, aeroelastic problems are inherently coupled problems.

To treat aeroelastic problems, it is necessary to define an aerodynamic model that describes where aerodynamic forces will be applied on a structural model and how theses aerodynamic forces will be evaluated.

The aerodynamic model consists of a number of the following aerodynamic elements.

3.2.1 Air points

An air point is a point rigidly attached to a rigid body. Aerodynamic forces will be computed at the air point and applied to the corresponding rigid body. For some problems, wings or rotor blades can be assumed to be rigid bodies. In this case, the integrated aerodynamic loading on the rigid body consists of a force and moment applied at a point of the rigid body. The aerodynamic loads could be computed using approximate methods such tabulated wind tunnel measurements. On the other

hand, if the aerodynamic loads are computed with the help of a computational fluid dynamics code, pressures are evaluated throughout the flow field and integration over the surface of the wing or rotor blade then yields the desired aerodynamic load and moment. With both options, aerodynamic computations yield the load and moment at a point that form an approximation to the distributed aerodynamic forces and moments that should be applied to the rigid body.

3.2.2 Lifting lines

A lifting line is a collection of airstations that are rigidly connected at specific point along a beam. Aerodynamic loads will be computed at each airstation and applied to the associated beam. For some problems, it is common to model wings or rotor blades structures using one dimensional beam elements. In this case, the aerodynamic loading on the beam consists of a field of distributed forces and moments. If the aerodynamic loads are computed using approximate methods such as thin-airfoil theory and tabulated wind tunnel measurements, the sectional lift, drag and moment can be readily computed. On the other hand, if the aerodynamic loads are computed with the help of a computational fluid dynamics code, pressures are evaluated throughout the flow field. Integration of this pressure distribution over an airfoil then yields sectional lift, drag and moment. With both options, aerodynamic computations yield sectional lift, drag and moment at a number of stations along the blade that form a discrete approximation to the distributed aerodynamic forces and

3.2.3 Rotors

A rotor is a collection of air points and/or lifting lines that are connected to a rotating shaft. The aerodynamic loading on the rotor is the combined loading acting on the associated air points and/or lifting lines. The aerodynamic elements forming a rotor are shown in fig. 23.

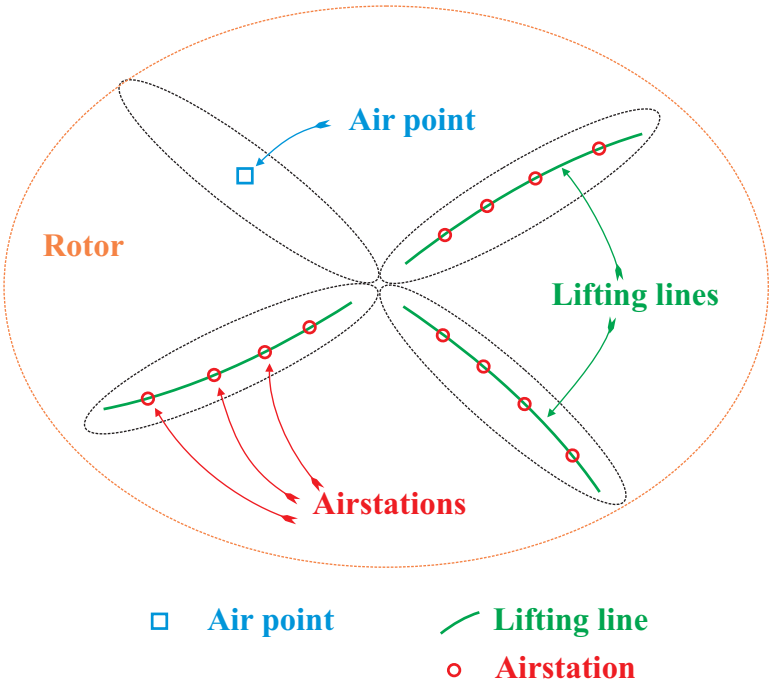

Figure 23: Schematic of the aerodynamic elements forming a rotor.

3.2.4 Wings

A wing is a collection of air points and/or lifting lines that are connected to a fuselage. The aerodynamic loading on the wing is the combined loading acting on the associated air points and/or lifting lines. The aerodynamic elements forming a wing are shown in fig. 24.

3.2.5 Inflows

An inflow is an aerodynamic element that computes an induced flow over a disk.

3.2.6 Aerodynamic interfaces

An aerodynamic interface specifies how the aerodynamic loads at the air points and lifting lines will be computed.

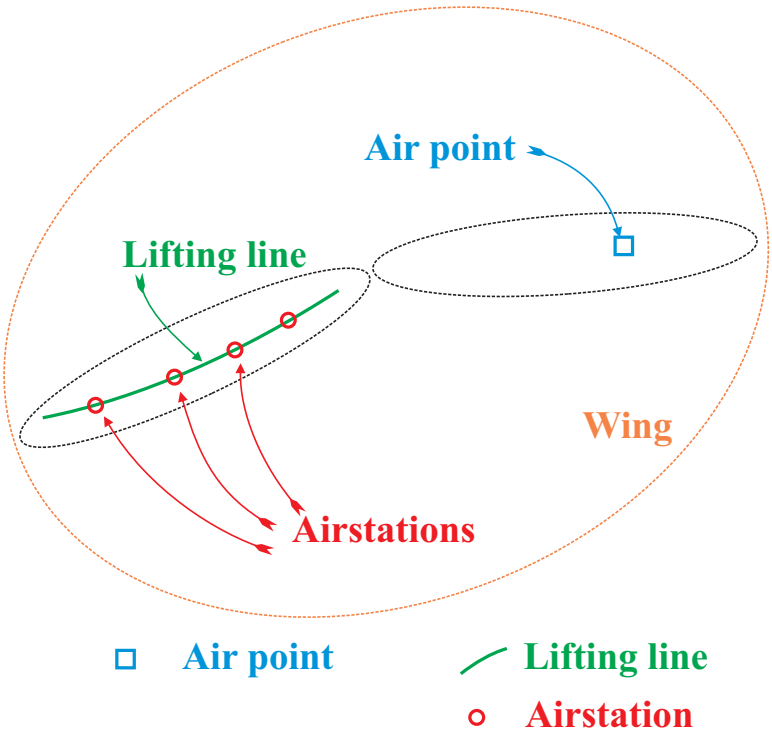

Figure 24: Schematic of the aerodynamic elements forming a wing.

3.3 Components in the coupling analysis

With this in mind, the coupling between structural and fluid dynamics within the context of rotorcraft aeroelastic analysis involves the following components.

3.3.1 Computational structural analysis tool

A *computational structural dynamics* (CSD) code.

This code requires the knowledge of distributed aerodynamic forces and moments and predicts the resulting displacements and velocities of the structure.

3.3.2 Computational fluid analysis tool

A *computational fluid dynamics* (CFD) or a simplified airloads computation code.

Both code requires the knowledge of positions and velocities of the blade surface and predict the resulting aerodynamic forces and moments.

3.3.3 Optional components

An *optional wake model*.

This code requires the knowledge of blade circulation and predicts the resulting inflow over the rotor blade. When using a CFD code that models the entire flow field around the rotor, the wake model is not required.

3.3.4 Relationship among the analysis codes

These three modules interact by exchanging data at a set of air points and/or airstations defining lifting lines. The interactions between these three modules is schematically described in fig. 25. Two main interfaces are clearly needed: a kinematics interface that transfers the displacements and velocities computed by the CSD code to the CFD code and a load interface that transfers the aerodynamic forces and moments computed by the CFD code to the CSD code. The data to be exchanged through both interfaces is clearly associated with air points or airstations.

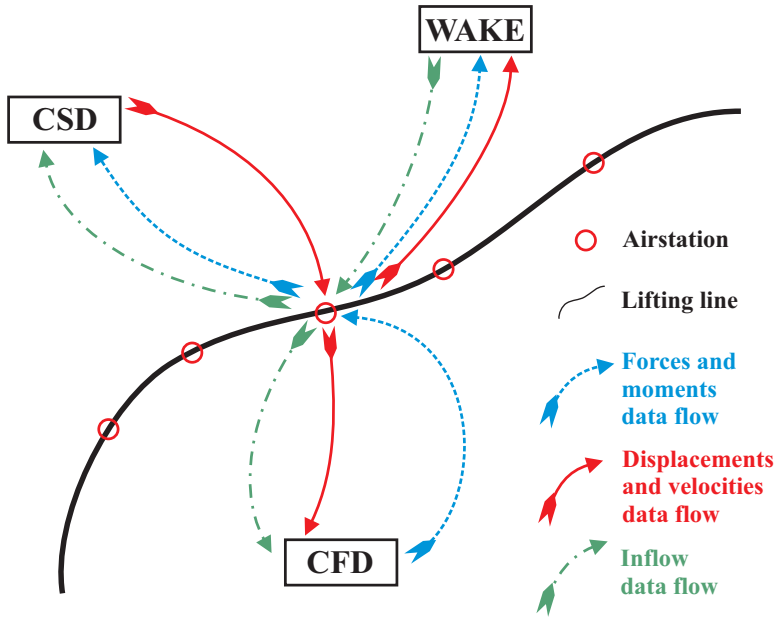

Figure 25: Schematics of the aerodynamics interface.

3.4 Aerodynamic Interface

An aerodynamic interface is the component of an aerodynamic model that describes the procedure used to compute the aerodynamic loads associated with an aerodynamic model. The implementation of the aerodynamic interface depends on the nature of the code used for the evaluation of the airloads. The following options are available.

1. **Airloads are computed internally**

   In this case, the aerodynamic loads are computed using a simplified airloads computation tool that is internal to the CSD code. The kinematic and load interfaces involve calls to subroutine within this single code, and little input is required from the user. Data exchange between the CSD code and its aerodynamics module occur at each time step of the analysis.

2. **Airloads are computed by an external CFD code** and exchanged through formatted files

   In this case, the aerodynamic loads are computed using an external CFD code. The kinematics interface transfers the positions or displacements computed by the CSD code to the CFD code. The loads interface transfers the aerodynamic loads computed by the CFD code to the CSD code. The detailed information about the kinematic and load interfaces are described in Appendix A. The data is exchanged between the codes though a set of formatted files.

3. **Airloads are computed by an external code** that is compiled together with the comprehensive code

   In this case, the aerodynamic loads are computed using an external code. The kinematics interface transfers the positions or displacements computed by the CSD code to the external code. The loads interface transfers the aerodynamic

loads computed by the external code to the CSD code. The data is exchanged between the codes through a set of interface routines.

3.5 Coupling Strategies

3.5.1 Tight coupling

Two strategies are available to couple CSD code with CFD code, namely, loose coupling strategy and tight coupling strategy.

3.5.2 Loose coupling

In the tight coupling strategy, data are exchanged between the two codes at each time step of the analysis. In the loose coupling strategy, data are exchanged between the two codes at regular intervals that could include many time steps on a periodic basis.

3.5.3 Delta-airloads method

The loose coupling strategy is particularly useful when periodic rotorcraft aeroelastic problems are dealt with and involves the following steps.

1. **Iteration 0:** run the comprehensive code with its internal aerodynamic model until a trimmed, periodic aeroelastic solution is obtained. For the last revolution, archive the dynamic response of the system, $R^{(0)}$, and the predicted airloads, $A^{(0)}_{\text{LL}}$.

2. **Iteration 0:** run the external CFD code based on the present dynamic response of the system, $R^{(0)}$, to obtain a new set of periodic airloads $A^{(0)}_{\text{CFD}}$. Compute the difference between the airloads predicted between the two codes, $\Delta A^{(0)} = A^{(0)}_{\text{CFD}} - A^{(0)}_{\text{LL}}$, these are called the "delta airloads."

3. **Iteration k:** run the comprehensive code until a trimmed, periodic aeroelastic solution is obtained. The applied aerodynamic loads are the sum of those predicted the internal aerodynamic model and the delta airloads, $\Delta A^{(k-1)}$. For

the last revolution, archive the dynamic response of the system, $R^{(k)}$, and the airloads predicted by the internal aerodynamic model, $A_{\mathrm{LL}}^{(k)}$.

4. **Iteration k:** run the external CFD code based on the present dynamic response of the system, $R^{(k)}$, to obtain a new set of periodic airloads $A_{\mathrm{CFD}}^{(k)}$. Compute the difference between the airloads predicted between the two codes, $\Delta A^{(k)} = A_{\mathrm{CFD}}^{(k)} - A_{\mathrm{LL}}^{(k)}$.

5. Repeat step 3 and 4 until convergence is achieved.

This procedure is clearly shown in fig.(26).

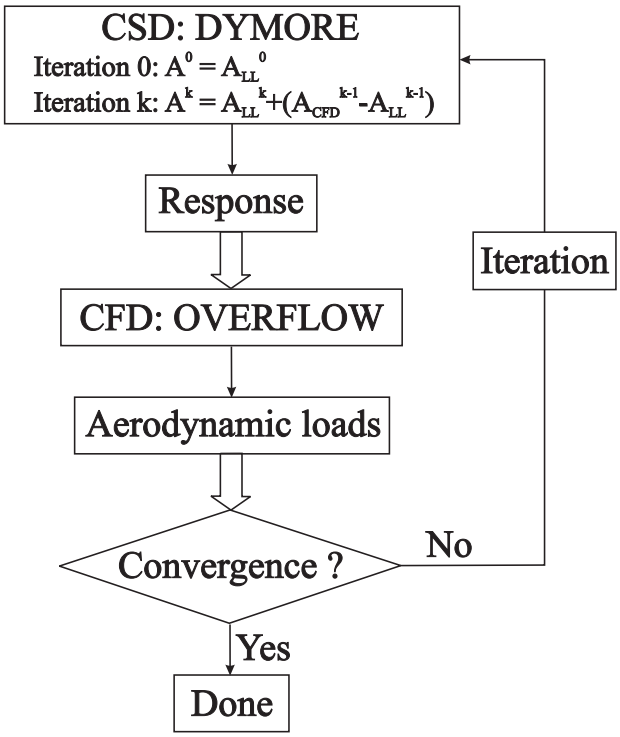

Figure 26: Topology modeling of rotor

3.6 Coupling Programs

In the coupling procedure, comprehensive rotorcraft analysis code, DYMORE developed by Georgia Institute of Technology [13], is employed to calculate the structural

response and rotor trim. In DYMORE, the aerodynamic model is based on two-dimensional lifting-line theory. The induced inflow field is computed using dynamic flow model developed by Peters et al. [81]. Trim analysis is accomplished using DYMORE's internal auto-pilot [80].

The CFD program used in this coupling procedure is OVERFLOW-2 [40], which is developed based on well known NASA OVERFLOW code and has been significantly enhanced to accommodate moving body applications. Basically, OVERFLOW-2 is a general Navier-Stokes solver for problems that may involve relative motion between configuration components. The code uses overset structured grids to accommodate arbitrarily complex geometries. OVERFLOW-2 has the ability to capture the three-dimensional effect and nonlinearities, especially at the tip region of blades.

3.7 Coupling Examples

The Sikorsky UH-60 helicopter rotor model used in the previous chapter is applied here again. For simplicity, the swash plate and the pitch link are taken off. The initial pitch angle of each blade is set through a revolute joint attached at the hinge connecting the root retention and blade. The rest of the model is the same as described in previous chapter.

Figure 27 shows frame definitions used in the simulations. In the interface, the structure motions are quantities measured in hub frame which is a frame moving with the blade which it attaches to. The linear motions are the displacements nondimensionalized by the radius of rotor blade, and the angular motions are Euler angles describing the movements from undeflected configuration to present configuration. The aerodynamic loads are concentrated forces and moments which are dimensional values measured in inertial frame. The units are [lb] and [ft·lb] for forces and moments, respectively.

Two level flights, C8534 and C9017 [84], listed in Table 2, have been used to

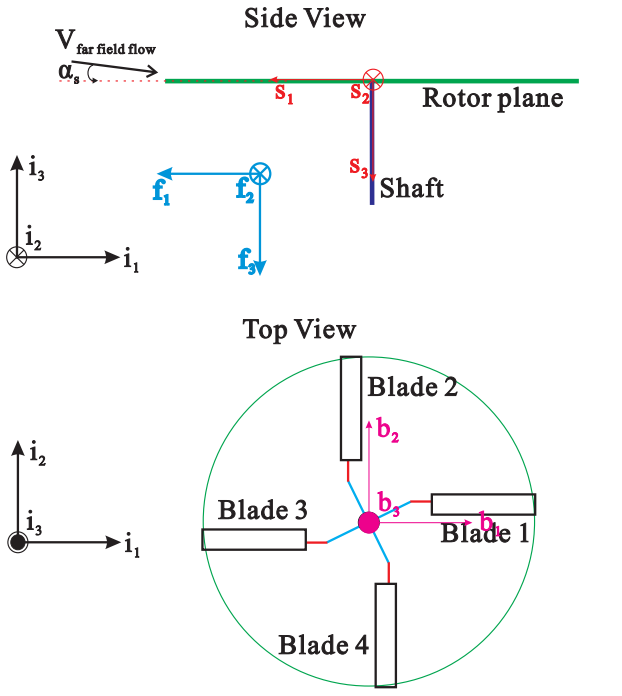

Figure 27: side view and top view of rotor definition

validate the loose coupling procedure.

3.7.1 High-Speed Flight

Flight counter 8534 is a high-speed level flight with high vibratory loads which are typically caused by negative loading on the advancing side of the rotor. In this work, the convergence criterion for the loose coupling algorithm is based on convergence of

Table 2: UH-60 flight test counters

Counter	C_T/σ	μ	M_∞	M_{tip}	α_s(deg)
C8534	0.084	0.37	0.236	0.642	-7.31
C9017	0.129	0.24	0.157	0.665	-0.15

rotor parameters: rotor thrust, moments, and control angles. The trimmed hub loads and control angles for each iteration of coupling are shown in Table 3 and 4. The results demonstrate that the thrust, roll moment and pitch moment can be trimmed to their target values within less than 2% after four iterations only. Figure 28 shows that this loose coupling procedure converges in terms of the hub loads and control angles.

Figures 29 to 32 show the airloads predicted using this coupling procedure. These plots demonstrate that the airloads prediction using loose coupling strategy are in good agreement with experimental measurements. But it should be noted that in the advancing side of the rotor, the normal force and pitching moment converge slower than those in the retreating side, which may caused by negative lift due to high speed in the advancing side. This negative lift becomes more severe at the outer portion of the rotor blades. In the pitching moment figures, the trends of curves agree with experimental data, but some peak values can not be well captured. Notice that the experimental data signals were passed to the fixed data recording system through slip-rings. Therefore, the constant signal component, *i.e.* the signal D.C. component, is unreliable, whereas higher frequencies are accurate within expected measurement errors.

Table 3: DYMORE trimmed hub loads

	targets	iter 0	iter 1	iter 2	iter 3	iter 4
F_z (lb)	17,944	17943	17,940	17,947	17,948	17,944
M_x (ft·lb)	6,884	6,906	6,814	6,917	6,886	6,851
M_y (ft·lb)	-2,583	-2,587	-2,640	-2,574	-2,489	-2,539

Table 4: DYMORE trimmed control angles

(deg)	CAMRAD	iter 0	iter 1	iter 2	iter 3	iter 4
θ_0	13.26	14.93	13.70	13.71	13.77	13.85
θ_{1s}	-8.35	-10.58	-9.39	-9.30	-9.02	-8.87
θ_{1c}	2.43	3.08	3.87	2.40	2.20	2.22

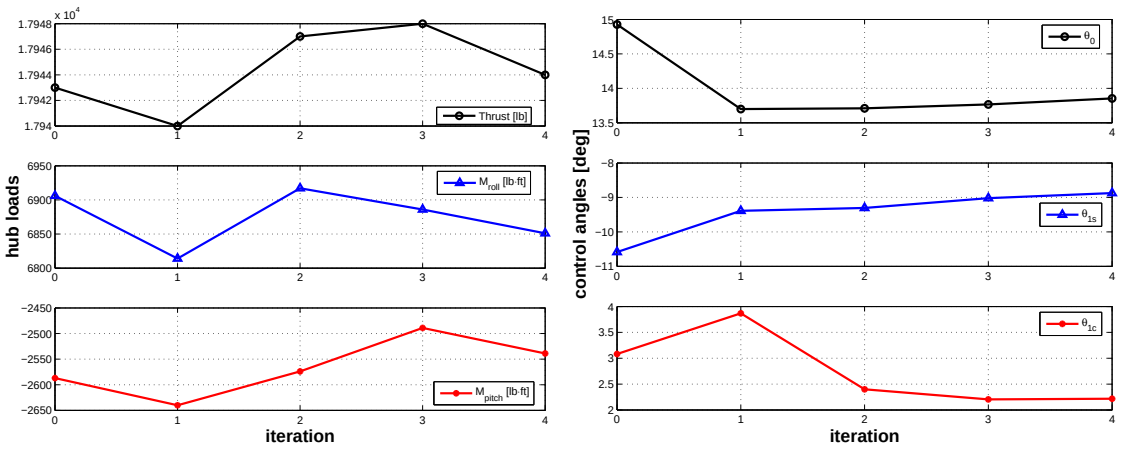

Figure 28: C8534: convergence of hub loads and control angles

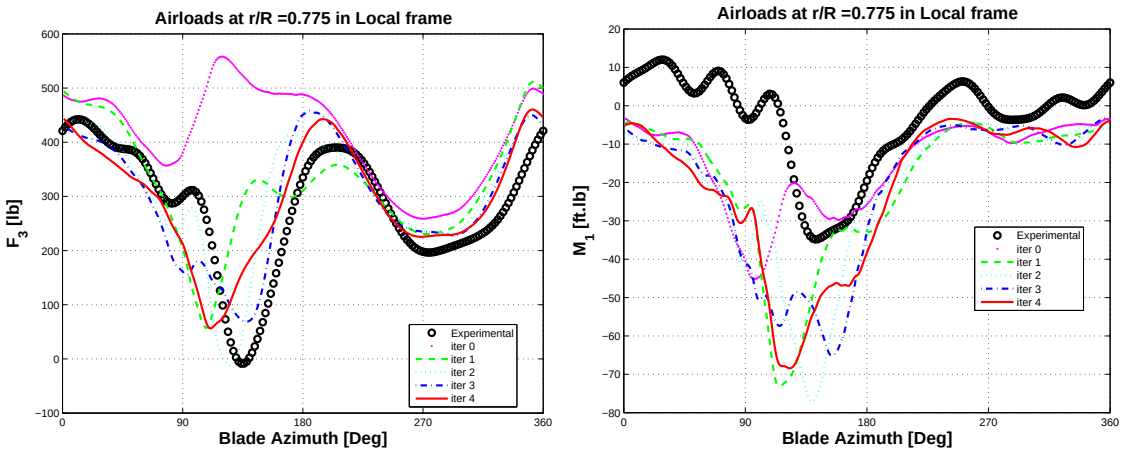

Figure 29: C8534: airloads at $r/R = 0.775$. iter0, point; iter1, dash line; iter2, dotted line; iter3, dashdot line; iter4, dotted line;

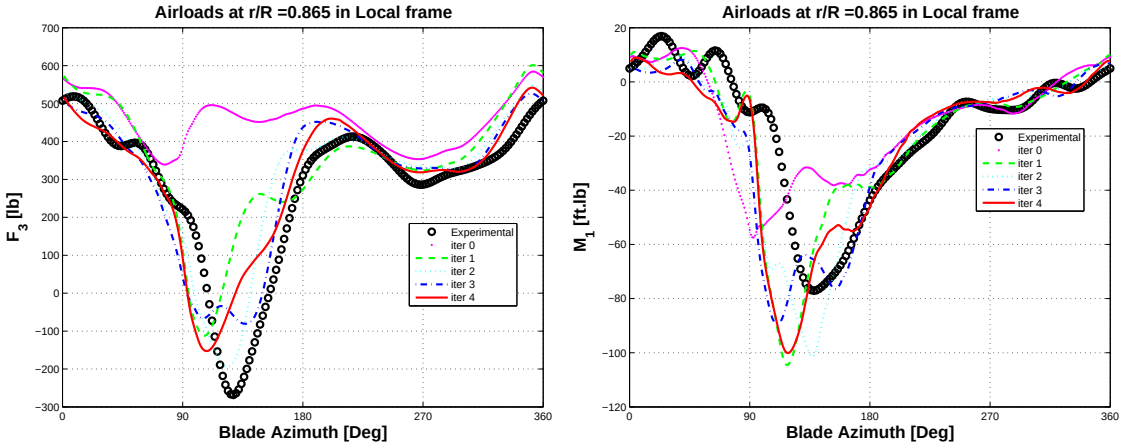

Figure 30: C8534: airloads at $r/R = 0.865$. iter0, point; iter1, dash line; iter2, dotted line; iter3, dashdot line; iter4, solid line;

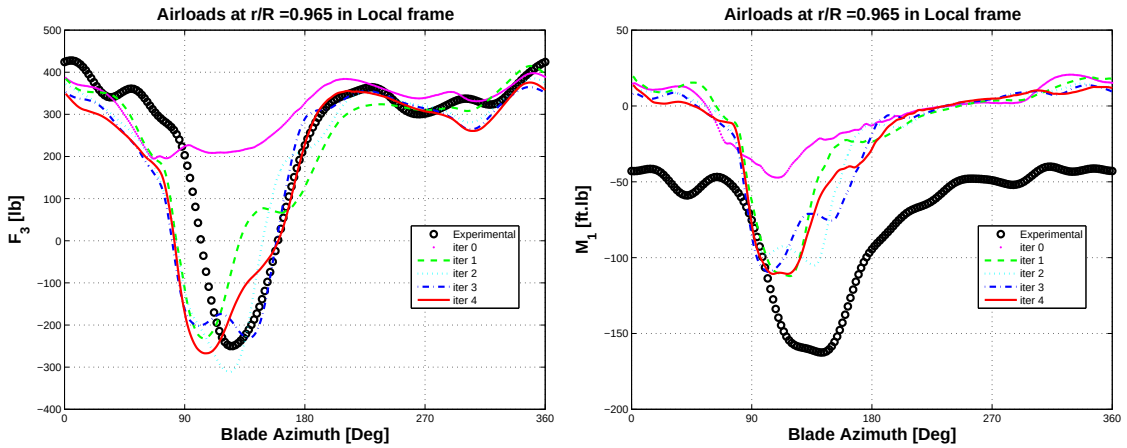

Figure 31: C8534: airloads at $r/R = 0.965$. iter0, point; iter1, dash line; iter2, dotted line; iter3, dashdot line; iter4, solid line;

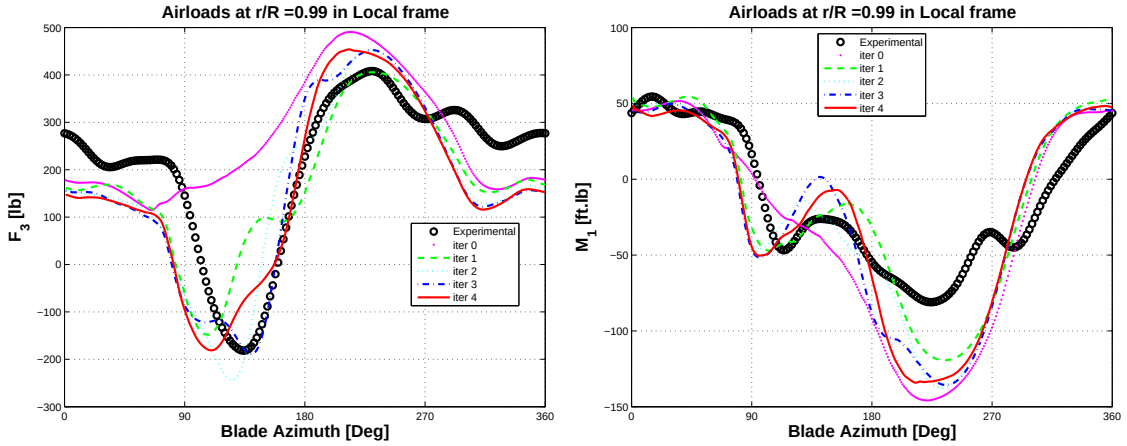

Figure 32: C8534: airloads at $r/R = 0.99$. iter0, point; iter1, dash line; iter2, dotted line; iter3, dashdot line; iter4, solid line;

3.7.2 High-Altitude Flight

Flight counter 9017 is a high thrust level flight in a high altitude. The main problem encountered in this flight is the stall phenomenon emerging in the retreating side of the rotor. The trimmed hub loads and control angles for each iteration of coupling are shown in Table 5 and Table 6. The results tell that the trimmed solution are close to target values, especially, thrust can be trimmed very well. The quick convergence of this loose coupling procedure can be again observed in fig. 33. Figs. 34 to 37 are the comparisons of the normal force and pitch moment predicted using loose coupling procedure with experimental measurements. The convergence of airloads prediction can be seen again in these figures. The trends of normal force agree with experiment, the peak value in retreating side of the rotor can be predicted, but missed in the advancing side. The predicted values are lower than experiments. The loose coupling procedure can predict the number of oscillations per revolution. Disappointedly, the peak values of pitching moment in the retreating side are under predicted.

Table 5: DYMORE trimmed hub loads

	targets	iter 0	iter 1	iter 2	iter 3	iter 4	iter 5
F_z (lb)	16,688	16,688	16,685	16,685	16,686	16,686	16,686
M_x (ft·lb)	-320	-280	-319	-317	-299	-292	-297
M_y (ft·lb)	112	127	123	142	150	153	149

Table 6: DYMORE trimmed control angles

	iter 0	iter 1	iter 2	iter 3	iter 4	iter 5
θ_0 (deg)	12.53	11.90	11.60	11.49	11.45	11.44
θ_{1s} (deg)	-6.47	-7.12	-7.61	-7.80	-7.71	-7.58
θ_{1c} (deg)	1.30	3.02	3.12	2.53	2.20	2.12

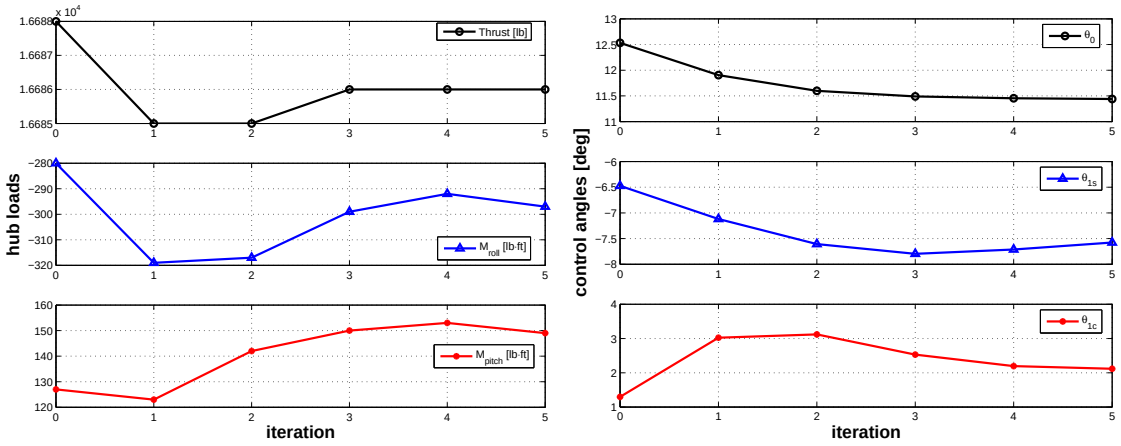

Figure 33: C9017: convergence of hub loads and control angles

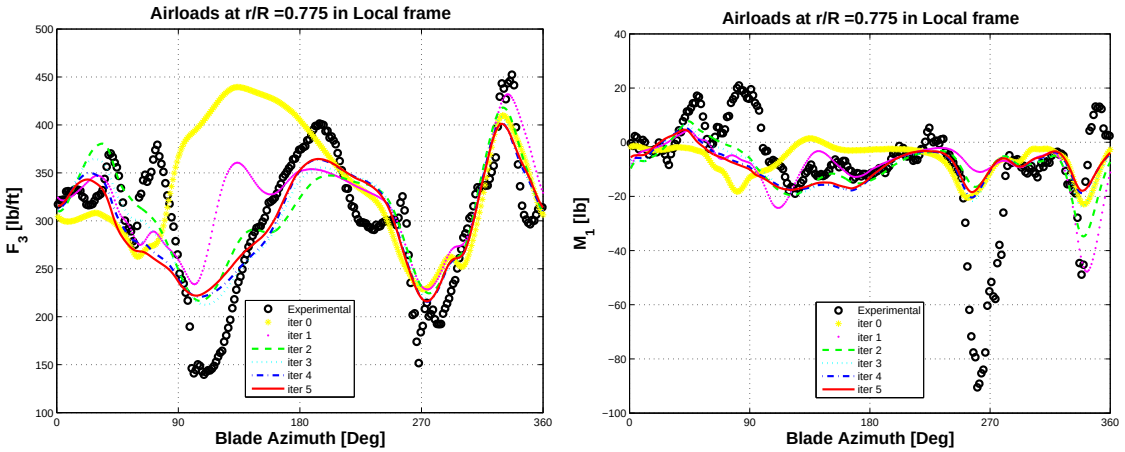

Figure 34: C9017: airloads at $r/R = 0.775$. iter0, star; iter1, point; iter2, dash line; iter3, dotted line; iter4, dashdot line; iter5, solid line

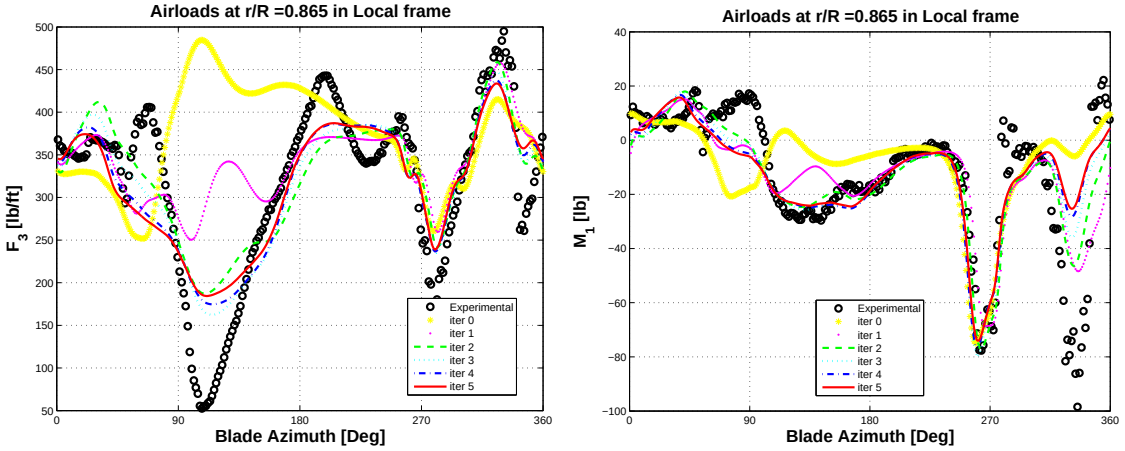

Figure 35: C9017: airloads at $r/R = 0.865$. iter0, star; iter1, point; iter2, dash line; iter3, dotted line; iter4, dashdot line; iter5, solid line

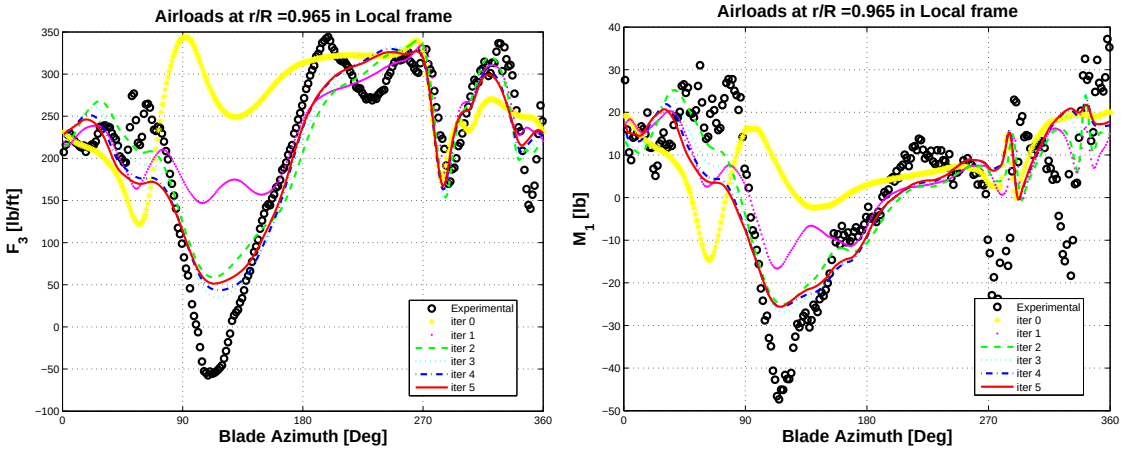

Figure 36: C9017: airloads at $r/R = 0.965$. iter0, star; iter1, point; iter2, dash line; iter3, dotted line; iter4, dashdot line; iter5, solid line

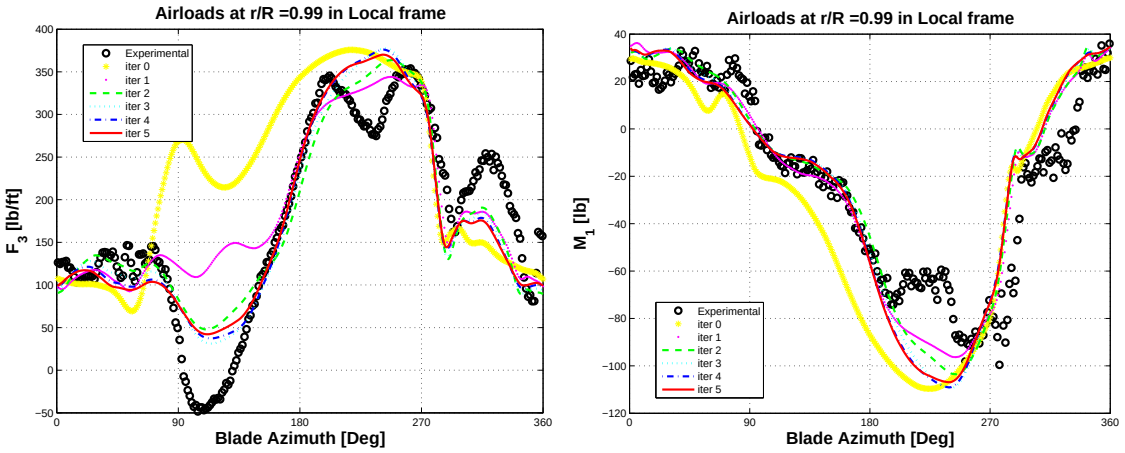

Figure 37: C9017: airloads at $r/R = 0.99$. iter0, star; iter1, point; iter2, dash line; iter3, dotted line; iter4, dashdot line; iter5, solid line

3.8 Conclusions

1. An aerodynamic interface is established to enable data communication between DYMORE, a finite element method based multibody dynamics formulation, and OVERFLOW-2 which is a Navier-Stokes equation solver based on NASA OVERFLOW code using overset structured grids to accommodate arbitrarily complex geometries.

2. A delta airloads method is employed to improve the convergence in the loose coupling approach.

3. This interface is validated by coupling OVERFLOW-2 with DYMORE through the prediction of the airloads for UH-60 aircraft for different flight conditions, such as high-speed flight and high-altitude flight.

4. This loose coupling approach converges quickly in terms of aerodynamic loads and control angles. The predicted airloads agreed well with the experimental data. The trends of normal force and pitch moment have good agreement with experimental data, but some peak values can not be recovered using loose coupling approach.

5. Better correlation with flight test data can be obtained by using finer meshes and improved turbulence models in CFD simulations.

CHAPTER IV

ROTOR WAKE MODELING

4.1 Introduction

4.1.1 Background and Previous work

The ability to accurately predict helicopter rotor performance is critical for the design of future rotorcraft. To achieve this goal, it is necessary to accurately capture the rotor wake, which is dominated by strong vortices that are trailed from the rotor blade tips and by vortex sheets forming the blade's near wake. The strength, location and structure of these primary flow features must be accurately represented and predicted by wake models.

One way of modeling rotor wakes is a first-principles based method, referred to as Computational Fluid Dynamics (CFD) method, that models the entire rotor and its complete wake structure. This methodology can capture the flow environment near blade tips, where three-dimensional flow and compressibility effects dominate the problem. Hariharan and Sankar [52] reviewed the existing computational techniques for modeling the rotor wake and emphasized the need for Navier-Stokes based "first-principles" wake capturing techniques. However, the high computational cost of CFD methods have deferred their application to many practical problems that require an accurate treatment of the rotor wake.

In comprehensive rotorcraft analysis, wakes models [71] have been used extensively for predicting airloads on helicopter rotor blades. This modeling approach combines two main elements: a two-dimensional, unsteady aerodynamic model and a wake model. First, a two-dimensional, unsteady aerodynamic model evaluates the airloads acting on an airfoil section, based its motion, the far-field flow velocity, and the inflow

velocity. Various unsteady models have been used for this purpose such as those of Peters *et al.* [82] or Leishman and Beddoes [20, 21, 72, 70]. Most formulations are linear and model the airfoil as a symmetric airfoil (flat plate); however, specific coefficients of the models can be replaced by empirical data, such as wind tunnel measurements of airfoil lift, drag and pitching moment. Empirical models are also added to capture unsteady drag [68, 67] and dynamic stall effects [69].

Second, a wake model predicts the location and strength of the vorticity in the flow field based on the distribution of the blade circulation. Various types of wake models have been developed, such as vortex wake models [73] and dynamic inflow model [81]. The combination of unsteady aerodynamic models and wake models provides a much lower computational cost alternative to CFD approaches.

In wake models, the convection of vortices along a filament is explicitly traced through the flow field behind the rotor. Vortex diffusion and vortex convection are treated separately. Vortex convection is governed by Helmholtz's law [9], also called the vorticity transportation theorem. Typically, the vortex wake is modeled as vortex lines that are discretized into the form of a regular lattice with straight elements, continuous curved vortex lines, or vortex "blobs." Vortex method, also known as vortex filament method, has been applied to a helicopter rotor wake analysis as early as 1965 [41]. These methods have become very popular tools for the analysis of many aerodynamic problems in the last two decades.

In the application of vortex methods to helicopter wakes modeling, vortex filament methods have encompassed a variety of different approaches, ranging from prescribed vortex techniques to free-wake methods. In prescribed wake methods, the wake structure and geometry are prescribed according to empirical observations and trailed vortices are specified based on semi-empirical rules [64, 63, 59, 89, 22]. Therefore, prescribed wakes assume that the vorticity is convected with the far-field flow and hence, the structure of the vorticity distribution is known. The dynamic

inflow model developed by Peters et al. [81] is based on a similar assumption. Although prescribed wake methods are simple, effective, and computationally efficient, their applicability is limited to rotors having geometries similar to those for which experimental measurements are available. Prescribing a simple helical structure for the wake will limit the accuracy of the simulation. Furthermore, it is difficult to apply the methodology to maneuvering flights, since it is difficult to assign, a priori, a specific structure to the wake.

One solution to these barriers confronting prescribed methods is free-wake methods or free-vortex methods, which have fewer fundamental limitations and are used to model more challenging flight conditions [36, 24, 25]. In free-wake methods [71, 5, 7], the rotor vorticity field is represented using a series of line vortices. These vortical elements, tracked in a Lagrangian manner (fluid particles move with time), are allowed to follow force-free paths in accordance with the equation known as vorticity transportation theorem, which governs their convection. Essentially, the vortical elements are allowed to convect and deform under the action of the local velocity to the force-free locations. Thus, free-wake methods account for self induced distortions of a rotor wake in forward flight such as roll up. The structure of the vorticity distribution is computed based on both far-field flow and the self induced flow velocities, which can be obtained with the help of the Biot-Savart law.

In free-wake methods, various techniques have been used to model the configuration of the filaments including straight [28] or curved [31, 76] vortex elements. Several numerical schemes [6, 27, 29] have been developed to obtain a stable numerical process. Empirical laws, such as the Lamb-Oseen [71] or Vatistas [99] models are used to approximate viscous flow effects through a core size that varies in time. free-wake methods have been applied into many areas, such as vortex ring state modeling and stability analysis [65, 66].

The primary task handled by free-vortex methods is to solve the problem of the

convection of the vortex elements through the rotor flow field. This transport problem may also include the representation of viscous diffusion, vorticity intensification due to the stretching of the vortex filaments and possibly viscous dissipation. The representation of viscous effects in vortex wake methods is usually based on the use of semi-empirical rules [26]. However, the ability to properly integrate the convection of vorticity in a form consistent with viscous effects is an aspect of the transport problem that is critical for accurate predictions of the rotor wake geometry and its induced velocity field [3]. Although free-wake methods, which allows the wake vorticity field to evolve in free motion, are accurate and physically correct approaches to rotor aerodynamics, the calculations have been hindered by the several difficulties encountered by free-wake methods, including the inadequacy of oversimplified physical wake models, excessive computation time, and convergence problems.

4.1.2 Objective and Present Approach

The structure of the vorticity field is often approximated as two-dimensional sheets or as a single dimensional filaments. Whereas sheets are often used to represent the near wake right behind the blade, the far wake is most efficiently captured by vortex filaments. The basic equation governing the evolution of a free-wake filament is

$$\frac{\mathrm{d}\underline{r}}{\mathrm{d}t} = \underline{V}, \tag{17}$$

where $\underline{r}$ is the position vector of an element of vorticity and $\underline{V}$ the local velocity equal to the sum of the far-field flow and induced velocities at that point. The induced velocity, $\mathrm{d}\underline{v}_i$, due to a vortex filament segment of length $\mathrm{d}s$ with the vortex strength Γ can be calculated using the Biot-Savart law as

$$\mathrm{d}\underline{v}_i = \frac{\Gamma}{4\pi} \frac{\bar{t} \times (\underline{r}_p - \underline{r})}{\|\underline{r}_p - \underline{r}\|^3} \mathrm{d}s \tag{18}$$

where $\underline{r}_p$ is the point of interest at which the induced velocity is evaluated, $\underline{r}$ is the position vector of the vortex segment, $\Gamma \mathrm{d}s$, and $\bar{t}$ is the tangent to the vortex

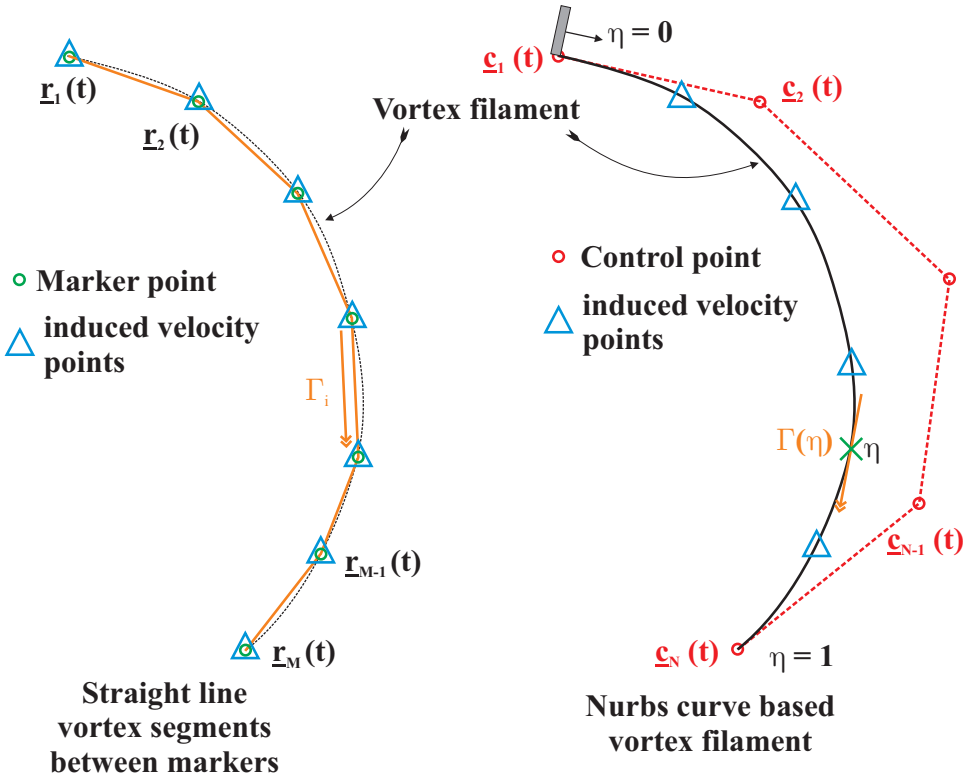

Figure 38: Configuration of a vortex filament. Left figure: Lagrangian marker points and straight segments of constant vorticity. Right figure: NURBS based representation.

filament and its direction is determined by the vorticity of the vortex filament. The wake structure is often represented by a collection of M points, called Lagrangian marker points, located along the vortex filament and connected by straight segments of constant vorticity, Γ_i, as depicted on the left portion of fig. 38. To solve the basic equation of the free-wake problem, eq. (17), the induced velocity must be computed at the M marker points, as indicated in fig. 38, to compute the unknowns of the problem: the location of the M marker points.

If the number of marker points is large, the computational cost associated with the evaluation of induced velocities at marker points will be large. For this reason, a different approach will be taken in this work: the geometry of the vortex filament will be represented by a time dependent NURBS curve [47, 83] such that the vortex

filament becomes a continuous curve. This idea is proposed in light of the unique properties of NURBS curves, as listed below.

1. NURBS curve formulations can represent virtually any desired shape, from conic sections to free-form curves with arbitrary shapes, and provide great control over the shape of a curve.

2. NURBS curve formulations provide the ability to represent complex shapes with remarkably little data.

3. NURBS algorithms are fast and numerically stable.

4. NURBS curves are invariant under common geometric transformations, such as translation, rotation, parallel and perspective projections.

5. NURBS curves have the ability to control the smoothness of a curve.

6. Another important property is that NURBS provide local shape control, *i.e.* the ability to make localized changes to the curve by moving individual control points without affecting its overall shape.

The focus of this chapter is to develop a NURBS-based vortex wake modeling approach and this work is organized in the following manner. The first section describes the representation of vortex filaments using NURBS curves, and the time integration procedure of the governing equation of the vorticity motion. Next, aerodynamic models for two-dimensional airfoils and three-dimensional wings will be introduced, focusing on the solution process for circulations. Then, the calculation of the flow induced by the vortex wake will be presented. Numerical examples will be shown to validate the proposed method. Finally, the conclusions drawn from this study will be given.

4.2 NURBS Description of the Vortex Wake

4.2.1 NURBS Description of a Vortex Filament

As shown on the right portion of fig. 38: the geometry of the vortex filament will be represented by a time dependent NURBS curve. The position vector of a point on the filament is denoted

$$\underline{p}_0(\eta, t) = \sum_{k=0}^{N-1} b_k(\eta)\ \underline{c}_k(t), \tag{19}$$

where η is the variable that parameterizes the NURBS curve, $b_k(\eta)$ are Bernstein polynomials [47], $\underline{c}_k(t)$ the time dependent coordinates of the control points, and N is the number of the control points. The tangent to the curve is

$$\underline{p}_1(\eta, t) = \frac{\partial \underline{p}_0}{\partial \eta}. \tag{20}$$

Note that NURBS describe general curves in terms of an arbitrary parametrization, η, which does not measure length along the curve. Hence, the tangent vector defined by eq. (20) is not a unit vector. The unit tangent vector is denoted

$$\bar{t}(\eta, t) = \frac{1}{p_1}\ \underline{p}_1(\eta, t), \tag{21}$$

where $p_1 = \|\underline{p}_1\|$.

At a time instant t, the distribution of vorticity at η along this curve has a magnitude, $\Gamma(\eta, t)$, and the position vector, $\underline{r}$, of an element of vorticity is denoted as

$$\underline{r}(\eta, t) = \underline{p}_0(\eta, t). \tag{22}$$

The orientation of the vorticity vector is along the tangent to the curve, and hence, the vorticity vector becomes

$$\underline{\Gamma}(\eta, t) = \Gamma(\eta, t)\ \bar{t}(\eta, t), \tag{23}$$

where $\bar{t}$ is given by eq. (21). Since vorticity elements travel along the vortex filament, $\eta = \eta(t)$, and the time derivative of their position vector becomes

$$\dot{\underline{r}}(\eta, t) = \sum_{k=0}^{N-1} \left[\dot{\eta} b_k'(\eta)\ \underline{c}_k(t) + b_k(\eta)\ \dot{\underline{c}}_k(t)\right], \tag{24}$$

where $()^{\cdot}$ denotes a derivative with respect to time and $()'$ a derivative with respect to η, and $\sigma = \mathrm{d}\eta/\mathrm{d}t$. Introducing these results into eq. (24) yields

$$\dot{\underline{r}}(\eta,t) = \sigma\ \bar{t}(\eta,t)\underline{p}_1(\eta,t) + \sum_{k=0}^{N-1} b_k(\eta)\ \dot{\underline{c}}_k(t), \tag{25}$$

where the first term represent the velocity of the vortex element due to convection along the filament at speed σ and the second term is the velocity component due to the time rate of change of the coordinates of the control points.

With the help of eq. (24), the basic equation of the problem, eq. (17), now becomes

$$\sigma b_0'(\eta)\underline{c}_0(t) + b_0(\eta)\ \dot{\underline{c}}_0(t) + \sigma\underline{B}'^T(\eta)\ \underline{\mathcal{C}}(t) + \underline{B}^T(\eta)\ \dot{\underline{\mathcal{C}}}(t) = \underline{V}(\eta,t), \tag{26}$$

where the following notations were defined

$$\underline{\mathcal{C}}(t) = \begin{bmatrix} \underline{c}_1 \\ \underline{c}_2 \\ \vdots \\ \underline{c}_{N-1} \end{bmatrix}, \tag{27}$$

$$\underline{B}^T(\eta) = \begin{bmatrix} b_1 & b_2 & \dots & b_{N-1} \end{bmatrix}, \quad \text{and} \quad \underline{B}'^T(\eta) = \begin{bmatrix} b_1' & b_2' & \dots & b_{N-1}' \end{bmatrix}. \tag{28}$$

Array $\underline{\mathcal{C}}$ stores the unknowns of the problem: the coordinates of the control points that defined the shape of the NURBS curve. Note that the coordinates, $\underline{c}_0$, of the first control point are known as they remains attached to the airfoil, at the location where the vorticity is created. To solve eq. (26), the local velocity must be found at $N-1$ locations, that is, the induced velocity must be computed at $N-1$ locations, $\eta_1, \eta_2, \dots, \eta_{N-1}$, to yield $3(N-1)$ equations for the $3(N-1)$ coordinates of the control point

$$\begin{aligned}
\sigma b_0'(\eta_1)\underline{c}_0(t) + b_0(\eta_1)\ \dot{\underline{c}}_0(t) + \sigma\underline{B}'^T(\eta_1)\ \underline{\mathcal{C}}(t) + \underline{B}^T(\eta_1)\ \dot{\underline{\mathcal{C}}}(t) &= \underline{V}(\eta_1,t), \\
\sigma b_0'(\eta_2)\underline{c}_0(t) + b_0(\eta_2)\ \dot{\underline{c}}_0(t) + \sigma\underline{B}'^T(\eta_2)\ \underline{\mathcal{C}}(t) + \underline{B}^T(\eta_2)\ \dot{\underline{\mathcal{C}}}(t) &= \underline{V}(\eta_2,t), \\
\vdots &= \vdots \\
\sigma b_0'(\eta_{N-1})\underline{c}_0(t) + b_0(\eta_{N-1})\ \dot{\underline{c}}_0(t) + \sigma\underline{B}'^T(\eta_{N-1})\ \underline{\mathcal{C}}(t) + \underline{B}^T(\eta_{N-1})\ \dot{\underline{\mathcal{C}}}(t) &= \underline{V}(\eta_{N-1},t).
\end{aligned} \tag{29}$$

These $3(N-1)$ ordinary differential equations in time for the $3(N-1)$ unknowns are recast in a matrix form as

$$\mathcal{B}\dot{\underline{\mathcal{C}}} = \underline{\mathcal{V}} - \sigma\mathcal{B}'\underline{\mathcal{C}} - \sigma\mathcal{B}'_0\underline{c}_0 - \mathcal{B}_0\dot{\underline{c}}_0, \tag{30}$$

where the following notation was introduced

$$\underline{\mathcal{V}} = \begin{bmatrix} \underline{V}(\eta_1) \\ \underline{V}(\eta_2) \\ \vdots \\ \underline{V}(\eta_{N-1}) \end{bmatrix}, \tag{31}$$

$$\mathcal{B} = \begin{bmatrix} \underline{B}^T(\eta_1) \\ \underline{B}^T(\eta_2) \\ \vdots \\ \underline{B}^T(\eta_{N-1}) \end{bmatrix}, \mathcal{B}' = \begin{bmatrix} \underline{B}'^T(\eta_1) \\ \underline{B}'^T(\eta_2) \\ \vdots \\ \underline{B}'^T(\eta_{N-1}) \end{bmatrix}, \mathcal{B}_0 = \begin{bmatrix} b_0(\eta_1) \\ b_0(\eta_2) \\ \vdots \\ b_0(\eta_{N-1}) \end{bmatrix}, \quad \mathcal{B}'_0 = \begin{bmatrix} b'_0(\eta_1) \\ b'_0(\eta_2) \\ \vdots \\ b'_0(\eta_{N-1}) \end{bmatrix}, \tag{32}$$

the induced velocity must be computed at $N-1$ points along the filament, as indicated in fig. 38, to compute the unknowns of the problem: the location of the $N-1$ control points.

This new representation is likely to bring the following advantages.

1. The geometry of the vortex filament and the distribution of vorticity as now *continuous variables*.

2. The geometry of the vortex filament is represented by a small number of control point because of the inherent ability of NURBS to represent complex curves. Hence, it is expected that for a same level of geometric accuracy, the number of control points will be significantly smaller than the number of marker points, *i.e.* $N < M$.

3. A corollary of the previous item is that in the proposed approach, induced velocities must be computed at fewer points in the solution process.

4. In the traditional approach, the evaluation of the induced velocity at a point relies on the application of Biot-Savart's law for each straight line segment of vorticity. Hence, computation of the induced velocity at a point required $M-1$ application of Biot-Savart's law. In the proposed approach, the computation of the inflow at a point involves an integral of Biot-Savart's law along the continuous vortex filament. This operation is efficiently performed by Gaussian integration which requires application of Biot-Savart's law at Gauss' points. In view of the high order of accuracy of Gaussian integration, fewer application of Biot-Savart's law should be required in the proposed approach.

5. Since numerous tools [47, 83] are available for constructing NURBS curves meeting specific requirements, adaptivity can easily be included in the solution process.

4.2.2 NURBS Description of a Vortex Sheet

As shown in fig. 39, the vortex sheet behind a wing or rotor blade can be represented by a NURBS surface, whose shape is defined as a tensor product of NURBS curves. In this figure, points 1 to 16 are the control points, curves 0 to 3 are the boundaries of the surface. At least four control points at the vertices of the surface are required to define four boundary curves, thus, a NURBS surface. If more control points are defined, a more detailed representation of the NURBS surface is achieved. The position vector of a point on the NURBS surface is denoted as

$$\underline{p}_0(u,v,t) = \sum_{i=0}^{M-1}\sum_{j=0}^{N-1} B_i(u)B_j(v)\underline{c}_{ij}(t), \quad 0 \le u, \quad v \le 1, \tag{33}$$

where $\underline{c}_{ij}(t)$ are the time dependent control points of the surface that form the control net. u, v are the variables that parameterize the NURBS surface. $B_i(u)$ and $B_j(v)$ are Bernstein polynomials.

The near wake behind a wing or rotor blade can be approximated by a vortex

sheet, whose geometry will be represented by a NURBS surface. A simple quadrangular surface behind a wing is easily defined by a NURBS surface featuring four control points at the corner of the quadrangle. Once the NURBS surface is defined, the position vector of any of its point can be defined in a continuous manner. The vorticity distribution over the sheet can be represented through Chebyshev polynomial expansions, and hence a continuous vorticity distribution over the vortex sheet becomes available. Gaussian Quadrature can be used to calculated the integral of the Biot-Savart law over a surface, leading to an efficient evaluation of the inflow generated by the sheet vorticity.

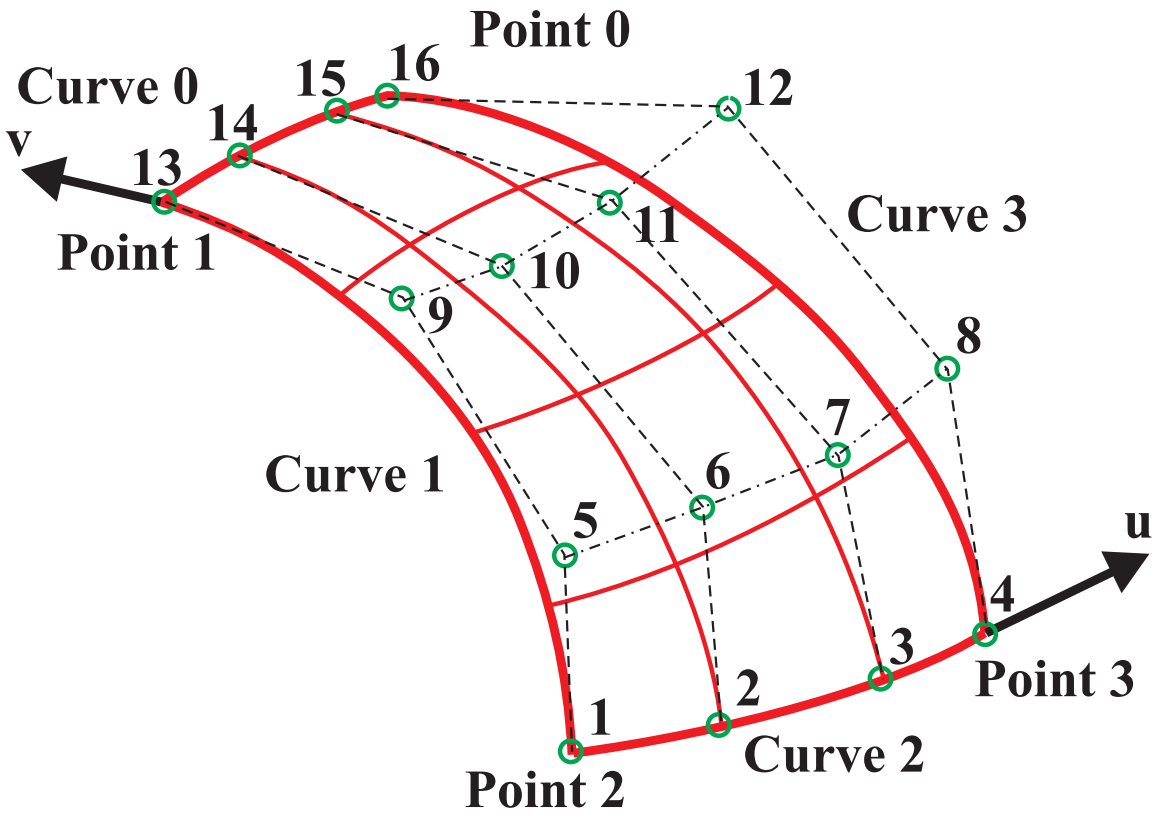

Figure 39: Configuration of a vortex sheet.

4.3 Time Integration Procedure

The governing equation of the problem, eq. (30), will be recast as

$$\dot{\underline{\mathcal{C}}} = \mathcal{B}^{-1}\left[\underline{\mathcal{V}} - \sigma\mathcal{B}'\underline{\mathcal{C}} - \underline{g}\right] = \underline{f}, \tag{34}$$

where $\underline{g} = \sigma\mathcal{B}'_0\underline{c}_0 + \mathcal{B}_0\dot{\underline{c}}_0$ is the array that takes into account the boundary conditions of the problem.

4.3.1 Predictor Corrector Algorithm

To solve this first order system of ordinary differential equations, one approach is to use the Adams-Bashforth [85] predictor corrector algorithm. The initial and final time of a time step are denoted t_i and t_f, respectively, and the time step size is $\Delta t = t_f - t_i$. The subscripts $()_i$ and $()_f$ will be used to indicated quantities computed at time t_i and t_f, respectively; furthermore, the subscripts $()_1$, $()_2$ and $()_3$, indicate quantities computed at times $t_i - \Delta t$, $t_i - 2\Delta t$ and $t_i - 3\Delta t$, respectively. The predictor step of the Adams-Bashforth algorithm is

$$\hat{\underline{\mathcal{C}}}_f = \underline{\mathcal{C}}_i + \frac{\Delta t}{24}\left[55\underline{f}_i - 59\underline{f}_1 + 37\underline{f}_2 - 9\underline{f}_3\right], \tag{35}$$

where $\hat{\underline{\mathcal{C}}}_f$ are the predicted coordinates of the NURBS control points. With these predicted coordinates, it is possible to evaluate an estimate of the induced velocities at the end of the time step, and thus the total local velocity, $\hat{\underline{\mathcal{V}}}_f$.

Next, the corrector step of the Adams-Bashforth yields the final coordinates of the NURBS control points as

$$\underline{\mathcal{C}}_f = \underline{\mathcal{C}}_i + \frac{\Delta t}{24}\left[9\mathcal{B}^{-1}\left(\hat{\underline{\mathcal{V}}}_f - \sigma\mathcal{B}'\underline{\mathcal{C}}_f - \underline{g}_f\right) + 19\underline{f}_i - 5\underline{f}_1 + \underline{f}_2\right]. \tag{36}$$

Note that as suggested by Leishman *et al.* [6, 29], a pseudo-implicit approach is taken here since the second term in the parenthesis was written as $-\sigma\mathcal{B}'\underline{\mathcal{C}}_f$ instead of $-\sigma\mathcal{B}'\hat{\underline{\mathcal{C}}}_f$. Simple algebraic manipulations then lead to

$$\underline{\mathcal{C}}_f = (\mathcal{B} + \frac{9\Delta\eta}{24}\mathcal{B}')^{-1}\left\{\frac{9\Delta t}{24}\left(\hat{\underline{\mathcal{V}}}_f - \underline{g}_f\right) + \mathcal{B}\left[\underline{\mathcal{C}}_i + \frac{\Delta t}{24}\left(19\underline{f}_i - 5\underline{f}_1 + \underline{f}_2\right)\right]\right\}. \tag{37}$$

With these corrected final coordinates, the induced velocities at the end of the time step are evaluated again, that is, the local velocity, $\underline{\mathcal{V}}_f$, is updated again, and $\underline{f}_f = \mathcal{B}^{-1}(\underline{\mathcal{V}}_f - \sigma\mathcal{B}'\underline{\mathcal{C}}_f - \underline{g}_f)$; all variables are then updated to proceed with the next time step.

4.3.2 Central Difference Algorithm

Another simple approach is to use second order central difference formula. Then, eq. (34) is recast as

$$\frac{\underline{\mathcal{C}}_f - \underline{\mathcal{C}}_i}{\Delta t} = \mathcal{B}^{-1}\left[\underline{\mathcal{V}}_i - \sigma\mathcal{B}'\frac{\underline{\mathcal{C}}_f + \underline{\mathcal{C}}_i}{2} - \underline{g}\right] \tag{38}$$

Note that all quantities are expressed as their mid-point value in time, leading to an implicit scheme, although the induced velocity term is computed based on the time step initial values. The velocity term is still chosen as the value at the initial time instant. Reorganizing the above equation leads to

$$\left(\mathcal{B} + \frac{\sigma\Delta t}{2}\mathcal{B}'\right)\underline{\mathcal{C}}_f = \left(\mathcal{B} - \frac{\sigma\Delta t}{2}\mathcal{B}'\right)\underline{\mathcal{C}}_i + \Delta t\left(\underline{\mathcal{V}}_i - \underline{g}\right). \tag{39}$$

The solution of these equations yields the final coordinates of the NURBS control points, and thus the new geometry of the vortex filament. In this work, central difference algorithm is used to solve the equation governing the motion of the vortex filament.

4.4 Filament Deformation Criterion

If the induced velocity, more accurately, the local velocity, were to be constant at all points along the vortex filament, it would translate as a rigid body. Hence, $\partial\underline{v}/\partial\eta$ is a good indicator of the expected local rate of deformation of the filament. Taking a derivative of eq. (17) with respect to η yields $\partial/\partial\eta(\mathrm{d}\underline{r}/\mathrm{d}t) = \partial\underline{v}/\partial\eta$. Since $\partial\underline{r}/\partial\eta = \underline{p}_1$, the tangent to the filament, it follows that

$$\frac{\partial\underline{v}}{\partial\eta} = \frac{\mathrm{d}\underline{p}_1}{\mathrm{d}t}. \tag{40}$$

The expected local rate of deformation of the filament is equal to the time rate of change of the tangent vector. With the proposed formulation, this last quantity is easily computed and can be used to adapt the local description of the filament in areas where its local rate of deformation is expected to be high.

4.5 The Aerodynamic Model

In this section, aerodynamic models used to solve for the circulations released into the wake will be introduced. First, a two-dimensional, thin-airfoil aerodynamic model is introduced and then generalized to arbitrary airfoils. Next, the approach is extended to three-dimensional case to solve for circulations along a wing structure.

4.5.1 Two-Dimensional Aerodynamic Model

Figure 40 shows the configuration of an arbitrary airfoil, together with the points and the frame used to describe its geometry. Point **A** is the quarter-chord point; point **Q** is located at the three-quarter chord, and finally, point **G** is half-way between the quarter chord and the trailing edge (TE). Basis $\mathcal{I} = (\bar{\imath}_1, \bar{\imath}_2, \bar{\imath}_3)$ is an inertial frame. The airfoil attached frame is $\mathcal{F}^A = (\mathbf{A}, \mathcal{A})$, where $\mathcal{A}$ is an orthonormal basis, $\mathcal{A} = (\bar{a}_1, \bar{a}_2, \bar{a}_3)$. Unit vectors $\bar{a}_2$ and $\bar{a}_3$ define the plane of the airfoil: unit vector $\bar{a}_2$ is along with the airfoil zero-lift line and points towards the leading edge (LE), vector $\bar{a}_3$ is perpendicular to $\bar{a}_2$, and vector $\bar{a}_1$ is determined by the right-hand rule. $\mathcal{F}^Q = (\mathbf{Q}, \mathcal{A}^Q)$, where $\mathcal{A}^Q = (\bar{a}_1^Q, \bar{a}_2^Q, \bar{a}_3^Q)$ is parallel to $\mathcal{A}$.

4.5.1.1 Thin-Airfoil Model

A thin airfoil at an angle of attack α in a two-dimensional incompressible, inviscid flow is shown in fig. 41. In this figure, $\underline{V}_t$ is the local relative wind vector at point **Q**. Basis $\mathcal{A}^L = (\bar{a}_1^L, \bar{a}_2^L, \bar{a}_3^L)$ corresponds to a planar rotation of basis $\mathcal{A}^Q$ about axis $\bar{a}_1^Q$ in such a manner that $\bar{a}_2^L$ is along the opposite direction of the relative wind velocity; $\bar{a}_3^L$ is perpendicular to $\bar{a}_2^L$, hence the lift direction is parallel to unit vector $\bar{a}_3^L$.

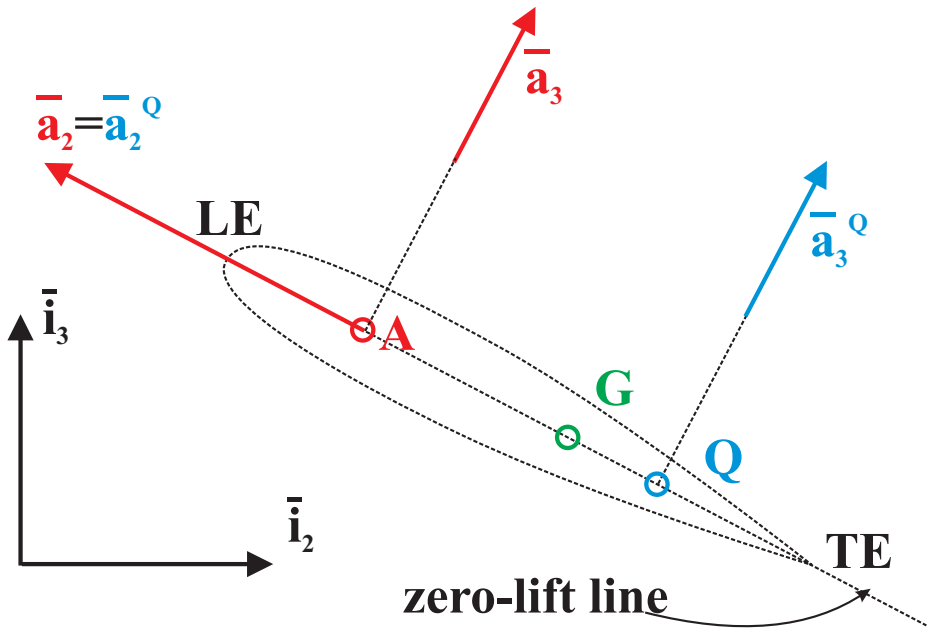

Figure 40: Schematic geometry and frame system of an airfoil

The 2D thin airfoil in fig. 41 can be replaced with a distributed vortex sheet of strength $\gamma(s)$ per unit length along the curvilinear variable, s, describing the outer surface of the airfoil, see fig. 42. Furthermore, if the airfoil is thin, its outer surface can be approximated by its camber line. It follows that the thin airfoil can be replaced with a single vortex sheet distributed along the airfoil's camber line, as shown in fig. 42. Finally, when the airfoil is thin, the camber line cab approximated by the chord line, and hence, the distributed vortex sheet can be located along the airfoil's chord line.

Under the condition of small-disturbance flow, the distributed vortex sheet can be shrunk to a concentrated vortex of strength Γ^b located at the airfoil's quarter chord point, denoted point **A** in fig. 43. Note that for a thin symmetric airfoil, the zero-lift line coincides with chord line. Therefore, fig. 43 shows chord line instead of showing zero-lift line. Let c be the chord length of the airfoil, then the strength of the bound vortex is

$$\Gamma^b = \int_0^c \gamma(s)\mathrm{d}s. \tag{41}$$

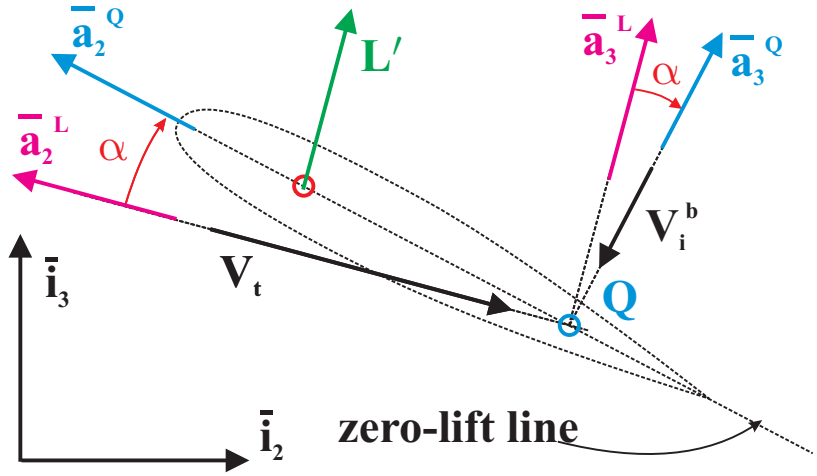

Figure 41: Flow around a thin airfoil in a two-dimensional incompressible, inviscid flow

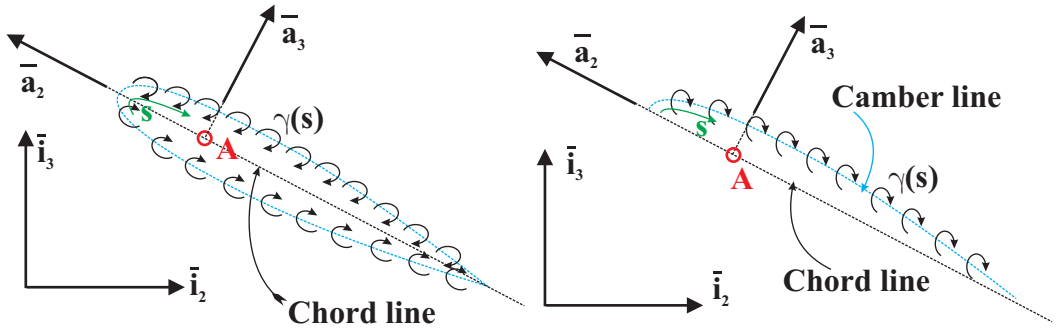

Figure 42: Representation of an airfoil by a distributed vortex sheet $\gamma(s)$ over the airfoil outer surface, left figure, and by a distributed vortex sheet $\gamma(s)$ over the airfoil camber line, right figure.

Hence, the thin airfoil shown in fig. 41 can be modeled approximately as an infinitely long vortex filament of strength Γ^b, bound to the quarter chord of the airfoil. The main problem of the classical 2D thin-airfoil theory [4] is to solve for the vorticity distribution, $\gamma(s)$, such that the camber line becomes a streamline for the flow, and such that the Kutta condition is satisfied at the trailing edge, that is, the value of circulation around the airfoil at a given angle of attack is such that the flow leaves the trailing edge smoothly. The Kutta condition states that the trailing edge vortex must vanish, *i.e.* $\gamma(TE) = V_1 - V_2 = 0$, where V_1, V_2 denote the magnitudes of velocities

along the top surface and the bottom surface.

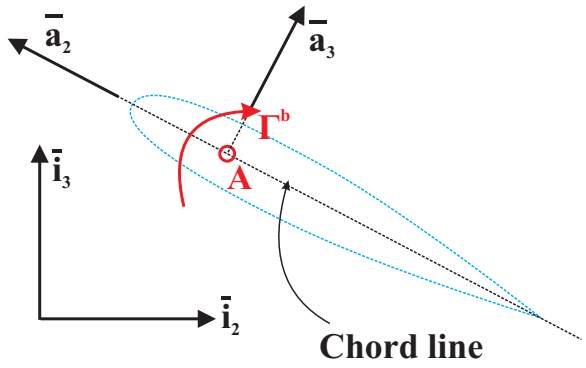

Figure 43: Representation of an airfoil by a bound vortex of strength Γ^b placed at the airfoil's quarter-chord location.

When using a lumped parameter approach, the determination of the vorticity distribution, $\gamma(s)$, that satisfies the Kutta condition, becomes equivalent to the determination of the bound circulation, Γ_b, that satisfies the non penetration condition for the flow at a collocation point, typically selected as the airfoil's three-quarter chord point. Let $\underline{U}_\infty$ denote the far-field free-stream velocity and $\underline{V}_Q$ the structural velocity of point **Q**. The relative velocity at point **Q**, denoted $\underline{V}_\infty$, then becomes

$$\underline{V}_\infty = \underline{U}_\infty - \underline{V}_Q. \tag{42}$$

The local relative flow velocity at point **Q**, denoted, $\underline{V}_t$, is then

$$\underline{V}_t = \underline{V}_\infty + \underline{V}_i, \tag{43}$$

where $\underline{V}_i$ is the induced velocity at point **Q** due to the vortices shed in the wake behind the airfoil. Finally, considering the notation defined in fig. 41, the non-penetration condition can be written as

$$\bar{a}_3^{QT}(\underline{V}_i^b + \underline{V}_t) = 0, \tag{44}$$

where $\underline{V}_i^b$ is the induced velocity at point **Q** due to the bound circulation, Γ^b, at point **A**.

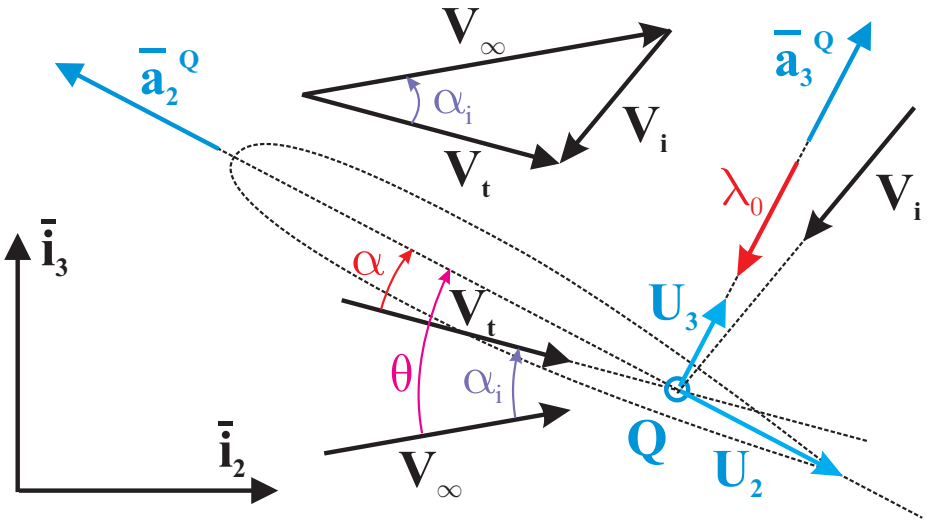

Figure 44: The relationship of velocity vectors around an airfoil in a two-dimensional incompressible, inviscid flow

Figure 44 shows the relationship between the velocity vectors. In this figure, angle θ is the angle between the chord line of the airfoil and the relative velocity vector, $\underline{V}_\infty$. The components of the relative wind velocity expressed in the airfoil attached frame are defined as

$$\begin{aligned} U_2 &= -\bar{a}_2^{QT}\underline{V}_t = -V_\infty \cos\theta - \underline{V}_i^T \bar{a}_2^Q, \\ U_3 &= \bar{a}_3^{QT}\underline{V}_t = V_\infty \sin\theta + \underline{V}_i^T \bar{a}_3^Q. \end{aligned} \tag{45}$$

Let λ_0 denote the component of the induced velocity, $\underline{V}_i$, perpendicular to the airfoil chord line and be positive as shown in the figure, hence, $\lambda_0 = -\bar{a}_3^{QT}\underline{V}_i$. In view of fig. 44, The effective angle of attack, $\alpha = \theta - \alpha_i$, where α_i is the induced angle of attack. It is clear that

$$\alpha = \tan^{-1}\frac{\underline{V}_t^T \bar{a}_3^Q}{-\underline{V}_t^T \bar{a}_2^Q} = \tan^{-1}\frac{U_3}{U_2}. \tag{46}$$

The induced velocity due to a vortex filament can be computed using the Biot-Savart law, see eq. (18). Helmholtz's laws [60] state that in an irrotational inviscid flow, the circulation around a contour enclosing a number of tagged fluid elements is invariable throughout its motion. Therefore, the circulation around a contour that

includes the airfoil and its wake, being zero before the motion began, remains zero. Thus the Kutta condition requires the formation of a starting vortex of circulation equal and opposite to that of the bound circulation. The induced velocity due to the wake, V_i, depends on the bound circulation as well, which means that eq. (44) is an equation with one unknown, Γ^b. In summary, the objective is to solve eq. (44) for the bound circulation that satisfies the non-penetration condition. The lift produced by the 2D thin airfoil in a two-dimensional incompressible, inviscid, steady flow, L', will then be found using the Kutta-Joukowski theorem,

$$L' = \rho V_A \Gamma^b \tag{47}$$

where the quantity V_A is the local relative wind velocity at point **A**, and ρ is the air flow density.

In view of eq. (207), the induced velocity at point **Q** due to an infinitely long bound vortex filament of strength Γ^b is

$$\underline{V}_i^b = -\frac{\Gamma^b}{2\pi(c/2)}\bar{a}_3^Q. \tag{48}$$

The starting vortex moves away from the trailing edge when the airfoil travels in the flow. Therefore, the shed wake behind the airfoil is composed of this starting vortex, which is of the same strength and opposite sign as the bound vortex, and those released into the wake during the earlier stages of the airfoil motion, Γ^w, see fig. 45.

Hence, the induced velocity at point **Q** due to the shed wake is expressed as

$$\underline{V}_i = -\frac{\Gamma^b}{2\pi(c/4)}\bar{a}_3^Q + \underline{V}_i^w. \tag{49}$$

The first term in above equation represents the induced velocity due to the starting vortex. The second term, $\underline{V}_i^w$, represents the induced velocity due to those circulations released into the wake at earlier times and its computation is detailed in section 4.6.1.

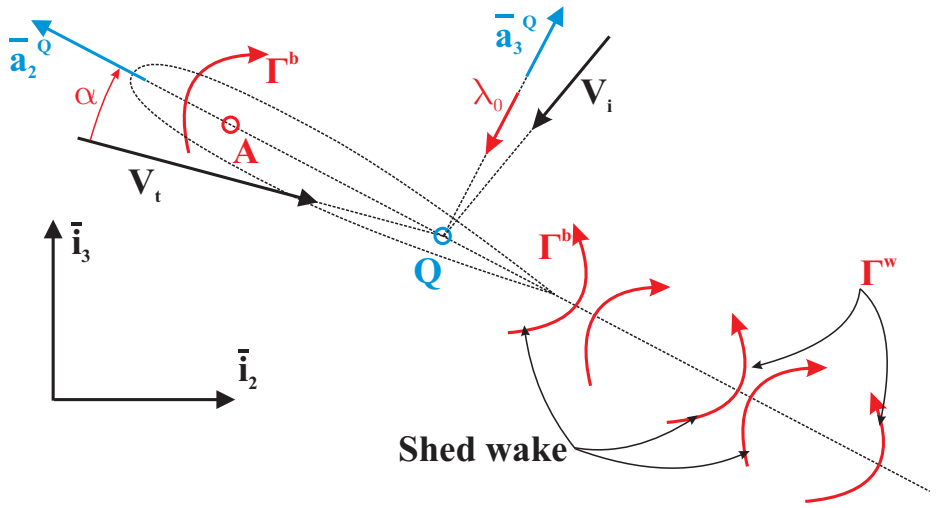

Figure 45: Shed wake structure behind an airfoil in a two-dimensional incompressible, inviscid flow

Substituting eq. (49) into eq. (43), the local relative wind vector now becomes

$$\underline{V}_t = \underline{V}_\infty - \frac{\Gamma^b}{2\pi(c/4)}\bar{a}_3^Q + \underline{V}_i^w. \tag{50}$$

The induced flow perpendicular to the chord line λ_0 due to the shed wake is then

$$\lambda_0 = -\bar{a}_3^{QT}\underline{V}_i = \frac{\Gamma^b}{2\pi(c/4)} - \bar{a}_3^{QT}\underline{V}_i^w. \tag{51}$$

With the help of eqs. (50) and (48), the non-penetration condition can be recast as

$$V_\infty \sin\theta - \frac{\Gamma^b}{\pi c} - \frac{\Gamma^b}{\pi(c/2)} + \bar{a}_3^{QT}\underline{V}_i^w = 0. \tag{52}$$

This equation gives the bound circulation Γ^b as

$$\Gamma^b = \frac{\pi c}{3}\left(V_\infty \sin\theta + \bar{a}_3^{QT}\underline{V}_i^w\right). \tag{53}$$

The induced flow, λ_0, can then be computed using eq. (51). Assuming the induced flow to be uniform over the chord, the local relative wind velocity vector at point **A** is computed as $\underline{V}_A = \underline{V}_{\infty,A} - \lambda_0\bar{a}_3^Q$, where $\underline{V}_{\infty,A}$ is the far-field free-stream velocity at point **A**. The airfoil lift is then computed using eq. (47).

4.5.1.2 General Airfoil Model

The lift produced by an airfoil in a two-dimensional, steady flow can also be computed by the following formula

$$L' = \frac{1}{2}\rho V_t^2 c C_\ell, \tag{54}$$

where C_ℓ is the lift coefficient and V_t is the velocity at the point at which the lift and lift coefficient are evaluated. According to two-dimensional thin-airfoil theory, the lift coefficient has a linear relationship with the angle of attack below the stall angle of attack, that is, $C_\ell = 2\pi\theta$ for a symmetric airfoil, $C_\ell = 2\pi(\theta+\theta_0)$ for a cambered airfoil, where θ is the geometric angle of attack and θ_0 the zero-lift angle of attack, usually a negative value. However, for general flow conditions, the lift coefficient depends on the effective angle of attack, α, the Mach number, Ma, Reynolds number, Re. The lift coefficient can be obtained from wind tunnel measurements or by computational fluid dynamics. Often, the measured data is compiled into a table giving the lift coefficient as a function of angle of attack and Mach number. The Mach number and Reynolds number are defined as

$$Ma = \frac{V_t}{a_\infty}, \tag{55}$$

$$Re = \frac{\rho V_t c}{\mu}, \tag{56}$$

where a_∞ is the speed of sound, and μ the viscosity coefficient of the fluid.

It should be noted that replacing an airfoil surface with a distributed vortex sheet over the airfoil camber line applies only to thin airfoils. The facts that the bound vortex can be placed at the quarter chord of the airfoil and the collocation point at the three-quarter chord are also based on this assumption. Hence, the non-penetration condition described in section 4.5.1.1 applies only to thin airfoils at small angles of attack. Clearly, this approach to the problem must be revised when dealing with finite thickness airfoils because the aerodynamic center is no longer located at the quarter-chord and the collocation point is not necessarily located at the three-quarter

chord. One way of dealing with this problem is to use vortex panel methods [4]. The accuracy of this method depends on the size and number of panels used and the manner in which they are distributed over the airfoil surface.

Another approach is to introduce the concept of an "equivalent flat plate." Two-dimensional airfoil theory is assumed to apply to the equivalent flat plate, which is constrained to produce the same lift as the real airfoil. This approach is described in detail in the next section.

4.5.1.3 The Equivalent Flat Plate Approach

The lift generated by a general airfoil at an angle of attack α, as shown in fig. 46, can be computed using eq. (54). To use this approach, it is necessary to find the lift coefficient, which is a function of the effective angle of attack, α. Indeed, once the angle of attack available, the lift coefficient can be obtained through a look-up procedure, if the airfoil aerodynamic tables are available. Finding the effective angle of attack first requires the knowledge of the induced angle of attack. However, the induced angle of attack is due to the downwash generated by the vortices in the airfoil's wake. For an unsteady aerodynamic problems, this wake comprises the circulation released at earlier times and the bound circulation, which is to be solved for. From the description in section 4.5.1.1, it is clear that solving for the circulation is equivalent to solve the equation of the non-penetration condition, see eq. (44).

For airfoils of finite thickness with realistic flow effects, the non-penetration condition is applied to the equivalent flat plate at an equivalent angle of attack, α^P, which is required to produce the same lift as the actual airfoil, see fig. 46. Geometrically, the equivalent flat plate has the same chord length as the real airfoil and their three-quarter chord point locations coincide. Frame $\mathcal{F}^P = (\mathbf{P}, \mathcal{A}^P)$, where orthonormal basis $\mathcal{A}^P = (\bar{a}_1^P, \bar{a}_2^P, \bar{a}_3^P)$, is defined; unit vector $\bar{a}_2^P$ points towards the leading edge of the equivalent flat plate, whereas $\bar{a}_3^P$ is perpendicular to $\bar{a}_2^P$. The problem is now

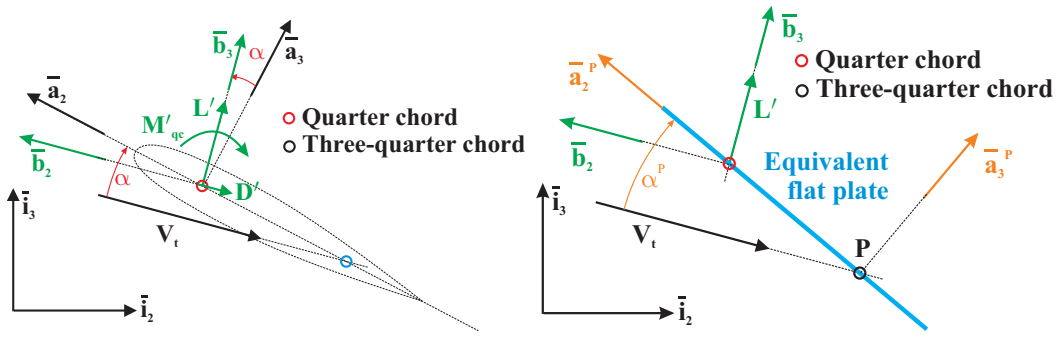

Figure 46: Left figure: real airfoil. Right figure: equivalent flat plate.

recast in the following terms: what is the angle of attack, α^P, of the equivalent flat plate such that the real airfoil and its flat plate equivalent produce the same lift?

Considering fig. 47, the non-penetration condition for the equivalent flat plate airfoil writes as

$$\bar{a}_3^{PT}\left(\underline{V}_t + \underline{V}_i^b\right) = 0. \tag{57}$$

Substituting eqs. (50) and (48) into eq. (57) leads to

$$\bar{a}_3^{PT}\underline{V}_\infty^T - \frac{\Gamma^b}{\pi(c/2)}\bar{a}_3^{PT}\bar{a}_3^Q + \bar{a}_3^{PT}\underline{V}_i^w - \frac{\Gamma^b}{\pi c}\bar{a}_3^{PT}\bar{a}_3^Q = 0. \tag{58}$$

The bound circulation can then be solved from this equation

$$\Gamma^b = \frac{\pi c}{3(\bar{a}_3^{QT}\bar{a}_3^P)}\bar{a}_3^{PT}\left(\underline{V}_\infty + \underline{V}_i^w\right). \tag{59}$$

Let β be the angle between unit vectors $\bar{a}_2^Q$ and $\bar{a}_2^P$, counted positive in the direction shown in fig. 47; *i.e.* $\cos\beta = \bar{a}_3^{QT}\bar{a}_3^P$. Clearly, β is the difference between the effective angles of attack α and α^P of the actual airfoil and its flat plate equivalent, respectively, and hence,

$$\beta = \alpha^P - \alpha. \tag{60}$$

The relationship between the unit vectors of orthonormal bases $\mathcal{A}^P$ and $\mathcal{A}^Q$ is then readily found as

$$\bar{a}_2^P = \bar{a}_2^Q\cos\beta + \bar{a}_3^Q\sin\beta, \quad \bar{a}_3^P = \bar{a}_3^Q\cos\beta - \bar{a}_2^Q\sin\beta. \tag{61}$$

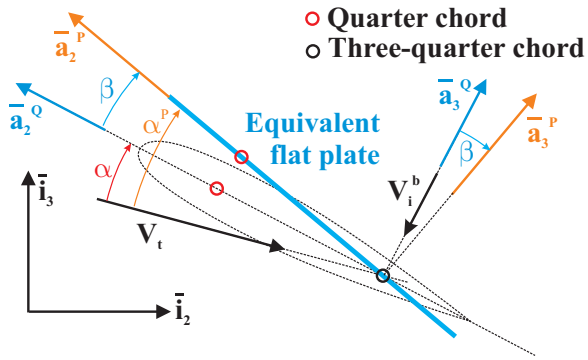

Figure 47: The equivalent flat plate producing the same amount of lift as an airfoil in a two-dimensional incompressible, inviscid flow

Eq. (59) now becomes

$$\Gamma^b = \frac{\pi c}{3\cos\beta}\left(\underline{V}_\infty + \underline{V}_i^w\right)^T \left(\bar{a}_3^Q \cos\beta - \bar{a}_2^Q \sin\beta\right). \tag{62}$$

On the other hand, the equivalent flat plate must produce the same lift as the real airfoil, that is,

$$L' = \frac{\rho V_t^2}{2} c C_\ell = \frac{\rho V_t^2}{2} c(2\pi)\alpha^P. \tag{63}$$

The above equation gives the equivalent angle of attack α^P as

$$\alpha^P = \frac{C_\ell}{2\pi}, \tag{64}$$

where C_ℓ is determined by the effective angle of attack α and Mach number M, and is obtained from the airfoil table look-up. Substituting eq. (50) into eq. (46) gives the effective angle of attack as

$$\alpha = \tan^{-1}\left[\frac{\bar{a}_3^{QT}(\underline{V}_\infty + \underline{V}_i^w) - 2\Gamma^b/\pi c}{-\bar{a}_2^{QT}(\underline{V}_\infty + \underline{V}_i^w)}\right]. \tag{65}$$

Substituting eq. (64) and (65) into eq. (60) leads to

$$\beta = \frac{C_\ell}{2\pi} - \tan^{-1}\left[\frac{\bar{a}_3^{QT}(\underline{V}_\infty + \underline{V}_i^w) - 2\Gamma^b/\pi c}{-\bar{a}_2^{QT}(\underline{V}_\infty + \underline{V}_i^w)}\right]. \tag{66}$$

In summary, the problem involves the solution of two nonlinear equations, eqs. (62) and (66), for two unknowns, Γ^b and β. Since the equations are nonlinear, the solution process relies on a linearization of these nonlinear equations.

4.5.1.4 Linearization of Governing Equations

Consider a set nonlinear equations dependent on a set of variables $\underline{x}$,

$$\underline{f}(\underline{x}) = 0. \tag{67}$$

Assume that an approximate solution, $\bar{\underline{x}}$, of these equations is available, *i.e.*, $\underline{f}(\bar{\underline{x}}) \approx 0$. A correction to this approximate solution, $\Delta\underline{x}$, is sought such that $\underline{f}(\bar{\underline{x}} + \Delta\underline{x}) = 0$. Expanding this expression in Taylor series about the point $\underline{x} = \bar{\underline{x}}$ and neglecting higher order terms leads to

$$\underline{f}(\bar{\underline{x}}) + \left[\frac{\partial \underline{f}}{\partial \underline{x}}\right]_{\underline{x}=\bar{\underline{x}}} \Delta\underline{x} = 0. \tag{68}$$

Rearranging the terms leads to

$$\left[\frac{\partial \underline{f}}{\partial \underline{x}}\right]_{\underline{x}=\bar{\underline{x}}} \Delta\underline{x} = -\underline{f}(\bar{\underline{x}}) \tag{69}$$

Iterative solution of this linear set of equations will yield an solution of the original nonlinear set of equations.

Similarly, linearization of eqs. (62) and (66) yields

$$\Gamma^b + \Delta\Gamma^b = \frac{\pi c}{3\cos\beta}\,(\underline{V}_\infty + \underline{V}_i^w)^T \left(\bar{a}_3^Q \cos\beta - \bar{a}_2^Q \sin\beta\right) - \frac{\pi c\ \bar{a}_2^{QT}\underline{V}_\infty}{3\cos^2\beta}\Delta\beta, \tag{70}$$

and

$$\beta + \Delta\beta = \frac{C_\ell}{2\pi} - \alpha + (1 - \frac{1}{2\pi}\frac{\partial C_\ell}{\partial \alpha})\frac{2\cos^2\alpha}{\pi c U_2}\Delta\Gamma^b, \tag{71}$$

where α is given by eq. (65) and U_2 by eq. (45). Reorganizing the terms and writing the two equations in matrix form leads to

$$K \begin{bmatrix} \Delta\Gamma^b \\ \Delta\beta \end{bmatrix} = \underline{Q}, \tag{72}$$

where

$$K = \begin{bmatrix} 1 & \dfrac{\pi c\ \bar{a}_2^{QT}\underline{V}_\infty}{3\cos^2\beta} \\ -(1 - \dfrac{1}{2\pi}\dfrac{\partial C_\ell}{\partial \alpha})\dfrac{2\cos^2\alpha}{\pi c U_2} & 1 \end{bmatrix}, \tag{73}$$

and

$$\underline{Q} = \begin{bmatrix} \dfrac{\pi c}{3\cos\beta}\,(\underline{V}_\infty + \underline{V}_i^w)^T \left(\bar{a}_3^Q \cos\beta - \bar{a}_2^Q \sin\beta\right) - \Gamma^b \\ \dfrac{C_\ell}{2\pi} - \alpha - \beta \end{bmatrix}. \tag{74}$$

After linearization, the solution of the two nonlinear equations, eqs. (62) and (66), is reduced to the iterative solution of the system of linear equations defined by eqs. (72), where K and $\underline{Q}$ given in eqs. (73) and (74), respectively. At convergence, the solution of the original nonlinear equations is obtained.

Once the bound circulation is found, the effective angle of attack and the local relative wind velocity can be found using eqs. (65) and (50), respectively. The lift coefficient corresponding to the present angle of attack can then be obtained by the airfoil table look-up. Finally, the lift produced by the airfoil is obtained from eq. (54).

4.5.1.5 Finite-State Unsteady Thin-Airfoil Theory of Peters et al.

The total lift of a thin airfoil shown in fig. 41 in an inviscid, incompressible flow includes two parts, the non-circulatory part and the circulatory part, and is expressed as following

$$L' = \pi\rho b^2(\ddot{h} + U_\infty\dot{\theta} - ba\ddot{\theta}) + 2\pi\rho U_\infty b\left[\dot{h} + U_\infty\theta + b(\frac{1}{2} - a)\dot{\theta} - \lambda_0\right], \tag{75}$$

where ρ is the air flow density, b the half-chord length, ab the distance the elastic axis is aft the mid-chord, θ the geometric angle of attack, h the plunging motion of the elastic axis, U_∞ the far-field free stream velocity, and λ_0 the average induced flow from free vortices in the wake counted positive in the opposite direction of unit vector $\bar{a}_3^Q$. The lift is assumed to be perpendicular to the relative wind vector, *i.e.* along unit vector $\bar{a}_3^L$. The first part in eq. (75) represents the non circulatory lift, and the second part represents the circulatory lift that plays an important role in the lift contribution. The average inflow is computed using the finite-state method developed by Peters *et al.* [82]. The N inflow modes, stored in array $\underline{\lambda}^T = [\lambda_1, \lambda_2, \ldots, \lambda_N]$, are

obtained by solving the following equation

$$\hat{A}\dot{\underline{\lambda}} + \frac{U_\infty}{b}\underline{\lambda} = \underline{\hat{c}}\left[\ddot{h} + U_\infty\dot{\theta} + b\left(\frac{1}{2} - a\right)\ddot{\theta}\right], \tag{76}$$

and the average inflow over the chord is then

$$\lambda_0 = \frac{1}{2}\hat{\underline{b}}^T\underline{\lambda}. \tag{77}$$

$\hat{A}$, $\underline{\hat{c}}$, $\underline{\hat{b}}$ are known matrix and vectors. Matrix $\hat{A}$ is defined as

$$\hat{A} = D + \underline{\hat{d}}\,\hat{\underline{b}}^T + \underline{\hat{c}}\,\hat{\underline{d}}^T + \frac{1}{2}\underline{\hat{c}}\,\hat{\underline{b}}^T. \tag{78}$$

The entries of matrix D are given by

$$D_{nm} = \begin{cases} \frac{1}{2n} & n = m+1, \\ -\frac{1}{2n} & n = m-1, \\ 0 & n \neq m \pm 1, \end{cases} \tag{79}$$

where $n, m = 1, 2, \ldots, N$. Vectors $\underline{\hat{b}}$, $\underline{\hat{c}}$, and $\underline{\hat{d}}$ are computed using formulas below

$$b_n = \begin{cases} (-1)^{n-1}\dfrac{(N+n-1)!}{(N-n-1)!}\dfrac{1}{(n!)^2} & n \neq N, \\ (-1)^{n-1} & n = N, \end{cases} \tag{80}$$

$$c_n = \frac{2}{n}, \tag{81}$$

$$d_n = \begin{cases} \frac{1}{2} & n = 1, \\ 0 & n \neq 1. \end{cases} \tag{82}$$

For an airfoil only pitching about the axis passing through the mid-chord, parameter $a = 0$. The plunging motion of the airfoil $h(t)$ is zero. Then the lift expressed in eq. (75) is simplified as

$$L' = 2\pi\rho b U_\infty^2\left(\theta + \frac{b\dot{\theta}}{U_\infty} - \frac{\lambda_0}{U_\infty}\right) \tag{83}$$

and the inflow λ_0 is computed using method described above.

4.5.1.6 Theodorsen's Unsteady Thin-Airfoil Theory

In Theodorsen's unsteady aerodynamic theory, the unsteady effects due to the shed vortices is approximated by the Theodorsen's function $C(k)$, which is a complex function of reduced frequency, $k = \omega b/U_\infty$, where ω is the pitching rate of the airfoil and U_∞ is the far-field free stream speed. Theodorsen's function $C(k)$ is given by

$$C(k) = \frac{H_1^{(2)}(k)}{H_1^{(2)}(k) + \mathrm{i}H_0^{(2)}(k)} = F(k) + \mathrm{i}G(k), \tag{84}$$

where, $H_n^{(2)}(k)$ are Hankel functions of the second kind, which can be expressed in terms of Bessel functions of the first and second kind, respectively,

$$H_n^{(2)}(k) = J_n(k) - \mathrm{i}Y_n(k). \tag{85}$$

Then the lift is given by

$$L' = \pi\rho b^2(\ddot{h} + U_\infty\dot{\theta} - ba\ddot{\theta}) + 2\pi\rho U_\infty bC(k)\left[\dot{h} + U_\infty\theta + b(\frac{1}{2} - a)\dot{\theta}\right]. \tag{86}$$

In practical situation, the Theodorsen's function may be approximated by

$$C(k) = F(k) + \mathrm{i}G(k) = \frac{-0.5\ k^2 + 0.2808\ \mathrm{i}k + 0.01365}{-k^2 + 0.3455\ \mathrm{i}k + 0.01365} \tag{87}$$

4.5.2 Three-Dimensional Aerodynamic Model

4.5.2.1 Finite-Wing Model

By extending the two-dimensional concept to the three-dimensional problem, each wing section can be viewed as a two-dimensional airfoil modeled in the manner described in section 4.5.1. Therefore, a thin finite wing of span S in an incompressible, inviscid, and irrotational flow can be modeled as a bound vortex filament with constant circulation placed at the wing's quarter-chord line along the span, line **AB** in fig. 48. Unlike the two-dimensional airfoil case, the vortex filament can not extend to infinity, and cannot end at the wing tips. Instead, it must form a complete circuit or extend to a boundary of the flow according to Helmholtz's law. Furthermore,

Helmholtz's law requires that there must be a starting vortex, line **CD**, of the strength equal and opposite to the bound vortex filament and two trailing vortices, line **BC** and **DA**, forming a complete vortex circuit, as shown in fig. 48.

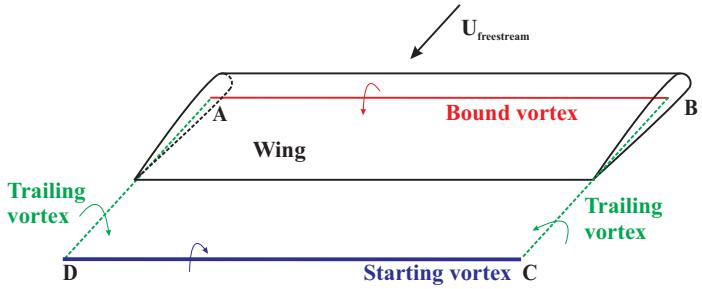

Figure 48: Finite wing in a steady flow.

In a steady flow, the trailing vortices extend to infinity. Therefore, the effect of the starting vortex filament, **CD**, on the wing is negligible and can be ignored; hence, a wing with constant circulation in a steady flow can be modeled as a horseshoe vortex. In reality, the wing is a superposition of an infinite number of horseshoe vortices and circulation varies along its span. The line along which the bound vortex filaments are located is placed at the wing's quarter-chord line. Since vortex lines do not begin or end in a fluid according to Helmholtz's law, any change in the circulation along the span must be accompanied by a circulation of equal magnitude in the direction perpendicular to the wing. Therefore, there must be a series of vortices trailing behind the wing, all extending to infinity, and forming the wake structure in a steady flow, as depicted in fig. 49.

In an unsteady flow, the wake structure is more complex and time-dependent. The wake consists not only of trailing vortices, but also shed vortices that are caused by the change of the circulation in the temporal domain, see fig. 50.

4.5.2.2 Prandtl Lifting-Line Theory

A thin finite wing moving with constant speed in an incompressible, irrotational, and steady flow is shown in fig. 51. The wing is at an angle of attack θ and the far-field

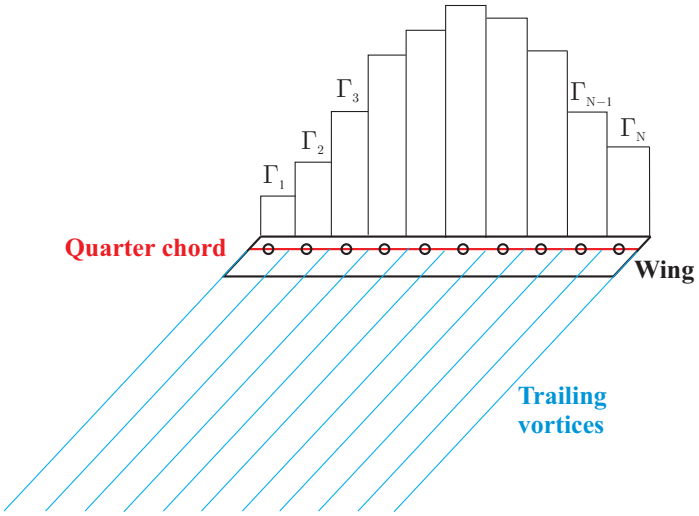

Figure 49: Finite wing in a steady flow.

flow velocity is along unit vector $\bar{\imath}_1$. The wake is assumed to be composed of trailing vortices all laying in the horizontal plane starting from the trailing edge of the wing. The non-penetration condition requires the vanishing of the flow velocity at the wing solid surface, assumed to be located approximately in the plane defined by unit vector $\bar{\imath}_1$ and $\bar{\imath}_2$. The condition implies

$$w_b + w_i + U_\infty \theta = 0, \tag{88}$$

where the induced flow, w, is defined positive along unit vector $\bar{\imath}_3$. Subscripts $(.)_b$ and $(.)_i$ indicate the flows induced by the bound and trailing vortex filaments, respectively. The non-penetration condition is satisfied at the three-quarter chord line along the span. According to the Biot-Savart law, the induced flow at a point $\mathbf{P} = (x_1, x_2, x_3)$ due to an infinitesimal bound vortex segment at position $(0, \eta, 0)$ of strength $\Gamma(\eta)\mathrm{d}\eta$ is

$$\mathrm{d}\underline{V} = \frac{1}{4\pi} \frac{\sqrt{x_1^2 + x_3^2}\, \Gamma(\eta)\mathrm{d}\eta}{[x_1^2 + (x_2 - \eta)^2 + x_3^2]^{3/2}} \bar{n}, \tag{89}$$

where $\bar{n}$ is a unit vector defining the direction of the induced velocity.

The total induced velocity due to the entire bound vortex filament is computed

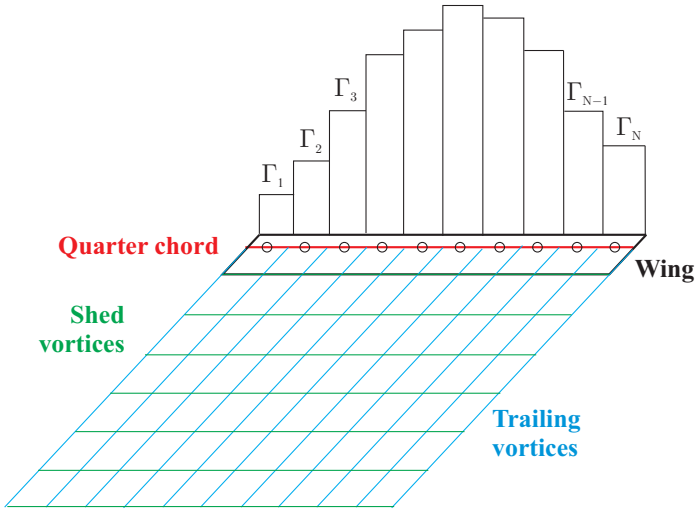

Figure 50: Finite wing in an unsteady flow.

by performing integration over the vortex filament

$$\underline{V} = \frac{1}{4\pi}\int_{-S/2}^{S/2} \frac{\sqrt{x_1^2+x_3^2}\,\Gamma(\eta)\mathrm{d}\eta}{[x_1^2+(x_2-\eta)^2+x_3^2]^{3/2}}\bar{n}, \tag{90}$$

where $\bar{n}$ is defined as

$$\bar{n} = \frac{x_3}{\sqrt{x_1^2+x_3^2}}\bar{\imath}_1 - \frac{x_1}{\sqrt{x_1^2+x_3^2}}\bar{\imath}_3. \tag{91}$$

The downwash produced by the bound vortex is obtained by projecting this equation along axis $\bar{\imath}_3$ to find

$$w_b(x_1,x_2,x_3) = -\frac{1}{4\pi}\int_{-S/2}^{S/2} \frac{x_1\Gamma(\eta)}{[x_1^2+(x_2-\eta)^2+x_3^2]^{3/2}}\,\mathrm{d}\eta. \tag{92}$$

Let $x_1 = b(x_2), x_3 = 0$, where $b(x_2) = c(x_2)$ is the semi-chord length of the wing section at the span-wise position x_2, eq. (92) becomes

$$w_b(b,x_2,0) = -\frac{1}{4\pi}\int_{-S/2}^{S/2} \frac{b\Gamma(\eta)}{[b^2+(x_2-\eta)^2]^{3/2}}\,\mathrm{d}\eta. \tag{93}$$

Integration by parts with respect to η then leads to

$$w_b(b,x_2,0) = -\frac{1}{4\pi}\left[\frac{-\Gamma(\eta)(x_2-\eta)}{b\sqrt{b^2+(x_2-\eta)^2}}\right]_{-S/2}^{S/2} - \frac{1}{4\pi}\int_{-S/2}^{S/2}\frac{\mathrm{d}\Gamma}{\mathrm{d}\eta}\frac{(x_2-\eta)\mathrm{d}\eta}{b\sqrt{b^2+(x_2-\eta)^2}}. \tag{94}$$

The first term in the above equation represents the boundary terms, which is zero because circulation vanishes at the wing tips.

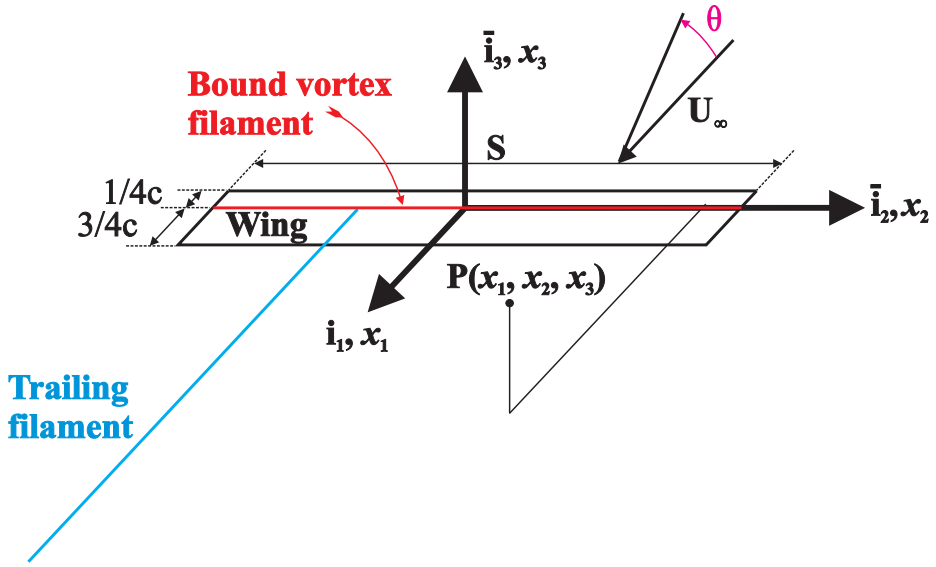

Figure 51: Evaluation of inflow due to a vortex filament

Large aspect ratio wings, that is $S \gg c(x_2)$, are considered here. Note that the coefficient of $\mathrm{d}\Gamma/\mathrm{d}\eta$ is an odd function of $(x_2 - \eta)$. For points near the wing tips, $|x_2 - \eta| \gg c(x_2)$. With the help of this assumption, the term $\sqrt{b^2 + (x_2 - \eta)^2}$ can be approximated as $|x_2 - \eta|$. The second term in eq. (94) then becomes

$$\int_{-S/2}^{S/2} \frac{\mathrm{d}\Gamma}{\mathrm{d}\eta} \frac{(x_2 - \eta)\mathrm{d}\eta}{b\sqrt{b^2 + (x_2 - \eta)^2}} \approx \int_{-S/2}^{S/2} \frac{(x_2 - \eta)\mathrm{d}\Gamma}{b|x_2 - \eta|} = \frac{1}{b}\left[\int_{-S/2}^{x_2} \mathrm{d}\Gamma - \int_{x_2}^{S/2} \mathrm{d}\Gamma\right] = \frac{2\Gamma(x_2)}{b}. \tag{95}$$

The downwash due to the bound vortex filament is simply computed as

$$w_b(b, x_2, 0) = -\frac{\Gamma(x_2)}{\pi c(x_2)}. \tag{96}$$

This equation means that the downwash at the point $\mathbf{P} = (c(x_2)/2, x_2, 0)$ is equivalent to the effect due to an infinitely long vortex filament of strength $\Gamma(x_2)$.

The strength of the trailing vortex filament at position x_2 is given as $[\mathrm{d}\Gamma(x_2)/\mathrm{d}\eta]\mathrm{d}\eta$, the induced flow due to a vortex filament with constant strength is given by eq. (200)

$$\underline{V} = \frac{1}{4\pi} \int_{-S/2}^{S/2} \frac{\mathrm{d}\Gamma/\mathrm{d}\eta}{\sqrt{(x_2 - \eta)^2 + x_3^2}} \left[\frac{x_1}{\sqrt{x_1^2 + (x_2 - \eta)^2 + x_3^2}} + 1\right] \bar{n}, \tag{97}$$

where $\bar{n}$ defines by the orientation of the induced velocity at point $\mathbf{P}$. Projecting this

equation along the unit vector $\bar{\imath}_3$ gives the downwash at point $\mathbf{P} = (b, x_2, 0)$ as

$$w_i(b, x_2, 0) = -\frac{1}{4\pi} \int_{-S/2}^{S/2} \frac{\mathrm{d}\Gamma/\mathrm{d}\eta}{x_2 - \eta} \left[\frac{b}{\sqrt{b^2 + (x_2 - \eta)^2}} + 1 \right] \mathrm{d}\eta. \tag{98}$$

Assuming large aspect ratio and $|x_2 - \eta| \gg c(x_2)$, the term $b/\sqrt{b^2 + (x_2 - \eta)^2}$ can be neglected, leading to

$$w_i(b, x_2, 0) = -\frac{1}{4\pi} \int_{-S/2}^{S/2} \frac{\mathrm{d}\Gamma/\mathrm{d}\eta}{x_2 - \eta} \, \mathrm{d}\eta. \tag{99}$$

This equation means that the induced flow due to the wake is equal that due to distributed semi-infinite vortex filaments. Substituting eqs. (96) and (99) into eq. (88) leads to

$$-\frac{\Gamma(x_2)}{\pi c(x_2)} - \frac{1}{4\pi} \int_{-S/2}^{S/2} \frac{(\mathrm{d}\Gamma/\mathrm{d}\eta)\mathrm{d}\eta}{x_2 - \eta} + U_\infty \theta = 0. \tag{100}$$

Dividing eq. (100) by the free-stream speed, U_∞, results in

$$-\frac{\Gamma(x_2)}{\pi c(x_2) U_\infty} - \frac{1}{4\pi U_\infty} \int_{-S/2}^{S/2} \frac{\mathrm{d}\Gamma/\mathrm{d}\eta}{x_2 - \eta} \, \mathrm{d}\eta + \theta = 0. \tag{101}$$

This is the fundamental equation of Prandtl lifting-line theory and is satisfied at every span-wise position x_2.

It should be noted that this equation was derived based on the assumption of $S \gg c(x_2)$ and the observation that $|x_2 - \eta| \gg c(x_2)$ over most of the surface of a large-aspect ration wing. Hence, Prandtl lifting-line theory is applicable for the large-aspect ratio, straight wings. Notice that $|x_2 - \eta| \gg c(x_2)$ does not hold at the wing tips, therefore, evaluation of the lift using Prandtl theory at the tip regions is not as accurate as for the inboard regions of the wing. The problem is to solve the equation (101) for the bound circulation $\Gamma(x_2)$ such that the Kutta condition is satisfied at the trailing edge. With the circulation available, the lift produced by the wing can be obtained using the Kutta-Joukowski theorem.

The Kutta-Joukowski theorem gives the lift per unit span, L', as

$$L' = \rho U_\infty \Gamma(x_2) = \frac{\rho U_\infty^2}{2} c(x_2) C_\ell = \frac{\rho U_\infty^2}{2} c(x_2) 2\pi\alpha(x_2). \tag{102}$$

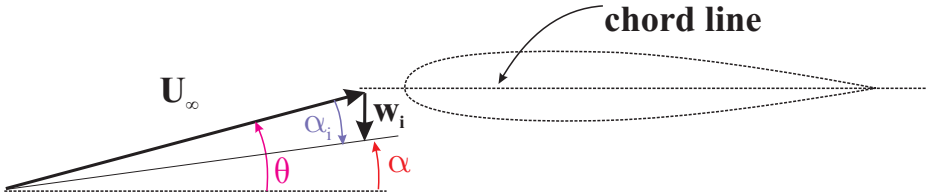

Figure 52: Two-dimensional cross-section (in the x_2 = constant plane) of a three-dimensional wing

Rearranging the terms gives

$$\alpha(x_2) = \frac{\Gamma(x_2)}{\pi c U_\infty}, \tag{103}$$

where $\alpha(x_2)$ is the effective angle of attack at the span-wise position x_2. This relationship holds for wings with thin airfoil cross-sections. Therefore, the first term in eq. (101) is related to the effective angle of attack. The second term essentially represents the induced angle of attack $\alpha_i(x_2)$, with the small angle assumptions, which is computed by

$$\alpha_i(x_2) \approx \frac{w_i(x_2)}{U_\infty}. \tag{104}$$

Therefore, eq. (101) can be viewed as a combination of the angles as shown in fig. 52,

$$\theta = \alpha - \alpha_i. \tag{105}$$

This relationship means that the effective of angle of attack of a wing section, $\alpha(x_2)$, is the sum of the geometric angle of attack, θ, and the induced angle of attack, $\alpha_i(x_2)$.

4.5.2.3 Discretized General Model

As described in section 4.5.2.2, Prandtl's theory only applies to lifting, thin, large aspect ratio wings at small angles of attack in a steady flow. It is necessary to develop a more general model that is applicable to wings with a large angle of attack, for instance, rotor blades, in an unsteady flow. In this section, the methodology is developed on the basis of section 4.5.1.3 from the numerical computation perspective.

A wing can be modeled as a lifting line formed by a finite number of airstations

located at the wing's quarter-chord line. Each airstation and its associated wing cross-section can be seen as a two-dimensional airfoil modeled in the manner introduced in section 4.5.1. Hence, a finite wing can be viewed as a series of strips with finite span ΔS and airstations located in the mid-span of each small element. The lift obtained using two-dimensional theory is constant over each strip. The radial integration of the lift of every strip will be the total lift produced by the wing.

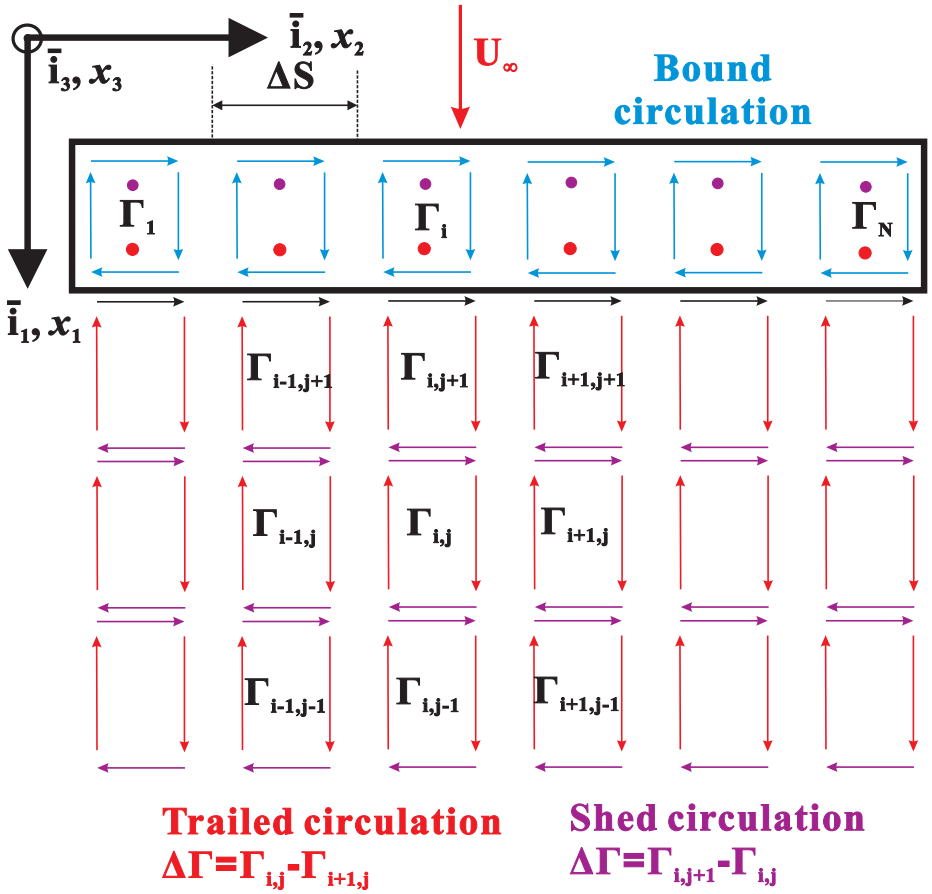

Figure 53: Lifting-line blade model in an unsteady flow

Fig. 53 shows a lifting-line blade model with a series of airstations. At the airstation i with the span of ΔS_i, there is a constant vortex of strength Γ_i over the span. The wing and the wake are modeled as vortex ring elements. A vortex ring consists of four vortex segments of equal strength and the directions are positive as shown in fig. 53. The geometry of the bound vortex ring is shown in fig. 54, where the left figure

shows the side view of the wing and the right figure shows the top view of the wing. System $\mathcal{A}^G = (\bar{a}_1^G, \bar{a}_2^G, \bar{a}_3^G)$ is the frame located at the geometric center of the vortex ring, **G**, and its orientation is parallel to the airfoil attached system, $\mathcal{A} = (\bar{a}_1, \bar{a}_2, \bar{a}_3)$.

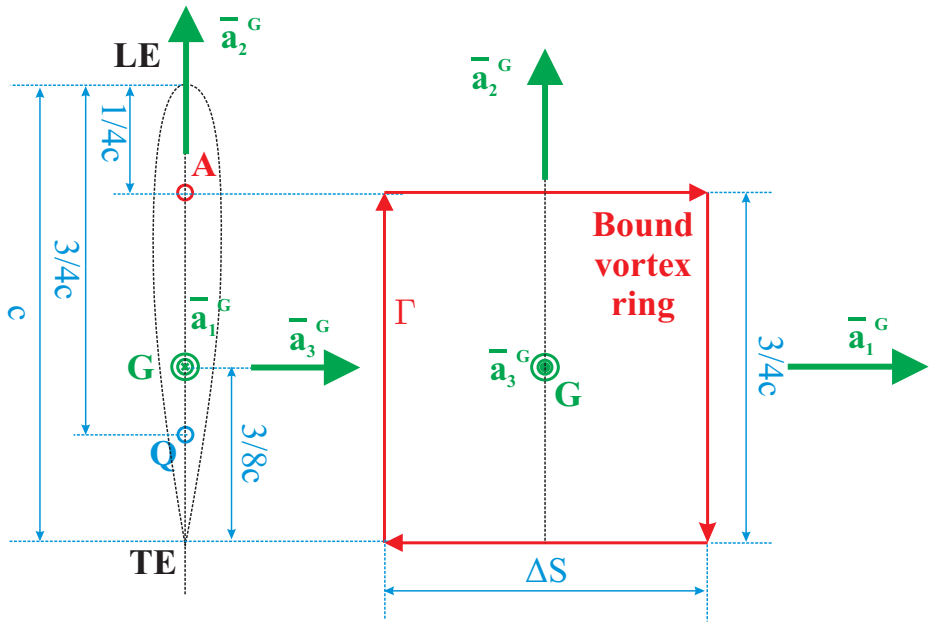

Figure 54: Geometry of a bound vortex ring

In the unsteady case, the bound circulation not only changes along the span, but also changes in the time domain, leading to a more complicated and time-dependent pattern of wake structure. The trailed vorticity is due to the span-wise variation of the bound circulation and is parallel to the local free stream at the instant it leaves the wing. The shed vorticity is due to the time variation of the bound circulation and its orientation is parallel to that of the wing. Vorticity differences of two horizontally adjacent vortex rings gives the trailed vorticity, whereas vorticity differences of two vertically adjacent vortex rings gives the shed vorticity, as shown in fig. 53. Therefore, the wake behind a wing consists of both shed circulations and trailed circulations. Each cell on the wing represents a vortex ring with strength of Γ_i, i denotes the span-wise position. The remaining cells represent the circulations, $\Gamma_{i,j}$, released into the wake behind the blade, indices i, and j denote the span-wise position, and the time

instant at which the circulation is released, respectively. If the bound circulations do not change with time, the shed circulations vanish and the strength of each trailed vortex segment at a specific span-wise position becomes constant, forming a vortex filament of constant strength. Hence, the problem then reverts to a steady problem.

By analogy to the two-dimensional case, non-penetration condition must be satisfied at each collocation point along the wing. The total downwash at a collocation point is not as simple as the 2D case presented in section 4.5.1. In addition to the contribution from the bound circulation at the corresponding airstation, the downwash also includes the effect of the bound circulations at other airstations. Furthermore, the wake structure behind a finite wing is composed of not only shed circulations but also of trailed circulations.

The total downwash at the k^{th} collocation point comes from three sources, the free stream velocity relative to the airfoil ($\underline{V}_k^{\infty}$), bound circulations ($\underline{V}_{ik}^{b}$), and the circulations released into the wake at the earlier time, ($\underline{V}_{ik}^{w}$). Hence, the non-penetration condition written at the k^{th} collocation point is written in the system attached to corresponding equivalent flat plate

$$\bar{a}_{3k}^{PT}\left[\underline{V}_k^{\infty}+\underline{V}_{ik}^{b}+\underline{V}_{ik}^{w}\right]=0, \tag{106}$$

where $\bar{a}_{3k}^{P}$ is the third unit vector of the system attached to the equivalent flat plate at the k^{th} collocation point. Let $\underline{V}_k$ denote the structural velocity of the k^{th} collocation point and $\underline{U}_{\infty}$ denote the free stream velocity vector, then the free stream velocity relative to the airfoil at the k^{th} collocation point is computed as

$$\underline{V}_k^{\infty}=\underline{U}_{\infty}-\underline{V}_k, \tag{107}$$

The term $\underline{V}_{ik}^{b}$ accounts for the effect of all bound vortex rings, see fig. 54 for its geometry, that is,

$$\underline{V}_{ik}^{b}=\sum_{\ell=1}^{N}\underline{V}_{k\ell}^{b}, \tag{108}$$

where N is the number of the airstations and $\underline{V}^b_{k\ell}$ is the induced velocity at k^{th} control point due to a vortex ring of strength Γ^b_ℓ at the ℓ^{th} airstation and computed as the addition of the velocity induced by four vortex segments forming the vortex ring, see fig. 55, which indicates point **C** where means the induced velocity is computed. The formula for calculating $\underline{V}^b_{k\ell}$ is derived in section B.2 as

$$\underline{V}^b_{k\ell} = \frac{\Gamma^b_\ell}{4\pi}\hat{\underline{V}}^b_{k\ell}, \tag{109}$$

where

$$\hat{\underline{V}}^b_{k\ell} = g_{1k\ell}\bar{a}^G_{\ell\ell} + g_{2k\ell}\bar{a}^G_{2\ell} + g_{3k\ell}\bar{a}^G_{3\ell}. \tag{110}$$

In eq. (110), unit vectors $\bar{a}^G_{i\ell}$, $i = 1, 2, 3$, are the axes of system $\mathcal{A}^G$ at the ℓ^{th} vortex ring. $g_{ik\ell}$, $i = 1, 2, 3$ are the components of vector $\hat{\underline{V}}^b_{k\ell}$ in system $\mathcal{A}^G_\ell$, as defined by eq. (220). Eq. (106) now becomes

$$\bar{a}^{PT}_{3k}\left[\underline{U}_\infty - \underline{V}_k + \sum_{\ell=1}^{N}\frac{\Gamma^b_\ell}{4\pi}\hat{\underline{V}}^b_{k\ell} + \underline{V}^w_{ik}\right] = 0. \tag{111}$$

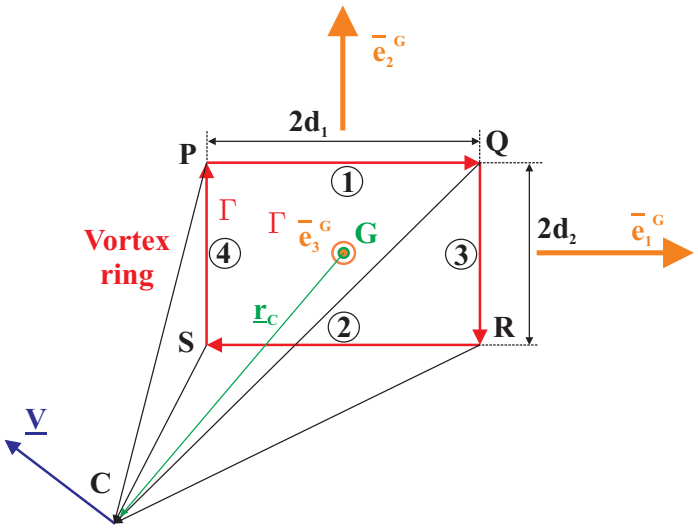

Figure 55: Evaluation of the induced velocity at a point due to a bound vortex ring

At each collocation point, the lift equivalence should also be satisfied. Based on the eq. (64), the lift coefficient and the equivalent angle of attack at the k^{th} airstation,

α_k^P, satisfies

$$C_{\ell k} = 2\pi\alpha_k^P. \tag{112}$$

At the same time, the difference between the effective angle of attack of the equivalent flat plate, α_k^P, and the effective angle of attack, α_k, at the k^{th} airstation is

$$\beta_k = \alpha_k^P - \alpha_k = \frac{C_{\ell k}}{2\pi} - \alpha_k. \tag{113}$$

System $\mathcal{A}_k^P$ is obtained by the rotation of the system $\mathcal{A}_k$ about unit vector $\bar{a}_1$ by an angle β_k, therefore, unit vector $\bar{a}_3^P$ of the system $\mathcal{A}_k^P$ is computed

$$\bar{a}_{3k}^P = \bar{a}_{3k}\cos\beta_k - \bar{a}_{2k}\sin\beta_k. \tag{114}$$

The effective angle of attack at the k^{th} airstation is computed as

$$\alpha_k = \tan^{-1}\frac{\bar{a}_{3k}^T\underline{V}_{tk}}{-\bar{a}_{2k}^T\underline{V}_{tk}} = \tan^{-1}\frac{U_{3k}}{U_{2k}}, \tag{115}$$

where the local relative flow velocity at the k^{th} collocation point $\underline{V}_{tk}$ is

$$\underline{V}_{tk} = \underline{U}_\infty - \underline{V}_k + \underline{V}_{ik}. \tag{116}$$

$\underline{V}_{ik}$ is the induced velocity at the k^{th} collocation point due to the entire vortex wake including the bound circulations and those released into the wake. The calculation of the induced flow, $\underline{V}_{ik}^w$ is detailed in the section 4.6.2. The calculation of the induced flow from the bound circulations is described in section B.2. It should be noted that the vortex segment located at the quarter chord should not be included in the computation of the inflow, that is, only vortex segments 2 to 4 are considered and denoted as $\underline{V}_{k\ell}^{b\prime}$, see fig. 55. Therefore, the quantity, $\underline{V}_{ik}$, is expressed as

$$\underline{V}_{ik} = \sum_{l=1}^{N}\underline{V}_{k\ell}^{b\prime} + \underline{V}_{ik}^w, \tag{117}$$

where

$$\underline{V}_{k\ell}^{b\prime} = \frac{\Gamma_\ell^b}{4\pi}\hat{\underline{V}}_{k\ell}^{b\prime}, \tag{118}$$

$$\underline{\hat{V}}^{b\prime}_{k\ell} = g'_{1k\ell}\bar{a}^G_{\ell\ell} + g'_{2k\ell}\bar{a}^G_{2\ell} + g'_{3k\ell}\bar{a}^G_{3\ell}. \tag{119}$$

Parameters $g'_{ik\ell}, i = 1, 2, 3$ are the components of vector $\underline{\hat{V}}^b_{k\ell}$ in system $\mathcal{A}^G_\ell$, as defined in eq. (223).

In summary, the two governing equations satisfied at the k^{th} collocation point are eqs. (111)and (113), which are nonlinear equations with $2N$ unknowns $\Gamma^b_1, \Gamma^b_2, \ldots, \Gamma^b_N$, and $\beta_1, \beta_2, \ldots, \beta_N$. To solve for these $2N$ unknowns, $2N$ equations are required. Note that such two equations can be written at the other $N-1$ collocation points. Therefore, we have $2N$ equations to solve for the $2N$ unknowns.

4.5.2.4 Linearization of Governing Equations

The above derivation shows that the equations to be solved are highly nonlinear. Therefore, linearization is required for the solution of the nonlinear equations. Rewriting eq. (111) gives

$$\frac{\bar{a}^{PT}_{3k}\underline{\hat{V}}^b_{kk}}{4\pi}\Gamma^b_k = -\bar{a}^{PT}_{3k}\left[\underline{U}_\infty - \underline{V}_k + \sum_{\ell=1,\ell\neq k}^{N}\frac{\Gamma^b_\ell}{4\pi}\underline{\hat{V}}^b_{k\ell} + \underline{V}^w_{ik}\right]. \tag{120}$$

Increments in Γ^b_k, denoted $\Delta\Gamma^b_k$, are written as

$$\frac{\bar{a}^{PT}_{3k}\underline{\hat{V}}^b_{kk}}{4\pi}\Delta\Gamma^b_k = -\sum_{\ell=1,\ell\neq k}^{N}\frac{\bar{a}^{PT}_{3k}\underline{\hat{V}}^b_{k\ell}}{4\pi}\Delta\Gamma^b_\ell + \bar{a}^{PT}_{2k}\left[\underline{U}_\infty - \underline{V}_k + \sum_{\ell=1}^{N}\frac{\Gamma^b_\ell}{4\pi}\underline{\hat{V}}^b_{k\ell} + \underline{V}^w_{ik}\right]\Delta\beta_k. \tag{121}$$

Increments in β_k, denoted $\Delta\beta_k$, are written as

$$\Delta\beta_k = \frac{\partial C_{\ell k}}{2\pi\partial\alpha_k}\Delta\alpha_k - \Delta\alpha_k. \tag{122}$$

Eq. (115) can be rewritten as $\tan\alpha_k = U_{3k}/U_{2k}$, increments in α_k, denoted $\Delta\alpha_k$, are written as

$$\frac{\Delta\alpha_k}{\cos^2\alpha_k} = \frac{U_{2k}\Delta U_{3k} - U_{3k}\Delta U_{2k}}{U^2_{2k}}, \tag{123}$$

and

$$\begin{aligned}\Delta U_{3k} &= \Delta\left(\bar{a}^T_{3k}\underline{V}_{tk}\right) = \Delta\bar{a}^T_{3k}\underline{V}_{tk},\\ \Delta U_{2k} &= \Delta\left(-\bar{a}^T_{2k}\underline{V}_{tk}\right) = -\Delta\bar{a}^T_{2k}\underline{V}_{tk}.\end{aligned} \tag{124}$$

Increment of the local relative wind vector at the k^{th} collocation point, denoted $\Delta\underline{V}_{tk}$, become

$$\Delta\underline{V}_{tk} = \Delta\underline{V}_{ik} = \frac{\hat{\underline{V}}^{b\prime}_{k\ell}}{4\pi}\Delta\Gamma^b_\ell. \tag{125}$$

With the help of eqs. (124) and (125), eq. (123) becomes

$$\frac{\Delta\alpha_k}{\cos^2\alpha_k} = \frac{1}{4\pi U^2_{2k}}\sum_{l=1}^{N}\left[U_{2k}\bar{a}^T_{3k}\hat{\underline{V}}^{b\prime}_{k\ell} + U_{3k}\bar{a}^T_{2k}\hat{\underline{V}}^{b\prime}_{k\ell}\right]\Delta\Gamma^b_\ell. \tag{126}$$

Substituting eq. (126) into eq. (122) yields

$$\Delta\beta_k = \left(\frac{\partial C_{\ell k}}{2\pi\partial\alpha_k} - 1\right)\frac{\cos^2\alpha_k}{4\pi U^2_{2k}}\sum_{\ell=1}^{N}\left[U_{2k}\ \bar{a}^T_{3k}\hat{\underline{V}}^{b\prime}_{k\ell} + U_{3k}\ \bar{a}^T_{2k}\hat{\underline{V}}^{b\prime}_{k\ell}\right]\Delta\Gamma^b_\ell. \tag{127}$$

With the help of eq. (121) and eq. (127), the linearization of eq. (111) and eq. (113), gives

$$A_k\Delta\underline{\Gamma}^b + D_k\Delta\beta_k = -\left[A_k\underline{\Gamma}^b_k + \bar{a}^{PT}_{3k}\left(\underline{U}_\infty - \underline{V}_k + \underline{V}^w_{ik}\right)\right], \tag{128}$$

and

$$B_k\Delta\underline{\Gamma}^b + \Delta\beta_k = \left(\frac{C_{\ell k}}{2\pi} - \alpha_k\right) - \beta_k, \tag{129}$$

where A_k and B_k are $1\times N$ row arrays expressed as $A_k = [A_{k1}, A_{k2}, \ldots, A_{kN}]$ and $B_k = [B_{k1}, B_{k2}, \ldots, B_{kN}]$ with entries given by eqs. (130) and (131), and D_k is a scalar expressed in eq. (132). The entries of arrays $A_{k\ell}$ and B_k and scalar D_k are given as followings

$$A_{k\ell} = \frac{1}{4\pi}\bar{a}^{PT}_{3k}\hat{\underline{V}}^b_{k\ell}, \tag{130}$$

$$B_{k\ell} = \left(1 - \frac{\partial C_{\ell k}}{2\pi\partial\alpha_k}\right)\frac{\cos^2\alpha_k}{4\pi U^2_{2k}}\left(U_{2k}\bar{a}^T_{3k} + U_{3k}\bar{a}^T_{2k}\right)\hat{\underline{V}}^{b\prime}_{k\ell}, \tag{131}$$

$$D_k = -\bar{a}^{PT}_{2k}\left[\underline{U}_\infty - \underline{V}_k + \sum_{\ell=1}^{N}\frac{\Gamma^b_\ell}{4\pi}\hat{\underline{V}}^b_{k\ell} + \underline{V}^w_{ik}\right] \tag{132}$$

where $\ell = 1, 2, \ldots, N$. Rewriting the above two equations into matrix form gives,

$$K_k\begin{bmatrix}\Delta\underline{\Gamma}^b\\ \Delta\beta_k\end{bmatrix} = \underline{Q}_k, \tag{133}$$

where K_k is the "stiffness matrix" with dimension $2 \times (N+1)$ and $\underline{Q}_k$ is the "unbalanced force vector" with dimension 2×1. These two quantities are given by the eq. (134) and eq. (135), respectively,

$$K_k = \begin{bmatrix} A_k & D_k \\ B_k & 1 \end{bmatrix}, \tag{134}$$

and

$$\underline{Q}_k = \begin{bmatrix} -A_k \underline{\Gamma}^b - \bar{a}_{3k}^{PT} \left(\underline{U}_\infty - \underline{V}_k + \underline{V}_{ik}^w \right) \\ (C_{\ell k}/2\pi - \alpha_k) - \beta_k \end{bmatrix}. \tag{135}$$

Eq. (133) is the set of linearized equations obtained at the k^{th} collocation point, so totally there will be N sets of such kind of equations. In summary, there will be $2N$ equations with $2N$ unknowns, $\underline{\Gamma}^{bT} = [\Gamma_1^b, \Gamma_2^b, \ldots, \Gamma_N^b]$ and $\underline{\beta}^T = [\beta_1, \beta_2, \ldots, \beta_N]$. Now the nonlinear system has been transformed into solving the following linear system of $2N$ equations for $2N$ unknowns, the bound circulations, $\underline{\Gamma}^b$, and the equivalent flat plate positions, $\underline{\beta}$,

$$\mathcal{K} \begin{bmatrix} \Delta\underline{\Gamma}^b \\ \Delta\underline{\beta} \end{bmatrix} = \underline{\mathcal{Q}}, \tag{136}$$

where the matrix $\mathcal{K}$ and vector $\underline{\mathcal{Q}}$ are given by

$$\mathcal{K} = \begin{bmatrix} \mathcal{A} & \mathcal{D} \\ \mathcal{B} & \mathcal{I} \end{bmatrix}, \tag{137}$$

$$\underline{\mathcal{Q}} = \begin{bmatrix} \underline{\mathcal{Q}}^\Gamma \\ \underline{\mathcal{Q}}^\beta \end{bmatrix}, \tag{138}$$

where $\mathcal{A}$ and $\mathcal{B}$ are fully populated $N \times N$ matrices and their entries are given by Eqs. (130) and (131), respectively; $\mathcal{D}$ is a $N \times N$ diagonal matrix and the diagonal entry D_k is given by eq. (132); $\mathcal{I}$ is the $N \times N$ identity matrix; $\underline{\mathcal{Q}}^\Gamma$ and $\underline{\mathcal{Q}}^\beta$ are $N \times 1$ vectors and their k^{th} entries are given as $Q_k(1)$ and $Q_k(2)$ in eq. (135), respectively.

Rewriting eq. (136) yields

$$\mathcal{A}\Delta\underline{\Gamma}^b + \mathcal{D}\Delta\underline{\beta} = \underline{\mathcal{Q}}^{\Gamma}, \tag{139}$$

$$\mathcal{B}\Delta\underline{\Gamma}^b + \Delta\underline{\beta} = \underline{\mathcal{Q}}^{\beta}, \tag{140}$$

solving eq. (140) gives

$$\Delta\underline{\beta} = \underline{\mathcal{Q}}^{\beta} - \mathcal{B}\Delta\underline{\Gamma}^b. \tag{141}$$

Substituting eq. (141) into eq. (139) yields

$$\left(\mathcal{A} - \mathcal{D}\mathcal{B}\right)\Delta\underline{\Gamma}^b = \underline{\mathcal{Q}}^{\Gamma} - \mathcal{D}\underline{\mathcal{Q}}^{\beta}. \tag{142}$$

With the help of this manipulation, instead of factorizing a $2N \times 2N$ matrix, the factorization of $N \times N$ matrix, $(\mathcal{A} - \mathcal{D}\mathcal{B})$, is required to solve the linear system, simplifying the computation of the solution. The solutions, $\underline{\Gamma}^{b'}$ and $\underline{\beta}'$, that satisfy the nonlinear system can be found by

$$\begin{aligned} \underline{\Gamma}^{b\prime} &= \underline{\Gamma}^b + \Delta\underline{\Gamma}^b, \\ \underline{\beta}' &= \underline{\beta} + \Delta\underline{\beta}. \end{aligned} \tag{143}$$

4.6 Inflow Computation

This section presents the evaluation of the inflow due to the vortex wake behind a two-dimensional airfoil or a three-dimensional finite wing. Typically, the wake is composed of vortex filaments or vortex sheets. The flow induced by a vortex filament or sheet is just the integral of the Biot-Savart law, see eq. (18), over the filament or sheet. The vortex wake behind a two-dimensional airfoil comprises of only shed vorticities, see fig. 45 for the wake structure, which are due to the time variation of the circulation bound around the airfoil. Except for such shed vorticities, the vortex wake behind a three-dimensional finite wing also includes the trailed vorticities that are due to the spatial variation of the bound circulations over the wing span, see fig. 50 for the wake structure. In a steady state, the shed vorticities vanish in both cases. Hence,

the total effect of the vortex wake becomes zero for the two-dimensional problem, while for the three-dimensional case, the bound circulations also vary spatially along the wing span, leading to non-vanishing trailed vorticities. Thus, the effect of trailed vorticities can not be ignored.

This section is organized in the following manner. First, the computation of the inflow for a two-dimensional airfoil is presented. Next, the inflow due to the wake behind a three-dimensional wing structure will be introduced. In these two cases, classical methods and Gaussian quadrature will be described. In the meantime, Chebyshev approximation of vorticity distribution over a vortex filament or sheet based on discretized data will be also introduced, with focus on finding the Chebyshev coefficients. By doing so, the vorticities at the Gauss points can be found so that Gaussian quadrature can be used to evaluate the Biot-Savart integral. One key problem in the inflow computation are the possible singularities encountered in the evaluation of the Biot-Savart law. This section also shows the effort paid to overcome the difficulty.

4.6.1 Inflow for a Two-Dimensional Airfoil

4.6.1.1 Classical Approach

Consider an airfoil in a two-dimensional incompressible, inviscid, and irrotational flow shown in fig. 45. In accordance with Helmholtz's law, the vortex must form a complete circuit. Therefore, at each time instant, there is a bound vortex ring around the airfoil and the bound vortex ring will convect downstream with free stream speed, U_∞, as time goes by, see the left part of the fig. 56. As described in section 4.5.1.1, the vortex sheet around a thin airfoil can be replaced by a concentrated vortex filament extending to infinity, therefore, the induced velocity due to the side segments (not shown in fig. 56) of the vortex ring is negligible. And the induced effect due to the top and bottom segments of the vortex ring can be computed using eq. (207) at each time instant. As shown in fig. 45, the vortex wake behind an airfoil is composed of

two parts. The first part comes from the starting vortex at the trailing edge that is of equal magnitude and opposite sign to the bound circulation located at the quarter-chord of the airfoil. This starting vortex, along with the bound circulation, forms a vortex pair. The contribution from this vortex is denoted $\underline{V}_i^s$. The second part is the contribution from those vortex pairs released into the wake during the earlier stage, which is denoted $\underline{V}_i^w$.

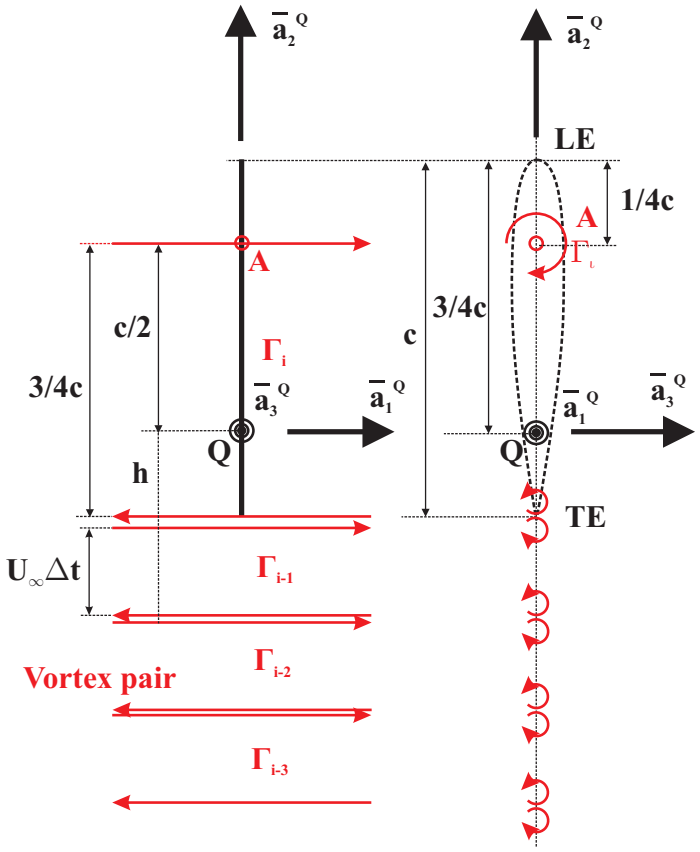

Figure 56: Discretized shed wake structure behind an airfoil in a two-dimensional incompressible, inviscid flow

In practical situations, dynamic problems are discretized in time. At each time instant, there is a vortex pair going into the wake behind the airfoil forming a vortex sheet composed of discrete infinitely long vortex filaments. Assume the time step size Δt. Let Γ_i denote the circulation at time step i and h the normal distance from the point at which the inflow is evaluated to an infinitely long vortex filament. In view

of eq. (207), the induced flow evaluated at the three-quarter chord at time step i due to the starting vortex filament at the trailing edge is simply computed as

$$\underline{V}_i^s = -\frac{2\Gamma_i}{\pi c}\bar{a}_3^Q, \tag{144}$$

where c is the chord length of the airfoil. The induced flow, $\underline{V}_i^w$, is the summation of the inflow due to each pair of the vortex filaments, which are shed from the first up to the $(i-1)^{th}$ time step, that is to sum up the contributions from all the circulations Γ_j, $1 \leq j \leq i-1$,

$$\underline{V}_i^w = \sum_{j=1}^{i-1} \frac{\Gamma_{i-j}}{2\pi} \left(\frac{1}{c/4 + (j-1)U_\infty \Delta t} - \frac{1}{c/4 + jU_\infty \Delta t} \right) \bar{a}_3^Q. \tag{145}$$

The total induced flow due to the vortex wake behind the airfoil is then obtained by adding these two parts,

$$\underline{V}_i = \left[-\frac{2\Gamma_i}{\pi c} + \sum_{j=1}^{i-1} \frac{\Gamma_{i-j}}{2\pi} \left(\frac{1}{c/4 + (j-1)U_\infty \Delta t} - \frac{1}{c/4 + jU_\infty \Delta t} \right) \right] \bar{a}_3^Q \tag{146}$$

4.6.1.2 Chebyshev Approximation of Vorticity Distribution

Another approach of computing the induced flow due to the vortex wake behind an airfoil is to use Gaussian quadrature. Gaussian quadrature requires the knowledge of the vorticity at Gauss points. Chebyshev approximation is chosen to obtain a continuous distribution of circulation, enabling the evaluation of the vorticity at the Gauss points. There are several reasons for choosing Chebyshev approximation technique. The first reason is that, as described in Appendix C, Chebyshev polynomials can be easily defined recursively. Secondly, once the Chebyshev coefficients are found it is easy to evaluate the function value at any point by using Clenshaw's recurrence. Most importantly, for a given level of approximation characterized by the highest order of Chebyshev polynomials, good approximation of the discrete representation are obtained and discrepancies between the two representations are minimized. In addition, once the Chebyshev coefficients that approximate the function are found,

the Chebyshev coefficients that approximate the derivative of the function and the integral of the function are easily found.

The first step is to create a Chebyshev approximation based on the discrete time values of the circulation. This can be achieved with the help of eqs. (239a) and (239b): circulations must be evaluated at the zeros of the Chebyshev polynomial, $T_n(x_k) = 0$. Because of the time domain discretization in dynamic simulations, only discrete function values are available. The function value at the zeros of the Chebyshev polynomial $T_n(x_k) = 0$ is interpolated linearly from the discrete sampling data.

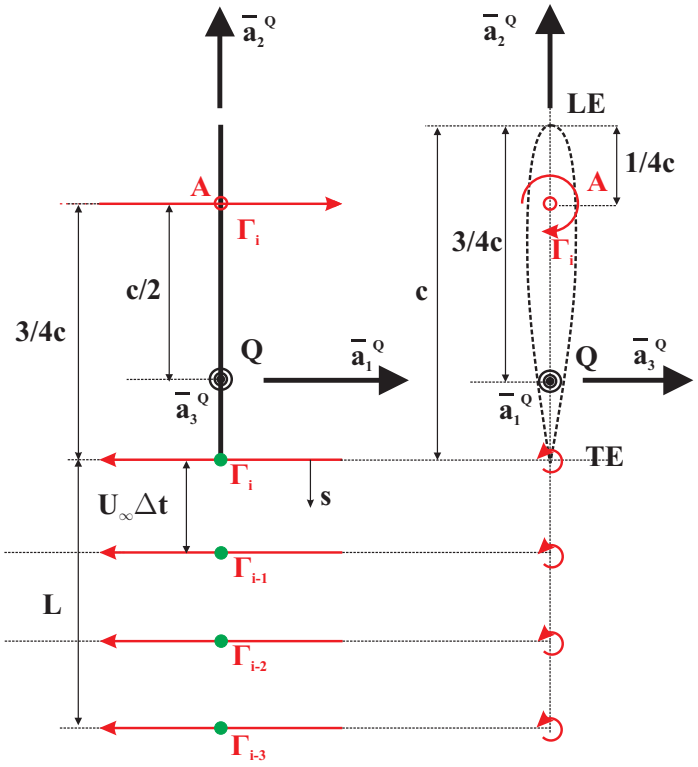

Figure 57: Generation of discrete sampling data of vorticity in the wake behind an airfoil in a two-dimensional incompressible, inviscid flow

As shown in fig. 57, at each time instant, the starting vortex is released into the wake and convected at the free-stream speed. A series of discrete circulation values, (t_i, Γ_i) are then available. The data set can also be expressed in terms of the distance from the vortex filament to the trailing edge of the airfoil, that is (ℓ_i, Γ_i). Because

of the fact that the induced effect from the vortex filament becomes smaller with a larger distance, the wake region considered in the analysis is finite, say the wake length is L. Non-dimensionalizing distance by the wake length, $\eta = \ell/L$, the available data set is (η_i, Γ_i). Note that array $\eta = [\eta_1, \eta_2, \ldots, \eta_M]$ is fixed and in the interval $[0, 1]$, where M is the number of the sampling points. Array $\Gamma = [\Gamma_1, \Gamma_2, \ldots, \Gamma_M]$ stores the circulation corresponding to ηs. If ηs are stored in ascending order, the first entry in circulation array Γ corresponds to the present circulation. While the last entry corresponds to the one released earlier. Based on these discrete data, the Chebyshev coefficients that approximate the function of the circulation with respect to η are computed with the reference of the eqs. (239a) and (239b). With the help of eq. (237), the function of the circulation in the wake is then approximated as

$$\Gamma(\eta) \approx \sum_{i=0}^{N-1} c_i T_i(\eta), \tag{147}$$

where N is the number of coefficients in Chebyshev expansion, c_i are given by the eqs. (239a) and (239b), and T_i is given by the eq. (226). With the coefficients that approximate the circulation function available, we can also easily find the coefficients that approximate the derivative of the circulation function with respect to η using eqs. (247a) and (247b). Let c_i' stand for the Chebyshev coefficients that approximate the derivative of circulation with respect to η, from eq. (246), we have

$$\frac{\mathrm{d}\Gamma(\eta)}{\mathrm{d}\eta} \approx \sum_{i=0}^{N-1} c_i' T_i(\eta), \tag{148}$$

4.6.1.3 Gaussian Quadrature

With Chebyshev approximation of the circulation distribution available, it now becomes possible to compute the induced flow due to the shed wake using Gaussian Quadrature. It should be noted that Gaussian quadrature is not applied directly to perform the integration of the Biot-Savart law. As described above, the wake structure behind an airfoil is a vortex sheet that is composed of a series of infinitely

long vortex filaments. Each infinitely long vortex filament of strength γ produces the induced flow at a point with a normal distance h away from the filament equal to

$$v = -\frac{\gamma}{2\pi h}. \tag{149}$$

The direction of this induced velocity is determined by the normal to the plane defined by the point and the vortex filament. The continuous vortex sheet is formed by an infinite number of such vortex filaments. The normal distance, h, is equal to $c/4 + s$, where s is the distance measured from the trailing edge of the airfoil to the end of the vortex sheet. Hence, the total induced effect due to the vortex sheet is

$$\underline{V} = -\int_0^L \frac{\gamma \bar{a}_3^Q}{2\pi(c/4+s)}\,\mathrm{d}s. \tag{150}$$

The vorticity γ actually is equal to $\mathrm{d}\Gamma/\mathrm{d}s$, as shown in the following derivation.

Rewriting eq. (146) with $\Gamma_0 = 0$ leads to

$$\underline{V}_i = \sum_{j=1}^{i} \frac{\Gamma_{i-1} - \Gamma_i}{(\pi c)/2 + (j-1)U_\infty \Delta t}\bar{a}_3^Q = \sum_{j=1}^{i} \frac{\frac{\Gamma_{i-1}-\Gamma_i}{\Delta s}\Delta s}{(\pi c)/2 + (j-1)U_\infty \Delta t}\bar{a}_3^Q, \tag{151}$$

where $\Delta s = U_\infty \Delta t$ and $s_j = (j-1)\Delta s$. The above equation now becomes

$$\underline{V}_i = \sum_{j=1}^{i} \frac{\frac{\Gamma_{i-1}-\Gamma_i}{\Delta s}\Delta s}{(\pi c)/2 + s_j}\bar{a}_3^Q. \tag{152}$$

In the limit for $\Delta s \to 0$, this equation reverts to eq. (150). In fact, eq. (152) can be viewed as a simple discretization of eq. (150) using the trapezoidal formula to evaluate the integral.

Note that the Chebyshev coefficients that approximate the derivative of the circulation function are indeed those approximating the derivative $\mathrm{d}\Gamma/\mathrm{d}\eta$. To take advantage of Chebyshev approximation, eq. (150) is recast as

$$\underline{V}_i = -\int_0^L \frac{\gamma \mathrm{d}\eta}{2\pi(c/4+\eta L)}\bar{a}_3^Q. \tag{153}$$

Application of the Gaussian quadrature formula then leads to

$$\underline{V}_i = -\sum_{k=1}^{n} w_k \frac{\gamma(g_k)}{2\pi(c/4+g_k L)}\bar{a}_3^Q, \tag{154}$$

where n is the number of Gauss points, g_k the Gauss points, and w_k the corresponding weights. The vorticities, $\gamma(g_k)$, at Gauss points are evaluated with the help of eq. (148).

Note that Gaussian quadrature combined with Chebyshev approximation does not bring a compelling computational advantage to this two-dimensional problem because of the very simple structure of the wake. It serves as an introduction to the more complex, three-dimensional problem developed in the next section.

4.6.2 Inflow for a Three-Dimensional Finite Wing

This section details the evaluation of the inflow due to the vortex wake behind a finite wing in an unsteady flow. Fig. 53 shows the vortex wake structure discretized in the time and spatial domains, leading to a wake comprising both trailing and shed vorticity in an unsteady problem. Due to the fact that trailed vorticity will bundle together forming a concentrated vortex filament in the region far from the wing tip, the vortex wake of a finite wing can be modeled as a near wake (vortex sheet) and a far wake (bundled vortex filament), as shown in fig. 58. This figure schematically demonstrated the wake structure of a finite wing (left) and a rotor blade (right). As mentioned in section 4.5.2.3, the inflow evaluated at the collocation points comes from three sources including the far-field free stream velocity, the bound circulations that are to be solved for, and those released into the wake at the earlier stage of the motion. Note that singularity can occur in the computation of the inflow when the vortex filament is passing through the inflow evaluation point. For example, the inflow evaluated at the point on the blade due to trailed vorticity produced by bound circulations. In addition, a free-wake analysis requires the computation of the geometry of the trailed vortex filaments. Hence, it is also necessary to compute the induced flow at points along those filaments. Singularities will also occur when computing the induced flow at a point on a free filament.

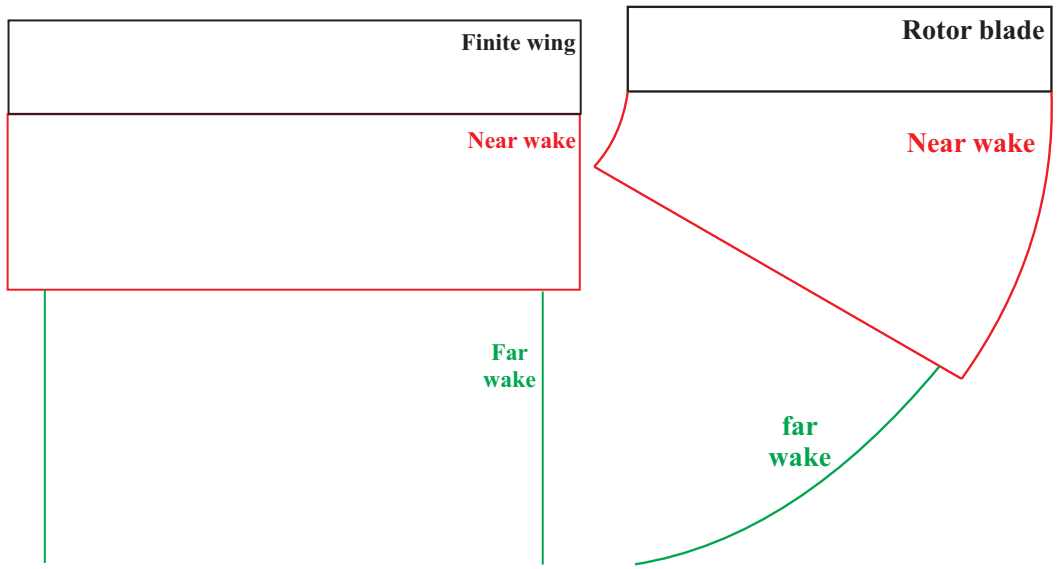

Figure 58: Vortex wake structure behind a finite wing (left figure) or rotor blade (right figure).

4.6.2.1 Classical Approach

In typical free-wake analysis based on vortex methods, a large number of Lagrangian markers are placed on a vortex filament. Any two successive markers on the vortex filament are linked together by straight lines, as shown in fig. 38. Eq. (200) can be used to compute the induced velocity due to each vortex segment along the vortex filament. The total velocity induced by the vortex filament is computed by summing up all the contributions from all vortex segments, that is,

$$\underline{V}_i = \sum_{k=1}^{N_s} \underline{V}_k^s, \tag{155}$$

where $\underline{V}_k^s$ is the induced flow generated by the k^{th} segment along the vortex filament and computed by eq. (200), N_s is the number of vortex segments.

A vortex sheet can be represented by a series of vortex rings, as shown in fig. 53. The vorticity distributed over the wing surface is represented by a row of vortex rings. Each vortex ring surrounds an airstation with a certain circulation. As time goes on, the row of vortex rings will move downstream with free-stream velocity forming a

vortex sheet with trailed and shed vorticity distributed over the sheet. The induced flow at a point due to a vortex ring is computed with the help of eq. (218). The total induced flow due to a vortex sheet is then obtained by adding up the contributions from all vortex rings,

$$\underline{V}_i = \sum_{k=1}^{N_r} \underline{V}_k^r, \tag{156}$$

where $\underline{V}_k^r$ is the induced flow due to each vortex ring on the vortex sheet and computed by eq. (218), N_r is the number of vortex rings.

4.6.2.2 Chebyshev Approximation of Vorticity Field

The vorticity over the vortex sheet behind the wing can be viewed as a distribution of vortex rings, each with a different circulation, as shown in fig. 59. In this figure, t_i represents the present time instant at time step i, $\Gamma_{i,j}$ denotes the circulation at time instant i and span-wise position j. Of course, the circulation released into the wake is a function of time and space. The changes in circulation with respect to time and space result in shed and trailed vorticities, respectively. Consider a vortex sheet covering a region with length L and width S along the directions of unit vectors $\bar{u}$ and $\bar{v}$, respectively. The vortex sheet then contains a number of vortex rings released during time interval $(t_{i-1}, t_{i-L/U_\infty \Delta t})$, where U_∞ is far-field free-stream velocity, and Δt the time step size. Note that spatial variable u is related to time t by $u = U_\infty(t - t_r)/L$, where t_r is the time at which the circulation was released. Hence, the circulation over the vortex sheet can be viewed as a function of the curvilinear variables u and v, measuring length along unit vectors $\bar{u}$ and $\bar{v}$, respectively, $\Gamma = \Gamma(u, v)$.

After discretization in the time and space domains, circulation becomes a discrete function of two variables, u, and v. As described in Appendix C.3, two-dimensional functions can be expanded in Chebyshev series using eq. (254) based on this discrete data. The Chebyshev expansion coefficients are computed using formulae in

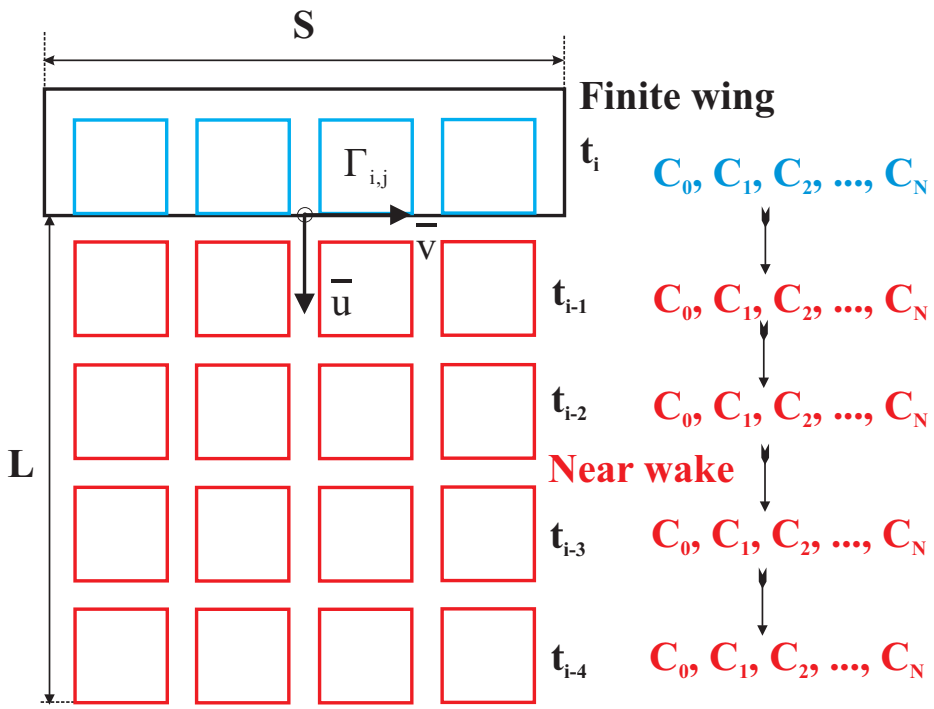

Figure 59: Circulation update in the vortex sheet and Chebyshev coefficients update

eqs. (256a) to (256d). The shed vorticity corresponds to the derivative of the circulation with respect to time, *i.e.* a derivative with respect to variable u, $\partial\Gamma(u,v)/\partial u$, whereas the trailed vorticity corresponds to the derivative of the circulation with respect to space, *i.e.* a derivative with respect to variable v, $\partial\Gamma(u,v)/\partial v$. Derivatives of Chebyshev expansions are easily evaluated see eqs. (264a) to (264e) and eqs. (266a) to (266e), for derivatives with respect to u and v, respectively.

At each instant, a new row of circulation enters the near wake and the last row exits the near wake. A one-dimensional Chebyshev expansion is performed to obtain the N Chebyshev coefficients, c_k, $k = 0, 1, 2, \ldots, N$, that approximate the bound circulation distributions, Γ^b, over the wing span,

$$\Gamma^b \approx \sum_{k=0}^{N} c_k T_k(v), \tag{157}$$

where N is the order of the Chebyshev polynomials, T_k, used for expansion along the $\bar{v}$ direction. Hence, the circulation distribution over the sheet changes at every

time instant. To evaluate the induced effect of the vortex sheet, a two-dimensional Chebyshev expansion has to be performed at every time step, which increases the computational cost of the approach. However, it must be noted that the circulation distribution changes in a well organized manner: the only new data coming into play at each time instant is that entering the first row of data. To take advantage of this fact, the Chebyshev coefficients at each time instant are stored because they are required to perform the two-dimensional Chebyshev approximation, as sketched in the right portion of fig. 59. The coefficients of the one-dimensional Chebyshev expansion, c_k, are a function of time, that is, a function of u, $c_k = c_k(u)$. Thus, the circulation function, Γ^w, in the near wake can then be approximated in a two-dimensional space using eq. (257)

$$\Gamma^w(u, v) \approx \sum_{k=0}^{N} c_k(u) T_k(v). \tag{158}$$

To find the Chebyshev coefficients in the eq. (254), only a one-dimensional Chebyshev expansion of Chebyshev coefficients, c_k, is required to obtain the coefficients c_{ij}, which can be computed by using eqs. (258a) and (258b). This requires to find c_k at the zeros, u_ℓ, $\ell = 1, 2, \ldots, M$, of Chebyshev polynomials in $\bar{u}$ direction, where M is the order of T_ℓ. To find the quantities $c_k(u_\ell)$, a linear interpolation is used based on c_k at every time instant. Hence, instead of performing a two-dimensional Chebyshev expansion based on data ($\Gamma_{i,j}$) at every time instant, only N one-dimensional Chebyshev expansions are required to find the coefficients c_{ij}, resulting in considerable computational savings. Once the coefficients c_{ij} have been obtained, the Chebyshev coefficients that approximate the shed and trailed vorticity can then be found using eqs. (264a) to (264e) and eqs. (266a) to (266e), respectively.

The trailed vorticity in the near wake behind a wing will roll up, forming a concentrated vortex filament at the tip region of the wing, as shown in fig. 60. With the help of the Chebyshev approximation, it is very easy to compute the vorticity released into the vortex filament. Let $\Gamma_t(u, v) = \partial\Gamma(u, v)/\partial v$ denote for the trailed

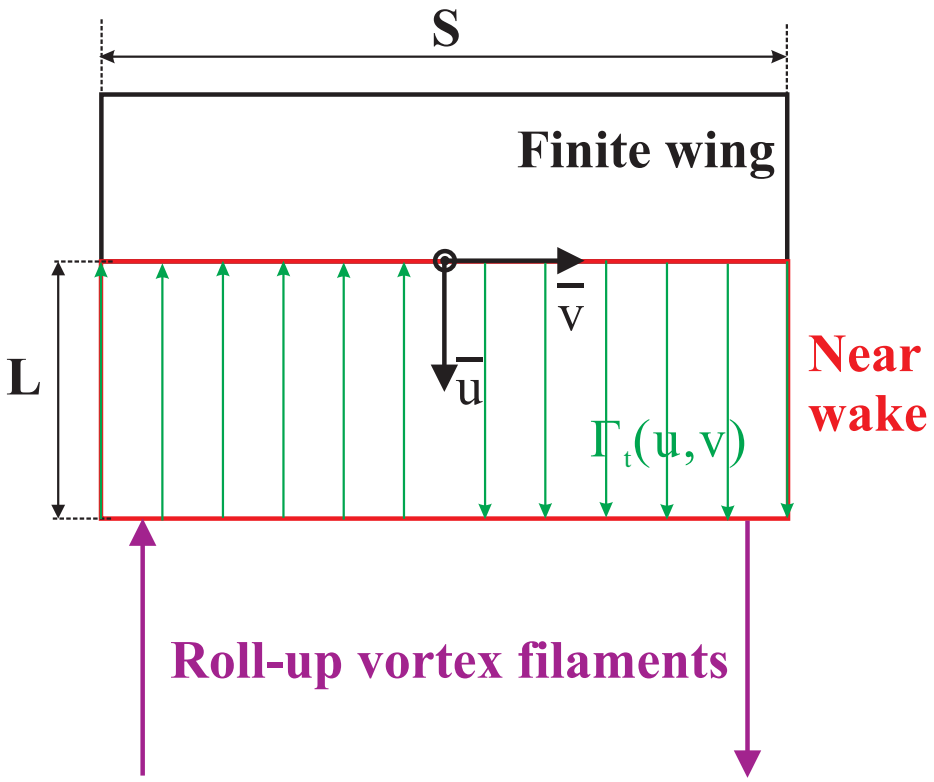

Figure 60: Rol-up of a vortex filament in the far wake of a finite wing

vorticity function; the vorticity distribution at the end of the near wake is then simply obtained obtained by letting $u = 1.0$. This vorticity will bundle together to form the roll-up vortex filament and its strength, Γ^r, is obtained by integrating of the trailed vorticity over the wing span at $u = 1.0$ to find

$$\Gamma^r = \int_0^1 \Gamma_t(1, v)\, \mathrm{d}v. \tag{159}$$

4.6.2.3 Gaussian Quadrature

With the Chebyshev approximation of vorticity distribution over a vortex filament or vortex sheet available, the vorticity at any point can be easily found. Gaussian quadrature can now be used to evaluate the integral of the Biot-Savart law, see eq. (18). Consider a vortex filament of strength $\Gamma(s)$ and the length L; the velocity

it induces is

$$\underline{V}_i = \frac{1}{4\pi} \int_0^L \frac{\Gamma(s)\bar{t} \times (\underline{r}_p - \underline{r})}{\|\underline{r}_p - \underline{r}\|^3} \, \mathrm{d}s, \tag{160}$$

where s is the curvilinear variable measuring length along the vortex filament, and $\bar{t}$ the unit tangent vector to the filament. Since the vortex filament is represented by a NURBS curve, the unit vector $\bar{t}$ can be computed using the eq. (21), and eq. (160) then becomes

$$\underline{V}_i = \frac{1}{4\pi} \int_0^L \frac{\Gamma(s)\bar{t} \times (\underline{r}_p - \underline{r})}{\|\underline{r}_p - \underline{r}\|^3} \, \mathrm{d}s = \frac{L}{4\pi} \int_0^1 \frac{\Gamma(\eta)\bar{t} \times (\underline{r}_p - \underline{r})}{\|\underline{r}_p - \underline{r}\|^3} \, \mathrm{d}\eta, \tag{161}$$

where $\eta = s/L$. Approximation of this integral using Gaussian quadrature then yields

$$\underline{V}_i \approx \frac{L}{4\pi} \sum_{k=1}^{n} \frac{\Gamma(g_k)\bar{t} \times \big(\underline{r}_p - \underline{r}(g_k)\big)}{\|\underline{r}_p - \underline{r}(g_k)\|^3} w_k \tag{162}$$

where n is the number of Gauss points, g_k the Gauss points, and w_k the corresponding weights.

Integrating eq. (18) over a vortex sheet yields the induced velocity due to the vortex sheet. Typically, vortex sheets comprise both shed and trailed vorticities, whose directions are perpendicular to each other, see fig. 61; hence, the induced velocity due to shed and trailed vorticities can be computed separately. First, the computation of the induced velocity due to trailed vorticity is considered. Assume a vortex sheet of distributed vorticity function $\Gamma(x_1, x_2)$ in a $x_1 - x_2$ plane, x_1, x_2 are dimensional variables in the directions perpendicular and parallel to the wing span, respectively. Variables u, v are non-dimensional quantities normalized by the length L and width S of the sheet, respectively, *i.e.* $u = x_1/L, v = x_2/S$. The trailed vorticity, $\Gamma_t(x_1, x_2)$, is the derivative of $\Gamma(x_1, x_2)$ with respect to x_2 and oriented as shown in $\bar{u}$ direction, that is,

$$\Gamma_t(x_1, x_2) = \frac{\partial \Gamma(x_1, x_2)}{\partial x_2} = \frac{\partial \Gamma(u, v)}{\partial v} \frac{\mathrm{d}v}{\mathrm{d}x_2}. \tag{163}$$

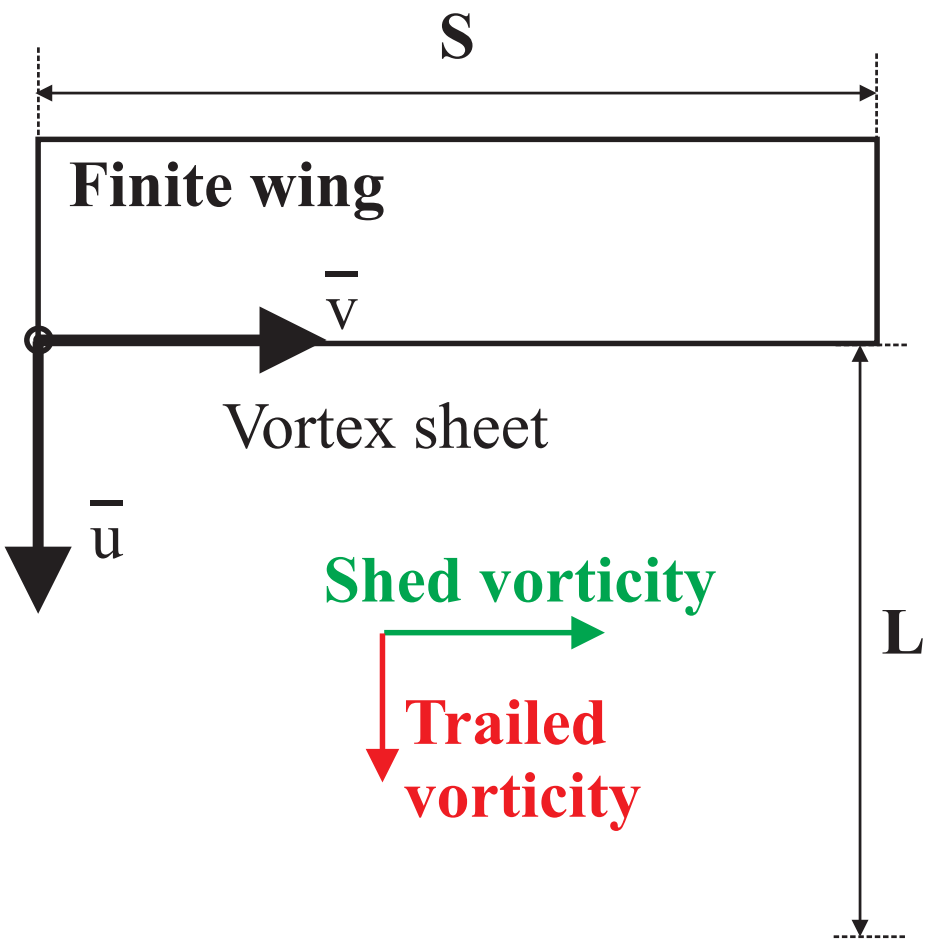

Figure 61: Directions of trailed and shed vorticity over a vortex sheet

The induced velocity due to trailed vorticity, $\underline{V}_{it}$, is computed as

$$\underline{V}_{it} = \frac{1}{4\pi}\int_0^L \int_0^S \frac{\Gamma_t(x_1,x_2)\bar{u}\times(\underline{r}_p-\underline{r})}{\|\underline{r}_p-\underline{r}\|^3}\,\mathrm{d}x_1\mathrm{d}x_2 = \frac{L}{4\pi}\int_0^1\int_0^1 \frac{\partial\Gamma(u,v)}{\partial v}\frac{\bar{u}\times(\underline{r}_p-\underline{r})}{\|\underline{r}_p-\underline{r}\|^3}\,\mathrm{d}u\mathrm{d}v, \tag{164}$$

where unit vector $\bar{u}$ can be found by taking first derivative of position vector of a point on the NURBS surface representing the vortex sheet with respect to u. The formula of Gaussian quadrature is then expressed as

$$\underline{V}_{it} \approx \frac{L}{4\pi}\sum_{i=1}^{n}\sum_{j=1}^{m}\frac{\partial\Gamma(u,v)}{\partial v}(g_i,g_j)\frac{\bar{u}\times\big(\underline{r}_p-\underline{r}(g_i,g_j)\big)}{\|\underline{r}_p-\underline{r}(g_i,g_j)\|^3}w_iw_j, \tag{165}$$

where n, m are the number of the Gauss points in the $\bar{u}$ and $\bar{v}$ directions, respectively.

Similar equations can be derived for the shed vorticity as

$$\Gamma_s(x_1, x_2) = \frac{\partial \Gamma(x_1, x_2)}{\partial x_1} = \frac{\partial \Gamma(u, v)}{\partial u} \frac{\mathrm{d}u}{\mathrm{d}x_1}. \tag{166}$$

Computation of the induced velocity due to shed vorticity then becomes

$$\underline{V}_{is} = \frac{1}{4\pi} \int_0^L \int_0^S \frac{\Gamma_s(x_1, x_2) \bar{v} \times (\underline{r}_p - \underline{r})}{\|\underline{r}_p - \underline{r}\|^3} \, \mathrm{d}x_1 \mathrm{d}x_2 = \frac{S}{4\pi} \int_0^1 \int_0^1 \frac{\partial \Gamma(u, v)}{\partial u} \frac{\bar{v} \times (\underline{r}_p - \underline{r})}{\|\underline{r}_p - \underline{r}\|^3} \, \mathrm{d}u \mathrm{d}v, \tag{167}$$

and the Gaussian quadrature formula yields

$$\underline{V}_{is} \approx \frac{S}{4\pi} \sum_{i=1}^{n} \sum_{j=1}^{m} \frac{\partial \Gamma(u, v)}{\partial u(g_i, g_j)} \frac{\bar{v} \times \big(\underline{r}_p - \underline{r}(g_i, g_j)\big)}{\|\underline{r}_p - \underline{r}(g_i, g_j)\|^3} w_i w_j. \tag{168}$$

4.6.2.4 Inflow Due to Bound circulations

It is important to recognize the possible occurrence of singularities when computing the inflow at a collocation point due to bound circulations on the wing. Consider a finite wing with span S in an incompressible, inviscid, and irrotational flow, as shown in fig. 62. The bound vortex filament is located at the quarter-chord line of the wing. The vortex strength along the bound vortex filament is $\Gamma(x_2)$ and positive along positive $\bar{\imath}_2$. The starting vortex filament at the trailing edge of the wing is then $-\Gamma(x_2)\bar{\imath}_2$. According to eq. (18), the induced flow at a point on the wing, $\mathbf{P} = (x_{1p}, x_{2p}, 0)$, due to the bound vortex filament, denoted as $\underline{V}_i^b$, is

$$\underline{V}_i^b = \frac{1}{4\pi} \int_{-S/2}^{S/2} \frac{\Gamma(x_2)\bar{\imath}_2 \times [x_{1p}\bar{\imath}_1 + (x_{2p} - x_2)\bar{\imath}_2]}{\|(x_{1p}\bar{\imath}_1 + (x_{2p} - x_2)\bar{\imath}_2)\|^3} \, \mathrm{d}x_2. \tag{169}$$

Similarly, the induced flow at point $\mathbf{P}$ due to the starting vortex, $\underline{V}_i^{bs}$, can be computed by

$$\underline{V}_i^{bs} = -\frac{1}{4\pi} \int_{-S/2}^{S/2} \frac{\Gamma(x_2)\bar{\imath}_2 \times [(x_{1p} - 3c/4)\bar{\imath}_1 + (x_{2p} - x_2)\bar{\imath}_2]}{\|((x_{2p} - 3c/4)\bar{\imath}_1 + (x_{2p} - x_2)\bar{\imath}_2)\|^3} \, \mathrm{d}x_2, \tag{170}$$

where c is the wing chord length assumed to be constant over the span.

The trailed vorticity at a span-wise position x_2' along the wing is $[\mathrm{d}\Gamma(x_2)/\mathrm{d}x_2]_{x_2=x_2'} \mathrm{d}x_2 \, \bar{\imath}_1$ is located along segment **AB** and is assumed to be constant chordwise. The induced

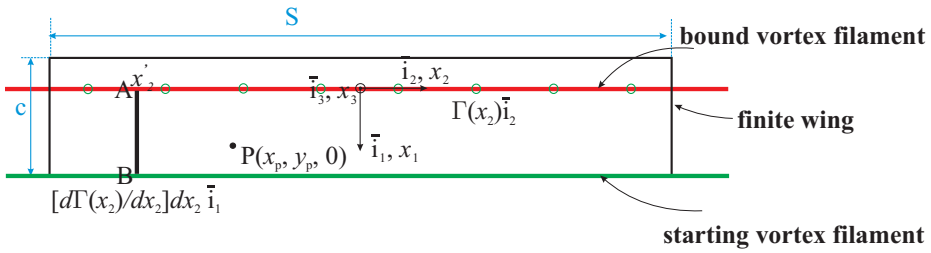

Figure 62: Evaluation of inflow at a point on the wing due to a bound vortex filament

inflow at point **P**, denoted as $\underline{V}_i^{bt}$, is then

$$\underline{V}_i^{bt} = \frac{1}{4\pi}\int_0^{3c/4} \frac{([\mathrm{d}\Gamma(x_2)/\mathrm{d}x_2]_{x_2=x_2'}\mathrm{d}x_2)\bar{\imath}_1 \times [(x_{1p}-x_1)\bar{\imath}_1 + (x_{2p}-x_2')\bar{\imath}_2]}{\|(x_{1p}-x_1)\bar{\imath}_1 + (x_{2p}-x_2')\bar{\imath}_2\|^3}\,\mathrm{d}x_1. \quad (171)$$

When the point **P** is located on the vortex filament over which the integral of the Biot-Savart law is evaluated, a singularity occurs. Therefore, to avoid these singularities, classical approaches are used to compute the induced flow at collocation points on the wing due to the bound circulations: the vorticity distributed over the wing is modeled as a series of vortex rings, and the computation of the induced flow due to the vortex rings is described in section 4.6.2.1. However, for a fixed wing aircraft, the bound circulations will not create a singularity when the induced velocity at a point on a free filament is evaluated. Hence, Gaussian quadrature is used to computed such induced velocities. Singularities could occur when rotor problems are considered. When such a problem is encountered, an initial core radius will be given to avoid singularities.

4.6.2.5 Inflow Due to a Planar Vortex Sheet

In this work, the vortex sheet behind a finite wing or blade is modeled as a planar sheet, rectangular for wings and helical for rotor blades, as shown in fig. 58. When the wing is in motion, the vortex sheet behind the wing is assumed to remain planar, fixed relative to the wing, and its orientation is parallel to the free stream velocity, as shown in fig. 63. Therefore, the geometry of the vortex sheet is prescribed and its position relative to the wing is fixed. Since there is no need to compute the induced

velocity at a point on the sheet, singularities will not occur for fixed-wing problems. As for the rotor problem, when the free-vortex filament is long enough to encounter the succeeding vortex sheet, singularities will occur.

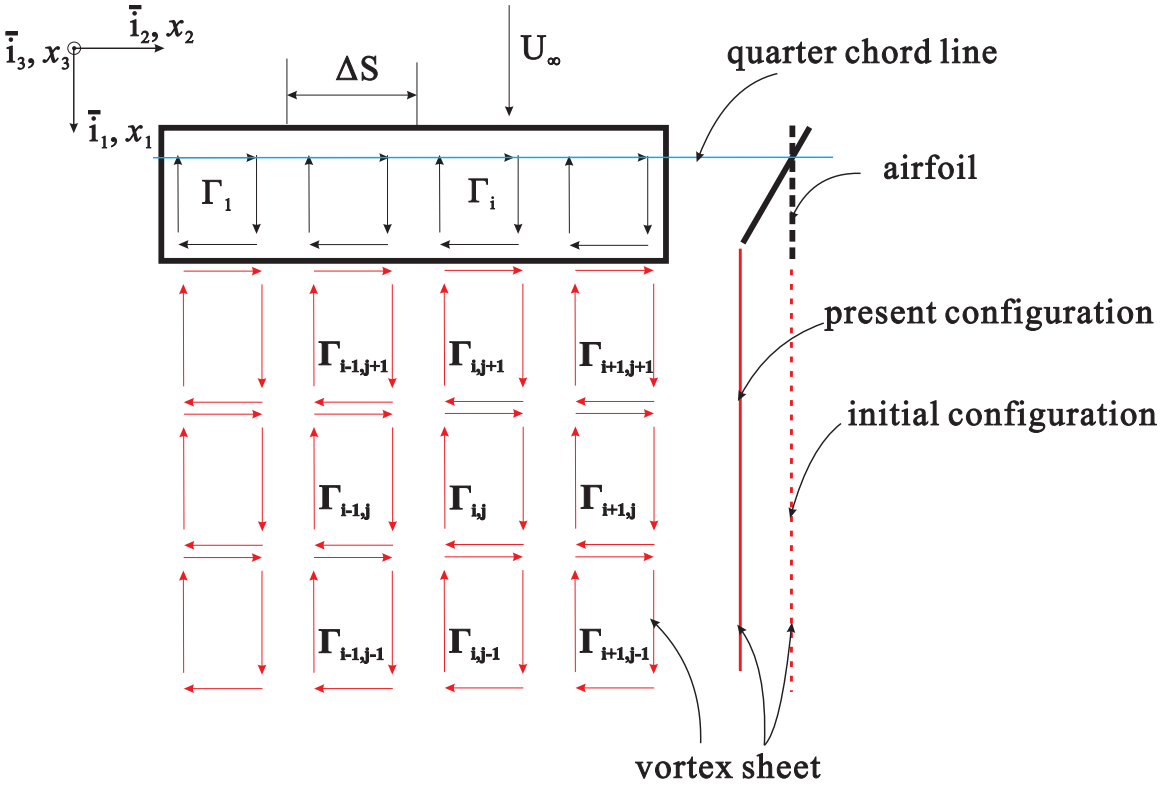

Figure 63: Vortex sheet behind a finite wing represented by vortex rings

Because of the fact that the velocity induced by a given vortex varies reciprocally with the distance from the vortex to the velocity evaluation point, the classical approach is chosen to compute the induced velocities at the collocation points on the wing. While, Gaussian quadrature combined with the Chebyshev approximation is applied to the computation of the induced flow at the points on the free filaments in free-wake analysis.

4.6.2.6 Inflow Due to a Curved Vortex Filament

For a fixed-wing aircraft at level flight condition, the roll-up vortex filament in the far wake is typically a straight line. The roll-up vortex filament for a rotor aircraft is a

curved filament, typically of a helical shape. Moreover, when a fixed wing aircraft in a maneuver flight, the trailed far-field vortex filament becomes a curved vortex filament. In such situations, the vorticity orientation will vary with time. If classical approach is selected to calculate the induced velocity, a large number of markers is required to maintain accuracy. On the other hand, in free-wake analysis, the position of each marker must be updated, requiring computation of the induced flow for each marker due to all other markers. Clearly, the computational complexity of the problem is $\mathcal{O}(N)$, where N is the number of markers. The Gaussian quadrature and Chebyshev approximation technique described in sections 4.6.2.2 and 4.6.2.3, respectively, aim at reducing this computational cost. When the induced flow at a point on the free filament itself is computed, singularities can occur. An initial core radius is introduced to overcome this problem.

4.7 Numerical Examples

This section presents some numerical examples of two- and three-dimensional problems to valid the present approach of computing the induced flow due to a vortex wake described earlier in this chapter. First presented here is a rigid airfoil with only pitching motion in a two-dimensional incompressible, inviscid, and irrotational flow. The results obtained using the present inflow model to compute the inflow due to the vortex wake are compared with the results of the Peters finite-state inflow model. Next, numerical examples of a fixed-wing aircraft performing level cruise and maneuver flights are then shown to test the validity of the present approach for finding the circulations, and thus the induced flow due to these circulations.

4.7.1 The Two-Dimensional Airfoil

Consider a rigid airfoil in a two-dimensional incompressible, inviscid, and irrotational flow pitching about the axis located at the quarter chord and the prescribed pitching

is given by

$$\theta(t) = \begin{cases} \theta_0(1 - \cos\omega t) & t \leq \pi/\omega \\ 2\theta_0 & t > \pi/\omega \end{cases} \tag{172}$$

where θ_0 is the pitching amplitude and ω is the pitching rate. The parameters used in this analysis are listed in Table 7, where c is the chord length, U_∞ is the far-field free-

Table 7: Parameters used in a 2D thin-airfoil analysis

c [ft]	U_∞ [ft/sec]	ρ [lb/ft^3]	θ_0 [rad]	ω [rad/sec]
6	480	2.18810×10^{-3}	0.0175	4

stream speed, and ρ is the air density. Assume the lift coefficient is only a function of the effective angle of attack α,

$$C_\ell = 2\pi\alpha + b\alpha^2, \tag{173}$$

where b is a given parameter.

If $b = 0$, the lift coefficient is a linear function of the angle of attack, and the slope of the lift curve is equal to 2π. If $b \neq 0$, the lift coefficient is a parabolic function of the angle of attack, see eq. (173). Assuming that for an angle of attack of 15 degrees the lift coefficient decreases by 20%, $b = -4.8$ and the expression for the lift coefficient becomes $C_\ell = 2\pi\alpha - 4.8\alpha^2$. The lift computed based on 2D thin-airfoil theory and its extension described in section 4.5.1.3 is compared with the finite-state unsteady thin-airfoil theory of Peters *et al.*, for which the number of the modes of inflow states N is chosen to be 10. The computation of the lift in the present approach is based on the eq. (54) .

4.7.1.1 2D Thin Airfoil

The simulation time is 5 seconds, and the time step size was selected to be $\Delta t = 0.001$ sec to achieve converged results, as shown in fig. 64(b). The results are shown in

figs. 65 to 67. Figure 65 shows the prescribed pitching motion of the airfoil, θ, effective angle of attack of the airfoil, α, and the angle of attack of the equivalent flat plate, α^P. Since the lift coefficient is a linear function of the angle of attack, $b = 0$, the airfoil and its equivalent flat plate are identical, and angle β should be zero, as can be verified in fig. 67. The comparison between the present approach and Peters finite-state inflow model in terms of lift, bound circulation, and downwash demonstrates that the present approach provides accurate predictions. Note that the downwash predicted by Peters inflow model decays to zero faster than that predicted by the present model. To resolve this issue, different numbers of the inflow states were used in Peters inflow model, as shown in fig. 64(a). As the number of inflow states increases, the discrepancy between the two models becomes smaller. Figure. 67(b) shows the number of iterations required to solve for the bound circulation at every time step; clearly, convergence is easy to achieve.

4.7.1.2 2D General Airfoil

The simulation time is 5 seconds, and the time step size used in this analysis is $\Delta t = 0.001$ sec to achieve the convergence. Figures 68 to 70 show the results computed using the present approach for the case of the general airfoil. In this case, $b = -4.8$ and the difference between angles of attack of the real airfoil and that of the equivalent flat plate is not zero, as shown in these figures. Moreover, the present approach converges quickly, as seen in fig. 70(b). Results obtained using Peters finite-state inflow model are shown here for reference only; indeed, linear aerodynamics are assumed in that case.

4.7.1.3 2D General Airfoil with a Large Angle of Attack

In previous example, the effective angle of attack was still small. Consequently, the equivalent flat plate model was not fully validated. In this example, the prescribed pitching amplitude is increased and given as $\theta_0 = 0.14$ rad, that is, the prescribed

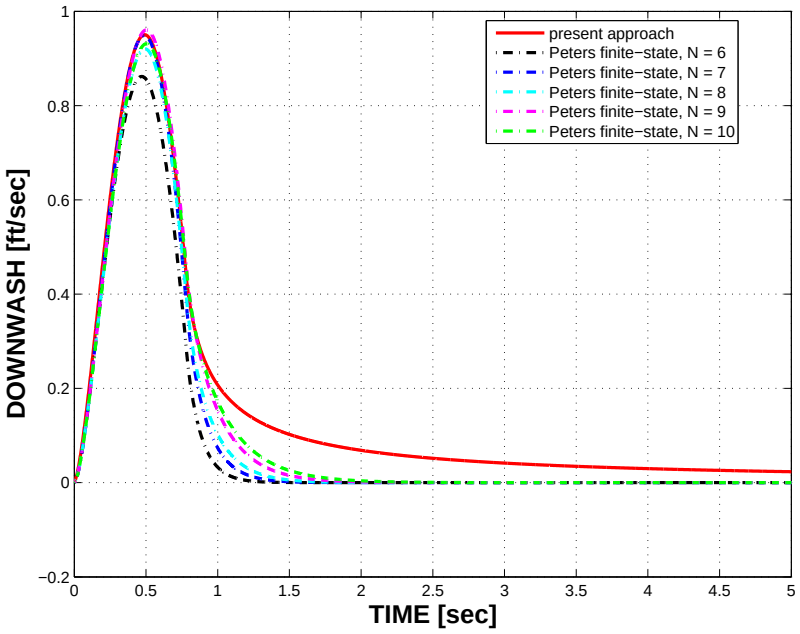

(a) convergence of Peters-finite state model

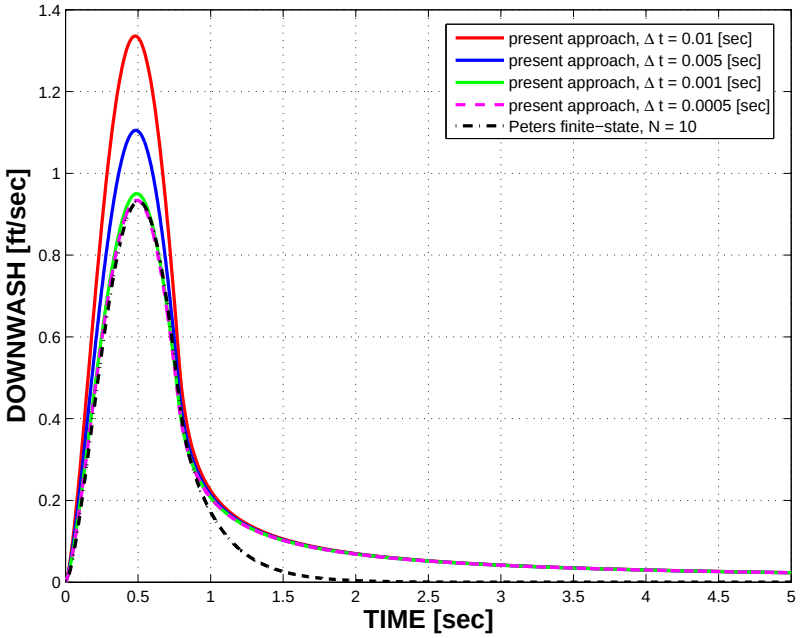

(b) convergence of present model

Figure 64: 2D thin airfoil, $\theta_0 = 0.0175$ rad, $C_\ell = 2\pi\alpha$

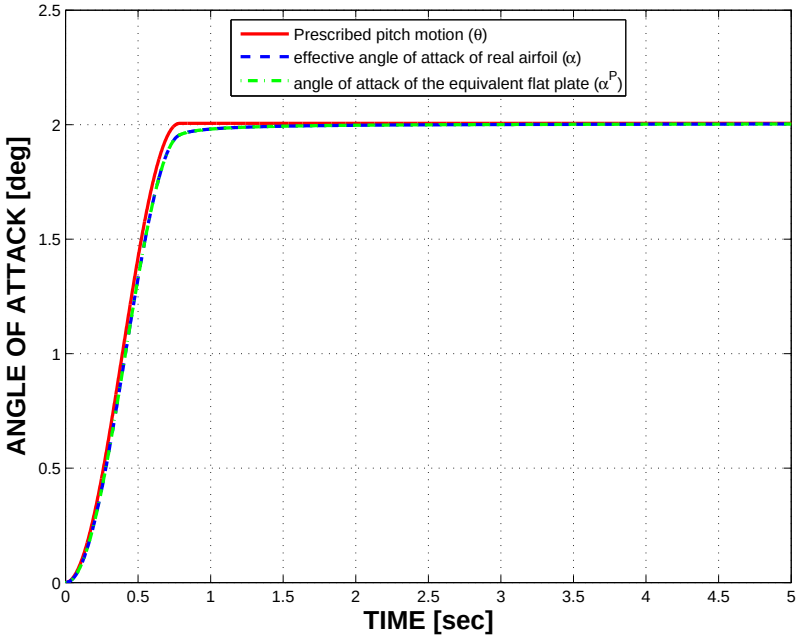

(a) time history of the angle of attack

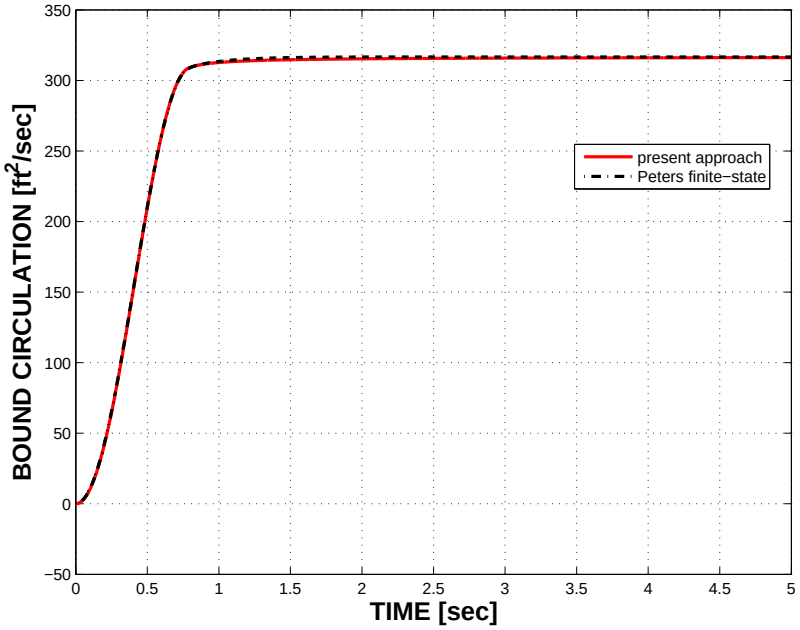

(b) time history of the circulation

Figure 65: 2D thin airfoil, $\theta_0 = 0.0175$ rad, $C_\ell = 2\pi\alpha$

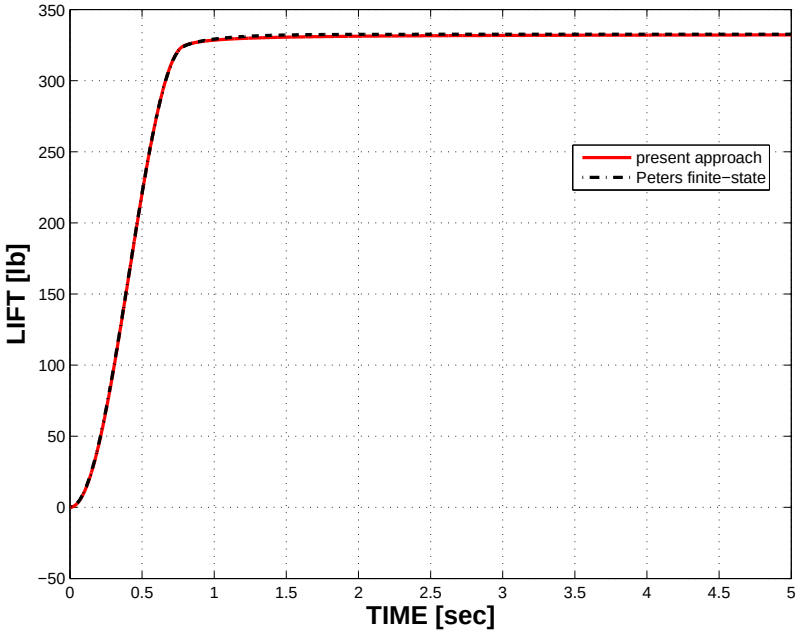

(a) time history of the lift

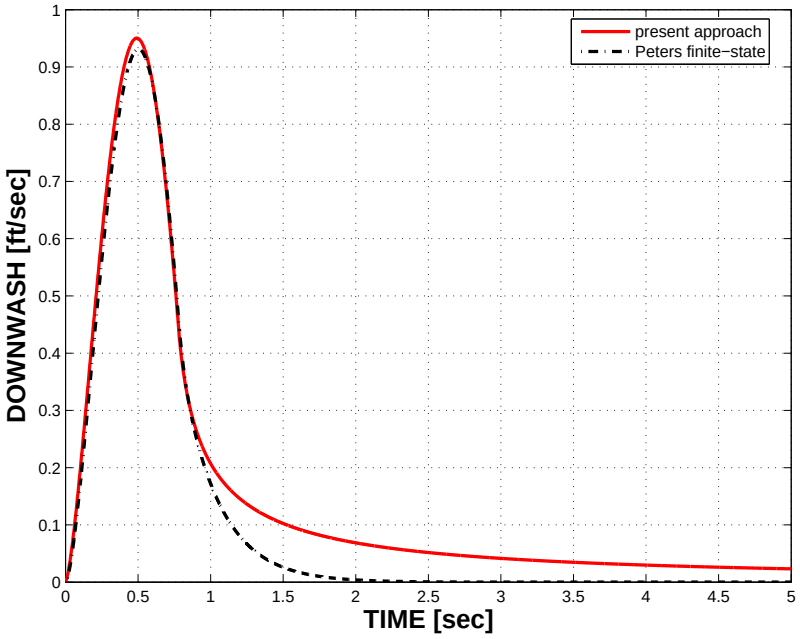

(b) time history of the downwash

Figure 66: 2D thin airfoil, $\theta_0 = 0.0175$ rad, $C_\ell = 2\pi\alpha$

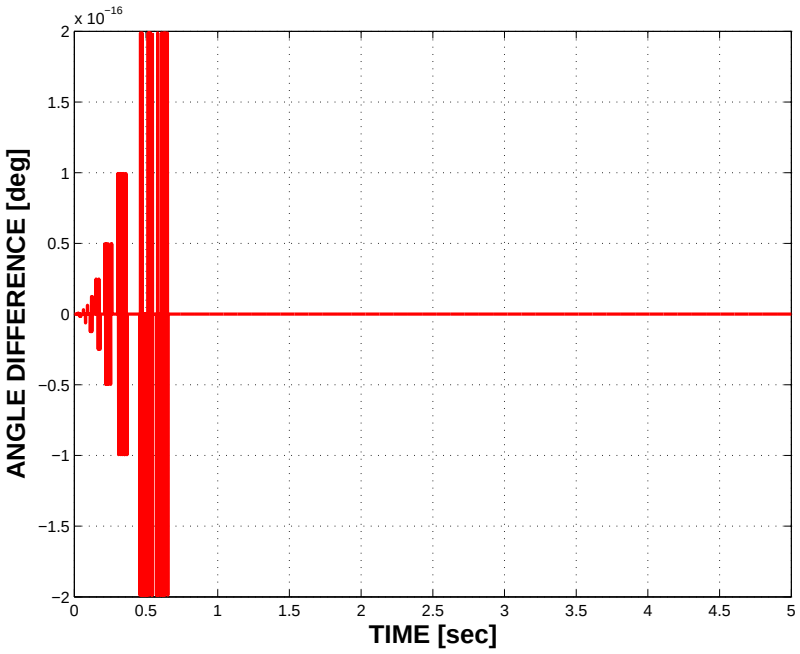

(a) angle difference between α and α^P

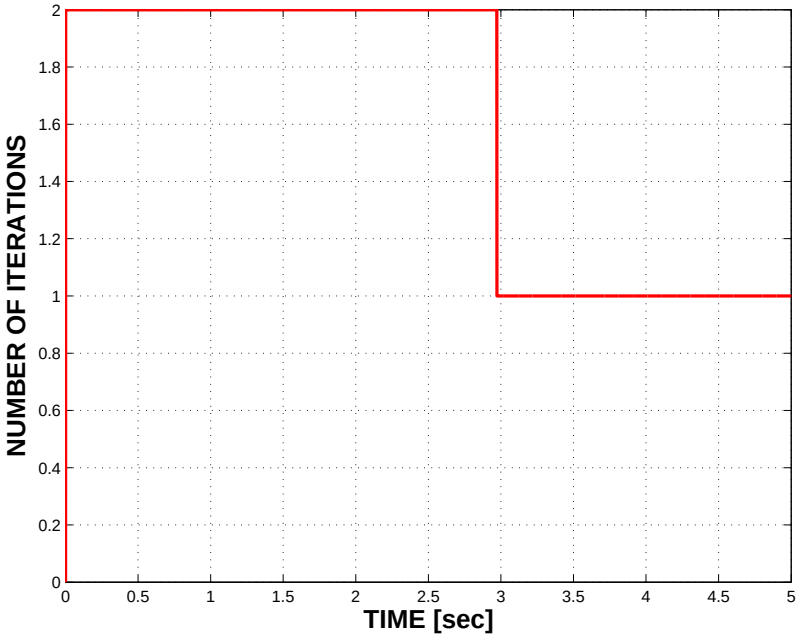

(b) the number of iterations in each time step

Figure 67: 2D thin airfoil, $\theta_0 = 0.0175$ rad, $C_\ell = 2\pi\alpha$

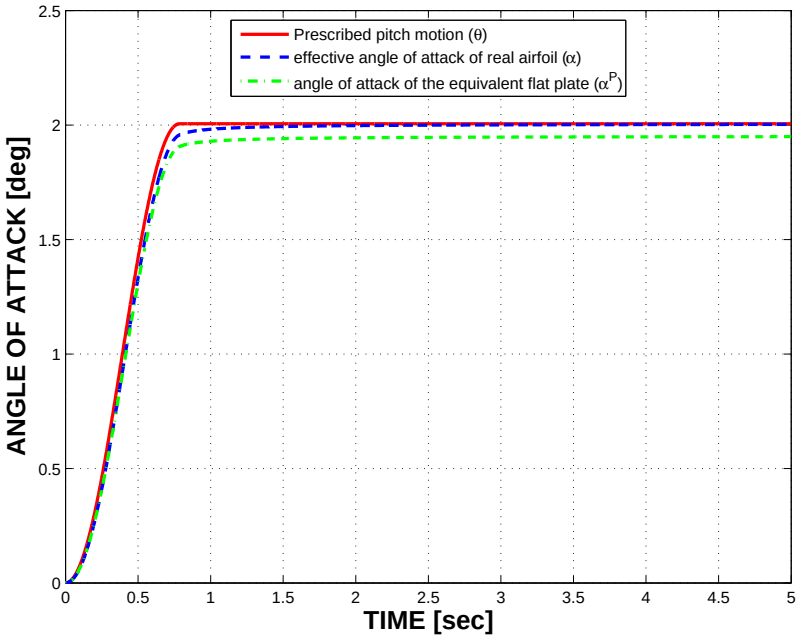

(a) time history of the angle of attack

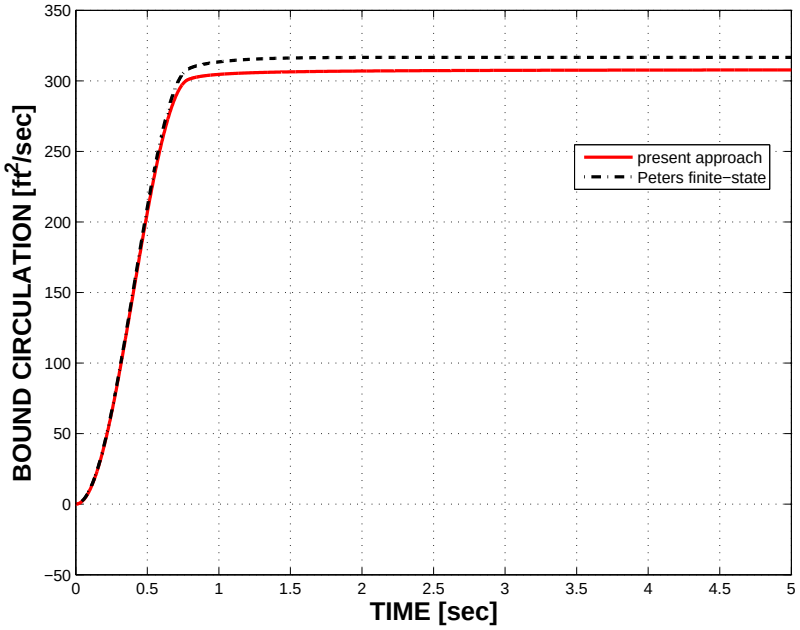

(b) time history of the circulation

Figure 68: 2D general airfoil, $\theta_0 = 0.0175$ rad, $C_\ell = 2\pi\alpha - 4.8\alpha^2$

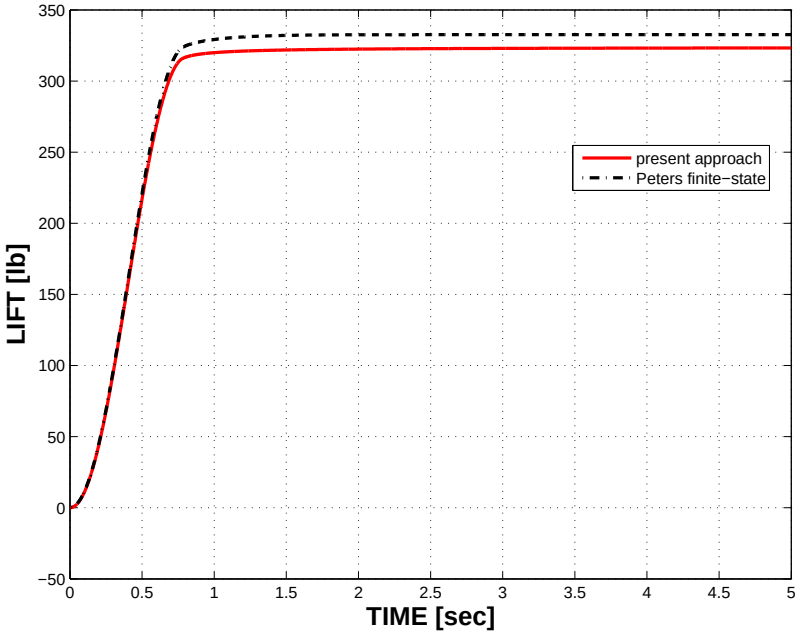

(a) time history of the lift

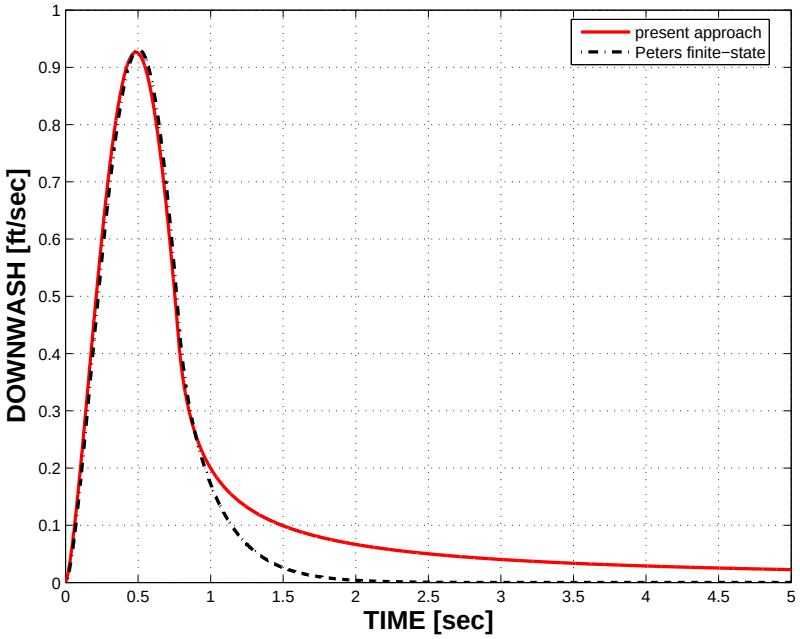

(b) time history of the downwash

Figure 69: 2D general airfoil, $\theta_0 = 0.0175$ rad, $C_\ell = 2\pi\alpha - 4.8\alpha^2$

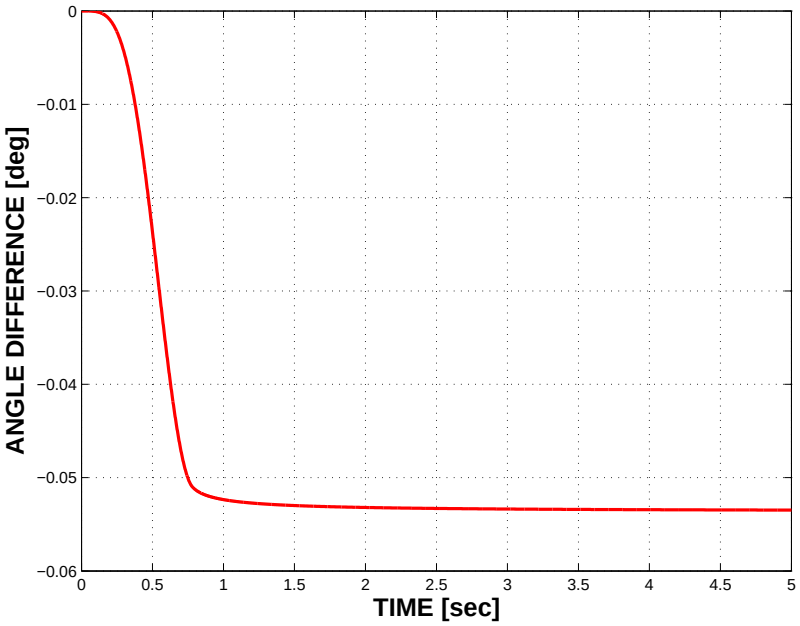

(a) angle difference between α and α^P

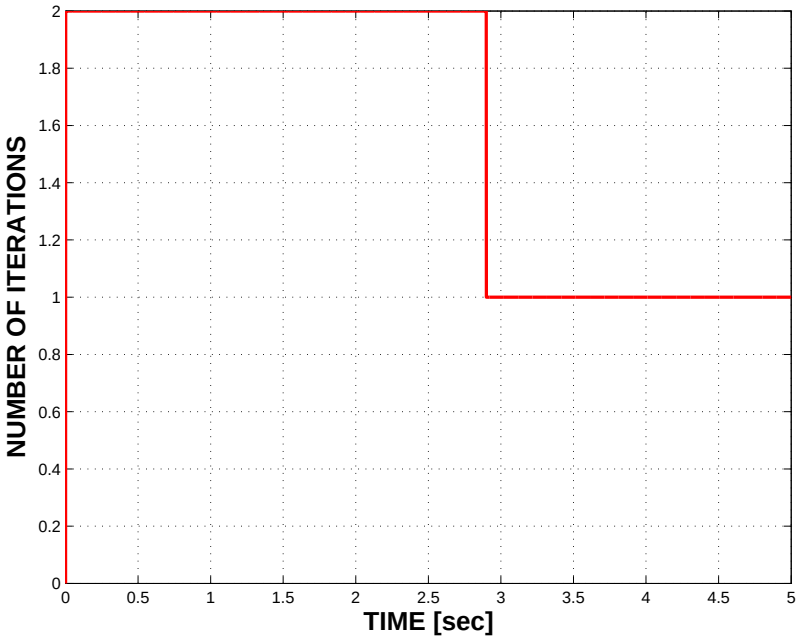

(b) the number of iterations in each time step

Figure 70: 2D general airfoil, $\theta_0 = 0.0175$ rad, $C_\ell = 2\pi\alpha - 4.8\alpha^2$

angle of attack reaches to 15 degrees. The other parameters are the same as those listed in Table 7. The simulation time is 5 seconds, and the time step size used in this analysis is $\Delta t = 0.001$ sec to achieve convergence. Fig. 71 to fig. 73 shows the results with a larger prescribed angle of attack. Same conclusions can be drawn from the figures shown here. Figure 72(a) shows that, as the effective angle of attack of the general airfoil reaches to about 15 degrees, the lift decreases by about 20% of the lift with the slope of the lift curve equal to 2π. Results obtained using Peters finite-state inflow model are shown here for reference only; indeed, linear aerodynamics are assumed in that case.

4.7.2 The Three-Dimensional Finite Wing

In this section, the first numerical example deals with a three-dimensional rigid finite wing with a prescribed vortex sheet behind the wing. The structure of the wake is prescribed. Next, examples considering the roll-up effect of vorticity in the far region behind a wing will be shown, that is, the vortex wake behind the wing is composed of a short, prescribed vortex sheet and a long free-vortex filament. In this example, free-vortex wake analysis is performed to test the validity of the present approach. Two flight conditions are investigated, level cruise flight and level maneuver flight.

4.7.2.1 3D Finite Wing with Prescribed Vortex Sheet

At first, consider a rigid finite wing with a rectangular planform, as depicted fig. (74), in an incompressible and inviscid flow in a level cruise flight condition. The pitching motion of the wing is given by

$$\theta(t) = \begin{cases} \theta_0(1 - \cos\omega t) & t \le \pi/\omega, \\ 2\theta_0 & t > \pi/\omega, \end{cases} \tag{174}$$

where θ_0 is the pitching magnitude and ω is the pitching rate. The parameters used in this analysis are listed in Table 8, where $S_0 = S/2$ is half-wing span, c is the chord length, U_∞ is the far-field free stream speed, and ρ is the air density.

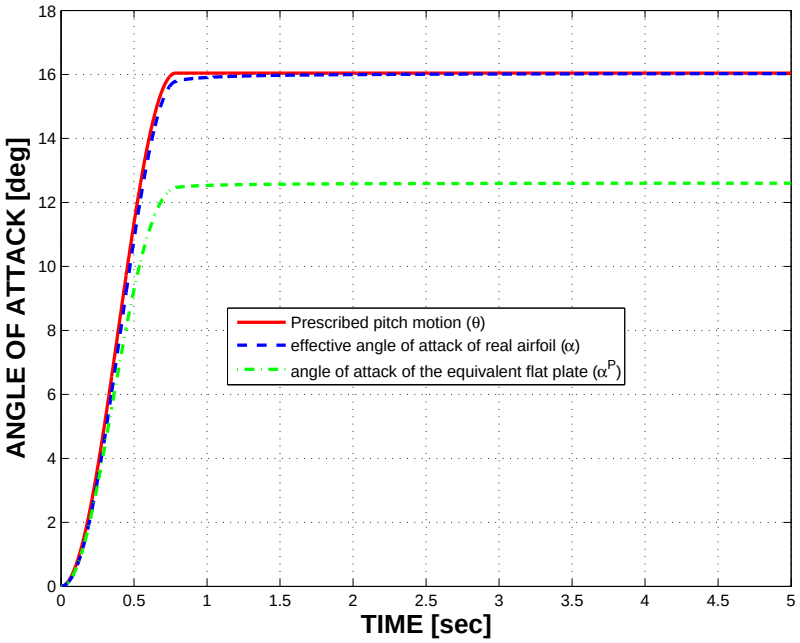

(a) time history of the angle of attack

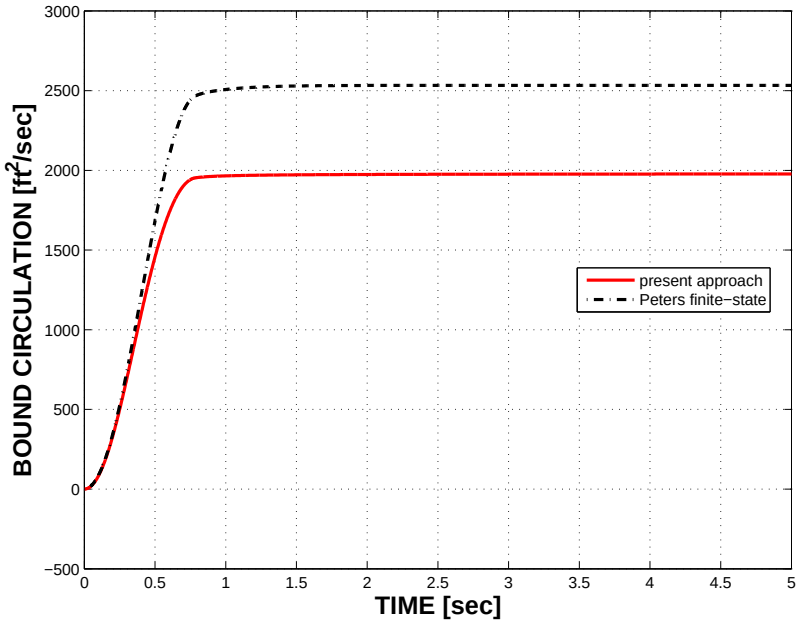

(b) time history of the circulation

Figure 71: 2D general airfoil, $\theta_0 = 0.14$ rad, $C_\ell = 2\pi\alpha - 4.8\alpha^2$

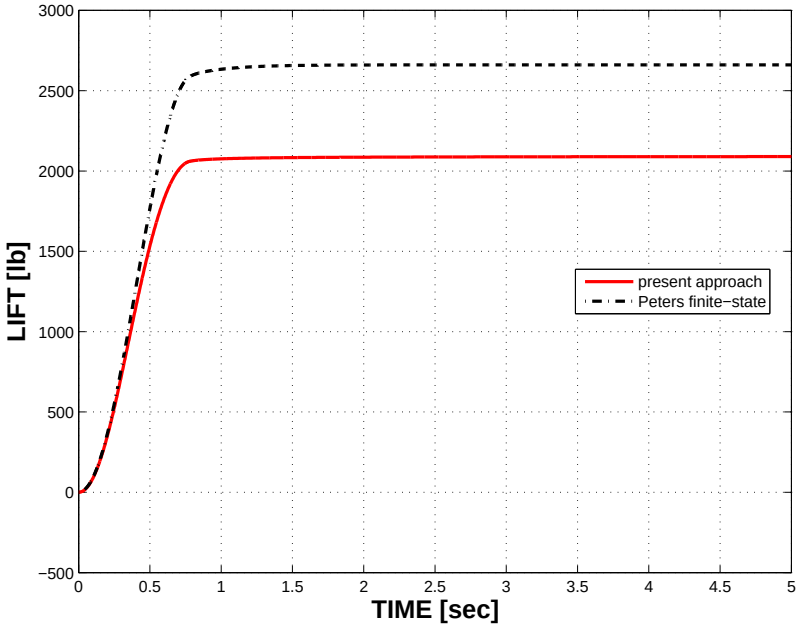

(a) time history of the lift

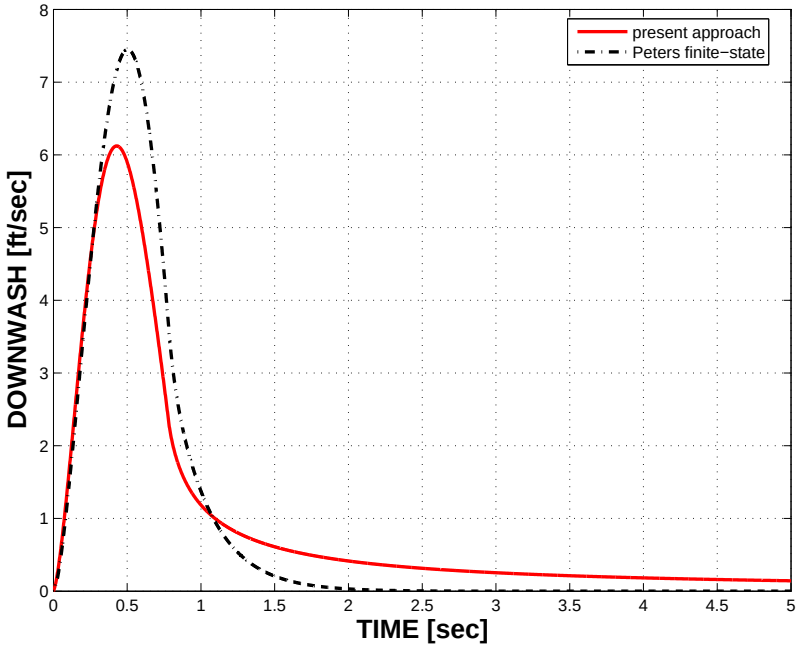

(b) time history of the downwash

Figure 72: 2D general airfoil, $\theta_0 = 0.14$ rad, $C_\ell = 2\pi\alpha - 4.8\alpha^2$

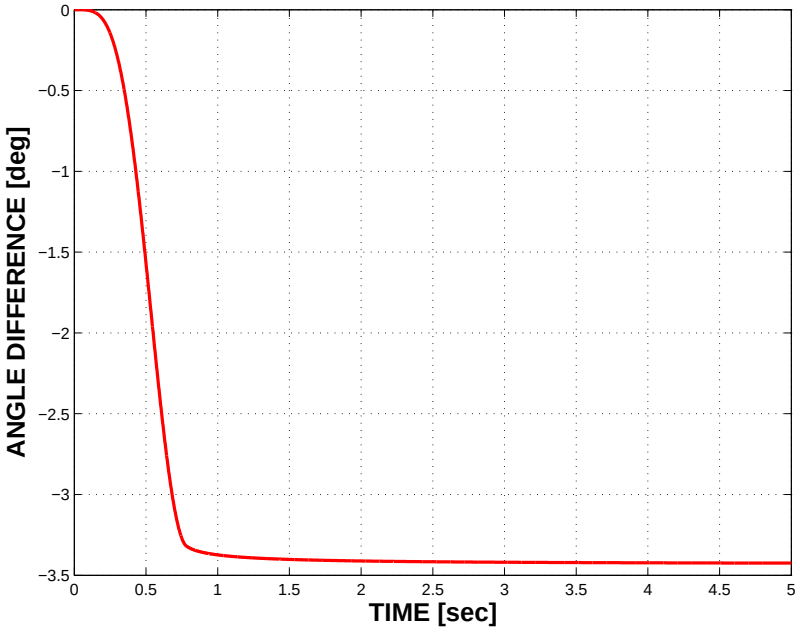

(a) angle difference between α and α^P

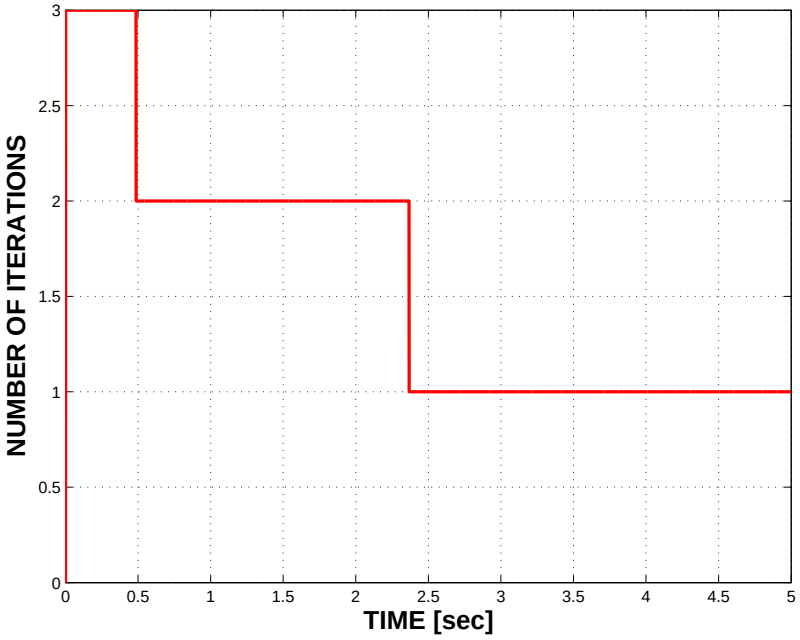

(b) the number of iterations in each time step

Figure 73: 2D general airfoil, $\theta_0 = 0.14$ rad, $C_\ell = 2\pi\alpha - 4.8\alpha^2$

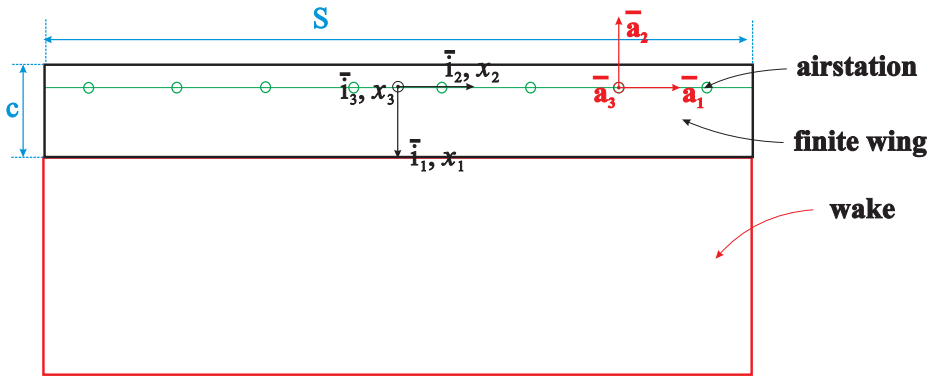

Figure 74: Geometry and system definition of a finite wing

Table 8: Parameters used in a 3D finite-wing analysis

S_0 [ft]	c [ft]	U_∞ [ft/sec]	ρ [lb/ft^3]	θ_0 [rad]	ω [rad/sec]
20	6	480	2.18810 $\times 10^{-3}$	0.105	5π

The lift coefficient at each station along the wing is given as follows

$$C_\ell(x_2) = 2\pi\alpha(x_2) + b\alpha(x_2)^2, \tag{175}$$

where α is the effective angle of attack at the span position x_2. Two values of coefficient b will be contrasted, as before, $b = 0$ and $b = -4.8$. The lift computed by the approach described in section 4.5.2.3 is compared with the Prandtl theory in section 4.5.2.2 for a rigid wing for which the number of the inflow states, N, is chosen to be 20, and Peters unsteady aerodynamic model and finite-state inflow model in which the number of the inflow states is chosen as 6. The time step size of this simulation is $\Delta t = 0.001$ sec.

- Wing cross section is a 2D thin airfoil

  Fig. 75 to fig. 77 shows the results of the finite wing with a prescribed wake solely composed of a long vortex sheet. The results shown here are the time history of the angle of attack, the lift at the root and tip of the wing, and the distribution along the wing span of the angle of attack and lift. The time

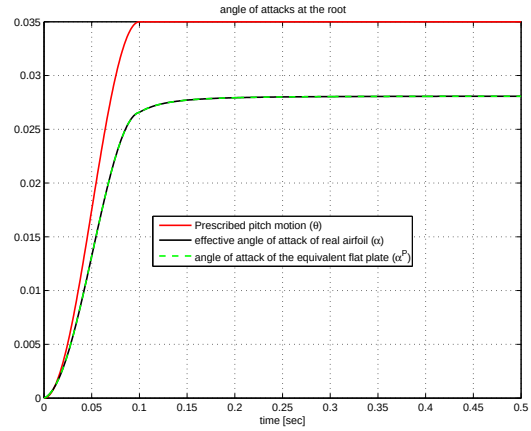

(a) time history of angles of attack at the root of the wing

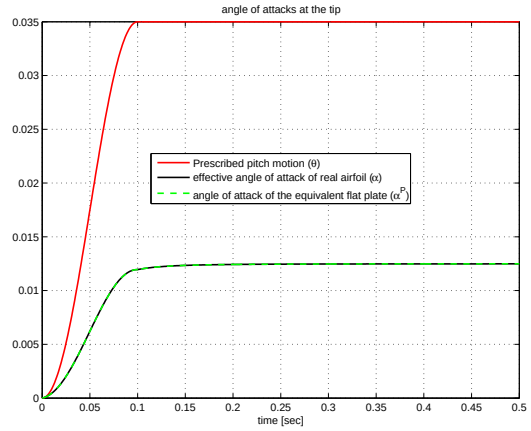

(b) time history of angles of attack at the tip of the wing

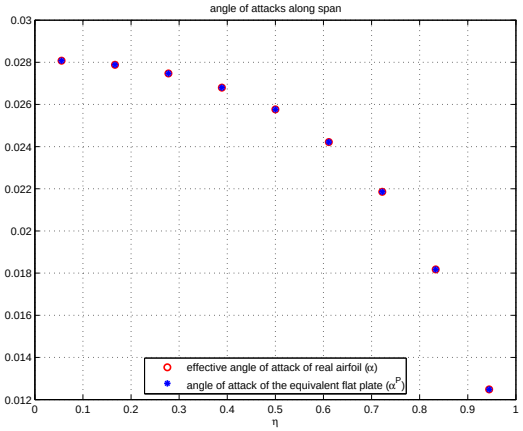

(c) angles of attack along span

Figure 75: Finite wing with thin airfoil section

history and distribution along the wing span of flat plate position β are also shown. Because the wing cross section is a 2D thin airfoil β is zero along the span, as seen in fig. 78.

- Wing cross section is a general airfoil

  The lift coefficient of such a general airfoil is determined by the eq. (175) with $b = -4.8$. Figures 79 to 82 shows the results of the finite wing with a prescribed wake solely composed of only a long vortex sheet. The results shown here are the time history of the angles of attack, the lift at the root and tip of the wing, and the distribution along the wing span of the angle of attack and lift. The

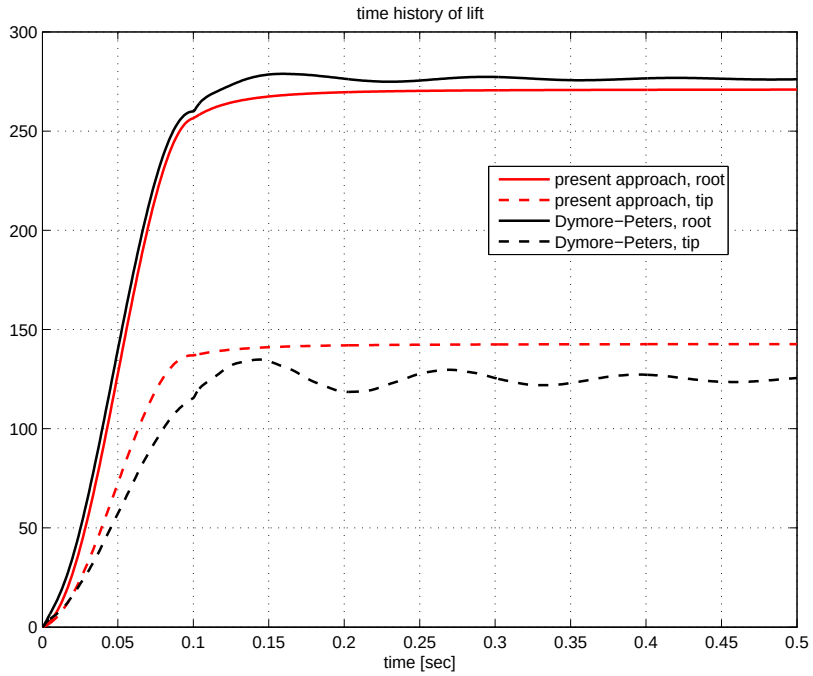

(a) time history of the lift

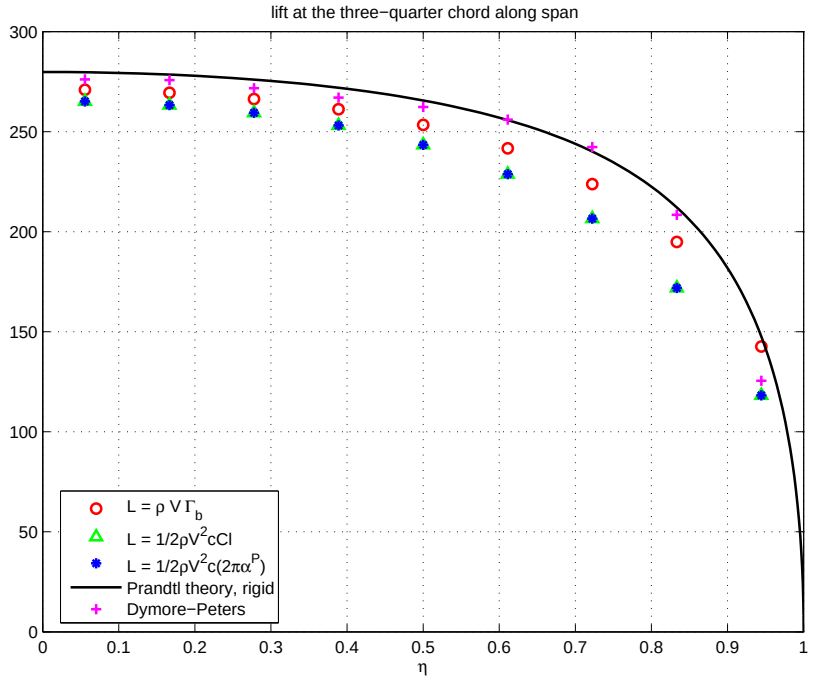

(b) lift along span

Figure 76: Finite wing with thin airfoil section

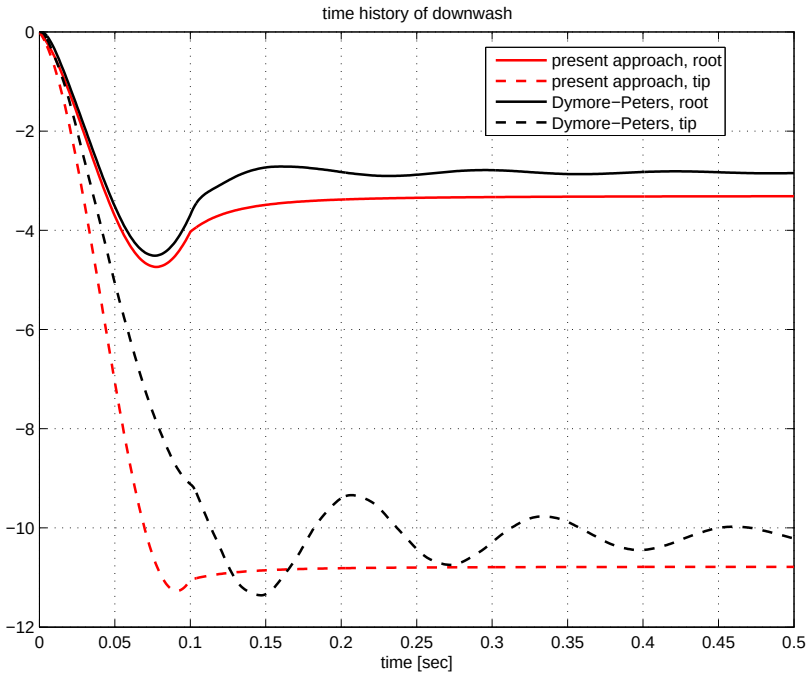

(a) time history of the downwash

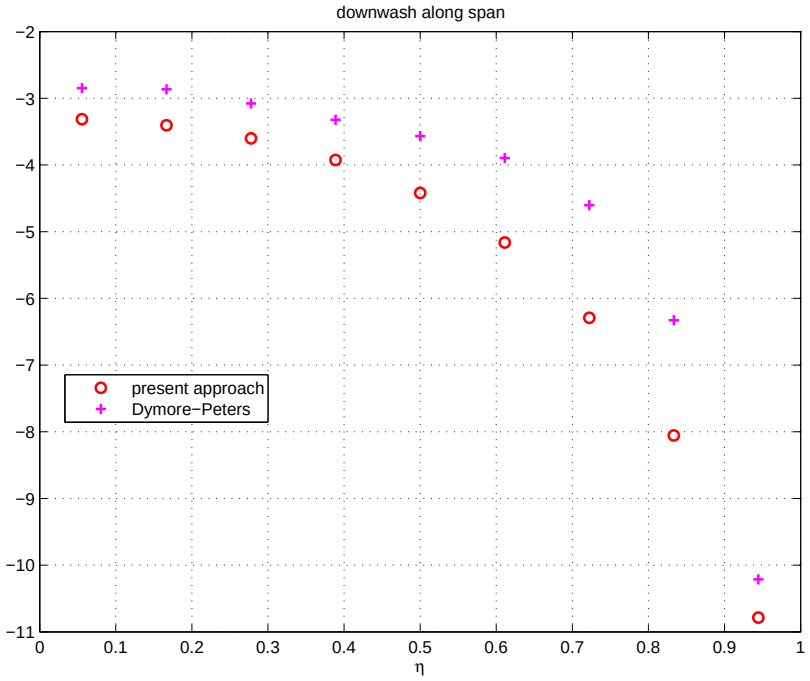

(b) downwash along span

Figure 77: Finite wing with thin airfoil section

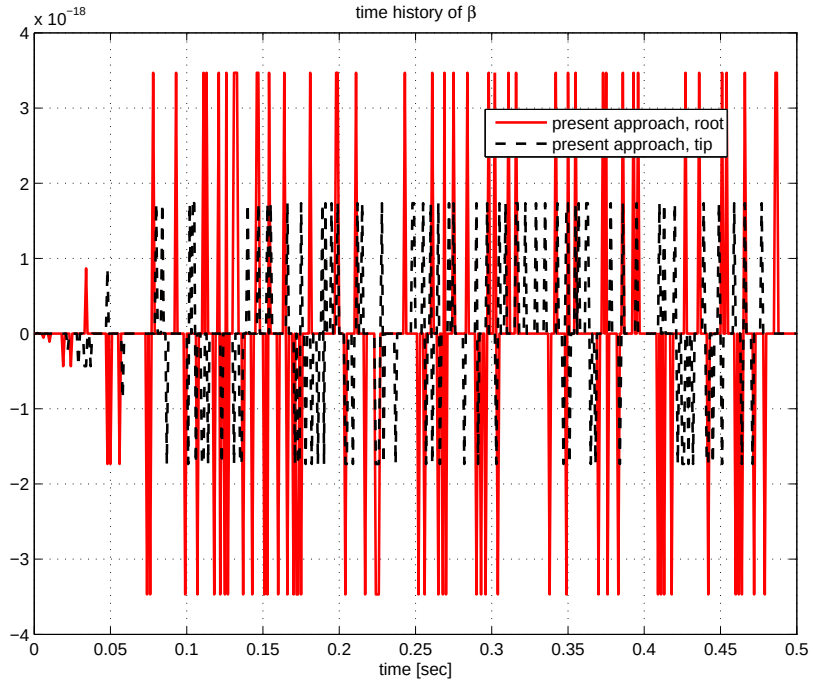

(a) time history of β at the root and tip of the wing

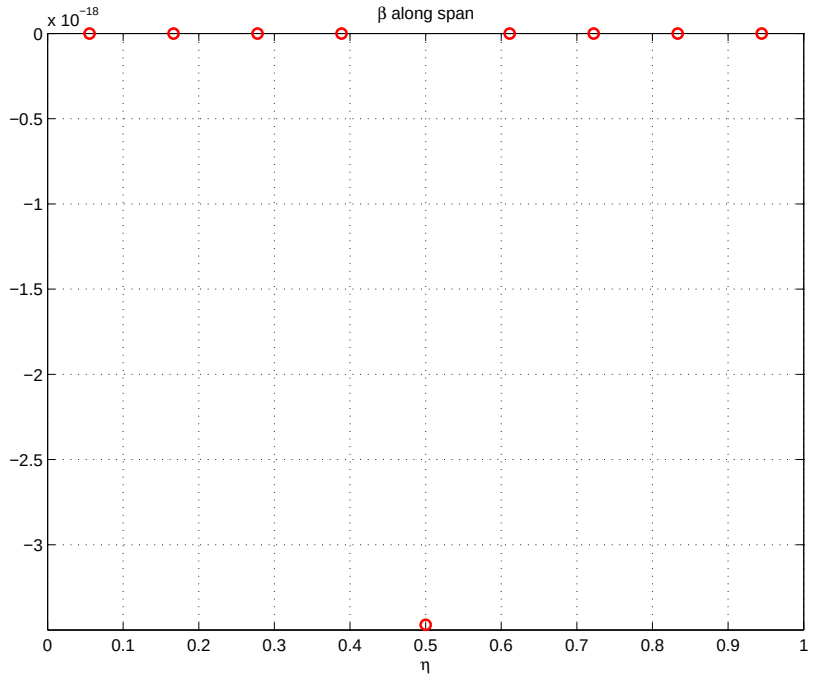

(b) β along span

Figure 78: Finite wing with thin airfoil section

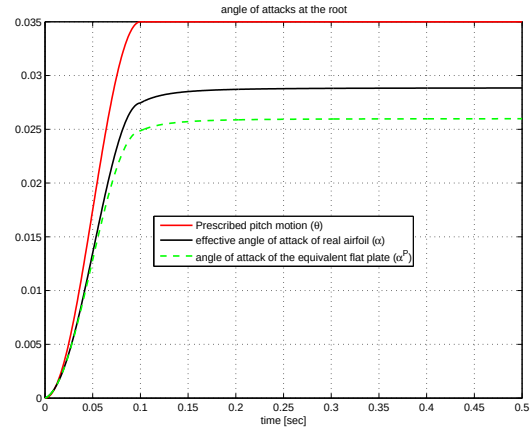

(a) time history of angles of attack at the root of the wing

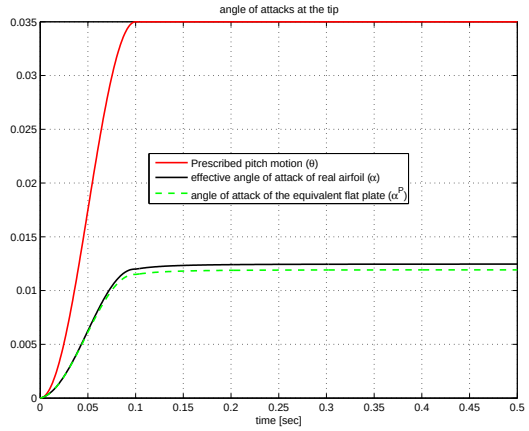

(b) time history of angles of attack at the tip of the wing

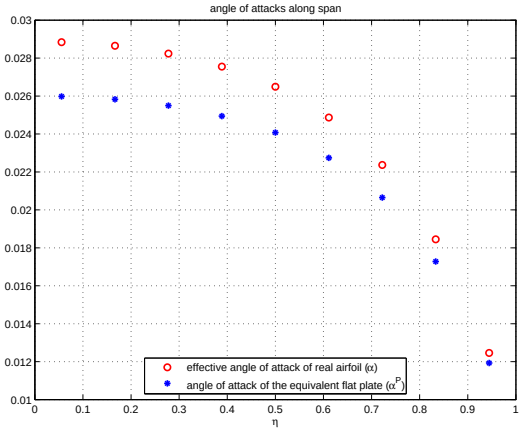

(c) angles of attack along span

Figure 79: Finite wing with general airfoil section

time history and distribution along the wing span of flat plate position β are also shown. At this time, the wing cross section is a general airfoil and β is not equal to zero and varies along the span , as seen in fig. 82.

4.7.2.2 3D Finite Wing with Prescribed Vortex Sheet and Free-Vortex Filament

This section deals with an analysis of a fixed-wing aircraft. The wing has a rectangular planform. The structural properties of the cantilevered wing are as follows: bending stiffness, $EI = 2.4 \times 10^{10}$ lbs·ft^2, torsional stiffness, $GJ = 2.4 \times 10^{10}$ lbs·ft^2, mass per unit span, $m = 0.75$ slugs/ft, polar moment of inertia, $I = 1.95$ slugs·ft. The airfoil quarter-chord is located at the elastic axis of the wing, and the center of mass

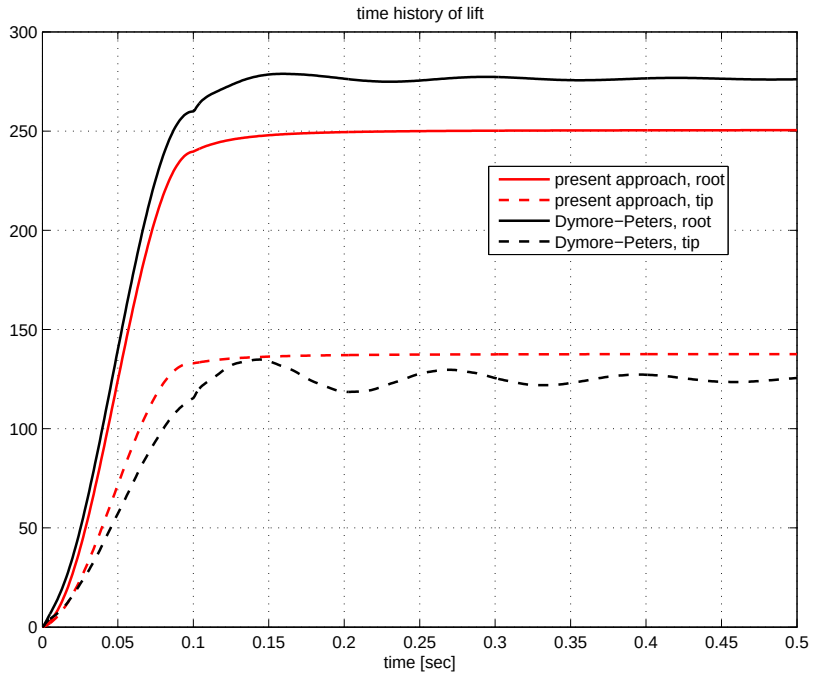

(a) time history of the lift

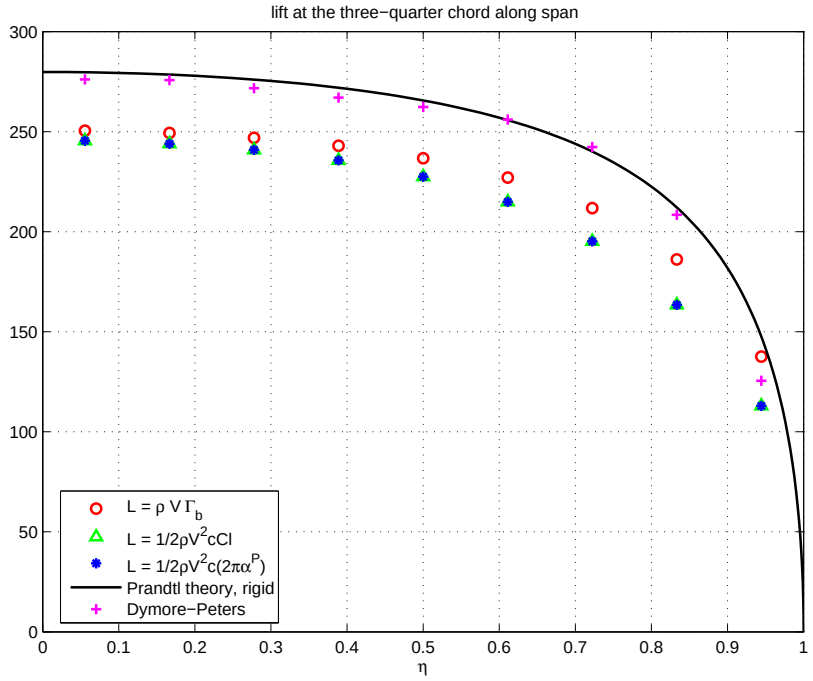

(b) lift along span

Figure 80: Finite wing with general airfoil section

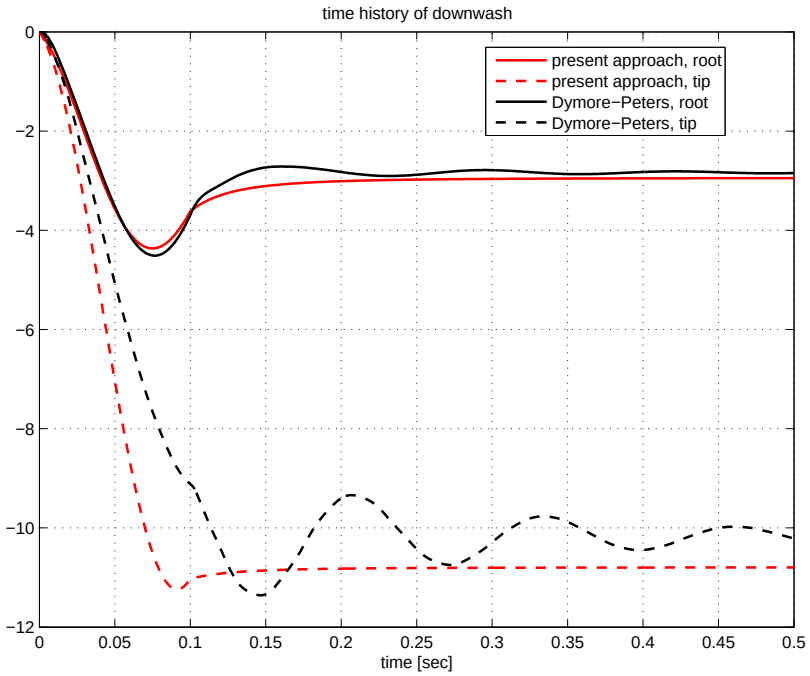

(a) time history of the downwash

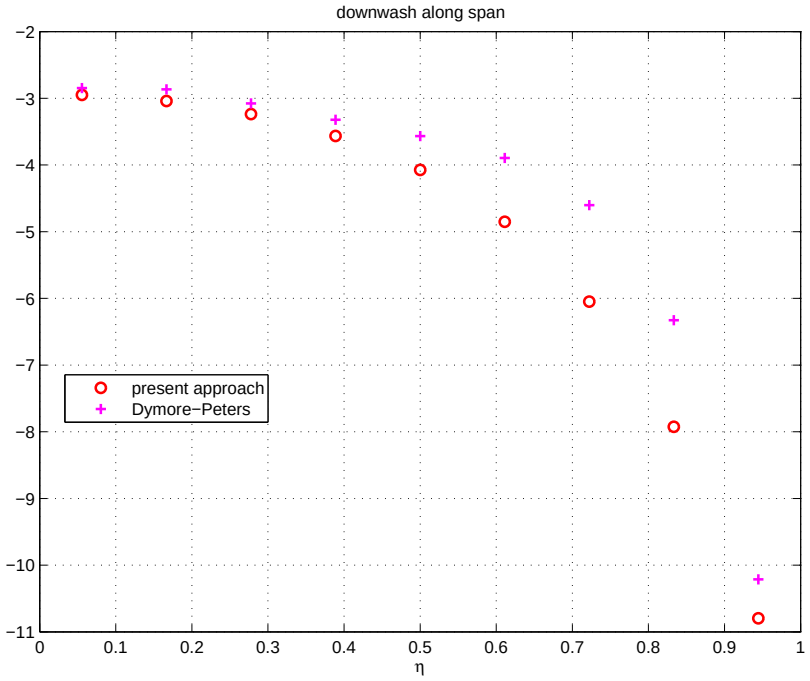

(b) downwash along span

Figure 81: Finite wing with general airfoil section

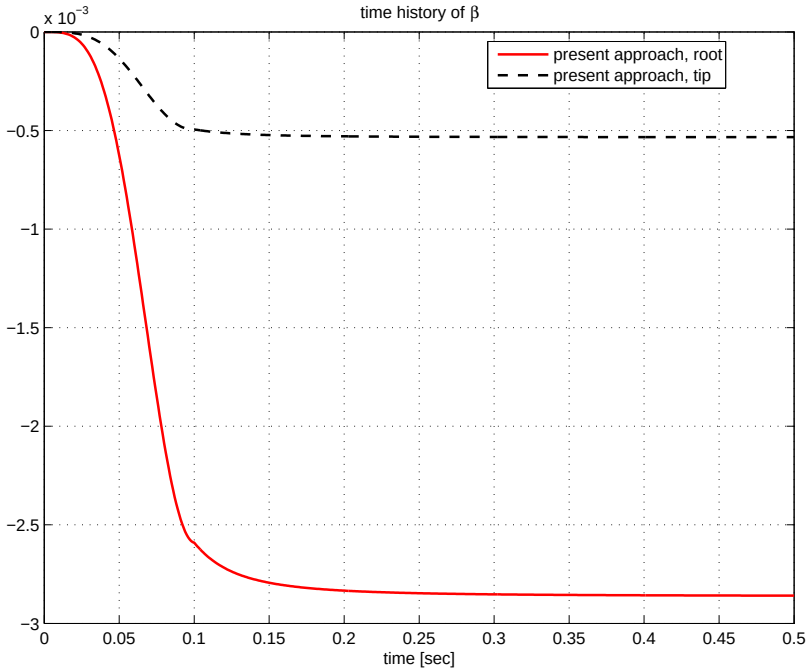

(a) time history of β at the root and tip of the wing

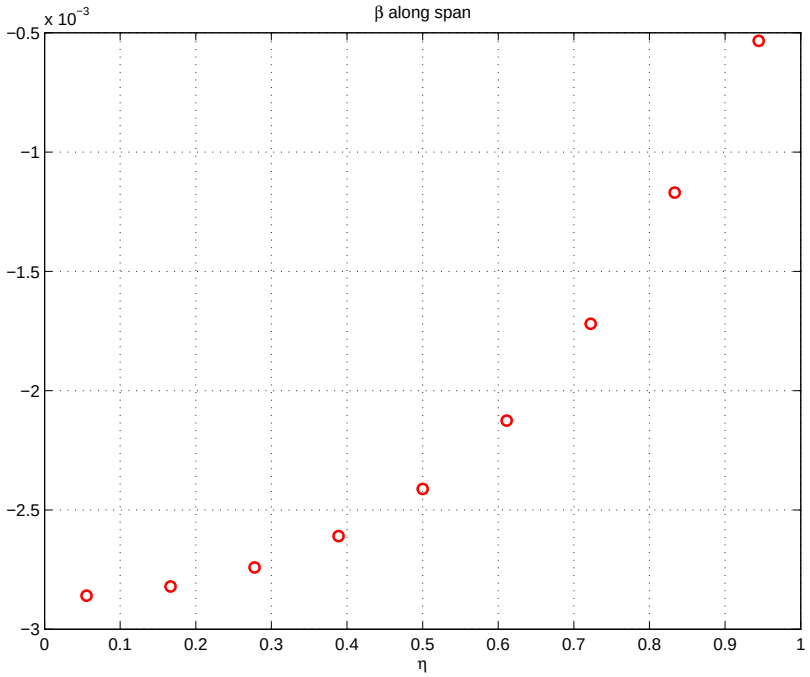

(b) β along span

Figure 82: Finite wing with general airfoil section

is located 0.6 ft aft the elastic axis of the wing. The wing span is modeled with two cubic beam elements.

Peters model is chosen as the two-dimensional unsteady aerodynamic model and the local inflow is computed using the proposed model. Airloads were computed at 9 stations, which are equally spaced along the wing span. In one case, a linear relationship between the lift coefficient and the effective angle of attack was used, and the moment coefficient about the quarter-chord was selected to zero. In the other case, the NACA0012 airfoil table was used to determine the lift coefficient. For the maneuver case, pure rolling motion and the combination of rolling and pitching were considered together with the proposed wake model. The parameters used in this analysis are given in Table 9.

Table 9: Parameters used in a fixed-wing aircraft analysis

S_0 [ft]	c [ft]	U_∞ [ft/sec]	ρ [lb/ft^3]
20	6	480	2.18810 $\times 10^{-3}$

1. **Level Cruise Flight**

   - The lift coefficient of the airfoil of the wing is constant and equal to 2π. The pitching motion of the wing is given as

$$\theta(t) = \begin{cases} \theta_0(1 - \cos\omega t), & t \leq \pi/\omega, \\ 2\theta_0, & t > \pi/\omega, \end{cases} \tag{176}$$

     where the pitching amplitude $\theta_0 = 0.0175$ rad and the pitching rate $\omega = 5\pi$ rad/sec. Figures. 83 and 84 shows the predicted effective angle of attack, lift, circulation, and inflow at three different locations, the root, mid-span, and tip of the wing.

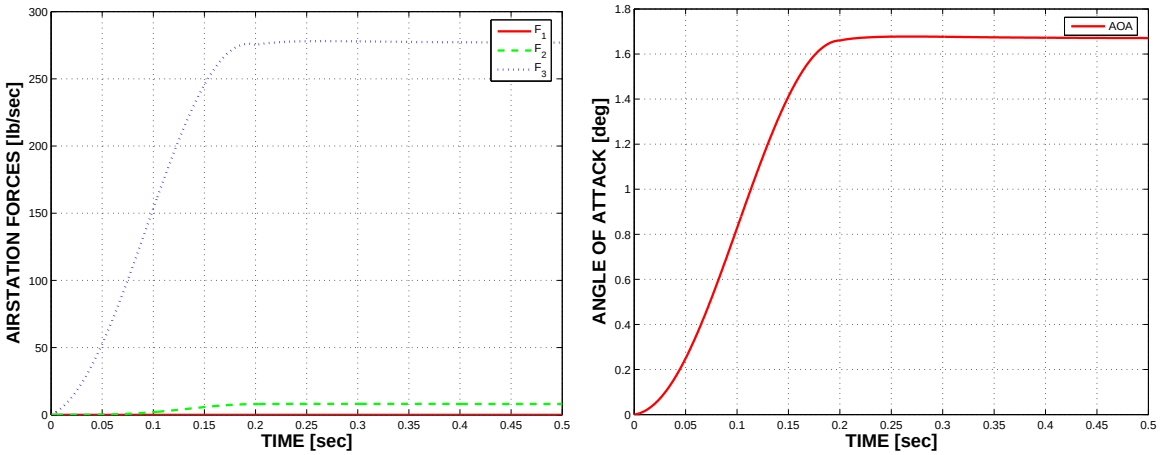

(a) at the root of the wing

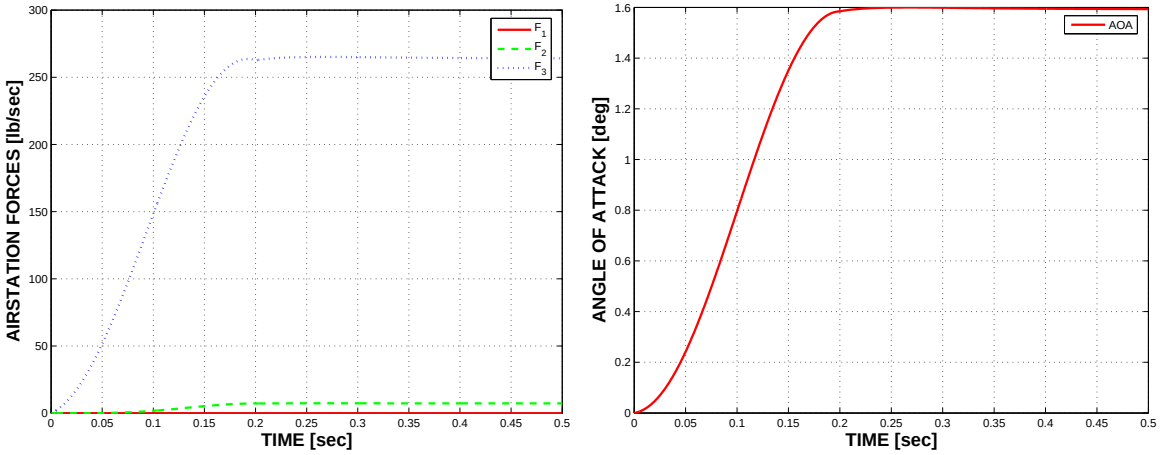

(b) at the mid-span of the wing

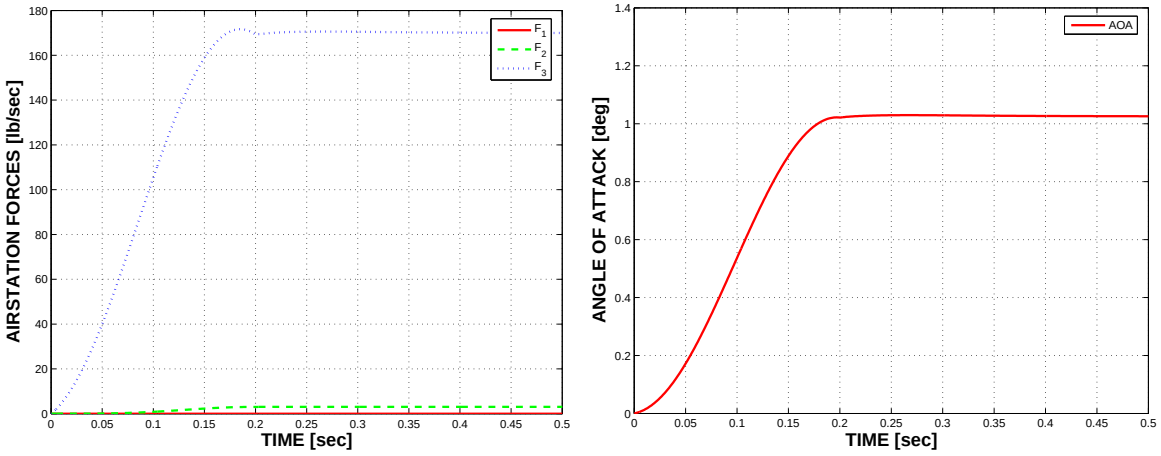

(c) at the tip of the wing

Figure 83: Constant lift coefficient: effective angle of attack and lift at different locations

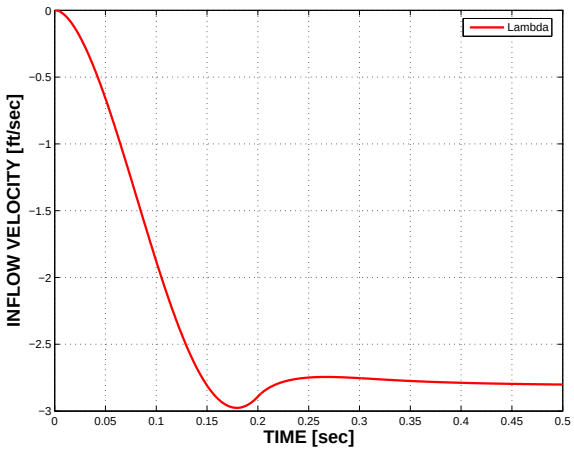

(a) at the root of the wing

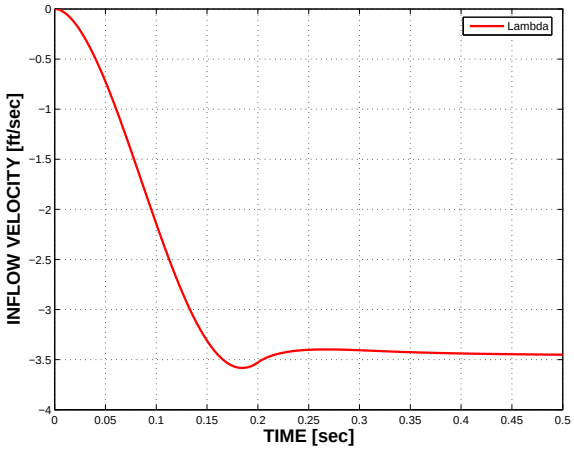

(b) at the mid-span of the wing

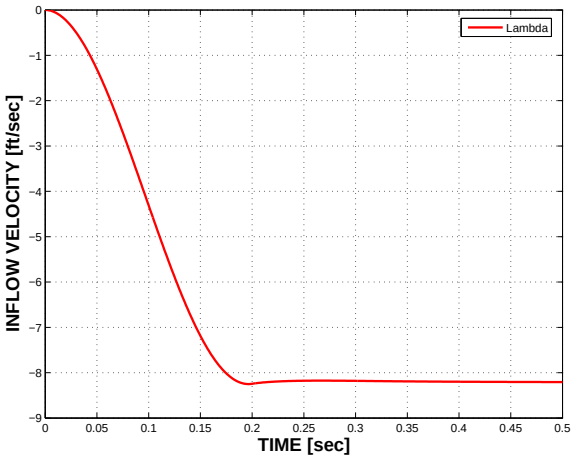

(c) at the tip of the wing

Figure 84: Constant lift coefficient: downwash at different locations

- The aerodynamic coefficients of the airfoil are given by the NACA0012 airfoil table.

  The pitching motion of the wing is given as

$$\theta(t) = \begin{cases} \theta_0(1 - \cos\omega t), & t \leq \pi/\omega, \\ 2\theta_0, & t > \pi/\omega, \end{cases} \tag{177}$$

  where the pitching amplitude $\theta_0 = 0.105$ rad and the pitching rate $\omega = 5\pi$ rad/sec. Figs. 85 and 86 show the angle of attack, lift, and downwash at the root, mid-span, and the tip of the wing.

2. **Steady Maneuver Flight**

- Maneuver with pure rolling motion

  The rolling motion of the aircraft is defined as

$$\phi(t) = 4\pi t. \tag{178}$$

  The aerodynamic coefficients are given by an airfoil table, NACA0012. Figures 87 and 88 show the result obtained from the present approach. When the aircraft rolls with a constant rotation speed, the induced flow due to the wake behind the wings reached a steady values and the wing loading becomes constant in time, which can be observed in the figures. Note that the results at the beginning of the simulation are associated with the onset of the maneuver, when the wake has not yet reached its final, steady configuration.

- Maneuver with rolling and pitching motion

  The rolling motion of the aircraft is given as

$$\phi(t) = \begin{cases} \phi_0(1 - \cos\omega_r t) & t \leq \pi/\omega_r, \\ 2\phi_0, & t > \pi/\omega_r, \end{cases} \tag{179}$$

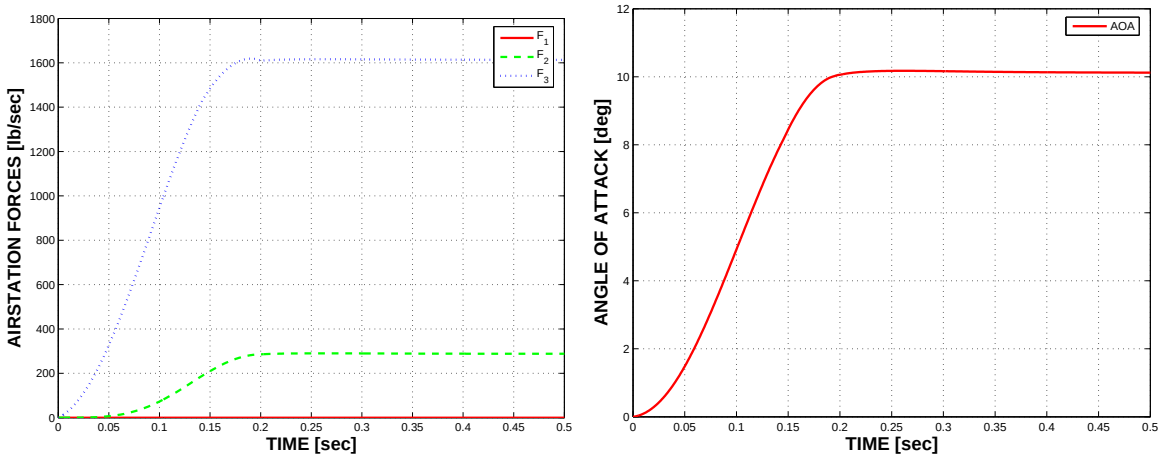

(a) at the root of the wing

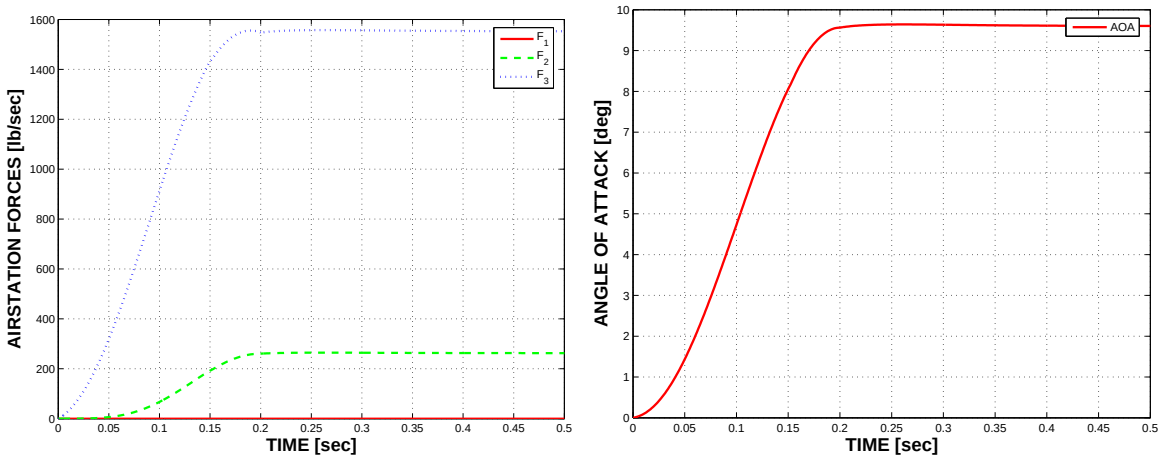

(b) at the mid-span of the wing

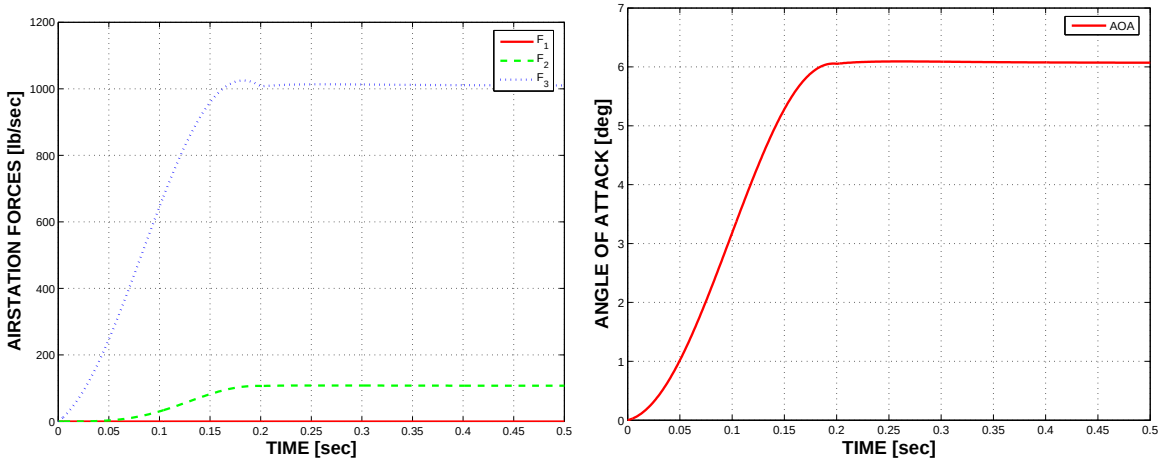

(c) at the tip of the wing

Figure 85: Lift coefficient is given by an airfoil table: effective angle of attack and lift at different locations

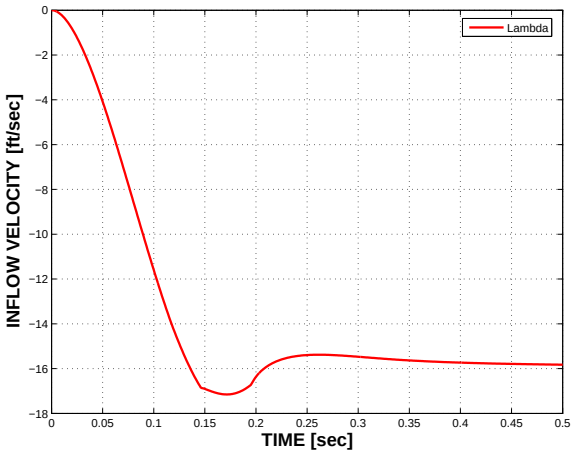

(a) at the root of the wing

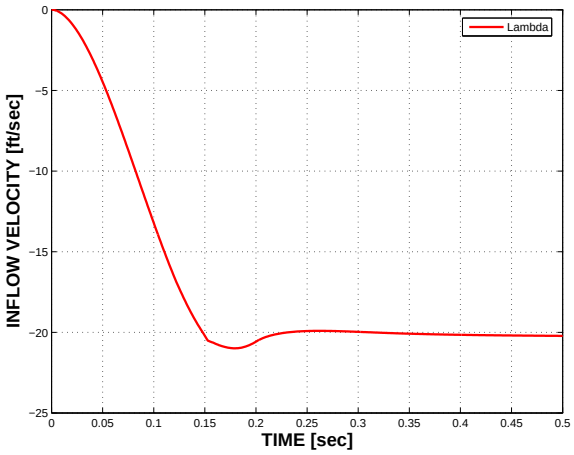

(b) at the mid-span of the wing

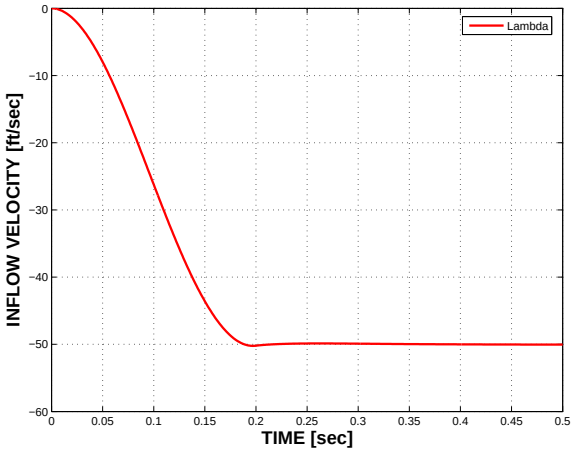

(c) at the tip of the wing

Figure 86: Lift coefficient is given by an airfoil table: downwash at different locations

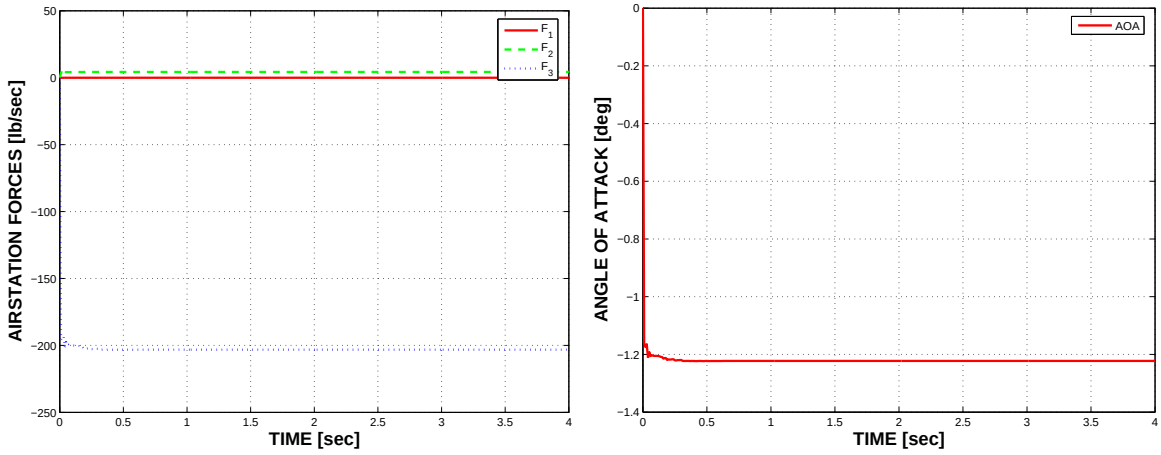

(a) at the root of the wing

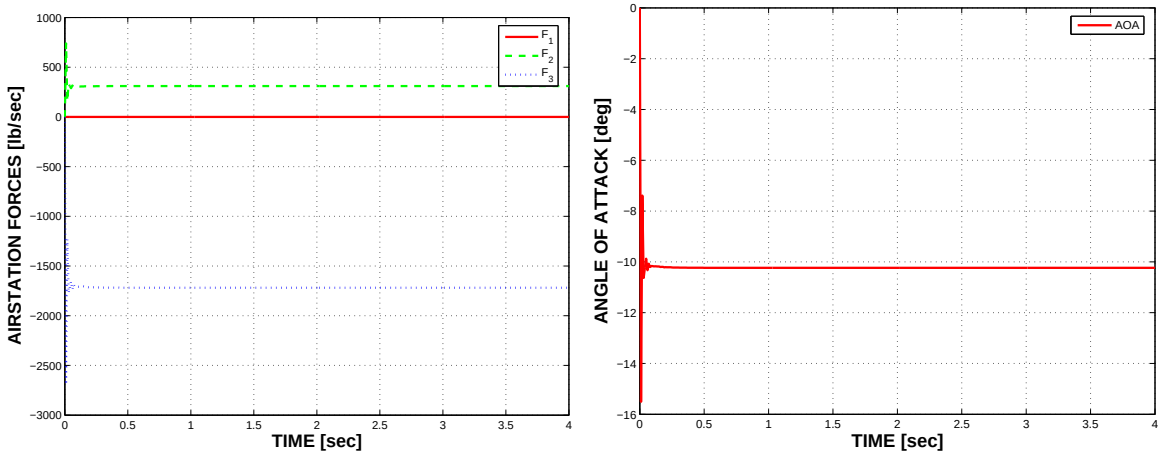

(b) at the mid-span of the wing

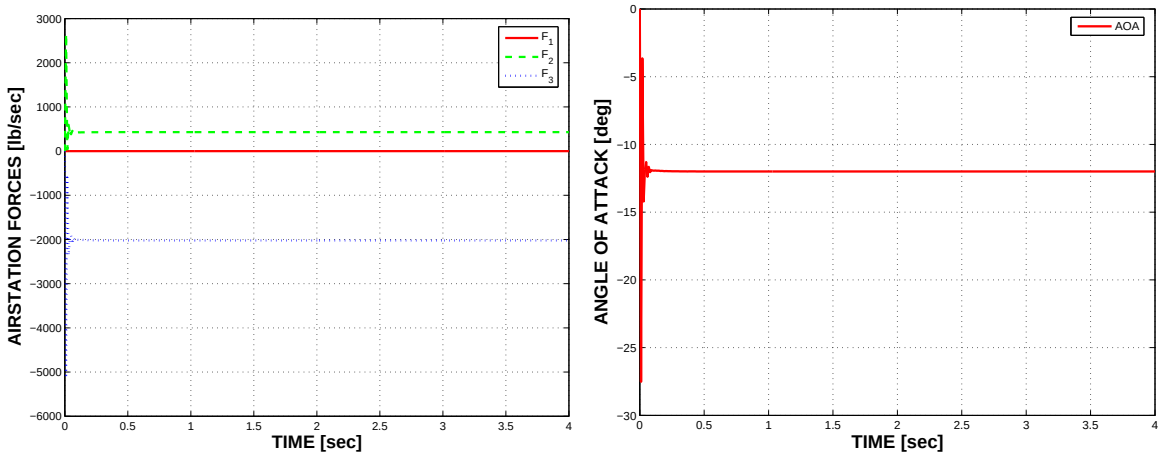

(c) at the tip of the wing

Figure 87: Pure roll motion: effective angle of attack and lift at different locations

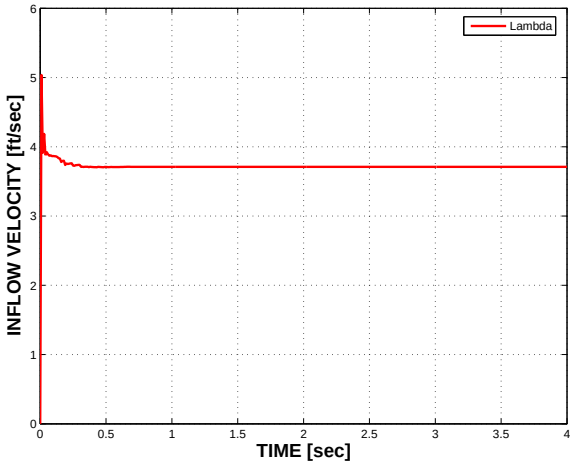

(a) at the root of the wing

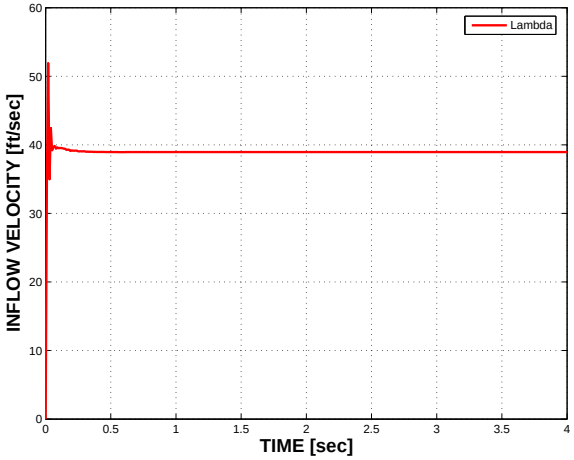

(b) at the mid-span of the wing

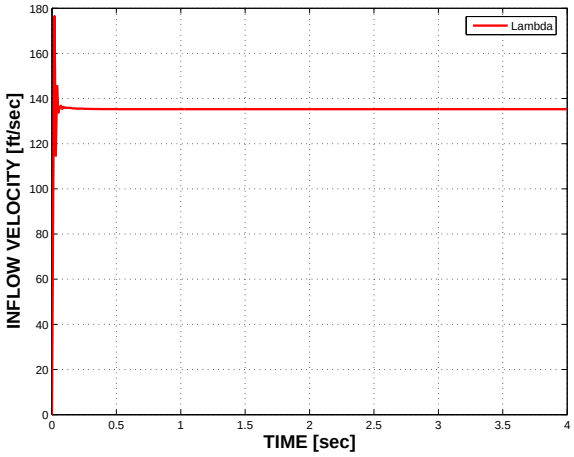

(c) at the tip of the wing

Figure 88: Pure roll motion: downwash at different locations

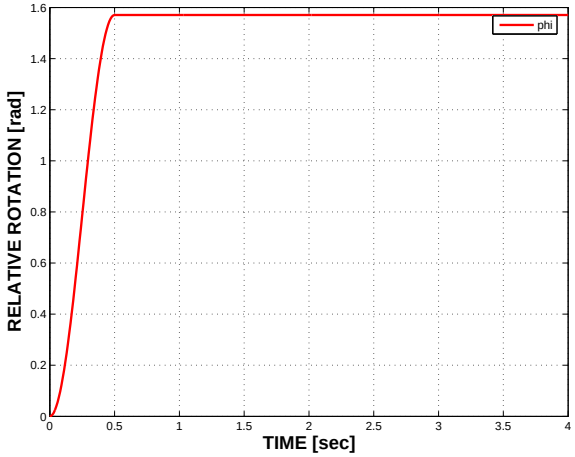

(a) Prescribed rolling motion

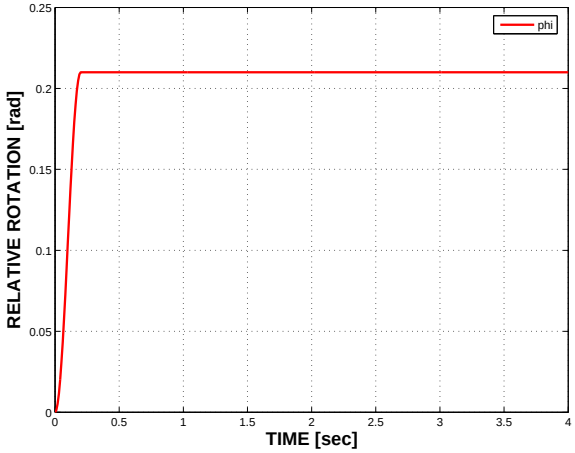

(b) Prescribed pitching motion

Figure 89: Prescribed motions of the fixed-wing aircraft

where the rolling amplitude $\phi_0 = 0.785398$ rad, the rolling rate $\omega_r = 2\pi$, and when $t \geq 0.5$ sec, $\phi(t) = \phi(0.5)$. The pitching motion of the aircraft is given as

$$\theta(t) = \begin{cases} \theta_0(1 - \cos\omega_p t) & t \leq \pi/\omega_p, \\ 2\theta_0, & t > \pi/\omega_p, \end{cases} \tag{180}$$

where the pitching amplitude $\theta_0 = 0.105$ rad, the pitching rate $\omega_p = 5\pi$ rad/sec, and when $t \geq 0.2$ sec, $\theta(t) = \theta(0.2)$. The prescribed rolling and pitching motions are plotted in fig. 89. The aerodynamic coefficients are obtained from a NACA0012 airfoil table. Figure 90 shows the time history of the lift and angle of attack at three different locations along the wing, whereas fig. 91 gives the corresponding downwash along the wing span.

4.8 Conclusions

This chapter presented the development and validation of inflow models based on vortex methods. The geometry of the wake has been represented by NURBS curves and surfaces to model vortex filaments and sheets. In this work, the vorticity transportation equation is solved using central difference algorithm. The integration of the Biot-Savart law has been performed by using Gaussian quadrature combined with Chebyshev approximation technique to obtain the vorticity distribution in the wake. The wake model was implemented in a comprehensive aeroelastic tool. The following conclusions can be drawn from this analysis.

1. A formulation of vortex wake problems based on a NURBS representation of the curves and surfaces characterizing the wake structure was developed and implemented. The equations of motion characterizing the NURBS description of vortex filaments were derived and solved using central difference integration schemes.

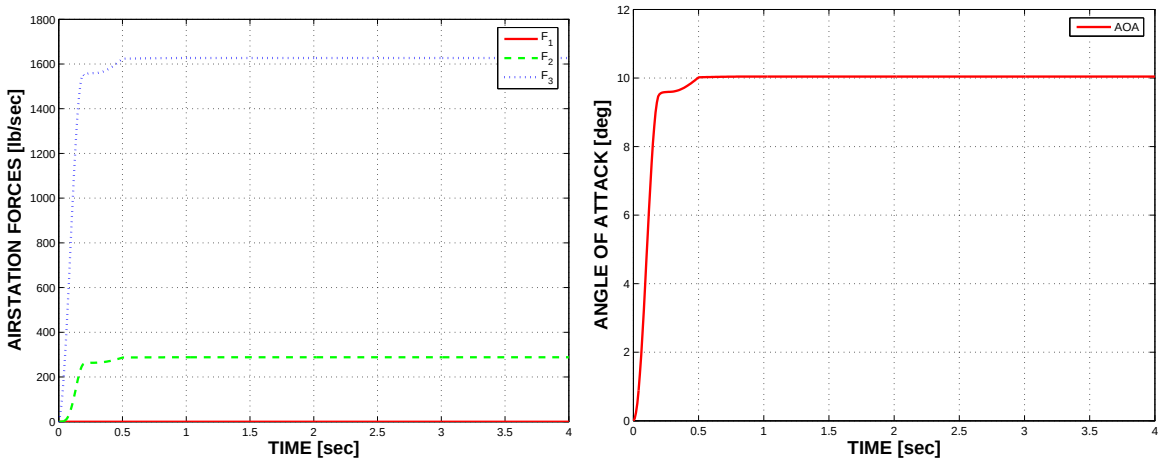

(a) at the root of the wing

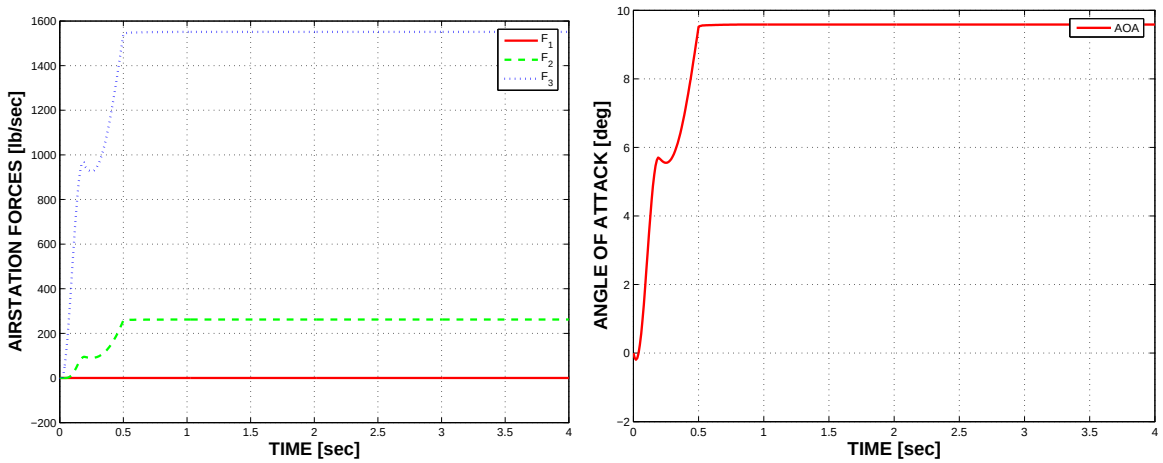

(b) at the mid-span of the wing

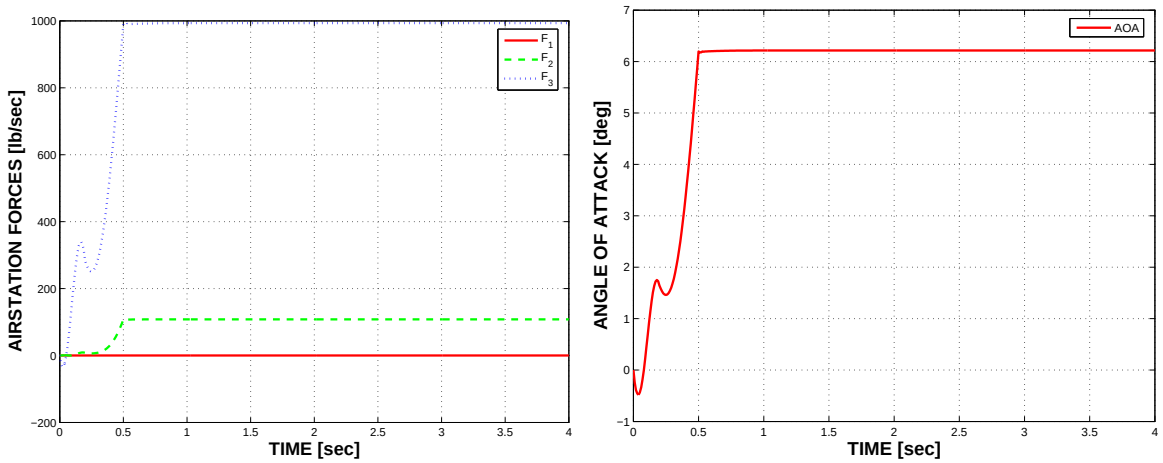

(c) at the tip of the wing

Figure 90: Roll and pitch motion: effective angle of attack and lift at different locations

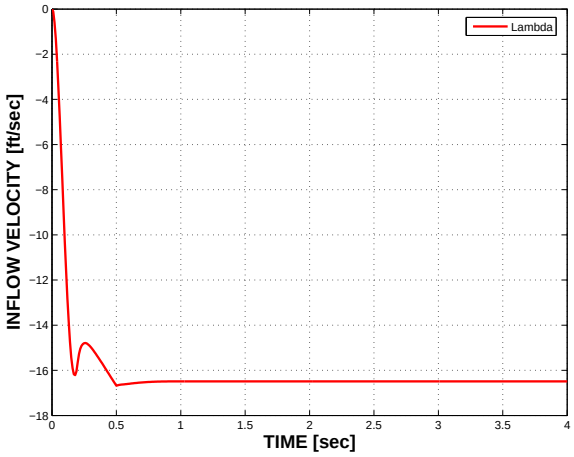

(a) at the root of the wing

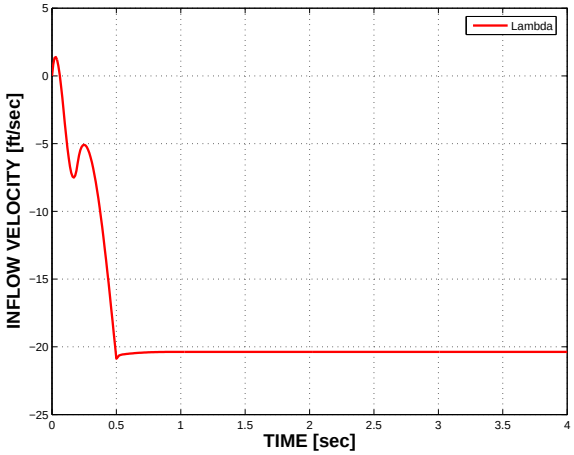

(b) at the mid-span of the wing

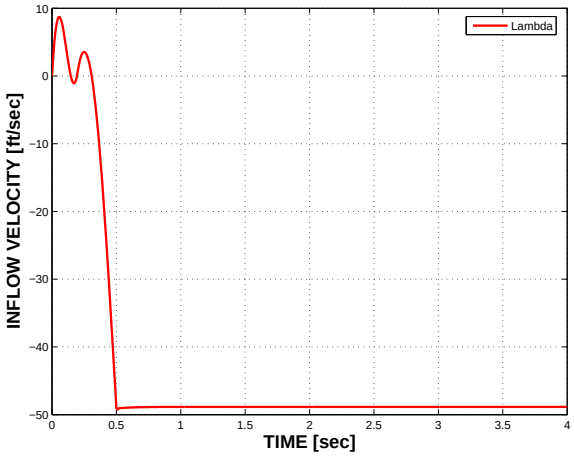

(c) at the tip of the wing

Figure 91: Roll and pitch motion: downwash at different locations

2. Chebyshev polynomials were used to approximate the circulation distribution along the vortex filaments and over vortex sheets. These one- and two-dimensional Chebyshev approximations of circulations, together with the NURBS representation of the geometry of the problem, provide a continuous, rather than discrete, representation of the problem.

3. With continuous representations of the problem, Gaussian quadrature or other integration schemes can be used to evaluate the integral of the Biot-Savart law over vortex filaments and sheets. These techniques promise great computational efficiency gains when compared to the tradition application of Biot-Savart law to discrete, straight vortex segments.

4. Two-dimensional, unsteady aerodynamic theory was used to predict the lift and pitching moments on the airfoil. The concept of equivalent flat plate airfoil was used to enable the use of table look-up procedures, accommodating the use of wind tunnel measured data.

5. Both prescribed and free-wake models were developed and implemented. The models are successfully validated through the numerical example of a fixed wing aircraft with rectangular wing in cruise flight and steady maneuver flight conditions. The results of cruise flight are compared with the results based on Peters finite-state, dynamic inflow model. In both cases, the predictions of the proposed free-wake approach agree with those of the dynamic inflow model.

CHAPTER V

CONCLUSIONS AND FUTURE WORK

This chapter summarizes the work presented in this thesis and the the majors conclusions that can be drawn. Several issues to be investigated in the future are also recommended.

5.1 Conclusions

This thesis has focused on three area pertaining the comprehensive analysis of rotorcraft: the modeling hydraulic dampers and actuators, the coupling between computational fluid dynamics and computational structural dynamics codes, and a novel formulation of prescribed and free-wake models for fixed and rotary-wing aircraft. This section summarizes the work done in each area and the main accomplishments of the thesis.

5.1.1 Physics-based Hydraulic Component Modeling

1. A methodology allowing physics based modeling of hydraulic devices within multibody-based comprehensive models of rotorcraft systems was developed.

2. The new mathematical models of hydraulic devices were implemented in a multibody code and calibrated by comparing their predictions with bench test measurements. While predicted peak damping forces were found to be in good agreement with measurements, the model did not predict the entire time history of damper force to the same level of accuracy.

3. The validated model of the UH-60 lead-lag damper model was coupled with a

comprehensive model of the rotor system. Measured aerodynamic loads were applied to the blade and predicted damper forces were compared with experimental measurements. A marked improvement in the prediction was observed when using the proposed model rather than a linear approximation of the damper behavior.

4. The proposed model also evaluates relevant hydraulic quantities such as chamber pressures, orifice flow rates, and pressure relief valve displacements. Hence, the present model could be used to design lead-lag dampers presenting desirable force and damping characteristics.

5.1.2 Fluid-Structure Interface

1. An aerodynamic interface was developed that enables the loose coupling between computational fluid dynamics and computational structural dynamics codes. The proposed coupling strategy was implemented and validated using DYMORE, a finite element method based multibody dynamics formulation, and OVERFLOW-2, a Navier-Stokes equation solver based on the NASA OVERFLOW code, which uses overset structured grids to accommodate arbitrarily complex geometries.

2. A delta-airloads method was employed to improve the convergence of the loose coupling approach.

3. The resulting aeroelastic simulations were validated by comparing the predicted response of the UH-60 aircraft for different flight conditions, such as high-speed and high-altitude flights. Measured airloads, strain gage data and performance indices were compared with their predicted counterparts.

4. The loose coupling approach converges quickly in terms of aerodynamic loads and control angles. The predicted airloads agreed well with the experimental

data. The predicted of normal forces and pitch moments were found to be in good agreement with experimental data, but some peak values could not be recovered using the proposed loose coupling approach.

5.1.3 NURBS-based Vortex Wake Modeling

1. A formulation of vortex wake problems based on a NURBS representation of the curves and surfaces characterizing the wake structure was developed and implemented. The equations of motion characterizing the NURBS description of vortex filaments were derived and solved using central difference integration schemes.

2. Chebyshev polynomials were used to approximate the circulation distribution along the vortex filaments and over vortex sheets. These one- and two-dimensional Chebyshev approximations of circulations, together with the NURBS representation of the geometry of the problem, provide a continuous, rather than discrete, representation of the problem.

3. With continuous representations of the problem, Gaussian quadrature or other integration schemes can be used to evaluate the integral of the Biot-Savart law over vortex filaments and sheets. These techniques promise great computational efficiency gains when compared to the tradition application of Biot-Savart law to discrete, straight vortex segments.

4. Two-dimensional, unsteady aerodynamic theory was used to predict the lift and pitching moments on the airfoil. The concept of equivalent flat plate airfoil was used to enable the use of table look-up procedures, accommodating the use of wind tunnel measured data.

5. Both prescribed and a free-wake models were developed and implemented. The models are successfully validated through the numerical example of a fixed

wing aircraft with rectangular wing in cruise flight and steady maneuver flight conditions. The results of cruise flight are compared with the results based on Peters finite-state, dynamic inflow model. In both cases, the predictions of the proposed free-wake approach agree with those of the dynamic inflow model.

5.2 Future Work

The accurate and efficient wake model plays a critical role in the aerodynamic performance of aircrafts. Although the proposed NURBS-based vortex model has been validated for fixed-wing aircraft, the proposed approach for free-wake modeling should be tested for rotorcraft problems. This is the first recommendation for future work. In spite of the accomplishments that have been made, other issues require further considerations.

1. The use of Biot-Savart law to calculate the velocity induced often encounters singularities, or near-singularities. Efficient procedures for dealing with this problem should be developed and implemented.

2. In the proposed approach, many parameters will impact the accuracy and efficiency of the computational scheme: the number of the control points used to define NURBS curves and surfaces, the order of the NURBS curves, the order of the Chebyshev polynomials, and the number of the Gaussian points. It is necessary to perform parametric studies to investigate the effect of these parameters and recommend optimal values. Other integration schemes should also be investigated.

3. The computational efficiency of the proposed approach must be compared with that of the classical formulations. Prior to this evaluation, optimal values of the parameters involved in the proposed approach must be determined.

APPENDIX A

KINEMATICS OF AERODYNAMIC INTERFACE

A.1 Details of the kinematics interface

The kinematics interface involves the computation of the airstation configuration, including positions or displacements and velocities. These quantities could be computed in the inertial frame, or, more often than not, in the hub frame. Figure 92 shows a lifting line and associated airstations in the reference and present configurations. The components of the position vector of the hub frame, $\mathcal{F}^H$, with respect to the inertial frame, $\mathcal{I}$, measured in the inertial frame, are denoted $\underline{u}_h$. The components of the rotation tensor that brings triad $\mathcal{B}$ to triad $\mathcal{B}^H$, measured in the inertial frame $\mathcal{I}$, are denoted R_h. Similar notations are used to the position and orientation of an airstation. Finally, the superscript $(\cdot)^0$ indicates that a quantity is evaluated in the reference configuration.

A.1.1 Relative airstation *position* in hub frame

The components of the relative position vector of the airstation with respect to the hub frame are $\underline{w}_a = \underline{u}_a - \underline{u}_h$, measured in the inertial frame. The components of this relative position vector measured in the hub frame, denoted $\underline{w}_a^*$, are then

$$\underline{w}_a^* = R_h^T(\underline{u}_a - \underline{u}_h). \tag{181}$$

Note that the same relationships also hold in the reference configuration,

$$\underline{w}_a^{0*} = R_h^{0T}(\underline{u}_a^0 - \underline{u}_h^0). \tag{182}$$

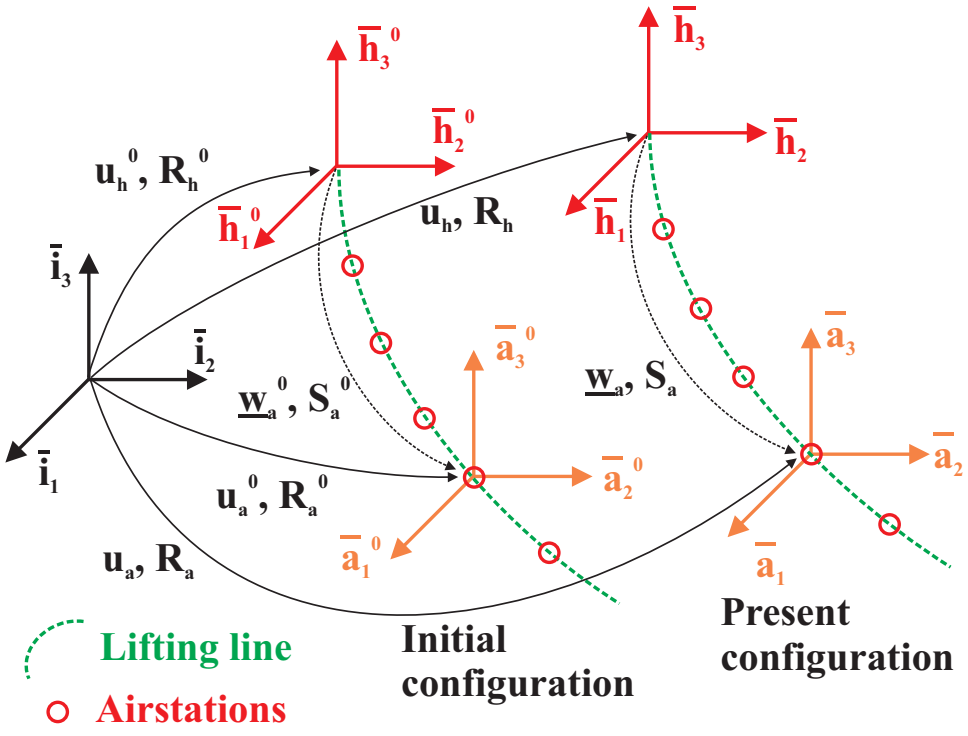

Figure 92: Reference and present configurations of an airstation.

A.1.2 Relative airstation *displacement* in hub frame

If instead of relative position, the components of the relative displacement vector, (or change in relative position), measured in the hub frame, denoted $\underline{\hat{w}}_a^*$, are to be evaluated, the following equation is used

$$\underline{\hat{w}}_a^* = \underline{w}_a^* - \underline{w}_a^{0*} = R_h^T(\underline{u}_a - \underline{u}_h) - R_h^{0T}(\underline{u}_a^0 - \underline{u}_h^0). \tag{183}$$

A.1.3 Relative airstation *orientation* in hub frame

The components of the rotation tensor that brings the hub triad, $\mathcal{B}^H$, to the airstation triad, $\mathcal{B}^A$, measured in the inertial frame, are $S_a = R_a R_h^T$. The components of the same tensor in the hub frame then become

$$S_a^* = R_h^T S_a R_h = R_h^T R_a. \tag{184}$$

Note that the same relationships also hold in the reference configuration,

$$S_a^{0*} = R_h^{0T} R_a^0. \tag{185}$$

A.1.4 Relative airstation *orientation change* in hub frame

If instead of relative orientation, the components of the relative change in orientation tensor, measured in the hub frame, denoted $\hat{S}_a^*$, are to be evaluated, the following equation is used

$$\hat{S}_a^* = (R_h^T R_a)(R_h^{0T} R_a^0)^T. \tag{186}$$

A.1.5 The airstation lag, flap and pitch angles

The relative rotation tensor from the hub triad to the airstation triad was derived in the previous paragraphs. These rotation tensors can be parameterized using the Wiener-Milenkovic parameters, see section. On the other hand, it is customary to use angles to represent the same tensors. If the rotation tensor is parameterized using Euler angles with the *3-2-1 sequence*, see section, these Euler angles will correspond to the lag-flap-pitch sequence. The lag, flap and pitch angles are positive for positive rotations about the $\bar{h}_3$, $\bar{h}_2$ and $\bar{h}_1$ axes, respectively. In other words, a lag angle is positive towards the leading edge, a flap angle is positive down, a pitch angle is positive nose up.

A.1.6 The azimuthal angle Ψ

The azimuthal angle Ψ is defined by the relative orientations of the rotor frame and hub frame of the blade, see fig. 93, as

$$\cos\Psi = \bar{h}_1^T \bar{r}_2; \quad \sin\Psi = \bar{h}_1^T \bar{r}_1. \tag{187}$$

A.2 Definition of the kinematics and loads interfaces

The kinematics and loads interfaces for each airloads scheme are defined in Table 10

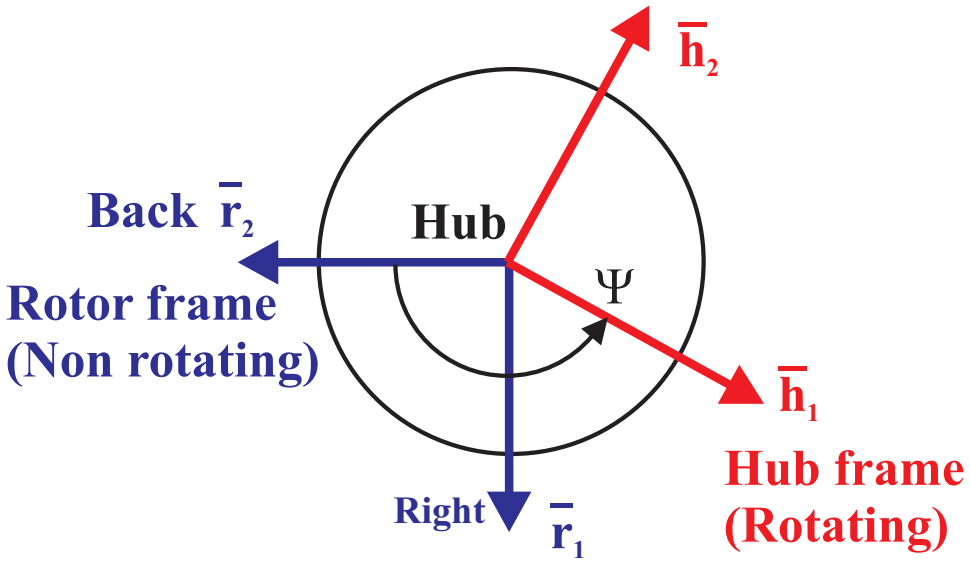

Figure 93: Definition of the azimuthal angle Ψ.

	2D_AIRFOIL	MEASURED_AIRLOADS	OVERFLOW
FrameKin	INERTIAL	LOCAL	LOCAL
KinematicsDim	DIMENSIONAL	NON_DIMENSIONAL	NON_DIMENSIONAL
LinMotionRep	DISPLACEMENTS	DISPLACEMENTS	DISPLACEMENTS
AngMotionRep	POSITIONS	DISPLACEMENTS	DISPLACEMENTS
RotationRep	CRV	ANGLE321	ANGLE321
LoadsDim	DIMENSIONAL	DIMENSIONAL	DIMENSIONAL
FrameLoads	LOCAL	LOCAL	INERTIAL
ForceNor	FORCES_PER_SPAN	FORCES_PER_SPAN	FORCES

Table 10: Available kinematics and loads interface definitions for each airloads scheme

APPENDIX B

BIOT-SAVART LAW

B.1 Evaluation of the Biot-Savart law over a line vortex

The Biot-Savart law is used to calculate the induced velocity due to vortex lines in aerodynamic theory. As shown in fig. 94, the velocity at point **P** induced by a line vortex of strength Γ and length L is given by

$$\underline{V} = \frac{\Gamma}{4\pi} \int_0^L \frac{\bar{u} \times \underline{r}}{||\underline{r}||^3} \mathrm{d}s, \tag{188}$$

where s is a variable in the interval $[0,\ L]$, $\underline{r}$ is the distance from a point on the line vortex to the point **P** at which the induced velocity is evaluated, and $||\cdot||$ is the norm of a vector. $\bar{u}$ is a unit vector that shows the direction of the circulation, can be computed as

$$\bar{u} = \frac{\underline{r}_1 - \underline{r}_2}{||\underline{r}_1 - \underline{r}_2||}. \tag{189}$$

where $\underline{r}_1$ and $\underline{r}_2$ are the distance vectors from points **A** and **B** to point **P**, respectively.

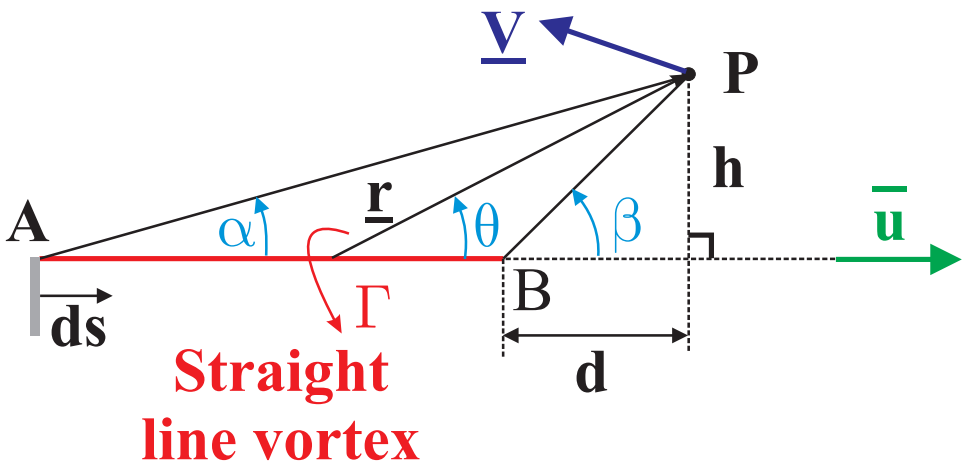

Figure 94: Evaluation of the Biot-Savart law over a line vortex

This equation can be simplified as

$$\underline{V} = \frac{\Gamma}{4\pi}\left[\int_0^L \frac{\sin\theta}{||\underline{r}||^2}\mathrm{d}s\right]\bar{n}, \tag{190}$$

where θ is the angle between vectors $\bar{u}$ and $\underline{r}$, and positive as shown in fig. 94. Unit vector $\bar{n}$ is the direction of the induced velocity, and normal to the plane defined by line vortex **AB** and point **P**. By the change of the variables, the above equation can be recast as

$$\underline{V} = \frac{\Gamma}{4\pi}\left[\int_\alpha^\beta \frac{\sin\theta}{||\underline{r}||^2}\frac{\mathrm{d}s}{\mathrm{d}\theta}\mathrm{d}\theta\right]\bar{n}, \tag{191}$$

The following trigonometric relationships are readily obtained from fig. 94

$$h = r\sin\theta, \tag{192}$$

$$L + d - s = r\cos\theta, \tag{193}$$

$$r^2 = (L + d - s)^2 + h^2, \tag{194}$$

where $r = ||\underline{r}||$, h is the normal distance from point **P** to the line vortex **AB**, d the distance defined in fig. 94. Taking derivatives of eqs. (192) and (194) yields

$$0 = \sin\theta\mathrm{d}r + r\cos\theta\mathrm{d}\theta, \tag{195}$$

$$r\mathrm{d}r = -(L + d - s)\mathrm{d}s. \tag{196}$$

Equation. (195) gives

$$\mathrm{d}\theta = -\frac{\sin\theta}{r\cos\theta}\mathrm{d}r, \tag{197}$$

with the help of eq. (193), eq. (196) becomes

$$\mathrm{d}r = -\cos\theta\mathrm{d}s, \tag{198}$$

substituting eq. (198) into eq. (197) leads to

$$\frac{\mathrm{d}s}{\mathrm{d}\theta} = \frac{r}{\sin\theta}. \tag{199}$$

By references of eqs. (199) and (192), the Biot-Savart integral in eq. (191) becomes

$$\underline{V} = \frac{\Gamma}{4\pi h}\left[\int_\alpha^\beta \sin\theta\mathrm{d}\theta\right]\bar{n} = \frac{\Gamma}{4\pi h}(\cos\alpha - \cos\beta)\bar{n}. \tag{200}$$

In this equation, $\cos\alpha$, $\cos\beta$, $\bar{n}$, and h are given by

$$\cos\alpha = \frac{(\underline{r}_1 - \underline{r}_2)^T \underline{r}_1}{||(\underline{r}_1 - \underline{r}_2)|| \cdot ||\underline{r}_1||}, \tag{201}$$

$$\cos\beta = \frac{(\underline{r}_1 - \underline{r}_2)^T \underline{r}_2}{||(\underline{r}_1 - \underline{r}_2)|| \cdot ||\underline{r}_2||}, \tag{202}$$

$$\bar{n} = \frac{\bar{u} \times \underline{r}}{||\bar{u} \times \underline{r}||}, \tag{203}$$

$$h = ||\underline{r}_1|| \sin\alpha. \tag{204}$$

Notice that vector $\underline{r}$ can also be expressed in terms of $\underline{r}_1$ and $\bar{u}$,

$$\underline{r} = \underline{r}_1 - (L + d - s)\bar{u}, \tag{205}$$

then, eq. (203) becomes

$$\bar{n} = \frac{\bar{u} \times \underline{r}_1}{h}, \tag{206}$$

and $\bar{u}$ and h are given by eqs. (189) and (204), respectively.

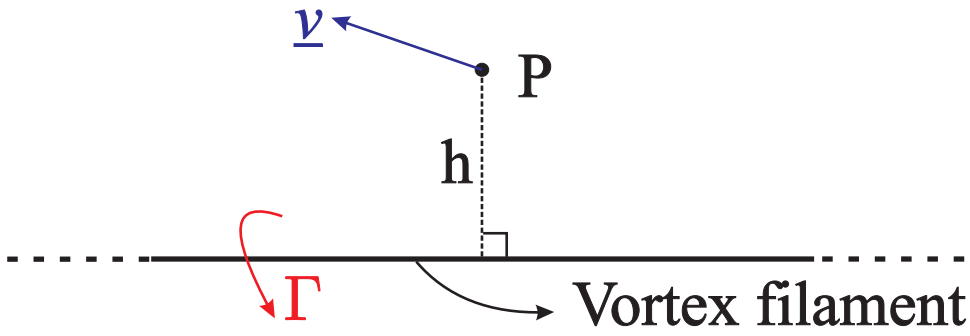

Figure 95: Evaluation of the induced velocity due to an infinite long vortex filament using the Biot-Savart law

Let's see an extreme case, for which a line vortex or vortex filament is infinitely long. This means angles $\alpha = 0$ and $\beta = \pi$, see fig. 95. Then, the induced velocity at point **P** due to this infinitely long vortex filament of strength Γ is

$$\underline{V} = \frac{\Gamma}{2\pi h}\bar{n}, \tag{207}$$

where h is the normal distance from point **P** to the infinitely long vortex filament, the unit vector $\bar{n}$ is normal to the plane defined by the vortex filament and point **P**, at which the induced velocity is evaluated.

B.2 Evaluation of the Biot-Savart law over a vortex ring

In practical aerodynamic analysis of a three-dimensional finite wing, the wing is represented by several airstations, around which is a vortex ring (cell) of strength Γ, distributed along a line, called lifting line, see fig. 96. The ordering of the vortex segments forming the vortex ring is as shown in fig. 96. The first vortex segment is located at the quarter chord of the airfoil attached to an airstation. Point **G** is half-way between the quarter chord and the trailing edge of the airfoil, referred to as the reference point, and point **C** is the point of interest, at which the induced velocity is evaluated, and referred to as the collocation point. Points $\mathbf{P}, \mathbf{Q}, \mathbf{R}$, and $\mathbf{S}$ are the four vertices of the vortex ring. Orthonormal basis, $\mathcal{A} = (\bar{a}_1, \bar{a}_2, \bar{a}_3)$, in which all variables are referenced, is the system attached at point **G** and has the same orientations as the airfoil attached system at the quarter chord. h_1, h_2, h_3, and h_4 are the normal distances from the collocation point **C** to the vortex segments of the vortex ring.

Based on the derivation in section B.1, the velocity induced by the vortex ring is the sum of the contributions of four line vortices,

$$\underline{V} = \sum_{k=1}^{4} \underline{V}_k, \tag{208}$$

and $\underline{V}_k$ is the induced velocity due to the k^{th} line vortex of the ring, and computed as

$$\underline{V}_k = \frac{\Gamma}{4\pi h_k} \left[\cos\alpha - \cos\beta\right]_k \bar{n}_k. \tag{209}$$

The position vector of the collocation point **C**, $\underline{r}_C$ expressed in system $\mathcal{A}$, is

$$\underline{r}_C = c_1\bar{a}_1 + c_2\bar{a}_2 + c_3\bar{a}_3, \tag{210}$$

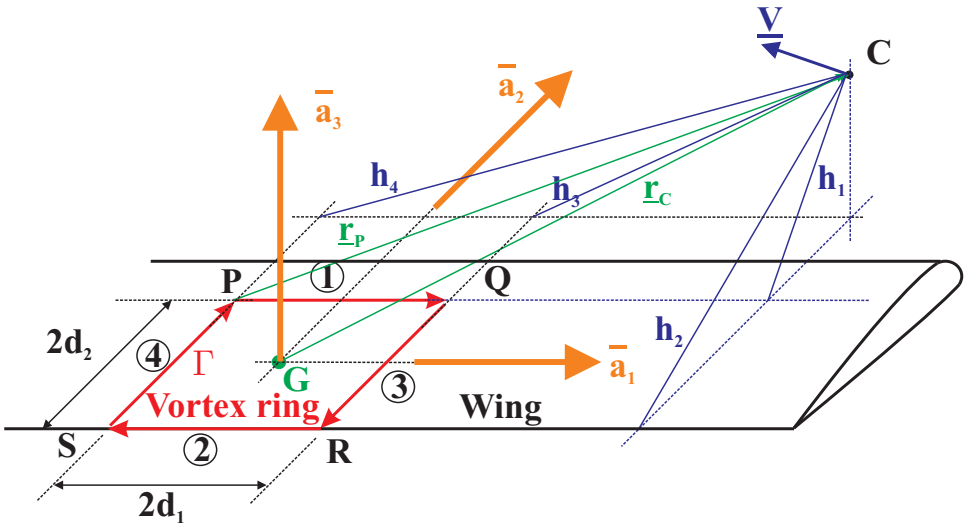

Figure 96: Evaluation of Biot-Savart law over a vortex ring

the distance vectors from four vertex points to point **C**, $\underline{r}_P, \underline{r}_Q, \underline{r}_R$, and $\underline{r}_S$ are

$$\begin{aligned}
\underline{r}_P &= (c_1 + d_1)\bar{a}_1 + (c_2 - d_2)\bar{a}_2 + c_3\bar{a}_3, \\
\underline{r}_Q &= (c_1 - d_1)\bar{a}_1 + (c_2 - d_2)\bar{a}_2 + c_3\bar{a}_3, \\
\underline{r}_R &= (c_1 - d_1)\bar{a}_1 + (c_2 + d_2)\bar{a}_2 + c_3\bar{a}_3, \\
\underline{r}_S &= (c_1 + d_1)\bar{a}_1 + (c_2 + d_2)\bar{a}_2 + c_3\bar{a}_3.
\end{aligned} \tag{211}$$

The directions of the vortex segments forming the vortex ring are given by

$$\begin{aligned}
\overline{\mathrm{PQ}} &= 2d_1\bar{a}_1, \\
\overline{\mathrm{RS}} &= -2d_1\bar{a}_1, \\
\overline{\mathrm{QR}} &= -2d_2\bar{a}_2, \\
\overline{\mathrm{SP}} &= 2d_2\bar{a}_2.
\end{aligned} \tag{212}$$

With the help of eq. (206), the direction of the velocity vector induced by each vortex segment is

$$\begin{aligned}
\bar{n}_1 &= \tfrac{(c_2-d_2)\bar{a}_3 - c_3\bar{a}_2}{h_1}, \\
\bar{n}_2 &= \tfrac{-(c_2+d_2)\bar{a}_3 + c_3\bar{a}_2}{h_2}, \\
\bar{n}_3 &= \tfrac{(c_1-d_1)\bar{a}_3 - c_3\bar{a}_1}{h_3}, \\
\bar{n}_4 &= \tfrac{-(c_1+d_1)\bar{a}_3 + c_3\bar{a}_1}{h_4}.
\end{aligned} \tag{213}$$

The difference of the cosines of each vortex segment is computed based on eqs. (201) and (202)

$$\begin{aligned}
[\cos\alpha - \cos\beta]_1 &= \tfrac{c_1+d_1}{r_P} - \tfrac{c_1-d_1}{r_Q}, \\
[\cos\alpha - \cos\beta]_2 &= \tfrac{-(c_1-d_1)}{r_R} + \tfrac{(c_1+d_1)}{r_S}, \\
[\cos\alpha - \cos\beta]_3 &= \tfrac{-(c_2-d_2)}{r_Q} + \tfrac{(c_2+d_2)}{r_R}, \\
[\cos\alpha - \cos\beta]_4 &= \tfrac{c_2+d_2}{r_S} - \tfrac{c_2-d_2}{r_P}.
\end{aligned} \tag{214}$$

Substituting eqs. (213) and (214) into eq. (209) leads to

$$\begin{aligned}
\underline{V}_1 &= \tfrac{\Gamma}{4\pi}\tfrac{-c_3\bar{a}_2+(c_2-d_2)\bar{a}_3}{h_1^2}\left[\tfrac{c_1+d_1}{r_P} - \tfrac{c_1-d_1}{r_Q}\right], \\
\underline{V}_2 &= \tfrac{\Gamma}{4\pi}\tfrac{c_3\bar{a}_2-(c_2+d_2)\bar{a}_3}{h_2^2}\left[\tfrac{c_1+d_1}{r_S} - \tfrac{c_1-d_1}{r_R}\right], \\
\underline{V}_3 &= \tfrac{\Gamma}{4\pi}\tfrac{-c_3\bar{a}_1+(c_1-d_1)\bar{a}_3}{h_3^2}\left[\tfrac{c_2+d_2}{r_R} - \tfrac{c_2-d_2}{r_Q}\right], \\
\underline{V}_4 &= \tfrac{\Gamma}{4\pi}\tfrac{c_3\bar{a}_1-(c_1+d_1)\bar{a}_3}{h_4^2}\left[\tfrac{c_2+d_2}{r_S} - \tfrac{c_2-d_2}{r_P}\right],
\end{aligned} \tag{215}$$

where the normal distances can be computed as followings with the reference of eq. (204)

$$\begin{aligned}
h_1 &= ||(c_2-d_2)\bar{a}_3 - c_3\bar{a}_2|| = \sqrt{(c_2-d_2)^2+c_3^2}, \\
h_2 &= ||-(c_2+d_2)\bar{a}_3 + c_3\bar{a}_2|| = \sqrt{(c_2+d_2)^2+c_3^2}, \\
h_3 &= ||(c_1-d_1)\bar{a}_3 - c_3\bar{a}_1|| = \sqrt{(c_1-d_1)^2+c_3^2}, \\
h_4 &= ||-(c_1+d_1)\bar{a}_3 + c_3\bar{a}_1|| = \sqrt{(c_1+d_1)^2+c_3^2},
\end{aligned} \tag{216}$$

and the distance from the collocation point $\mathbf{C}$ to each vertex of the vortex ring is

$$\begin{aligned}
r_P &= \sqrt{(c_1+d_1)^2+(c_2-d_2)^2+c_3^2} = \sqrt{r^2+d^2+2c_1d_1-2c_2d_2}, \\
r_Q &= \sqrt{(c_1-d_1)^2+(c_2-d_2)^2+c_3^2} = \sqrt{r^2+d^2-2c_1d_1-2c_2d_2}, \\
r_R &= \sqrt{(c_1-d_1)^2+(c_2+d_2)^2+c_3^2} = \sqrt{r^2+d^2-2c_1d_1+2c_2d_2}, \\
r_S &= \sqrt{(c_1+d_1)^2+(c_2+d_2)^2+c_3^2} = \sqrt{r^2+d^2+2c_1d_1+2c_2d_2},
\end{aligned} \tag{217}$$

where $r^2 = c_1^2+c_2^2+c_3^2$ and $d^2 = d_1^2+d_2^2$. With the contribution of each line vortex of the vortex ring available, the total induced velocity can be obtained using eq. (208),

$$\underline{V} = \frac{\Gamma}{4\pi}\underline{\hat{V}}, \tag{218}$$

where $\underline{\hat{V}}$ is given by

$$\underline{\hat{V}} = g_1\bar{a}_1 + g_2\bar{a}_2 + g_3\bar{a}_3. \tag{219}$$

Parameters g_1, g_2 and g_3 are computed by

$$\begin{aligned}
g_1 &= \tfrac{c_3}{h_4^2}\left(\tfrac{c_2+d_2}{r_S}-\tfrac{c_2-d_2}{r_P}\right)-\tfrac{c_3}{h_3^2}\left(\tfrac{c_2+d_2}{r_R}-\tfrac{c_2-d_2}{r_Q}\right),\\
g_2 &= \tfrac{c_3}{h_2^2}\left(\tfrac{c_1+d_1}{r_S}-\tfrac{c_1-d_1}{r_R}\right)-\tfrac{c_3}{h_1^2}\left(\tfrac{c_1+d_1}{r_P}-\tfrac{c_1-d_1}{r_Q}\right),\\
g_3 &= \tfrac{c_2-d_2}{h_1^2}\left[\tfrac{c_1+d_1}{r_P}-\tfrac{c_1-d_1}{r_Q}\right]-\tfrac{c_2+d_2}{h_2^2}\left[\tfrac{c_1+d_1}{r_S}-\tfrac{c_1-d_1}{r_R}\right]\\
&+ \tfrac{c_1-d_1}{h_3^2}\left[\tfrac{c_2+d_2}{r_R}-\tfrac{c_2-d_2}{r_Q}\right]-\tfrac{c_1+d_1}{h_4^2}\left[\tfrac{c_2+d_2}{r_S}-\tfrac{c_2-d_2}{r_P}\right].
\end{aligned} \tag{220}$$

As described in chapter 4, the change of bound circulations in the time and spacial domains generates the shed and trailed vorticities, respectively, that will be released into the wake. Therefore, when calculating the induced velocity at a point due to the bound circulations in the wake, only the contributions from vortex segments 2 to 4 are considered, which indicates that, the total induced velocity due to the bound vortex rings in the wake should be

$$\underline{V'} = \frac{\Gamma}{4\pi}\underline{\hat{V}'} \tag{221}$$

where $\underline{\hat{V}'}$ is given by

$$\underline{\hat{V}'} = g_1'\bar{a}_1 + g_2'\bar{a}_2 + g_3'\bar{a}_3 \tag{222}$$

Parameters g_1', g_2' and g_3' are

$$\begin{aligned}
g_1' &= \tfrac{c_3}{h_4^2}\left(\tfrac{c_2+d_2}{r_S}-\tfrac{c_2-d_2}{r_P}\right)-\tfrac{c_3}{h_3^2}\left(\tfrac{c_2+d_2}{r_R}-\tfrac{c_2-d_2}{r_Q}\right),\\
g_2' &= \tfrac{c_3}{h_2^2}\left(\tfrac{c_1+d_1}{r_S}-\tfrac{c_1-d_1}{r_R}\right),\\
g_3' &= -\tfrac{c_2+d_2}{h_2^2}\left[\tfrac{c_1+d_1}{r_S}-\tfrac{c_1-d_1}{r_R}\right]+\tfrac{c_1-d_1}{h_3^2}\left[\tfrac{c_2+d_2}{r_R}-\tfrac{c_2-d_2}{r_Q}\right]-\tfrac{c_1+d_1}{h_4^2}\left[\tfrac{c_2+d_2}{r_S}-\tfrac{c_2-d_2}{r_P}\right].
\end{aligned} \tag{223}$$

APPENDIX C

CHEBYSHEV APPROXIMATION

C.1 Chebyshev polynomials

C.1.1 Definition

Chebyshev polynomials [85, 1] form a series of orthogonal polynomials. The lowest polynomials are

$$T_0(x) = 1,\ T_1(x) = x,\ T_2(x) = 2x^2 - 1,\ T_3(x) = 4x^3 - 3x,\ T_4(x) = 8x^4 - 8x^2 + 1, \ldots \tag{224}$$

and are depicted in fig. 97. The polynomials can be generated from the following recurrence relationship

$$T_{n+1} = 2xT_n - T_{n-1}, \quad n \geq 1. \tag{225}$$

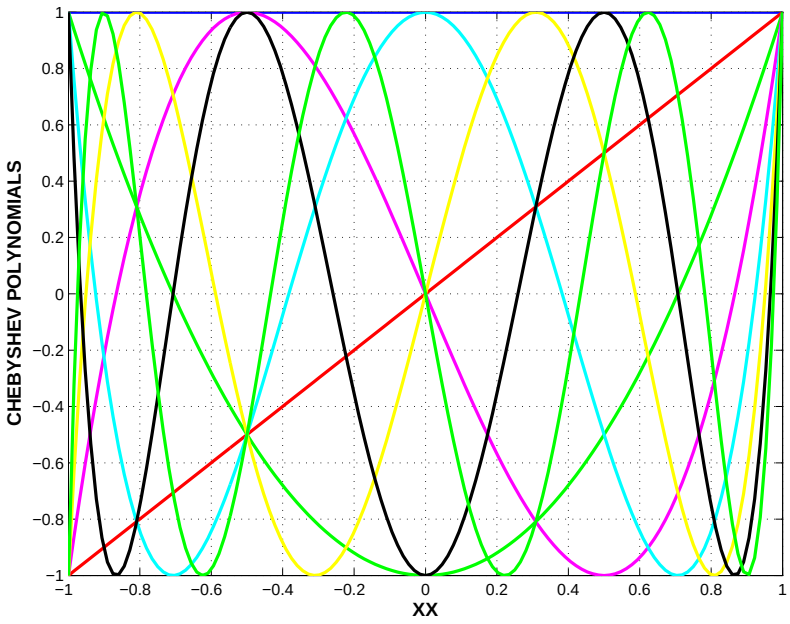

Figure 97: The seven lowest order Chebyshev polynomials

It is possible to give an explicit expression of Chebyshev polynomials as

$$T_n(x) = \cos\left[n \arccos x\right]. \tag{226}$$

This equation can be verified by using elementary trigonometric identities. For instance, it is clear, that $T_2 = \cos\left[2 \arccos x\right] = 2\cos^2(\arccos x) - 1 = 2x^2 - 1$, as expected from eq. (224).

C.1.2 Zeros and extrema

It is now easy to verify that $T_n(x)$ possesses n zeros within the interval $x \in [-1, +1]$: $T_n(x) = \cos\left[n \arccos x\right] = 0$ implies $n \arccos x = (2k-1)\pi/2$. Hence, the zeros of Chebyshev polynomial $T_n(x)$ are

$$x_k = \cos \frac{\pi(2k-1)}{2n}, \quad k = 1, 2, 3, \ldots, n. \tag{227}$$

For instance, since $T_3 = x(4x^2 - 3)$, its zeros are $\sqrt{3}/2$, 0, and $-\sqrt{3}/2$, which can be written as $\cos \pi/6 = \sqrt{3}/2$, $\cos 3\pi/6 = 0$, and $\cos 5\pi/6 = -\sqrt{3}/2$. The value of Chebyshev polynomial $T_i(x)$ at the zeros of $T_n(x)$ is easily found from eq. (226) as

$$T_i(x_k) = \cos \frac{i(2k-1)\pi}{2n}, \quad i < n. \tag{228}$$

It is also easy to find the extrema of Chebyshev polynomials; imposing $\mathrm{d}T_n/\mathrm{d}x = 0$ leads to $\sin\left[n \arccos x\right] = 0$, or

$$x_k = \cos \frac{k\pi}{n}, \quad k = 0, 1, 2, 3, \ldots, n. \tag{229}$$

For instance, $\mathrm{d}T_4/\mathrm{d}x = x(2x^2 - 1) = 0$ leads to extrema $\cos \pi/4 = \sqrt{2}/2$, $\cos \pi/2 = 0$, and $\cos 3\pi/4 = -\sqrt{2}/2$. The additional extrema, $\cos 0 = 1$ and $\cos \pi = -1$, occur at the ends of the interval. The value of Chebyshev polynomial $T_i(x)$ at the extrema of $T_n(x)$ is easily found from eq. (226) as

$$T_i(x_k) = \cos \frac{ik\pi}{n}, \quad i < n. \tag{230}$$

C.1.3 Orthogonality relationships

Chebyshev polynomials are orthogonal within the interval $x \in [-1, +1]$ with a weight of $(1-x^2)^{-1/2}$, *i.e.*

$$\int_{-1}^{+1} \frac{T_i(x)T_j(x)}{\sqrt{1-x^2}}\,\mathrm{d}x = \begin{cases} 0 & i \neq j \\ \pi/2 & i = j \neq 0 \\ \pi & i = j = 0 \end{cases} . \tag{231}$$

In addition to the orthogonality property defined by eq. (231), Chebyshev polynomials also enjoy the following discrete orthogonality relationship

$$\sum_{k=1}^{n} T_i(x_k)T_j(x_k) = \begin{cases} 0 & i \neq j \\ n/2 & i = j \neq 0 \\ n & i = j = 0 \end{cases} . \tag{232}$$

where x_k, $k = 1, 2, 3, \ldots, n$ are the zeros of T_n as given by eq. (227), and $i, j < n$. To prove this orthogonality relationship, trigonometric identities are used

$$\begin{aligned} \textstyle\sum_{k=1}^{n} T_i(x_k)T_j(x_k) &= \textstyle\sum_{k=1}^{n} \cos\frac{i(2k-1)\pi}{2n}\cos\frac{j(2k-1)\pi}{2n} \\ &= \tfrac{1}{2}\textstyle\sum_{k=0}^{n-1}\left[\cos\frac{(i+j)(2k+1)\pi}{2n} + \cos\frac{(i-j)(2k+1)\pi}{2n}\right], \\ = \tfrac{1}{2}\left[\frac{\sin\frac{n}{2}\frac{(i+j)\pi}{n}\cos\left[\frac{(i+j)\pi}{2n}+(n-1)\frac{(i+j)\pi}{2n}\right]}{\sin\frac{(i+j)\pi}{2n}} + \frac{\sin\frac{n}{2}\frac{(i-j)\pi}{n}\cos\left[\frac{(i-j)\pi}{2n}+(n-1)\frac{(i-j)\pi}{2n}\right]}{\sin\frac{(i-j)\pi}{2n}}\right] \\ &= \tfrac{1}{2}\left[\frac{\sin\frac{(i+j)\pi}{2}\cos\frac{(i+j)\pi}{2}}{\sin\frac{(i+j)\pi}{2n}} + \frac{\sin\frac{(i-j)\pi}{2}\cos\frac{(i-j)\pi}{2}}{\sin\frac{(i-j)\pi}{2n}}\right] = 0. \end{aligned}$$

The trigonometric identity, eq. (235) was used to eliminate the summation; the last equality results from the fact that $\cos(i+j)\pi/2 = \cos(i-j)\pi/2 = 0$. If $i = j \neq 0$, or $i = j = 0$, similar developments yield the discrete orthogonality given by eq. (232).

Chebyshev polynomials also enjoy an additional discrete orthogonality relationship

$$\sum_{k=0}^{n}{}'' T_i(x_k)T_j(x_k) = \begin{cases} 0 & i \neq j \\ n/2 & i = j \neq 0 \\ n & i = j = 0 \end{cases} . \tag{233}$$

where x_k, $k = 0, 1, 2, \cdots, n$ are the extrema of T_n as given by eq. (229), and $i, j < n$. The double prime after the summation sign indicates that the *first and last terms of the summation must be halved*. To prove this orthogonality relationship, trigonometric identities are used

$$\begin{aligned}
\textstyle\sum_{k=0}^{n} T_i(x_k)T_j(x_k) &= \textstyle\sum_{k=0}^{n} \cos\frac{ik\pi}{n}\cos\frac{jk\pi}{n}, \\
&= \tfrac{1}{2}\textstyle\sum_{k=0}^{n}\left[\cos k\frac{(i+j)\pi}{n} + \cos k\frac{(i-j)\pi}{n}\right] \\
&= \tfrac{1}{2}\left[\frac{\sin\frac{n+1}{2}\frac{(i+j)\pi}{n}\cos\frac{n}{2}\frac{(i+j)\pi}{n}}{\sin\frac{(i+j)\pi}{2n}} + \frac{\sin\frac{n+1}{2}\frac{(i-j)\pi}{n}\cos\frac{n}{2}\frac{(i-j)\pi}{n}}{\sin\frac{(i-j)\pi}{2n}}\right] \\
&= \tfrac{1}{4}\left[\frac{\sin\frac{2n+1}{2}\frac{(i+j)\pi}{n}+\sin\frac{(i+j)\pi}{2n}}{\sin\frac{(i+j)\pi}{2n}} + \frac{\sin\frac{2n+1}{2}\frac{(i-j)\pi}{n}+\sin\frac{(i-j)\pi}{2n}}{\sin\frac{(i-j)\pi}{2n}}\right] \\
&= \tfrac{1}{4}\left[2 + \frac{\sin\left[(i+j)\pi+\frac{(i+j)\pi}{2n}\right]}{\sin\frac{(i+j)\pi}{2n}} + \frac{\sin\left[(i-j)\pi+\frac{(i-j)\pi}{2n}\right]}{\sin\frac{(i-j)\pi}{2n}}\right] \\
&= \tfrac{1}{4}\left[2 + \cos(i+j)\pi + \cos(i-j)\pi\right] = \tfrac{1}{2}\left[1 + \cos i\pi\cos j\pi\right].
\end{aligned}$$

The first term in the last bracket is the term of the sum corresponding to $k = 0$, whereas the second term in the last bracket is that corresponding to $k = n$. Bringing these two terms to the left hand side is identical to replacing the summation sign, $\sum$, by $\sum''$. Here again, the trigonometric identity, eq. (235) was used to eliminate the summation. If $i = j \neq 0$, or $i = j = 0$, similar developments yield the discrete orthogonality given by eq. (233).

The following trigonometric identities were used in the derivation of the above discrete orthogonality relationships

$$\sin(a)+\sin(a+b)+\ldots+\sin(a+nb) = \sum_{k=0}^{n}\sin(a+kb) = \frac{\sin\frac{(n+1)b}{2}\sin(a+\frac{nb}{2})}{\sin\frac{b}{2}}, \quad (234)$$

$$\cos(a)+\cos(a+b)+\ldots+\cos(a+nb) = \sum_{k=0}^{n}\cos(a+kb) = \frac{\sin\frac{(n+1)b}{2}\cos(a+\frac{nb}{2})}{\sin\frac{b}{2}}. \quad (235)$$

C.1.4 Derivatives of Chebyshev polynomials

The following expression for the derivatives of Chebyshev polynomials

$$T_n' = \begin{cases} 2n\left[T_{n-1} + T_{n-3} + \ldots + T_1\right] & n \text{ even}, \\ 2n\left[T_{n-1} + T_{n-3} + \ldots + T_2\right] + nT_0 & n \text{ odd}, \end{cases} \tag{236}$$

where the notation $(\cdot)'$ indicates a derivative with respect to x, can be proved by mathematical induction. Indeed, they are verified for the lowest polynomials, $T_1' = T_0$, $T_2' = 2 \times 2\ T_1$, $T_3' = 2 \times 3\ T_2 + 3T_0$, $T_4' = 2 \times 4\ (T_3 + T_1)$, etc. It then remains to prove that if it is correct for n it is still correct for $n+1$. Taking a derivative of the basic recurrence for Chebyshev polynomials, eq. (225), leads to $T_{n+1}' = 2xT_n' + 2T_n - T_{n-1}'$. Introducing eq. (236) into this recurrence, it is then easy to show that eq. (236) is true for $n+1$.

C.2 Chebyshev approximation of functions of a single variable

C.2.1 Expansion of a function in Chebyshev polynomials

A function $f(x)$ can be approximated in terms of Chebyshev polynomials as

$$f(x) \approx \sum_{i=0}^{N-1} c_i T_i(x), \tag{237}$$

where c_i are the coefficients of the expansion. N is the number of coefficients in the expansion, whereas $N-1$ is the *order of the expansion*, *i.e.* the highest order polynomial in the expansion. To find these coefficients given function $f(x)$, the above relationship is expressed at the $x = x_k$, where x_k are the zeros of $T_N(x)$, as given by eq. (227). This yields $f(x_k) = \sum_{i=0}^{N-1} c_i T_i(x_k)$. Multiplying both sides of this equation by $T_j(x_k)$ and summing the resulting equations expressed at all zeros of $T_N(x)$ leads to

$$\sum_{k=1}^{N} f(x_k) T_j(x_k) = \sum_{i=0}^{N-1} c_i \left[\sum_{k=1}^{N} T_i(x_k) T_j(x_k)\right]. \tag{238}$$

In view of the discrete orthogonality relationship of Chebyshev polynomials, eq. (232), it then follows that

$$c_0 = \frac{1}{N}\sum_{k=1}^{N} f(x_k), \tag{239a}$$

$$c_i = \frac{2}{N}\sum_{k=1}^{N} f(x_k)T_i(x_k), \tag{239b}$$

where $T_i(x_k)$ is given by eq. (228).

The coefficients of the Chebyshev expansion can be obtained in an alternative manner. Relationship (237) is expressed at the $x = x_k$, where x_k are the extrema of $T_N(x)$, as given by eq. (229). This yields $f(x_k) = \sum_{i=0}^{N-1} c_i T_i(x_k)$. Multiplying both sides of this equation by $T_j(x_k)$ and summing the resulting equations expressed at all extrema of $T_N(x)$ leads to

$$\sum_{k=0}^{N}{}'' \, f(x_k)T_j(x_k) = \sum_{i=0}^{N-1} c_i \left[\sum_{k=0}^{N}{}'' \, T_i(x_k)T_j(x_k)\right]. \tag{240}$$

In view of the discrete orthogonality relationship of Chebyshev polynomials, eq. (233), it then follows that

$$c_0 = \frac{1}{N}\sum_{k=0}^{N}{}'' \, f(x_k), \tag{241a}$$

$$c_i = \frac{2}{N}\sum_{k=0}^{N}{}'' \, f(x_k)T_i(x_k), \tag{241b}$$

where $T_i(x_k)$ is given by eq. (230). Note that as required by the discrete orthogonality relationship of Chebyshev polynomials, eq. (233), the double prime after the summation sign indicates that the *first and last terms of the summation must be halved*.

C.2.2 Evaluation of Chebyshev expansions: Clenshaw's recurrence

On the other hand, if the coefficients of the Chebyshev expansion are known, the function can then be computed using eq. (237). However, rather than computing the

polynomials then summing all contributions, it is preferable to use the recurrence relation, eq. (225), to find

$$\begin{aligned}
f(x) &= c_0T_0 + c_1T_1 + \ldots + c_{N-2}T_{N-2} + c_{N-1}T_{N-1}, \\
&= c_0T_0 + c_1T_1 + \ldots + c_{N-2}T_{N-2} + y_{N-1}T_{N-1}, \\
&= c_0T_0 + c_1T_1 + \ldots + (c_{N-3} - y_{N-1})T_{N-3} + (c_{N-2} + 2x\ y_{N-1})T_{N-2}, \\
&= c_0T_0 + c_1T_1 + \ldots + (c_{N-3} - y_{N-1})T_{N-3} + y_{N-2}T_{N-2}, \\
&= c_0T_0 + c_1T_1 + \ldots + (c_{N-4} - y_{N-2})T_{N-4} + (c_{N-3} - y_{N-1} + 2x\ y_{N-2})T_{N-3}, \\
&= c_0T_0 + c_1T_1 + \ldots + (c_{N-4} - y_{N-2})T_{N-4} + y_{N-3}T_{N-3}, \\
&= (c_0 - y_2)T_0 + y_1T_1.
\end{aligned}$$

The following quantities have been defined

$$y_{N+1} = 0, \tag{242a}$$

$$y_N = 0, \tag{242b}$$

$$y_{N-1} = c_{N-1} - y_{N+1} + 2x\ y_N, \tag{242c}$$

$$\vdots$$

$$y_1 = c_1 - y_3 + 2x\ y_2, \tag{242d}$$

$$y_0 = c_0 - y_2 + 2x\ y_1. \tag{242e}$$

The value of the function now simply becomes

$$f(x) = (c_0 - y_2) + y_1\ x = y_0 - x\ y_1. \tag{243}$$

This approach to the evaluation of functions expressed in Chebyshev series is known as *Clenshaw's recurrence*. It provides a numerically stable approach to the evaluation of Chebyshev series.

C.2.3 Derivatives and integrals of Chebyshev expansions

Consider now a function and its derivative, both expanded in Chebyshev series

$$f(x) = \sum_{i=0}^{N-1} c_i T_i(x), \quad \text{and} \quad f'(x) = \sum_{i=0}^{N-2} c'_i T_i(x), \tag{244}$$

where the notation $(\cdot)'$ indicates a derivative with respect to x. What is the relationship between the coefficients of the two expansions, c_i and c'_i? Using the formula for the derivatives of Chebyshev polynomials, eq. (236), the following recurrence is found

$$c'_N = 0, \tag{245a}$$

$$c'_{N-1} = 0, \tag{245b}$$

$$c'_{N-2} = 2 \times (N-1)\ c_{N-1} + c'_N, \tag{245c}$$

$$\vdots$$

$$c'_1 = 2 \times 2\ c_2 + c'_3, \tag{245d}$$

$$c'_0 = (2 \times 1\ c_1 + c'_2)/2. \tag{245e}$$

Consider finally a function and its integral, both expanded in Chebyshev series

$$f'(x) = \sum_{i=0}^{N-1} c'_i T_i(x), \quad \text{and} \quad f(x) = \sum_{i=0}^{N} c_i T_i(x). \tag{246}$$

What is the relationship between the coefficients of the two expansions, c'_i and c_i? In view of the relationship established above, it is clear that

$$c_1 = \frac{2c'_0 - c'_2}{2}, \tag{247a}$$

$$c_i = \frac{c'_{i-1} - c'_{i+1}}{2i}, \quad i = 2, 3, \ldots, N. \tag{247b}$$

Of course, c_0 is the integration constant that can be selected arbitrarily.

C.2.4 Examples

To illustrate application of Chebyshev expansions, the following function will be approximated by Chebyshev polynomials

$$f(x) = \sin x, \quad x \in [0, \pi]. \tag{248}$$

Using the algorithm presented in section C.2.1 for $N = 12$, the coefficients of the Chebyshev approximation were found to be $c_0 = 6.0219\ 10^{-1}$, $c_1 = 5.1363\ 10^{-1}$, $c_2 = -1.0355\ 10^{-1}$, $c_3 = -1.3732\ 10^{-2}$, $c_4 = 1.3587\ 10^{-3}$, $c_5 = 1.0726\ 10^{-4}$, $c_6 = -7.0463\ 10^{-6}$, $c_7 = -3.9639\ 10^{-7}$, $c_8 = 1.9500\ 10^{-8}$, $c_9 = 8.5229\ 10^{-10}$, $c_{10} = -3.3516\ 10^{-11}$, $c_{11} = -1.1990\ 10^{-12}$. Note the rapid decay in the magnitudes of the coefficients.

Figure 98 shows the exact sine function and its Chebyshev approximation, together with the error incurred by the approximation. Note that the error is spread over the entire range of the approximation in a *nearly uniform manner*. This is due to the fact that the extrema of Chebyshev polynomials are distributed over the entire range of the approximation and have alternating values of plus or minus unity. These characteristics make Chebyshev polynomials an ideal basis for approximating functions.

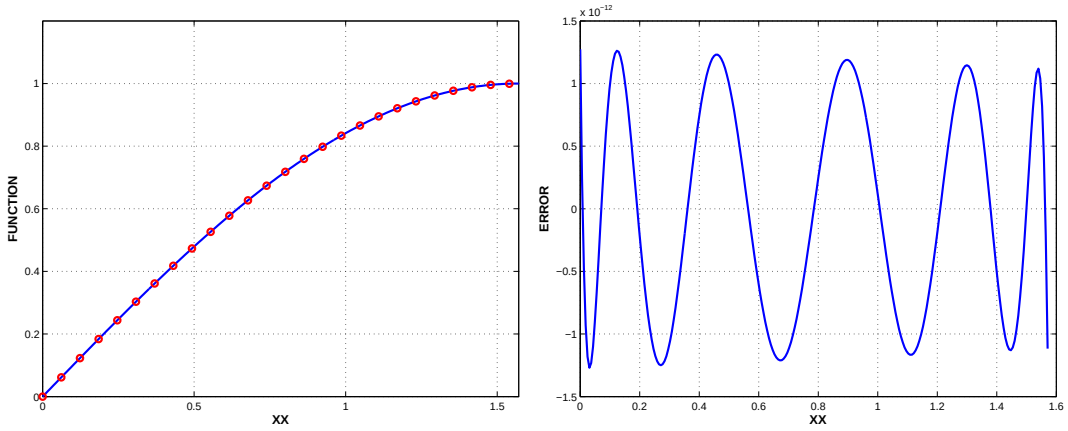

Figure 98: Left figure: Chebyshev polynomial expansion of function $f(x) = \sin x$, $x \in [0\pi]$. Function $f(x)$: solid line; Chebyshev expansion for N = 12: circles. Right figure: discrepancy between the exact function and its Chebyshev approximation.

Next, the sine function will be approximated using $N = 3$, only the terms c_0 to c_2 are retained in the expansion. Figure 99 shows the results of this crude approximation. Note that the error is nearly evenly distributed over the approximation range and that its magnitude can be estimated by looking at the magnitude of the first neglected

term of the expansion: $|c_3| = 1.3732\ 10^{-2}$. The results for an approximation including 5 terms, *i.e.* $N = 5$, are presented in fig. 100. Here again, the error is nearly evenly distributed over the approximation range and that its magnitude can be estimated by looking at the magnitude of the first neglected term of the expansion: $|c_5| = 1.0726\ 10^{-4}$.

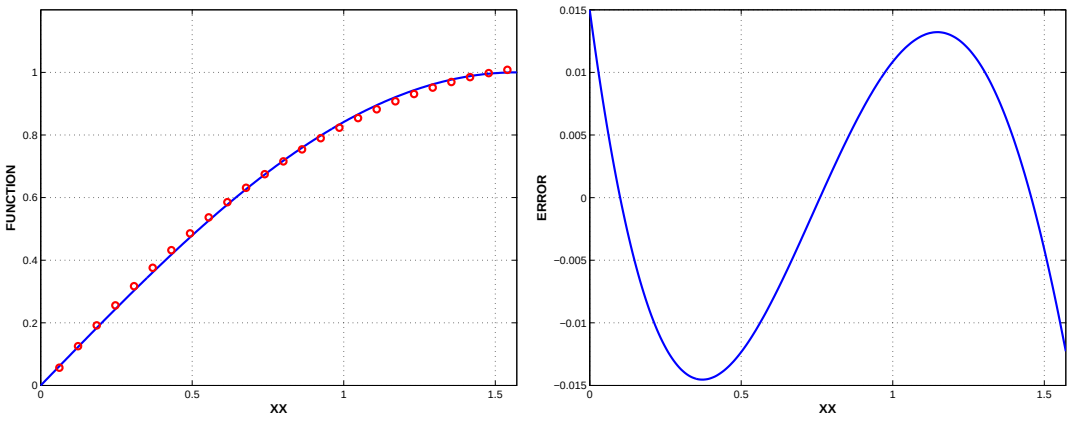

Figure 99: Left figure: Chebyshev polynomial expansion of function $f(x) = \sin x$, $x \in [0\pi]$. Function $f(x)$: solid line; Chebyshev expansion for N = 3: circles. Right figure: discrepancy between the exact function and its Chebyshev approximation.

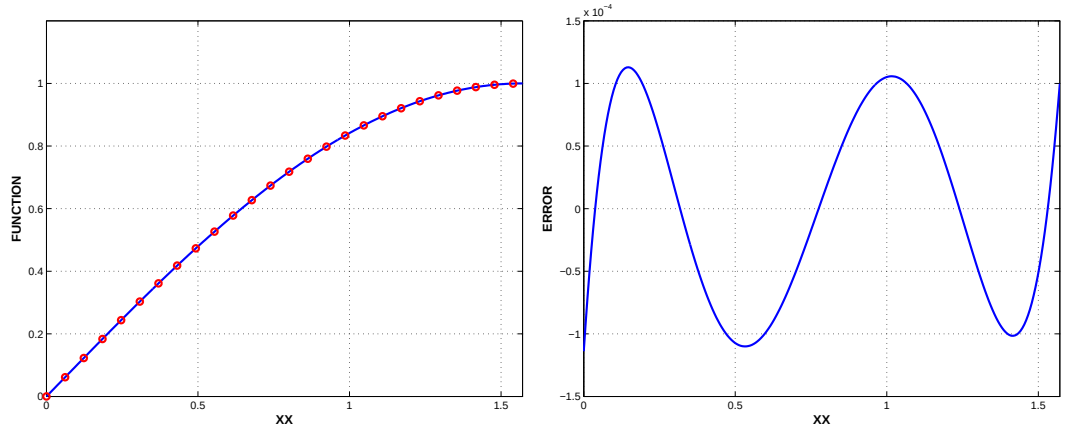

Figure 100: Left figure: Chebyshev polynomial expansion of function $f(x) = \sin x$, $x \in [0\pi]$. Function $f(x)$: solid line; Chebyshev expansion for N = 5: circles. Right figure: discrepancy between the exact function and its Chebyshev approximation.

Finally, the algorithm presented in section C.2.3 to evaluated the coefficients of

the Chebyshev expansion of the derivative of the function was used to compute the coefficients of the expansion $f'(x) = \cos x$. The following coefficients were found: $c'_0 = 6.0219\ 10^{-1}$, $c'_1 = -5.1363\ 10^{-1}$, $c'_2 = -1.0355\ 10^{-1}$, $c'_3 = 1.3732\ 10^{-2}$, $c'_4 = 1.3587\ 10^{-3}$, $c'_5 = -1.0726\ 10^{-4}$, $c'_6 = -7.0463\ 10^{-6}$, $c'_7 = 3.9639\ 10^{-7}$, $c'_8 = 1.9500\ 10^{-8}$, $c'_9 = -8.5349\ 10^{-10}$, $c'_{10} = -3.3586\ 10^{-11}$. Figure 101 shows the exact cosine function and its Chebyshev approximation, together with the error incurred by the approximation for $N = 10$. Note that the error is closely estimated by the magnitude of the first neglected term of the expansion: $|c'_{10}| = 3.3586\ 10^{-11}$.

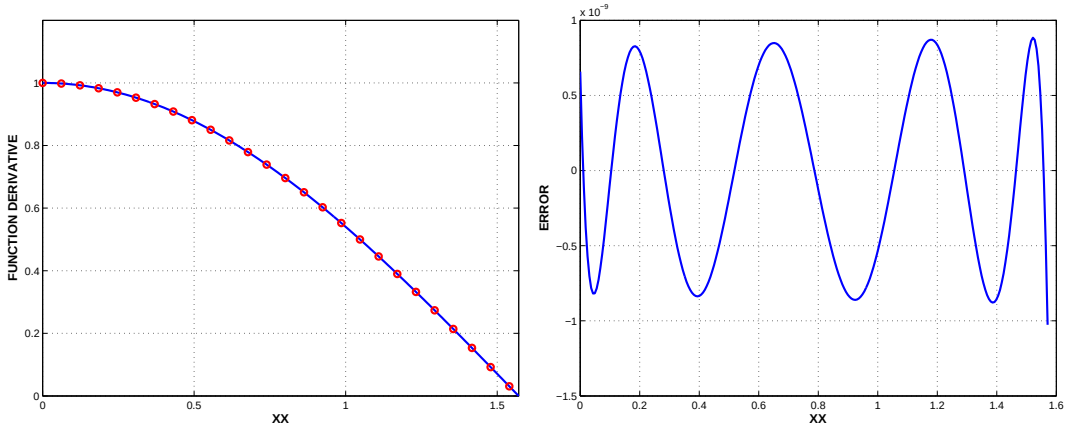

Figure 101: Left figure: Chebyshev polynomial expansion of function $f(x) = \sin x$, $x \in [0\pi]$. Function $f(x)$: solid line; Chebyshev expansion for N = 12: circles. Right figure: discrepancy between the exact function and its Chebyshev approximation.

C.2.5 Integral of Chebyshev polynomials

The following recurrence relationship is easy to prove

$$2T_n(x) = \frac{T'_{n+1}}{n+1} - \frac{T'_{n-1}}{n-1}, \tag{249}$$

with the help of eq. (236). It then follows that

$$2\int_{-1}^{+1} T_n(x)\ \mathrm{d}x = \begin{cases} \frac{2}{n+1} - \frac{2}{n-1} & n \text{ even}, \\ 0 & n \text{ odd} \end{cases} \tag{250}$$

These two equations are easily combined to yield

$$\int_{-1}^{+1} T_{2n}(x)\ \mathrm{d}x = -\frac{2}{4n^2-1}. \tag{251}$$

C.2.6 Clenshaw-Curtis quadrature

Consider the problem of evaluating the following integral $\int_a^b f(x)\ \mathrm{d}x$. To that effect, the function is first expanded in terms of Chebyshev polynomials,

$$\int_a^b f(x)\ \mathrm{d}x = \int_a^b \sum_{i=0}^{n} c_i T_i(x)\ \mathrm{d}x = \sum_{i=0}^{n} c_i \int_a^b T_i(x)\ \mathrm{d}x = \frac{b-a}{2} \sum_{i=0}^{n} c_i \int_{-1}^{+1} T_i(x)\ \mathrm{d}x, \tag{252}$$

where the coefficients c_i are found from eqs. (239a) and (239b) or eqs. (241a) and (241b). The integral of the Chebyshev polynomials are evaluated by eq. (251) to find

$$\int_a^b f(x)\ \mathrm{d}x = (b-a)\left[c_0 - \frac{c_2}{3} - \frac{c_4}{15} - \cdots - \frac{c_{2k}}{4k^2-1} - \cdots\right]. \tag{253}$$

C.3 Chebyshev approximation of functions of two variables

C.3.1 Expansion of a function in Chebyshev polynomials

Section C.2 describes the expansion of arbitrary functions of a single variable in series of Chebyshev polynomials. Clearly, functions of two variables can be similarly expanded in double series of Chebyshev polynomials

$$f(x,y) = \sum_{i=0}^{M-1} \sum_{j=0}^{N-1} c_{ij} T_i(x) T_j(y). \tag{254}$$

To find these coefficients given function $f(x,y)$, the above relationship is expressed at $x = x_k$, $y = y_\ell$, where x_k and y_ℓ the zeros of $T_M(x)$ and $T_N(y)$, respectively, as given by eq. (227). This yields $f(x_k, y_\ell) \approx \sum_{i=0}^{M-1} \sum_{j=0}^{N-1} c_{ij} T_i(x_k) T_j(y_\ell)$. Multiplying both sides of this equation by $T_p(x_k) T_q(y_\ell)$ and summing the resulting equations expressed at all zeros of $T_M(x)$ and $T_N(y)$ leads to

$$\sum_{k=1}^{M} \sum_{\ell=1}^{N} f(x_k, y_\ell) T_p(x_k) T_q(y_\ell) = \sum_{i=0}^{M-1} \sum_{j=0}^{N-1} c_{ij} \left[\sum_{k=1}^{M} T_i(x_k) T_p(x_k)\right] \left[\sum_{\ell=1}^{N} T_j(y_\ell) T_q(y_\ell)\right]. \tag{255}$$

In view of the discrete orthogonality relationship of Chebyshev polynomials, eq. (232), it then follows that

$$c_{00} = \frac{1}{MN} \sum_{k=1}^{M} \sum_{\ell=1}^{N} f(x_k, y_\ell), \tag{256a}$$

$$c_{i0} = \frac{2}{MN} \sum_{k=1}^{M} \sum_{\ell=1}^{N} f(x_k, y_\ell) T_i(x_k), \tag{256b}$$

$$c_{0j} = \frac{2}{MN} \sum_{k=1}^{M} \sum_{\ell=1}^{N} f(x_k, y_\ell) T_j(y_\ell), \tag{256c}$$

$$c_{ij} = \frac{4}{MN} \sum_{k=1}^{M} \sum_{\ell=1}^{N} f(x_k, y_\ell) T_i(x_k) T_j(y_\ell). \tag{256d}$$

In some cases, function $f(x, y)$ is partially expanded in Chebyshev series. For instance, the function dependency on the y variable is in the form of a Chebyshev expansion, whereas its dependency on the x variable is not, *i.e.*

$$f(x, y) = \sum_{j=0}^{N-1} g_j(x) T_j(y). \tag{257}$$

The coefficients of the complete Chebyshev expansion are found by introducing the above expression into eqs. (256a) and (256d) to find

$$c_{0j} = \frac{1}{M} \sum_{k=1}^{M} g_j(x_k), \tag{258a}$$

$$c_{ij} = \frac{2}{M} \sum_{k=1}^{M} g_j(x_k) T_i(x_k). \tag{258b}$$

C.3.2 Evaluation of Chebyshev expansions: Clenshaw's recurrence

If the coefficients of the two dimensional Chebyshev expansion are known, the function can be evaluated using eq. (254). However, here again, rather than computing the polynomials then summing all contributions, it is preferable to use Clenshaw's recurrence defined by eq. (243). To that effect, eq. (254) is rewritten as

$$f(x, y) = \sum_{i=0}^{M-1} \left[\sum_{j=0}^{N-1} c_{ij} T_j(y) \right] T_i(x) = \sum_{i=0}^{M-1} d_i(y) T_i(x). \tag{259}$$

Clenshaw's recurrence, eq. (243), is first used M times to compute the coefficients d_i, $i = 0, 1, \ldots, M-1$. Finally, one more application of Clenshaw's recurrence yields the desired value of the function. Of course, it is also possible to recast eq. (254) as

$$f(x,y) = \sum_{j=0}^{N-1} \left[\sum_{i=0}^{M-1} c_{ij} T_i(x) \right] T_j(y) = \sum_{j=0}^{N-1} g_j(x) T_j(y). \tag{260}$$

At first, N applications of Clenshaw's recurrence yield the coefficients g_j, $j = 0, 1, \ldots, N-1$, and one additional step yields the desired function value.

Using this second option, Clenshaw's recurrence, characterized by eqs. (242a) to (242e), is rewritten as

$$y_{M+1,j} = 0, \tag{261a}$$

$$y_{M,j} = 0, \tag{261b}$$

$$y_{M-1,j} = c_{M-1,j} - y_{M+1,j} + 2x\ y_{M,j}, \tag{261c}$$

$$\vdots$$

$$y_{1,j} = c_{1,j} - y_{3,j} + 2x\ y_{2,j}, \tag{261d}$$

$$y_{0,j} = c_{0,j} - y_{2,j} + 2x\ y_{1,j}. \tag{261e}$$

The coefficients, $g_j(x)$, now simply become

$$g_j(x) = (c_{0,j} - y_{2,j}) + y_{1,j}\ x = y_{0,j} - x\ y_{1,j}. \tag{262}$$

Clenshaw's recurrence applied to the coefficients $g_j(x)$ then yields the desired function value.

C.3.3 Derivatives of Chebyshev expansions

Consider now a function of two variables and its derivative with respect to x, both expanded in Chebyshev series

$$f(x,y) = \sum_{i=0}^{M-1} \sum_{j=0}^{N-1} c_{ij} T_i(x) T_j(y), \quad \text{and} \quad f'(x,y) = \sum_{i=0}^{M-2} \sum_{j=0}^{N-1} c'_{ij} T_i(x) T_j(y), \tag{263}$$

where the notation $(\cdot)'$ indicates a derivative with respect to x. What is the relationship between the coefficients of the two expansions, c_{ij} and c'_{ij}? Using the formula for the derivatives of Chebyshev polynomials, eq. (236), the following recurrence is found

$$c'_{M,j} = 0, \tag{264a}$$

$$c'_{M-1,j} = 0, \tag{264b}$$

$$c'_{M-2,j} = 2 \times (M-1)\ c_{M-1,j} + c'_{M,j}, \tag{264c}$$

$$\vdots$$

$$c'_{1,j} = 2 \times 2\ c_{2,j} + c'_{3,j}, \tag{264d}$$

$$c'_{0,j} = (2 \times 1\ c_{1,j} + c'_{2,j})/2. \tag{264e}$$

Consider next a function of two variables and its derivative with respect to y, both expanded in Chebyshev series

$$f(x,y) = \sum_{i=0}^{M-1} \sum_{j=0}^{N-1} c_{ij} T_i(x) T_j(y), \quad \text{and} \quad f^+(x,y) = \sum_{i=0}^{M-1} \sum_{j=0}^{N-2} c^+_{ij} T_i(x) T_j(y). \tag{265}$$

where the notation $(\cdot)^+$ indicates a derivative with respect to y. What is the relationship between the coefficients of the two expansions, c_{ij} and c^+_{ij}? Using the formula for the derivatives of Chebyshev polynomials, eq. (236), the following recurrence is found

$$c^+_{i,N} = 0, \tag{266a}$$

$$c^+_{i,N-1} = 0, \tag{266b}$$

$$c^+_{i,N-2} = 2 \times (N-1)\ c_{i,N-1} + c^+_{i,N}, \tag{266c}$$

$$\vdots$$

$$c^+_{i,1} = 2 \times 2\ c_{i,2} + c^+_{i,3}, \tag{266d}$$

$$c^+_{i,0} = (2 \times 1\ c_{i,1} + c^+_{i,2})/2. \tag{266e}$$

REFERENCES

[1] Abramowitz, M. and Stegun, I., *Handbook of Mathematical Functions*. New York: Dover Publications, Inc., 1964.

[2] Altmikus, A., Wagner, S., Beaumier, P., and Servera, G., "A comparison: Weak versus strong modular coupling for trimmed aeroelastic rotor simulations," in *American Helicopter Society 58th Annual Forum Proceedings*, (Montreal, Ouebec), June 2002.

[3] Ananthan, S., Leishman, J., and Ramaswamy, M., "The role of filament stretching in the free-vortex modeling of rotor wakes," in *Proceedings of the American Helicopter Society 58th Annual National Forum*, June 2002.

[4] Anderson, J., *Fundamentals of Aerodynamics*. McGraw-Hill Series in Aeronautical and Aerospace Engineering, New York, NY: McGraw-Hill Higher Education, 2001.

[5] Bagai, A. and Leishman, J., "Rotor free-wake modeling using a pseudo-implicit technique - Including comparisons with experimental data," *Journal of the American Helicopter Society*, vol. 40, no. 3, pp. 29–41, 1995.

[6] Bagai, A. and Leishman, J., "Rotor free-wake modeling using a pseudoimplicit relaxation algorithm," *Journal of Aircraft*, vol. 32, pp. 1276–1285, November-December 1995.

[7] Bagai, A. and Leishman, J., "Free-wake analysis of tandem, tilt-rotor and coaxial rotor configurations," *Journal of the American Helicopter Society*, vol. 41, pp. 196–207, July 1996.

[8] Bagai, A., Leishman, J., and Park, J., "Aerodynamic analysis of a helicopter in steady maneuvering flight using a free-vortex rotor wake model," *Journal of the American Helicopter Society*, vol. 44, no. 2, pp. 109–120, 1999.

[9] Batchelor, G., *An Introduction to Fluid Dynamics*. Cambridge, UK: Cambridge University Press, 1967.

[10] Bauchau, O., *DYMORE: A Finite Element Based Tool for the Analysis of Nonlinear Flexible Multibody Systems*. Georgia Institute of Technology.

[11] Bauchau, O., "Computational schemes for flexible, nonlinear multi-body systems," *Multibody System Dynamics*, vol. 2, pp. 169–225, 1998.

[12] Bauchau, O. and Bottasso, C., "On the design of energy preserving and decaying schemes for flexible, nonlinear multi-body systems," *Computer Methods in Applied Mechanics and Engineering*, vol. 169, pp. 61–79, 1999.

[13] Bauchau, O., Bottasso, C., and Nikishkov, Y., "Modeling rotorcraft dynamics with finite element multibody procedures," *Mathematical and Computer Modeling*, vol. 33, pp. 1113–1137, 2001.

[14] Bauchau, O., Bottasso, C., and Trainelli, L., "Robust integration schemes for flexible multibody systems," *Computer Methods in Applied Mechanics and Engineering*, vol. 192, pp. 395–420, 2003.

[15] Bauchau, O. and Liu, H., "On the modeling of hydraulic components in rotorcraft systems," *Journal of the American Helicopter Society*, vol. 51, no. 2, pp. 175–184, 2006.

[16] Bauchau, O. and Theron, N., "Energy decaying scheme for non-linear beam models," *Computer Methods in Applied Mechanics and Engineering*, vol. 134, pp. 37–56, 1996.

[17] Bauchau, O. and Theron, N., "Energy decaying schemes for nonlinear elastic multi-body systems," *Computers and Structures*, vol. 59, pp. 317–331, 1996.

[18] Bauchau, O. and Ahmad, J., "Advanced CFD and CSD methods for multidisciplinary applications in rotorcraft problems," in *AIAA, NASA, & ISSMO, Symposium on Multidisciplinary Analysis and Optimization*, (Bellevue, WA), September 4-6 1996.

[19] Beaumier, P., "A coupling procedure between a rotor dynamics code and a 3D unsteady full potential code," in *Amercian Helicopter Society 3rd Decennial Specialists' Conference on Aeromechanics*, (San Francisco, CA), January 1994.

[20] Beddoes, T., "Representation of airfoil behavior," *Vertica*, vol. 7, no. 2, pp. 183–197, 1983.

[21] Beddoes, T., "Practical computation of unsteady lift," *Vertica*, vol. 8, no. 1, pp. 55–71, 1984.

[22] Beddoes, T., "A wake model for high resolution airloads," in *Proceedings of the 2nd International Conference on Basic Rotorcraft Research*, (Univ. of Maryland, College Park, MD), Feburary 1985.

[23] Benoit, B., Dequin, A.-M., Kampa, K., Grunhagen, W., Basset, P.-M., and Gimonet, B., "Host: A general helicopter simulation tool for germany and france," in *American Helicopter Society 56th Annual Forum Proceedings*, (Virginia Beach, VA), May 2000.

[24] Bhagwat, M. and Leishman, G., "Time-accurate free-vortex wake model for dynamic rotor response," in *Aeromechanics 2000, American Helicopter Society Specialist Meeting*, (Altanta, GA), November 13-14 2000.

[25] Bhagwat, M. and Leishman, G., "Transient rotor inflow using a time-accurate free-vortex wake model," in *39th AIAA Aerospace Sciences Meeting & Exhibit*, (Reno, NV), January 8-11 2001.

[26] Bhagwat, M. and Leishman, J., "Correlation of helicopter tip vortex measurements," *AIAA Journal*, vol. 38, no. 2, pp. 301–308, 2000.

[27] Bhagwat, M. and Leishman, J., "Stability analysis of helicopter rotor wakes in axial flight," *Journal of the American Helicopter Society*, vol. 45, no. 3, pp. 165–178, 2000.

[28] Bhagwat, M. and Leishman, J., "Accuracy of straight-line segmentation applied to curvilinear vortex filaments," *Journal of the American Helicopter Society*, vol. 46, pp. 166–169, April 2001.

[29] Bhagwat, M. and Leishman, J., "Stability, consistency and convergence of time-marching free-vortex rotor wake algorithms," *Journal of the American Helicopter Society*, vol. 46, pp. 59–71, January 2001.

[30] Bhagwat, M., Ormiston, R., Saberi, H., and Hong, X., "Application of CFD/CSD coupling for analysis of rotorcraft airloads and blade loads in maneuvering flight," in *American Helicopter Society 63rd Annual Forum Proceedings*, (Virginia Beach, VA), May 1-3 2007.

[31] Bliss, D. and Miller, W., "Efficient free wake calculations using analytical/numerical matching," *Journal of the American Helicopter Society*, vol. 38, pp. 43–52, April 1993.

[32] Boniface, J.-C., *Calcul d'écoulements compressibles autour de rotors d'hélicoptères en vol stationaire ou en vol d'advancement par résolution des équations d'Euler*. PhD thesis, Ecole Nationale Supérieure des Arts et Métiers, December 1995.

[33] Bousman, W., "A qualitative examination of dynamic stall from flight test data," in *American Helicopter Society 53rd Annual Forum Proceedings*, (Virginia Beach, VA), April 1997.

[34] Bousman, W., "Putting the aero back into aeroelasticity," in *8th ARO Workshop on Aeroelasticity of Rotorcraft Systems*, (University Park, PA), October 1999.

[35] Bousman, W. and Maier, T., "An investigation of helicopter rotor blade flap vibratory loads," in *American Helicopter Society 48th Annual Forum Proceedings*, (Washington, DC), June 1992.

[36] Brown, R., "Rotor wake modeling for flight dynamic simulation of helicopters," *AIAA Journal*, vol. 38, January 2000.

[37] Canon, R., *Dynamics of Physical Systems*, ch. 4. New York: McGraw-Hill Book Company, 1967.

[38] Caradonna, F. and Isom, M., "Subsonic and transonic potential flow over helicopter rotor blades," *AIAA Journal*, vol. 10, January 1972.

[39] Cardona, A. and Géradin, M., "Modeling of a hydraulic actuator in flexible machine dynamics simulation," *Mechanisms and Machine Theory*, vol. 25, pp. 193–207, 1990.

[40] Chan, W., Meakin, R., and Potsdam, M., "CHSSI software for geometrically complex unsteady aerodynamic applicaitons," in *AIAA 39th Aerospace Sciences Meeting and Exhibit*, (Reno, NV), January 2001.

[41] Crimi, P., "Theoretical prediction of the flow in the wake of a helicopter rotor," Tech. Rep. BB-1994-5-1, Cornell Aeronautical Lab., Buffalo, NY, September 1965.

[42] Datta, A., Baeder, J., and Chopra, I., "Prediction of rotor aerodynamic and structural loads at three critical level flight conditions," in *31st European Protorcraft Forum*, (Florence, Italy), September 12-15 2005.

[43] Datta, A. and Chopra, I., "Prediction of UH-60A dynamic stall loads in high altitude level flight using CFD/CSD coupling," in *American Helicopter Society 61st Annual Forum*, (Grapevine, Texas), June 1-3 2005.

[44] Datta, A. and Chopra, I., "Prediction of UH-60 vibratory loads at three critical level flight conditions," in *32nd European Protorcraft Forum*, (Maastricht, Netherlands), September 2006.

[45] Datta, A., Sitaraman, J., Chopra, I., and Baeder, J., "Improved comprehensive analysis for prediction of rotor vibratory loads in high-speed forward flight," in *Amercian Helicopter Society 60th Annual Forum*, (Baltimore, MD), June 7-10 2004.

[46] Datta, A., Sitaraman, J., Chopra, I., and Baeder, J., "CFD/CSD prediction of rotor vibratory loads in high-speed flight," *Journal of Aircraft*, vol. 43, pp. 1698–1709, November-December 2006.

[47] Farin, G., *Curves and Surfaces for Computer Aided Geometric Design*. Boston: Academic Press Inc., 2 ed., 1992.

[48] Friedmann, P. P., "Renaissance of aeroelasticity and its future," *Journal of Aircraft*, vol. 36, no. 1, pp. 105–121, 1999.

[49] Friedmann, P. P., "Rotary-wing aeroelasticity: Current status and future trends," *Journal of Aircraft*, vol. 42, no. 10, pp. 1953–1971, 2004.

[50] Friedmann, P. P. and Hodges, H. D., "Rotary wing aeroelasticity - a historical perspective," *Journal of Aircraft*, vol. 40, no. 6, pp. 1019–1045, 2003.

[51] Gray, R., "On the motion of the helical vortex shed from a single bladed hovering model rotor and its application to the calculation of the spanwise aerodynamic loading," Tech. Rep. No. 313, Princeton University Aero. Engineering Department, September 1995.

[52] Hariharan, N. and Sankar, L., "Review of computational techniques for rotor wake modeling," in *AIAA 38th Aerospace Sciences Meeting and Exhibit*, (Reno, NV), 2000 January.

[53] Hill, M., *COUPLED FLUID-STRUCTURE SIMULATIONS OF HELICOPTER ROTORS*. PhD thesis, The Pennsylvania State University, August 2006.

[54] Howlett, J., "Uh-60A black hawk engineering simulation program: Vol. i - mathematical model," Tech. Rep. NASA CR-166309, National Aeronautics and Space Administration, December 1981.

[55] Johnson, W., "Development of a comprehensive analysis for rotorcraft - I. rotor model and wake analysis," *Vertica*, vol. 5, pp. 99–130, 1981.

[56] Johnson, W., "Development of a comprehensive analysis for rotorcraft - II. aircraft model, solution procedure and application," *Vertica*, vol. 5, pp. 185–216, 1981.

[57] Johnson, W., *CAMRAD/JA; A Comprehensive Analytical Model of Rotorcraft Aerodynamics and Dynamics; Johnson Aeronautics Version; Volume I, Theory Manual*. Johnson Aeronautics, Palo, Alto, California, 1988.

[58] Johnson, W., "Rotorcraft aerodyanmic models for a comprehensive analysis," in *American Helicopter Society 54th Annual Forum*, (Washington, D.C.), May 1998.

[59] Kocurek, J. and Berkovitz, L., "Velocity coupling: A new concept for hover and axial flow wake analysis and design," in *AGARD Prediction of Loads on Rotorcraft*, May 1982.

[60] Kuethe, A. M. and Chow, C.-Y., *Foundations of Aerodynamics*. New York, NY: John Wiley & Sons, Inc, 1998.

[61] Kufeld, R., Balough, D., Cross, J., Studebaker, K., Jennison, C., and Bousman, W., "Flight testing of the uh-60A airloads aircraft," in *American Helicopter Society 50th Annual Forum Proceedings*, (Washington, DC), May 1994.

[62] Kunz, L. D., "Comprehensive rotorcraft analysis: Past, present, and future," in *46th AIAA/SIME/ASCE/AHS/ASC Structures, Structural Dynamics & Materials Conference, April 18-21*, 2005.

[63] Landgrebe, A., "The wake geometry of a hovering rotor and its influence on rotor performance," *Journal of the American Helicopter Society*, vol. 17, no. 4, pp. 2–15, 1972.

[64] Landgrebe, A. and Cheney, M., "Rotor wakes - key to performance prediction," in *AGARD Conference on Aerodynamics of Rotary Wings*, February 1973.

[65] Leishman, G., Bhagwat, M., and Ananthan, S., "Free-vortex wake prediction of the vortex ring state for single-rotor and multi-rotor configurations," in *the American Helicopter Society International Specialists Meeting on Aerodynamics, Acoustics and test & Evaluation*, (San Francisco, CA), January 23-25 2002.

[66] Leishman, G., Bhagwat, M., and Ananthan, S., "Free-vortex wake prediction of the vortex ring state for single-rotor and multi-rotor configurations," in *58th Annual Forum and Technology Display of the American Helicopter Society International*, (Montréal, Canada), June 11-13 2002.

[67] Leishman, J., "Two dimensional model for airfoil unsteady drag below stall," *Journal of Aircraft*, vol. 25, no. 7, pp. 665–666, 1988.

[68] Leishman, J., "Validation of approximate indicial aerodynamic functions for two-dimensional subsonic flow," *Journal of Aircraft*, vol. 25, no. 10, pp. 914–922, 1988.

[69] Leishman, J., "Modeling sweep effects on dynamic stall," *Journal of the American Helicopter Society*, vol. 34, no. 3, pp. 18–29, 1989.

[70] Leishman, J., "Modeling of subsonic unsteady aerodynamics for rotary wing applications," *Journal of the American Helicopter Society*, vol. 35, no. 1, pp. 29–38, 1990.

[71] Leishman, J., *Principles of Helicopter Aerodynamics*. Cambridge, NY: Cambridge University Press, 2 ed., 2006.

[72] Leishman, J. and Beddoes, T., "A semi-empirical model for dynamic stall," *Journal of the American Helicopter Society*, vol. 34, no. 3, pp. 3–17, 1989.

[73] Leishman, J., Bhagwat, M., and Bagai, A., "Free-vortex filament methods for the analysis of helicopter rotor wakes," *Journal of Aircraft*, vol. 39, no. 5, pp. 759–775, 2002.

[74] Lim, J. and Anastassiades, T., "Correlation of 2gchas analysis with experimental data," *Journal of the American Helicopter Society*, vol. 40, pp. 18–33, October 1995.

[75] Livne, E., "Future of airplane aeroelasticity," *Journal of Aircraft*, vol. 40, no. 6, pp. 1066–1092, 2003.

[76] Miller, W. and Bliss, D., "Direct periodic solutions of rotor free wake calculations," *Journal of the American Helicopter Society*, vol. 38, pp. 53–60, April 1993.

[77] Nguyen, K. and Johnson, W., "Evaluation of dynamic stall models with flight test data," in *American Helicopter Society 54th Annual Forum Proceedings*, (Washington, DC), May 1998.

[78] Nygaard, A., Saberi, H., Ormiston, R., Strawn, C., and Potsdam, M., "CFD and CSD coupling algorithms and fluid structure interface for rotorcraft aeromechanics in steady and transient flight conditions," in *the American Helicopter Society 62nd Annual Forum*, (Phoenix, AZ), Many 9-11 2006.

[79] Pahlke, K. and van der Wall, B., "Calculation of multibladed rotors in high-speed forward flight with weak fluid-structure coupling," in *27th European Rotorcraft Forum*, (Moscow, Russia), September 2001.

[80] Peters, D. and Barwey, D., "A general theory of rotorcraft trim," *Mathematical Problems in Engineering*, vol. 2, pp. 1–34, 1996.

[81] Peters, D. and He, C., "Finite state induced flow models. Part II: Three-dimensional rotor disk," *Journal of Aircraft*, vol. 32, no. 2, pp. 323–333, 1995.

[82] Peters, D., Karunamoorthy, S., and Cao, W., "Finite state induced flow models. Part I: Two-dimensional thin airfoil," *Journal of Aircraft*, vol. 32, no. 2, pp. 313–322, 1995.

[83] Piegl, L. and Tiller, W., *The Nurbs Book*. Berlin, New Jersey: Springer-Verlag, 2 ed., 1997.

[84] Potsdam, M., Yeo, H., and Johnson, W., "Rotor airloads prediction using loose aerodynamic/strucutral coupling," in *American Helicopter Society 60th Annual Forum Proceedings*, (Baltimore, MD), June 2004.

[85] Press, W., Flannery, B., Teutolsky, S., and Vetterling, W., *Numerical Recipes. The Art of Scientific Computing*. Cambridge: Cambridge University Press, 1990.

[86] Sankar, L., Wake, B., and Lekoudis, S., "Solution of the unsteady EULER equations for fiexed and rotor wing configurations," *Journal of Aircraft*, vol. 23, April 1986.

[87] Schuster, M. D., Liu, D. D., and Huttselll, J. L., "Computational aeroelasticity: Success, progress, challenge," *Journal of Aircraft*, vol. 40, no. 5, pp. 843–855, 2003.

[88] Servera, G., Beaumier, P., and Costes, M., "A weak coupling method between the dynamics code host and he 3D unsteady EULER code waves," in *26th European Rotorcraft Forum*, (The Hague, Netherlands), September 2001.

[89] Shenoy, K. and Gray, R., "Iterative lifting surface method for thick bladed hovering helicopter rotors," *Journal of Aircraft*, vol. 18, pp. 417–424, June 1981.

[90] Sitaraman, J. and Baeder, J., "Evaluation of the wake prediction methodologies used in CFD based rotor airload computations," in *24th Applied Aerodynamics Conference*, (San Francisco, CA), June 5-8 2006.

[91] Sitaraman, J., Datta, A., Baeder, J., and Chopra, I., "Fundamental understanding and prediction of rotor vibratory loads in high-speed forward flight," in *29th European Rotorcraft Forum*, (Friedrichshafen, Germany), September 2003.

[92] Steihoff, J., Yonghu, W., Mersch, T., and Senge, H., "Computational vorticity capturing - application to helicopter rotor flow," in *AIAA 30th Aerospace Sciences Meeting*, (Reno, NV), January 1992.

[93] Strawn, R. and Bridgeman, J., "An improved three-dimensional aerodynamics model for helicopter airloads prediction,," in *AIAA 29th Aerospace Sciences Meeting and Exhibit*, (Reno, NV), January 1991.

[94] Strawn, R. and Caradonna, F., "Numerical modeling of rotor flows with a conservative form of the full potential equation," in *AIAA 24th Aerospace Sciences Meeting*, (Reno, NV), January 6-9 1986.

[95] Strawn, R. and Caradonna, F., "Conservative full potential model for unsteady transonic rotor flows," *AIAA Journal*, vol. 25, Feburary 1987.

[96] Strawn, R., Desopper, A., Miller, M., and Jones, A., "Correlation of puma airloads - evaluation of CFD predition methods," in *15th European Protorcraft Forum*, (Amsterdam, Netherlands), September 1989.

[97] Truesdell, C., *The Kinematics of Vorticity*. Bloomington, IN: Indiana Univ. Press, 1954.

[98] Tung, C., Caradonna, F., and Johnson, W., "The prediction of transonic flows on an advancing rotor," in *American Helicopter Society 40th Annual Forum Proceedings*, (Arlington, VA), May 1984.

[99] Vatistas, G., Kozel, V., and Mih, W., "A simpler model of concentrated vortices," *Experiments in Fluids*, vol. 11, pp. 73–76, 1991.

[100] Viersma, T., *Analysis, Synthesis and Design of Hydraulic Servo-Systems and Pipelines*, ch. 1-2. Amsterdam: Elsevier, 1981.

[101] Wake, B. and Sankar, L., "Solution of Navier-Stokes equations for the flow over a rotor blade," *Journal of American Helicopter Society*, 1989.

[102] Wang, C., Bridgeman, J., Steinhoff, J., and Yonghu, W., "The application of computational vorticity confinement ot helicopter rotor and body flows," in *American Helicopter Society 49th Annual Forum Proceedings*, (St. Louis, Missouri), May 1993.

[103] Welsh, W., "Simulation and correlation of a helicopter air-oil strut dynamic response," in *American Helicopter Society 43rd Annual Forum Proceedings*, (St. Louis, Missouri), May 1987.

[104] Welsh, W., "Dynamic modeling of a helicopter lubrication system," in *American Helicopter Society 44th Annual Forum Proceedings*, (Washington, DC), June 1988.

[105] Wereley, M. N., "Bring relevance to freshman aerospace engineering: Demonstation of model scale comanche helicopter lag mode damper," *Internaltion Journal of Engineering*, vol. 13, no. 5, pp. 369–375, 1997.

[106] Yeo, H. and Johnson, W., "Assessment of comprehensive analysis calculation on helicopter rotors," in *American Helicopter Society 4th Decennial Specialists' Conference on Aeromechanics*, (San Francisco, CA), January 2004.

VITA

Haiying Liu was born in Sichuan Province in P.R. China in 1977. She received her Bachelor of Science in July of 2000 and Master of Science in July of 2002 in the School of Jet Propulsion from the Beijing University of Aeronautics and Astronautics. From August 2002 to December 2007, she has been working as a graduate research assistant pursuing her doctoral degree in the School of Aerospace Engineering at the Georgia Institute of Technology, Atlanta, Georgia, USA. She became a Ph.D. candidate in October 2004, and received another Master's degree here in August, 2005. Her research interests include structural/multibody dynamics, aeroelastiticy, and aerodynamics. During her Ph.D. program, she accomplished a project that involved physics-based hydraulic device modeling with an application in lead-lag damper modeling in rotorcraft analysis, 2004. She established an interface between computational fluid dynamics analysis code (OVERFLOW-2) and computational structure dynamics analysis code (DYMORE) to perform computational aeroelastic analysis, 2005. This interface was employed to predict airloads of different flights for UH60 **B**lack **H**awk aircraft. She established a NURBS-based representation of vortex wake structures, based on which prescribed and free-wake models were developed and implemented in DYMORE. This work yielded an efficient free-wake analysis method and is of great importance in the preliminary rotorcraft designs.